

Dissertation zur Erlangung des Doktorgrades
der Fakultät für Chemie und Pharmazie
der Ludwig-Maximilians-Universität München

**Solvothermal and Ionothermal Approaches to
Carbon Nitride Chemistry**

Eva Antonie Wirnhier
aus
Landau / Isar, Deutschland

2013

Erklärung

Diese Dissertation wurde im Sinne von § 7 der Promotionsordnung vom 28. November 2011 von Herrn Prof. Dr. Wolfgang Schnick betreut.

Eidesstattliche Versicherung

Diese Dissertation wurde eigenständig und ohne unerlaubte Hilfe erarbeitet.

München, den 14.03.2013

.....
Eva Antonie Wirnhier

Dissertation eingereicht am 14.03.2013

1. Gutachter: Prof. Dr. Wolfgang Schnick

2. Gutachter: Prof. Dr. Jürgen Senker

Mündliche Prüfung am 08.05.2013

Meiner Familie

Acknowledgements

Herrn Prof. Dr. Wolfgang Schnick danke ich für die Aufnahme in seinen Arbeitskreis und die Betreuung meiner Doktorarbeit auf diesem sehr interessanten und interdisziplinären Thema. Besonders bedanken möchte ich mich für die Freiheit bei der Gestaltung der Arbeit sowie Möglichkeit, an zahlreichen Tagungen, Weiterbildungen und Kooperationen teilzuhaben.

Weiterhin möchte ich Herrn Prof. Dr. Jürgen Senker für die Übernahme des Korreferats und für die gute Zusammenarbeit in den letzten Jahren danken.

Frau Prof. Dr. Bettina V. Lotsch, Frau Prof. Dr. Christina Scheu, Herrn Prof. Dr. Konstantin Karaghiosoff und Herrn Prof. Dr. Hans-Christian Böttcher danke ich für die Bereitschaft, als weitere Prüfer zur Verfügung zu stehen.

Besonderer Dank geht an meine Vorgänger und Nachfolger auf dem CN-Thema, Nicole Braml, Dr. Barbara Jürgens, Prof. Dr. Bettina V. Lotsch, Dr. Sophia Makowski und Dr. Andreas Sattler für ihre Vorarbeiten, Ideen und Bereitschaft, dieses Thema immer wieder neu zu erfinden. Vor allem möchte ich unserem „Hahn im Korb“, Dr. Andreas Sattler, für seine Einführung in die CN-Chemie danken und Nicole Braml und Dr. Sophia Makowski für zahlreiche fachliche und nichtfachliche Diskussionen, die Abwechslung in den Laboralltag gebracht haben!

Allen meinen (Ex-)Laborkollegen in D2.103, Dr. Yamini Avadhut, Nicole Braml, Dr. Cordula Braun, Dajana Durach, Dr. Sophia Makowski, Christian Minke, Katrin Rudolf und Dr. Andreas Sattler, danke ich für die schöne und wortspielreiche Zeit und eine gute und (zumindest zumeist) ordentliche Arbeitsatmosphäre in unserem „Mädchenlabor“ ;-). Mögen unsere außeruniversitären Labortreffen auch weiterhin Bestand haben!

Bei meinen Bachelor- und F-Praktikanten Sandra Kiese, Manuel Güntner, Erika Mühlbauer und Ruth Boller möchte ich mich für ihre tatkräftige Unterstützung bedanken.

Für zahlreiche deliziose Mittagessen danke ich meiner Kochgruppe, die für Abwechslung im kulinarischen und chemischen Alltag und diverse „Fressnarkosen“ gesorgt hat: Dominik Baumann, Erik Flügel, Cora Hecht, Stephan Hug, Sebastian Junggeburth, Alexey Marchuk, Dr. Marianne Martin, Dr. Sandro Pagano, „Mâitre“ Florian Pucher, Dr. Stefan Sedlmaier, Linus Stegbauer, Stephan Werner und Dr. Martin Zeuner.

All meinen Kooperationspartnern danke ich für unzählige Messungen, hilfreiche Diskussionen und Ideen, abwechslungsreiche Treffen und einen vollen Emailaccount: Dr. Markus Döblinger, Prof. Dr. Bettina V. Lotsch und ihren Mitarbeitern Stephan Hug, Katharina Schwinghammer, Brian Tuffy und Hongji Wang; Prof. Dr. Alexander Moewes und Eamon McDermott; Prof. Dr. Oliver Oeckler, Dr. Tatjana Gorelik und Tobias Rosenthal; Prof. Dr. Christina Scheu und Kulpreet S. Viridi, Prof. Dr. Jürgen Senker und seinen Mitarbeiter Kilian Bärwinkel, Daniel Gunzelmann, Mario Lieb, Maria Mesch, Nadine Popp und Julia Wack.

Für technischen Support und die Durchführung zahlreicher Messungen hier am Department möchte ich danken:

- Christian Argyo für Photolumineszenzmessungen
- Nicole Braml und Dr. Sophia Makowski für DTA/TG-Messungen
- Brigitte Breitenstein für Massenspektren
- Robert Eicher, Gertraud Käser und Susanne Sauerer für Elementaranalysen
- Helmut „Pico“ Hartl für ICP-AES-Analysen
- Dr. Peter Mayer und Thomas Miller für Einkristallmessungen
- Peter Mayer und Christine Neumann für NMR-Messungen in Lösung
- Christian Minke für Festkörper-NMR-Messungen und REM/EDX-Sessions
- Florian Pucher für Unterstützung bei sämtlichen Pressen
- Marion Sokoll für IR-Spektren
- Wolfgang Wunschheim für Unterstützung in allen technischen Belangen

Allen weiteren Angehörigen der Arbeitskreise Schnick, Johrendt, Lotsch, Müller-Buschbaum, Oeckler und Schmedt auf der Günne danke ich für das offene, freundliche Arbeitsklima und ihre Unterstützung.

Ganz herzlicher Dank ergeht an meine Studienkollegen Pat Hanecker, André Heuer, Frauke Hintze, Andreas Maier, Sandra Lengger und Nicole Steinbach für eine tolle Studienzeit inklusive diverser regenerativer Maßnahmen ;-)

Mein allergrößter Dank gilt meiner (nun bald erweiterten) Familie, vor allem aber meinen Eltern und Martin, für ihre Unterstützung, Geduld und Ermutigungen während der gesamten Studiums- und Promotionszeit.

Life ... is a relationship between molecules.

(Linus Pauling)

Contents

1.	Introduction	1
2.	Summary	14
2.1	Melam, melam hydrate and a melam-melem adduct phase	15
2.2	Poly(triazine imide) with LiCl intercalation	16
2.3	Phosphorus-doped carbon nitride precursors	19
3.	On the Formation and Solvothermal Treatment of Melam	22
3.1	Introduction	24
3.2	Results and Discussion	26
3.3	Conclusion.....	37
3.4	Experimental Section	38
3.5	Bibliography.....	42
4.	Polytriazine Imide – Structure, Properties and Possible Applications	45
4.1	Poly(triazine Imide) with LiCl Intercalation (PTI/LiCl).....	46
4.1.1	Introduction	48
4.1.2	Results and Discussion.....	49
4.1.3	Conclusion.....	60
4.1.4	Experimental Section	61
4.1.5	Bibliography.....	64
4.2	Bandgap Determination of PTI/LiCl.....	68
4.2.1	Introduction	69
4.2.2	Experimental Section	71
4.2.3	DFT modeling	73
4.2.4	Experimental Discussion.....	76
4.2.5	Conclusions	81
4.2.6	Bibliography.....	83
4.3	Photocatalytic Activity of PTI/LiCl	85

5.	Phosphorus-doped Carbon Nitride Precursors	96
5.1	Biuretooxophosphates	97
5.1.1	Lithium, Potassium, Rubidium and Cesium Biuretooxophosphate	97
5.1.1.1	Introduction	98
5.1.1.2	Results and Discussion	99
5.1.1.3	Conclusion	107
5.1.1.4	Experimental Section	107
5.1.1.5	Bibliography	112
5.1.2	Calcium Biuretooxophosphate	115
5.1.2.2	Introduction	116
5.1.2.2	Results and Discussion	117
5.1.2.3	Conclusions	122
5.1.2.4	Experimental Section	123
5.1.2.5	Bibliography	125
5.2	<i>N,N'</i> -Bis(aminocarbonyl)phosphorodiamidates	127
5.2.1	Introduction	128
5.2.2	Results and Discussion	129
5.2.3	Conclusion	135
5.2.4	Experimental Section	135
5.2.5	Bibliography	138
6.	Discussion and Outlook	140
6.1	On the Formation and Solvothermal Treatment of Melam	140
6.2	Polytriazine Imide – Structure and Properties	142
6.3	Phosphorus-doped Carbon Nitride Precursors	144
6.4	Bibliography	147
7.	Appendix	148
7.1	Supporting Information	148
7.2	List of Publications	167
7.3	Contributions to Conferences	168
7.4	CSD and CCDC numbers	169
7.5	List of Abbreviations	170
7.6	Curriculum Vitae	173

1. Introduction

The search for new materials with outstanding chemical and physical properties is an ongoing quest in solid-state and materials science. With the isolation of graphene, a “flat monolayer of carbon atoms tightly packed into a two-dimensional (2D) honeycomb lattice” (Figure 1), *Geim* and *Novoselov* opened the gate to the prospering field of 2D materials and were therefore awarded with the nobel prize in physics in 2010.^[1,2] Theoretical calculations of *Landau* and *Peierls*^[3,4] considering strictly 2D materials thermodynamically unstable were thus disproved. However, this was not the first appearance of a 2D material. Already in 1962 *Boehm* et al. reported on very thin carbon foils with partial thicknesses of only 3 – 6 Å, pointing out to the formation of carbon monolayers.^[5] In the meantime, several papers on graphene synthesis, properties and possible applications appear every day, being reviewed frequently.^[6]

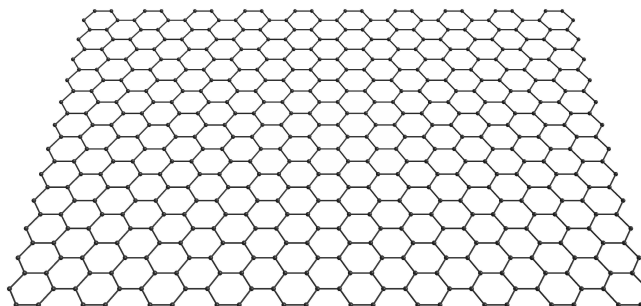


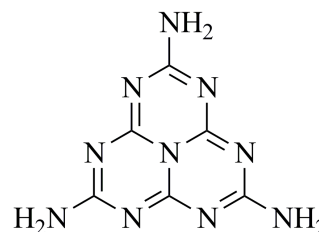
Figure 1. Graphen, a flat monolayer of carbon atoms packed into a 2D honeycomb lattice.

Nowadays, graphene is sometimes reckoned to be the new wonder material. Although being ultrathin, a tensile strength of 130 GPa, a breaking strength of 40 N m^{-1} and a Young's modulus of about 1 TPa ^[7] render graphene the strongest material ever measured, hundredfold stronger than steel. Moreover, its thermal conductivity reaches record values of around $5000 \text{ W m}^{-1} \text{ K}^{-1}$, thus significantly exceeding metals like copper, silver or gold.^[8] The electronic properties of graphene are unique as well, with its charge carriers mimicking massless Dirac fermions showing very high intrinsic mobilities and the integer quantum Hall effect at room temperature.^[9] A plethora of possible applications for graphene was discussed so far, sometimes praising this 2D material to be the new silicon. However, the lack of a

bandgap hinders graphene's use as semiconductor transistor and adds weight to a more "analogue" field of applications such as ultrahigh-frequency devices.^[10]

In the meantime, graphene has turned out to be only the tip of the 2D materials iceberg. Based on the methodology developed for graphene, a multitude of monolayered metal oxides, hydroxides and chalcogenides has been prepared, showing interesting distinct properties (mostly optoelectronic) compared to the bulk.^[11] Further investigations concentrate on the modification of graphene's properties by functionalization and doping^[12-15] or the fabrication of nanocomposites by sandwich-like stacking of the monolayers.^[16,17]

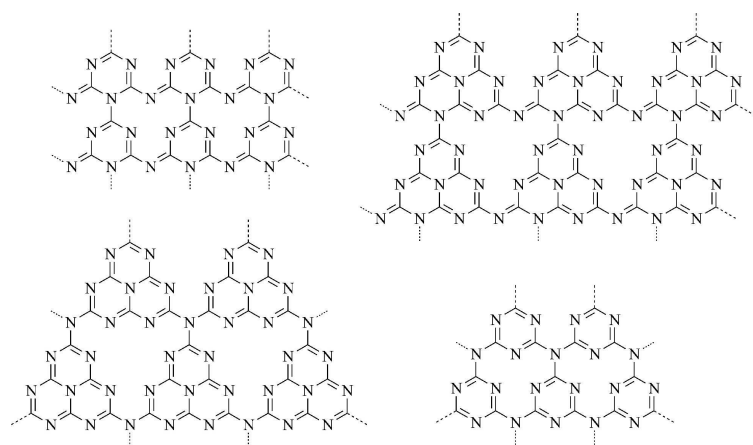
Compounds very similar to graphite, the "mother compound" of graphene, and therefore promising candidates for the formation of 2D materials with outstanding properties are graphite-like carbon nitride materials. First steps towards carbon nitride monolayers were conducted recently by *Müllen* and *Antonietti*, who prepared graphene-based carbon nitride nanocomposites by a nanocasting technology.^[18,19] By the use of graphene as template the low electrical conductivity of pure CN compounds ($<10^{-2} \text{ S cm}^{-1}$)^[20] could be overcome, yielding low-cost high-performance materials with long-term durability and high electrocatalytic activity for oxygen reduction reactions and the selective oxidation of saturated hydrocarbons. The features of these graphene-CN nanocomposites were proven to be superior to those observed for pure CN compounds whose revival inspired scientists during the last few years. Especially *Antonietti* et al. investigated intensively the properties and applicability of amorphous graphite-like carbon nitride compounds (often called "g-C₃N₄") which is mainly based on their electronic structure, classifying them as semiconductors with a bandgap of ~2.7 eV.^[21,22] Accordingly, absorption occurs in the visible region ($>420 \text{ nm}$, cf. diffuse reflectance spectra provided in [23]), rendering graphite-like carbon nitrides efficient photocatalysts, e.g. for hydrogen production by reduction of water. Theoretical calculations predicted these experimental results as the reduction level for H⁺ is well located in the middle of the above mentioned bandgap, therefore proving the reduction process to be energetically possible.^[23-25] Furthermore, DFT calculations revealed the HOMO of melem (2,5,8-triamino-tri-s-triazine,



Scheme 1: Melem, a tri-s-triazine-based precursor to polymeric carbon nitride networks.

Scheme 1, which was used as a model system for tri-*s*-triazine based polymeric carbon nitride networks) to consist exclusively of an antiphase combination of the p_z orbitals of the nitrogen atoms and therefore matching the symmetry of the highest unoccupied π type orbital in the Hückel model of benzene.^[21] This theoretical principle of “organic” activation of the benzene ring by transferring electron density from “g- C_3N_4 ” was corroborated by experimental result, proving “g- C_3N_4 ” to be a metal-free catalyst for Friedel-Crafts-reactions.^[26] The catalytic abilities of graphite-like carbon nitride materials were additionally demonstrated for the cyclization of nitriles and alkynes,^[27] the activation of CO_2 ,^[28] the selective oxidation of methane to methanol^[29] and the aerobic oxidative coupling of amines.^[30]

With the focus based on properties and possible applications of graphite-type networks, carbon nitride materials experience a third period of prosperity. Nearly quarter of a century ago, the pioneering work of Liu and Cohen evoked the “harder than diamond” fever, predicting compressibility comparable to diamond for still hypothetical binary sp^3 -hybridized carbon nitride C_3N_4 .^[31] Adopting β - Si_3N_4 structure, β - C_3N_4 was calculated to have a bulk modulus (which describes a substance’s resistance to uniform compression and is inversely proportional to both interatomic distances and ionicity) higher than diamond.^[32] Nevertheless, not only compression but also shearing strains have to be taken into account for the hardness of solids, thus suggesting a slightly lower hardness for β - C_3N_4 in comparison with



Scheme 2: Orthorhombic (top) and hexagonal (bottom) models of g - C_3N_4 , based on *s*-triazine (C_3N_3) and tri-*s*-triazine (C_6N_7) units.

published, including mostly physicochemical methods like CVD- and PVD processes, laser techniques and sputter processes.^[33-35] Another approach is derived from DFT-calculations, predicting the conversion of theoretically more stable layered graphitic C_3N_4 into sp^3 - C_3N_4 to

diamond.^[33] A multitude of further modifications for sp^3 -hybridized C_3N_4 was predicted to be stable, among these α - C_3N_4 (hexagonal), pseudocubic C_3N_4 (defect ZnS-type) and cubic C_3N_4 (Willemite-II-type).^[33] However, not only theoretical work but especially numerous attempts to synthesize sp^3 - C_3N_4 were

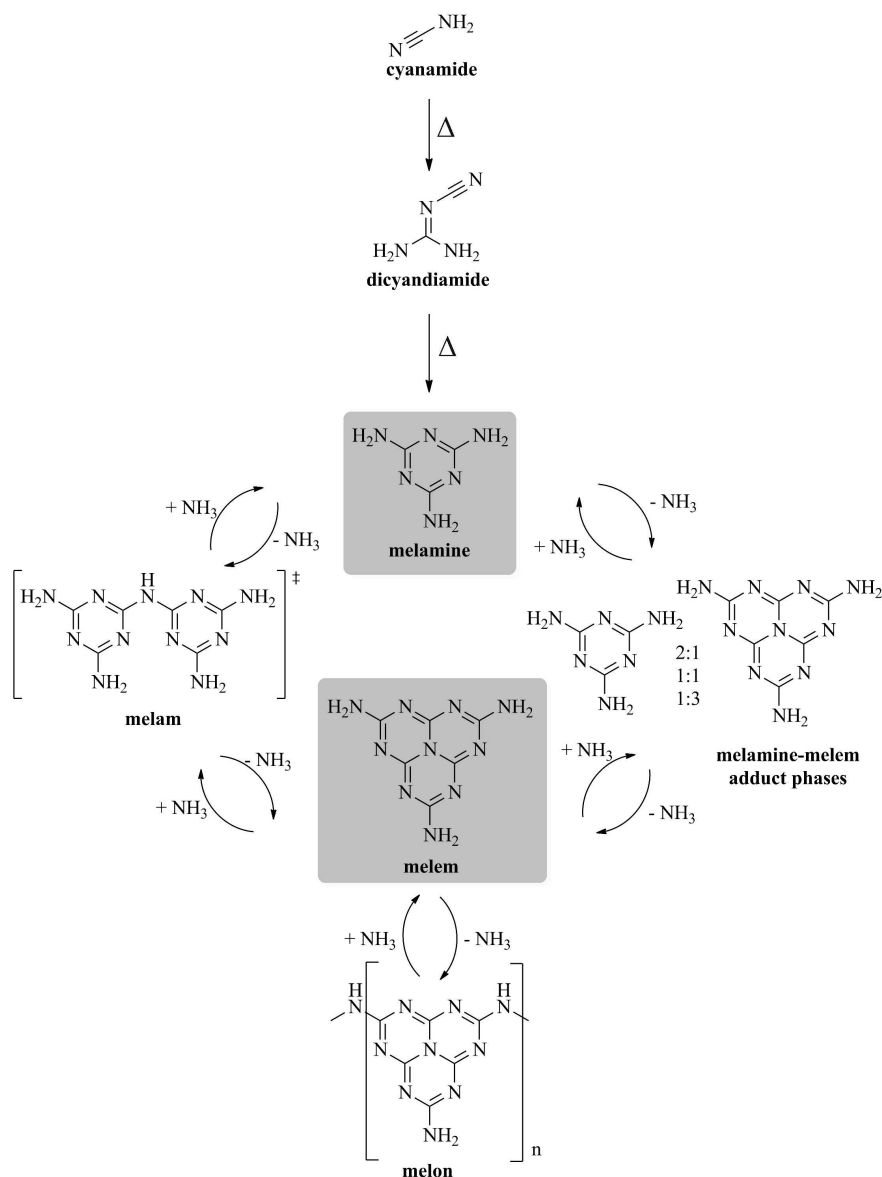
be viable at high pressure conditions (≤ 75 GPa).^[36,37] Henceforth, reams of groups intensified their efforts to find feasible synthetic pathways to g-C₃N₄. By introducing nitrogen atoms as well as ordered carbon vacancies in indefinite graphite layers, models with orthorhombic and hexagonal symmetry were derived, consisting of *s*-triazine (C₃N₃) or tri-*s*-triazine (C₆N₇, also called *s*-heptazine) building units (Scheme 2).^[36,38-42] A multitude of the attempts to synthesize g-C₃N₄ therefore emanates from precursors containing these building units such as melamine (2,4,6-triamino-*s*-triazine, C₃N₃(NH₂)₃) or cyanuric chloride (2,4,6-trichloro-*s*-triazine, C₃N₃Cl₃).^[43,44] The synthetic pathways to g-C₃N₄ include predominantly solid-state reactions at ambient and high pressure. For instance, cyanuric chloride was reacted with melamine, lithium- and sodium azide and several cyanamides to enforce condensation driven by the formation of stable or volatile by-products like LiCl or HCl.^[45-51] Further investigations concentrated on the thermal decomposition of triazido-*s*-triazine and -heptazine.^[52-54]

However, despite these efforts the synthesis of g-C₃N₄ cannot unambiguously be considered to be successful so far as all attempts were spoiled by the presence of hydrogen in the products, a wrong atomic ratio C:N or low crystallinity,

Table 1. Several “ammonocarbonic acids” x C₃N₄ · y NH₃.

“ammonocarbonic acid”	formula	x C ₃ N ₄ · y NH ₃
guanidine	HN=C(NH ₂) ₂	1 C ₃ N ₄ · 5 NH ₃
cyanamide	H ₂ NCN	1 C ₃ N ₄ · 2 NH ₃
dicyandiamide	(H ₂ N) ₂ C=NCN	1 C ₃ N ₄ · 2 NH ₃
melamine	C ₃ N ₃ (NH ₂) ₃	1 C ₃ N ₄ · 2 NH ₃
2melamine·melem	2C ₃ N ₃ (NH ₂) ₃ · C ₆ N ₇ (NH ₂) ₃	1 C ₃ N ₄ · 1½ NH ₃
melam	[C ₃ N ₃ (NH ₂) ₂] ₂ (NH)	1 C ₃ N ₄ · 1.5 NH ₃
melamine·melem	C ₃ N ₃ (NH ₂) ₃ · C ₆ N ₇ (NH ₂) ₃	1 C ₃ N ₄ · 1.5 NH ₃
melem	C ₆ N ₇ (NH ₂) ₃	1 C ₃ N ₄ · 1 NH ₃
melon	[C ₆ N ₇ (NH)(NH ₂)] _n	1 C ₃ N ₄ · 0.5 NH ₃

respectively. Many of the products seem to be a “melon-type” material, referring to a C/N/H-polymer which was first synthesized by *Berzelius* and given the arbitrary name “melon” by *Liebig*.^[55,56] This amorphous yellow compound was early known to be the final deammonation product of a series of formerly so called “ammonocarbonic acids” (x C₃N₄ · y NH₃) (cf. Table 1). A closer look to these compounds whose empirical formulas match those of ammonia adducts of C₃N₄, and the underlying concept, formally related to the system carbonic acid / water, provides a deeper insight into the thermal condensation process of these molecules and polymers (Scheme 3). These compounds, especially the smaller molecules like cyanamide, dicyanamides and melamine (derivates) are handled as suitable precursors for the synthesis of graphitic carbon nitride networks due to their pre-organized



Scheme 3. The formal concept of the formerly so called “ammonocarbonic acids”, undergoing cyclization and deamination processes when exposed to thermal treatment. The two thermodynamic drains (melamine and melem) are highlighted in gray.

s-triazine ring of the latter being highly stable at elevated temperatures, the thermal treatment of most non-cyclic carbon nitride precursors (cyanamide, dicyandiamide, several non-metal dicyanamides) leads to the formation of melamine by cyclization, before *s*-heptazine-based melem is formed at even higher temperatures.^[61,62] Just recently, the elucidation of three melamine-melem adduct phases with the molar ratio melamine : melem = 2:1, 1:1 and 1:3 shed new light on the condensation processes between these two drains, favoring the thesis of

C/N/H motifs and their easy accessibility.^[57-61] Owing to persistent research efforts, a multitude of intermediates between the two still hypothetical compounds with the highest and lowest possible degree of ammoniation (tetraamino carbon $C(NH_2)_4$ (= 1 $C_3N_4 \cdot 8 NH_3$) and C_3N_4) has been synthesized and characterized over the last few years. Investigations on the thermal behavior of these carbon nitride precursors revealed the existence of two thermodynamic “drains”, namely melamine and melon.^[57] With the

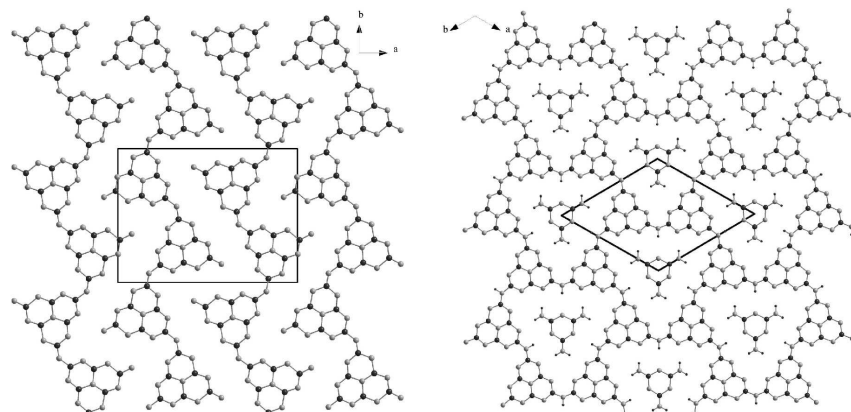


Figure 2. Crystal structure of the 1D polymer melon (left) and the 2D polymer poly(heptazine imide) (right). Carbon and hydrogen atoms are depicted in dark gray, nitrogen atoms in light gray.

melam being a highly reactive short-lived intermediate in this process accessible during condensation only by applying special reaction conditions.^[63,64]

The final deamination product of the thermal condensation process is the above mentioned melon, a 1D polymer consisting of heptazine-based zigzag strands (Figure 2, left).^[65] Although being a hydrogen-rich defect variant of binary carbon nitride, this compound is often mixed up with still not experimentally accessible graphitic C_3N_4 in literature for understandable reasons: the lack of a sharply defined composition and its low crystallinity. Numerous triazine- and heptazine-based models have been discussed for melon until its structure was solved by a complementary approach using solid-state NMR spectroscopy and electron diffraction in 2007.^[65-70] The latter method also revealed the existence of a second polymeric network found as side-product in the melon-synthesis when pyrolyzing melamine under autogenous pressure of ammonia. With its “holey” heptazine-based 2D network structure containing embedded melamine molecules (Figure 2, right), poly(heptazine imide) (PHI) states an intermediate condensation stage halfway between melon and theoretically predicted *s*-heptazine based $g-C_3N_4$.^[36,38-42,71] These two polymers are therefore joining the short queue of crystalline carbon nitride (imide) networks which is complemented by only two further compounds so far, both being synthesized by high-pressure methods. Carbon nitride imide $C_2N_2(NH)$ – synthesized by high-pressure-high-temperature (HP-HT) treatment of dicyandiamide in a laser-heated diamond-anvil cell - represents the first crystalline 3D carbon nitride (imide) network

The final deamination product of the

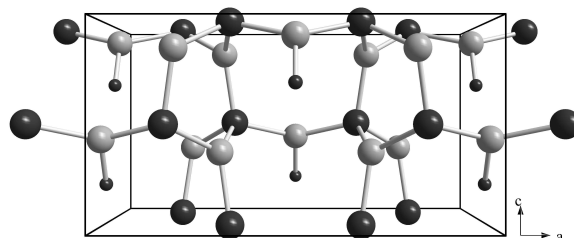


Figure 3. Crystal structure of $C_2N_2(NH)$, adopting the defect wurtzite-type. Carbon and hydrogen atoms are depicted in dark gray, nitrogen atoms in light gray.

described so far and adopts a defect wurtzite-type structure (Figure 3).^[72] The first triazine-based graphitic carbon nitride type network, namely $C_6N_9H_3 \cdot HCl$, was presented by *McMillan* et al., reacting melamine and cyanuric chloride in a piston cylinder apparatus.^[46,73]

Innumerable attempts to synthesize graphite-like carbon nitride materials have clearly shown that the crucial factor to achieve crystallinity is a careful choice of the reaction conditions, especially temperature and pressure.^[74] Solid-state reactions in open systems yielded mostly ill-defined amorphous products due to the tendency of melamine to sublime above 300 °C, thus hindering reversible gas-phase reactions which are necessary for the formation of crystalline products. Single crystals of the higher condensed precursors melem and the melamine-melem adduct phases were accordingly synthesized in sealed ampoules under autogenous ammonia pressure, as well as well-defined samples of melon and PHI.^[63,65,71,75] The low solubility of most carbon nitride precursors in common organic solvents spoiled the growth of single crystals by recrystallization processes in solution and hampered mechanistic investigations. However, despite the predominance of mechanistic investigations commonly carried out in solution true to *Aristotele's* principle “*Corpora non agunt, nisi fluida seu soluta*” (compounds that are not fluid or dissolved do not react), the detailed knowledge about intermediates and preferred reaction pathways in solid-state carbon nitride chemistry already yielded valuable findings for a targeted synthetic approach.^[63]

In the case of graphitic carbon nitride network synthesis, kinetic problems such as too fast and irreversible condensation processes and the immobility of the condensation intermediates inhibit complete reactions and yield amorphous, nonstoichiometric products. The usage of solvents could overcome these problems; however, the temperature range of the condensation processes exceeds the liquid range of conventional solvents by far. One way to enable higher temperatures for solvent-based reactions is the use of autoclaves, leading to solvothermal conditions. Up to now, only a few examples of solvothermal processes are known in the field of carbon nitride materials. *Li* et al. reported on the synthesis of self-assembled 1D carbon nitride nanostructures by reacting cyanuric chloride in cyclohexane at 230 – 290 °C.^[76] Benzene was used as solvent for the reaction of cyanuric chloride with Li_3N / Na_3N in a temperature range of 200 – 500 °C.^[77-80]

This thesis is providing first insights into carbon nitride high-temperature chemistry in solution, a field that has been investigated only scarcely so far. The behavior of potential carbon nitride precursors in inorganic solvents like ammonia, water and salt melts is studied and new molecular and polymeric compounds are thoroughly characterized by a multitude of analytical methods. Several aspects are explored to enlarge the basic knowledge about graphitic carbon nitride materials:

- **condensation processes:** the above mentioned thermally induced formation of melem from melamine still lacks a mechanism for the condensation process and the role of the highly reactive intermediate melam. Chapter 3 is devoted to this issue, presenting closer insights into the formation of melam under elevated ammonia pressure and to its reactivity in supercritical fluids.
- **solvent-effects on the structure:** the structure of a new carbon nitride imide network (poly(triazine imide) with LiCl intercalation, short PTI/LiCl), synthesized at high-temperature conditions stirs up the discussion about the (thermal) stability of triazine and heptazine building blocks anew. The structural characterization of this network is presented in the first part of Chapter 4.
- **photocatalysis and electronic properties:** with regards to the possible applicability of carbon nitride networks as heterogeneous metal-free photocatalysts,^[23] the performance of triazine based carbon nitride networks as catalysts for visible-light driven hydrogen production is examined. The electronic structure and the band gap of PTI/LiCl serving as model compound for this class is further investigated in the second part of Chapter 4.
- **chemical doping:** recently discovered effects of chemical doping on the properties of amorphous carbon nitride networks^[81-85] raised the question for structure-property-effects. To enable the synthesis of crystalline CNP networks, new phosphorus-containing cyanurate-related precursors were investigated. Details on structure and thermal treatment are summarized in Chapter 5.

Bibliography

- [1] A. K. Geim, K. S. Novoselov, *Nat. Mater.* **2007**, *6*, 183-191.
- [2] K. S. Novoselov, A. K. Geim, S. V. Morozov, D. Jiang, Y. Zhang, S. V. Dubonos, I. V. Grigorieva, A. A. Firsov, *Science* **2004**, *306*, 666-669.
- [3] L. Landau, *Phys. Z. Sowjetunion* **1937**, *11*, 545-555.
- [4] R. E. Peierls, *Ann. I. H. Poincare* **1935**, *5*, 177-222.
- [5] H. P. Boehm, A. Clauss, G. O. Fischer, U. Hofmann, *Z. Anorg. Allg. Chemie* **1962**, *316*, 119-127.
- [6] For current reviews see, for example: a) A. K. Geim, *Science* **2009**, *324*, 1530-1534; b) C. N. R. Rao, A. K. Sood, K. S. Subrahmanyam, A. Govindaraj, *Angew. Chem.* **2009**, *121*, 7890-7916; *Angew. Chem. Int. Ed.* **2009**, *48*, 7752-7777; c) K. Kim, J.-Y. Choi, T. Kim, S.-H. Cho, H.-J. Chung, *Nature* **2011**, *479*, 338-344.
- [7] C. Lee, X. Wei, J. W. Kysar, J. Hone, *Science* **2008**, *321*, 385-388.
- [8] A. A. Balandin, S. Ghosh, W. Bao, I. Calizo, D. Teweldebrhan, F. Miao, C. N. Lau, *Nano Lett.* **2008**, *8*, 902-907.
- [9] A. H. Castro Neto, F. Guinea, N. M. R. Peres, K. S. Novoselov, A. K. Geim, *Rev. Mod. Phys.* **2009**, *81*, 109-162.
- [10] Y.-M. Lin, K. A. Jenkins, A. Valdes-Garcia, J. P. Small, D. B. Farmer, P. Avouris, *Nano Lett.* **2009**, *9*, 422-426.
- [11] For current examples, see: a) R. Mas-Ballesté, C. Gómez-Navarro, J. Gómez-Herrero, F. Zamora, *Nanoscale* **2011**, *3*, 20-30; b) K. S. Novoselov, D. Jiang, F. Schedin, T. J. Booth, V. V. Khotkevich, S. V. Morozov, A. K. Geim, *Proc. Natl. Acad. Sci. U.S.A.* **2005**, *102*, 10451-10453; c) T. W. Kim, E. J. Oh, A. Y. Jee, S. T. Lim, D. H. Park, M. Lee, S. H. Hyun, J. H. Choy, S. J. Hwang, *Chem. Eur. J.* **2009**, *15*, 10752-10761; d) K. Fukuda, T. Saida, J. Sato, M. Yonezawa, Y. Takasu, W. Sugimoto, *Inorg. Chem.* **2010**, *49*, 4391-4393; e) S. Ida, C. Ogata, M. Eguchi, W. J. Youngblood, T. E. Mallouk, Y. Matsumoto, *J. Am. Chem. Soc.* **2008**, *130*, 7052-7059; f) K. Fukuda, K. Akatsuka, Y. Ebina, R. Ma, K. Takada, I. Nakai, T. Sasaki, *ACS Nano*, **2008**, *2*, 1689-1695; g) X. S. Wu, M. Sprinkle, X. B. Li, F. Ming, C. Berger, W. A. de Heer, *Phys.*

- Rev. Lett.* **2008**, *101*, 026801/1-026801/4; h) M. Osada, M. Itose, Y. Ebina, K. Ono, S. Ueda, K. Kobayashi, T. Sasaki, *Appl. Phys. Lett.* **2008**, *92*, 253110/1-253110/3.
- [12] C. Gómez-Navarro, M. Burghard, K. Kern, *Nano Lett.* **2008**, *2008*, 2045-2049.
- [13] C. Gómez-Navarro, R. T. Weitz, A. M. Bittner, M. Scolari, A. Mews, M. Burghard, K. Kern, *Nano Lett.* **2007**, *7*, 3499-3503.
- [14] D. C. Elias, R. R. Nair, T. M. G. Mohiuddin, S. V. Morozov, P. Blake, M. P. Halsall, A. C. Ferrari, D. W. Boukhvalov, M. I. Katnelson, A. K. Geim, K. S. Novoselov, *Science* **2009**, *323*, 610-613.
- [15] I. Gierz, C. Riedl, U. Starke, C. R. Ast, K. Kern, *Nano Lett.* **2008**, *8*, 4603-4607.
- [16] D. Wu, F. Zhang, P. Liu, X. Feng, *Chem. Eur. J.* **2011**, *17*, 10804-10812.
- [17] S. Yang, X. Feng, L. Wang, K. Tang, J. Maier, K. Müllen, *Angew. Chem.* **2010**, *122*, 4905-4909; *Angew. Chem. Int. Ed.* **2010**, *49*, 4795-4799.
- [18] S. Yang, X. Feng, X. Wang, K. Müllen, *Angew. Chem.* **2011**, *123*, 5451-5455; *Angew. Chem. Int. Ed.* **2011**, *50*, 5339-5343.
- [19] X.-H. Li, J.-S. Chen, X. Wang, J. Sun, M. Antonietti, *J. Am. Chem. Soc.* **2011**, *133*, 8074-8077.
- [20] Y. Sun, C. Li, Y. Hu, H. Bai, Z. Yao, G. Shi, *Chem. Commun.* **2010**, *46*, 4740-4742.
- [21] A. Thomas, A. Fischer, F. Goettmann, M. Antonietti, J.-O. Müller, R. Schlögl, J. M. Carlsson, *J. Mater. Chem.* **2008**, *18*, 4893-4908.
- [22] Y. Wang, X. Wang, M. Antonietti, *Angew. Chem.* **2012**, *124*, 70-92; *Angew. Chem. Int. Ed.* **2012**, *51*, 68-89.
- [23] X. Wang, K. Maeda, A. Thomas, K. Takanabe, G. Xin, J. M. Carlsson, K. Domen, M. Antonietti, *Nat. Mater.* **2009**, *8*, 76-80.
- [24] X. Wang, K. Maeda, X. Chen, K. Takanabe, K. Domen, Y. Hou, X. Fu, M. Antonietti, *J. Am. Chem. Soc.* **2009**, *131*, 1680-1681.
- [25] K. Maeda, X. Wang, Y. Nishihara, D. Lu, M. Antonietti, K. Domen, *J. Phys. Chem. C* **2009**, *113*, 4940-4947.
- [26] F. Goettmann, A. Fischer, A. Thomas, M. Antonietti, *Angew. Chem.* **2006**, *118*, 4579-4583; *Angew. Chem. Int. Ed.* **2006**, *45*, 4467-4471.
- [27] F. Goettmann, A. Fischer, M. Antonietti, A. Thomas, *New. J. Chem.* **2007**, *31*, 1455-1460.

- [28] F. Goettmann, A. Thomas, M. Antonietti, *Angew. Chem.* **2007**, *119*, 2773-2776; *Angew. Chem. Int. Ed.* **2007**, *46*, 2717-2720.
- [29] R. Palkovits, M. Antonietti, P. Kuhn, A. Thomas, F. Schüth, *Angew. Chem.* **2009**, *121*, 7042-7045; *Angew. Chem. Int. Ed.* **2009**, *48*, 6909-6912.
- [30] F. Su, S. C. Mathew, L. Moehlmann, M. Antonietti, X. Wang, S. Blechert, *Angew. Chem.* **2011**, *123*, 683-686; *Angew. Chem. Int. Ed.* **2011**, *50*, 657-660.
- [31] A. Y. Liu, M. L. Cohen, *Science* **1989**, *245*, 841-842.
- [32] A. Y. Liu, M. L. Cohen, *Phys. Rev. B* **1990**, *41*, 10727-10734.
- [33] E. Kroke, M. Schwarz, *Coord. Chem. Rev.* **2004**, *248*, 493-532.
- [34] S. Matsumoto, E.-Q. Xie, F. Izumi, *Diamond Relat. Mater.* **1999**, *8*, 1175.
- [35] Z. J. Zhang, S. Fan, C. M. Lieber, *Appl. Phys. Lett.* **1995**, *66*, 3582.
- [36] D. M. Teter, R. J. Hemley, *Science* **1996**, *271*, 53-55.
- [37] P. Kroll, R. J. Hoffmann, *J. Am. Chem. Soc.* **1999**, *121*, 4696.
- [38] D. T. Vodak, K. Kim, L. Iordanidis, P. G. Rasmussen, A. J. Matzger, O. M. Yaghi, *Chem. Eur. J.* **2003**, *9*, 4197-4201.
- [39] E. Kroke, M. Schwarz, E. Horvath-Bordon, P. Kroll, B. Noll, A. D. Norman, *New. J. Chem.* **2002**, *26*, 508-512.
- [40] A. Y. Liu, R. M. Wentzcovitch, *Phys. Rev. B* **1994**, *50*, 10362-10365.
- [41] J. Gracia, P. Kroll, *J. Mater. Chem.* **2009**, *19*, 3013-3019.
- [42] J. Sehnert, K. Baerwinkel, J. Senker, *J. Phys. Chem. B* **2007**, *111*, 10671-10680.
- [43] J. R. Holst, E. G. Gillan, *J. Am. Chem. Soc.* **2008**, *130*, 7373-7379.
- [44] D. R. Miller, J. Wang, E. G. Gillan, *J. Mater. Chem.* **2002**, *12*, 2463-2469.
- [45] Y. Gu, L. Chen, L. Shi, J. Ma, Z. Yang, Y. Qian, *Carbon* **2003**, *41*, 2674-2676.
- [46] Z. Zhang, K. Leinenweber, M. Bauer, L. A. J. Garvie, P. F. McMillan, G. H. Wolf, *J. Am. Chem. Soc.* **2001**, *123*, 7788-7796.
- [47] Q. Guo, Y. Xie, X. Wang, S. Lu, T. Hou, X. Liu, *Chem. Phys. Lett.* **2003**, *380*, 84-87.
- [48] J. L. Zimmermann, R. Williams, V. N. Khabashesku, *Nano Lett.* **2001**, *1*, 731-734.
- [49] S. Tragl, K. Gibson, J. Glaser, V. Duppel, A. Simon, H. J. Meyer, *Solid State Commun.* **2007**, *141*, 529-534.
- [50] M. Kawaguchi, *Chem. Mater.* **1995**, *7*, 257-264.
- [51] K. Gibson, J. Glaser, E. Milke, M. Marzini, S. Tragl, M. Binnewies, H. A. Mayer, H.-J. Meyer, *Mat. Chem. Phys.* **2008**, *112*, 52-56.

- [52] D. R. Miller, J. R. Holst, E. G. Gillan, *Inorg. Chem.* **2007**, *46*, 2767-2774.
- [53] E. G. Gillan, *Chem. Mater.* **2000**, *12*, 3906-3912.
- [54] D. R. Miller, D. C. Swenson, E. G. Gillan, *J. Am. Chem. Soc.* **2004**, *126*, 5372-5373.
- [55] E. C. Franklin, *J. Am. Chem. Soc.* **1922**, *44*, 486-509.
- [56] J. Liebig, *Ann. Pharm.* **1834**, *10*, 1.
- [57] B. Jürgens, E. Irran, J. Senker, P. Kroll, H. Müller, W. Schnick, *J. Am. Chem. Soc.* **2003**, *125*, 10288-10300.
- [58] B. Jürgens, H. A. Höppe, W. Schnick, *Inorg. Chem.* **2002**, *41*, 4849-4851.
- [59] B. V. Lotsch, J. Senker, W. Kockelmann, W. Schnick, *J. Solid State Chem.* **2003**, *176*, 180-191.
- [60] T. Komatsu, T. Nakamura, *J. Mater. Chem.* **2001**, *11*, 474-478.
- [61] B. V. Lotsch, W. Schnick, *Chem. Mater.* **2006**, *18*, 1891-1900.
- [62] B. V. Lotsch, W. Schnick, *New. J. Chem.* **2004**, *28*, 1129-1136.
- [63] A. Sattler, S. Pagano, M. Zeuner, A. Zurawski, D. Gunzelmann, J. Senker, K. Müller-Buschbaum, W. Schnick, *Chem. Eur. J.* **2009**, *15*, 13161-13170.
- [64] B. V. Lotsch, W. Schnick, *Chem. Eur. J.* **2007**, *13*, 4956-4968.
- [65] B. V. Lotsch, M. Döblinger, J. Sehnert, L. Seyfarth, J. Senker, O. Oeckler, W. Schnick, *Chem. Eur. J.* **2007**, *13*, 4969-4980.
- [66] C. E. Redemann, H. J. Lucas, *J. Am. Chem. Soc.* **1940**, *62*, 842-846.
- [67] H. May, *J. Appl. Chem.* **1959**, *9*, 340-344.
- [68] L. Costa, G. Camino, G. Martinasso, *Polym. Prepr. (Am. Chem. Soc., Div. Polym. Chem.)* **1989**, *30*, 531-533.
- [69] L. Pauling, J. H. Sturdivant, *Proc. Natl. Acad. Sci. U.S.A.* **1937**, *23*, 615-620.
- [70] T. Komatsu, *J. Mater. Chem.* **2001**, *11*, 802-805.
- [71] M. Döblinger, B. V. Lotsch, J. Wack, J. Thun, J. Senker, W. Schnick, *Chem. Commun.* **2009**, 1541-1543.
- [72] E. Horvath-Bordon, R. Riedel, P. F. McMillan, P. Kroll, G. Miehe, P. A. van Aken, A. Zerr, P. Hoppe, O. Shebanova, I. McLaren, S. Lauterbach, E. Kroke, R. Boehler, *Angew. Chem.* **2007**, *119*, 1498-1502; *Angew. Chem. Int. Ed.* **2007**, *46*, 1476-1480.
- [73] P. F. McMillan, V. Lees, E. Quirico, G. Montagnac, A. Sella, B. Reynard, P. Simon, E. Bailey, M. Deifallah, F. Corà, *J. Solid State Chem.* **2009**, *182*, 2670-2677.

- [74] an overview of numerous synthesis methods for carbon nitrides is for instance given in: a) E. Kroke, M. Schwarz, *Coord. Chem. Rev.* **2004**, 248, 493-532; b) A. Thomas, A. Fischer, F. Goettmann, M. Antonietti, J.-O. Müller, R. Schlögl, J. M. Carlsson, *J. Mater. Chem.* **2008**, 18, 4893-4908.
- [75] A. Sattler, W. Schnick, *Z. Anorg. Allg. Chemie* **2006**, 632, 238-242.
- [76] J. Li, C. Cao, J. Hao, H. Qiu, Y. Xu, H. Zhu, *Diamond Relat. Mater.* **2006**, 15, 1593-1600.
- [77] C.-B. Cao, Q. Lv, H.-S. Zhu, *Diamond Relat. Mater.* **2003**, 12, 1070-1074.
- [78] Q. Luv, C. B. Cao, J. T. Zhang, C. Li, H. S. Zhu, *Appl. Phys. A* **2004**, 79, 633-636.
- [79] Q. Lv, C.-B. Cao, J.-T. Zhang, C. Li, H.-S. Zhu, *Chem. Phys. Lett.* **2003**, 372, 469-475.
- [80] Q. Lv, C. Cao, C. Li, J. Zhang, H. Zhu, X. Kong, X. Duan, *J. Mater. Chem.* **2003**, 13, 1241-1243.
- [81] Y. Zhang, T. Mori, J. Ye, M. Antonietti, *J. Am. Chem. Soc.* **2010**, 132, 6294-6295.
- [82] D. Portehault, C. Giordano, C. Gervais, I. Senkowska, S. Kaskel, C. Sanchez, M. Antonietti, *Adv. Funct. Mater.* **2010**, 20, 1827-1833.
- [83] Y. Wang, J. Zhang, X. Wang, M. Antonietti, H. Li, *Angew. Chem.* **2010**, 122, 3428-3431; *Angew. Chem. Int. Ed.* **2010**, 49, 3356-3359.
- [84] Y. Wang, H. Li, J. Yao, X. Wang, M. Antonietti, *Chem. Sci.* **2011**, 2, 446-450.
- [85] G. Liu, P. Niu, C. Sun, S. C. Smith, Z. Chen, G. Q. Lu, H.-M. Cheng, *J. Am. Chem. Soc.* **2010**, 132, 11642-11648.

2. Summary

This thesis deals with investigations on the high-temperature treatment of carbon nitride precursors in various inorganic solvents. Particular attention was paid to the exploratory development of successful synthesis routes for the preparation of new graphite-like carbon nitride materials with improved crystallinity. Different molecular and polymeric *s*-triazine-based compounds have been synthesized by ammonothermal and hydrothermal treatment as well as by the utilization of salt melts. Furthermore, physical properties such as the bandgap and photocatalytic activity towards water splitting have been examined for individual compounds. A brief summary of the aspects discussed in this work is given below.

2.1 Melam, melam hydrate and a melam-melem adduct phase

(Chapter 3, published in *Chem. Eur. J.* **2013**, *19*, 2041-2049)

Fast condensation processes are well known issues in carbon nitride chemistry, thus hampering the isolation of stable intermediates except a few ones like melamine and melem. In chapter 3, a novel approach for the elucidation of these processes is introduced, applying ammonothermal and hydrothermal conditions to carbon nitride precursors. According to Le Chatelier's principle, the cleavage of ammonia is antagonized by elevated ammonia pressure, therefore slowing down condensation processes and enabling insights in the gradual transformation of melam to melem. By ammonothermal treatment of dicyandiamide in an autoclave (450 °C, 0.2 MPa NH₃, Figure 1) bulk melam, an *s*-triazine-based dimer, was synthesized in large yields for the first time. Longer treatment of dicyandiamide (9-10 days) at the same conditions allowed for the isolation of the first melam-melem adduct which was characterized by means of IR and solid-state NMR spectroscopy.



Figure 1. Autoclave for ammonothermal and hydrothermal reactions.

Whereas condensation reactions were observed at ammonothermal conditions, the hydrothermal treatment of melam (300 °C) led to the formation of single crystals of melam hydrate [C₃N₃(NH₂)₂]₂ · 2 H₂O (*P*2₁/*c*, *a* = 676.84(2), *b* = 1220.28(4), *c* = 1394.24(4) pm, *β* = 98.372(2)°, *V* = 1139.28(6)·10⁶ pm³, *Z* = 4), a compound which was so far only known as polycrystalline multiphased precursor for the synthesis of melamium salts in solution. Melam hydrate crystallizes in a layered structure composed of nearly planar melam molecules. The voids in the resulting ellipsoidal rosette-like motifs are filled with four water molecules which are removable by thermal treatment, accompanied by the rearrangement of the layered melam molecules to the screw-like formation of anhydrous melam.

2.2 Poly(triazine imide) with LiCl intercalation

Formation and structure of poly(triazine imide) with LiCl intercalation

(Chapter 4, published in *Chem. Eur. J.* **2011**, *17*, 3213 – 3221)

The first part of Chapter 4 presents the first structure solution of a carbon nitride network by means of powder X-ray diffraction methods in combination with electron diffraction and solid-state NMR spectroscopy. Poly(triazine imide) was synthesized by heating intimate mixtures of dicyandiamide and an eutectic mixture of lithium chloride and potassium chloride in sealed silica glass ampoules at 600 °C. Structural information was provided by elaborated 1D and 2D solid-state NMR spectroscopy investigations as well as FTIR spectroscopy and high-resolution TEM measurements. The high crystallinity of PTI/LiCl which is probably owed to the intercalation of Li^+ and Cl^- ions, allowed for a structure solution and refinement from both powder X-ray and electron diffraction patterns by using direct methods ($P6_3cm$, $a = 846.82(10)$, $c = 675.02(9)$ pm, $V = 419.21(9)$

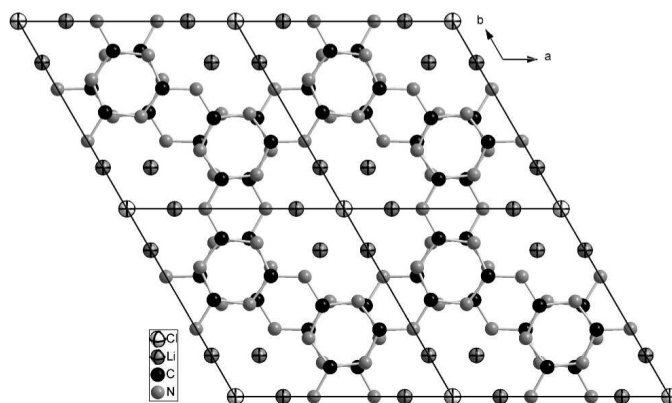


Figure 2. Parallel projection of the 2D structure of PTI/ Li^+Cl^- , formed by ABA-stacked layers. The voids in the layers are enlarged to channels running along the c axis, filled with Li^+Cl^- ions.

10^6 pm^3). As the name implies, the 2D network PTI/LiCl is built up from imide-bridged triazine units forming nearly planar layers with large hexagonal voids (Figure 2). By layer stacking, these voids are enlarged to channels running parallel to $[001]$, containing Li^+ and Cl^- ions. Partial substitution of the H-atoms of the imide units by Li (proven by ^{15}N direct excitation NMR measurements) introduces Li/H disorder in the channels which results in the formula $[(\text{C}_3\text{N}_3)_2(\text{NH}_x\text{Li}_{1-x})_3 \cdot \text{LiCl}]$, rendering PTI/LiCl an interesting candidate for further theoretical calculations.

Properties and possible applications of poly(triazine imide) with LiCl intercalation

(Chapter 4, published in a) *J. Phys. Chem. C* **2013**, *117*, 8806–8812; b) *Angew. Chem.* **2013**, *125*, 2495-2499; *Angew. Chem. Int. Ed.* **2013**, *52*, 2435-2439)

The second part of Chapter 4 deals with the determination of the band structure and band gap of PTI/LiCl. XES/XANES and VEELS measurements are presented (probing the partial and the total density of states), which yielded both a band gap of 2.2 eV, rendering PTI/LiCl an organic semiconductor. Several further samples with varying LiCl content (reduced from PTI/LiCl by soxhlet extraction with water) were examined as well, proving the band gap to be tunable in the region of 2.2 to 2.9 eV by gradually reducing the LiCl content to zero. For a deeper understanding, DFT calculations were performed using the WIEN2k code. Structure optimization processes were carried out to determine the most stable configuration for the structure of PTI/LiCl (especially regarding the H/Li substitution at the bridging imide units and the resulting disorder) for the simulation of the X-ray emission and absorption spectra. The band gap was shown to be based on N 2p \rightarrow N/C 2p transitions, which are influenced - according to the variability of the band gap considering the LiCl content - by hybridization of the N 2p and Cl 2p states as well as by the charge density of the hydrogen-stripped imide sites below the top of the valence band.

The activity of PTI/LiCl as photocatalyst towards hydrogen evolution from water is described in the third part of Chapter 4. Crystalline PTI/LiCl and several further amorphous and carbon-doped derivates were compared to heptazine-based melon-type carbon nitrides which were so far the most promising representatives of this class of metal-free organic semiconductors. Whereas the performance of crystalline and amorphous PTI/LiCl towards water splitting is in the range of melon, carbon-doped samples synthesized by ionothermal copolymerization of dicyandiamide with 4-amino-2,6-dihydropyrimidine (4AP) ruled out the others by a more than 5-fold increased photoactivity towards hydrogen evolution

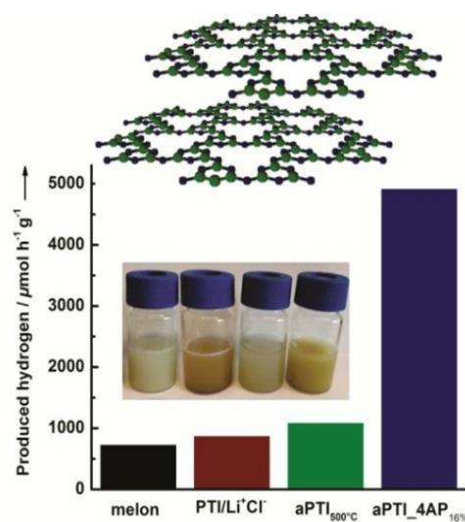


Figure 3. Comparison of melon with several PTI/LiCl derivates regarding the photoactivity towards hydrogen production from water.

(Figure 3) and proved the influence of the controlled introduction of defects and the level of structural definition.

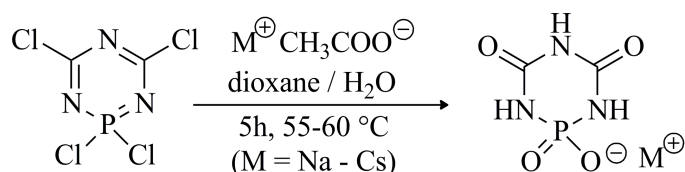
2.3 Phosphorus-doped carbon nitride precursors

Carbon-doped graphite-type carbon nitride networks have proven to be promising candidates towards photocatalytic water splitting. With regards to the synthesis of phosphorus-doped carbon nitride networks, several phosphorus containing carbon nitride precursors have been synthesized and comprehensively characterized.

Alkaline and alkaline earth biuretooxophosphates

(Chapter 5, published in a) *Eur. J. Inorg. Chem.* **2012**, 1840-1847; b) *Z. Anorg. Allg. Chem.* **2012**, 638, 920-924)

Biuretooxophosphates state a class of compounds closely related to cyanurates with one carbon atom of the *s*-triazine ring exchanged by phosphorus. Therefore they seem to be



Scheme 1. Preparation of alkali biuretooxophosphates by the controlled hydrolysis of 1,1,3,5-tetrachloro-1-phospha-2,4,6-*s*-triazine.

capable precursors for the synthesis of carbon nitride networks with a defined molar ratio C:N:P. A series of alkaline biuretooxophosphates $M[\text{PO}_2(\text{NH})_3(\text{CO})_2] \cdot x\text{H}_2\text{O}$ ($M = \text{Li}, \text{K}, \text{Rb}, \text{and Cs}; x = 1, 0, 0.5, 0$) and alkaline earth biuretooxophosphates $M[\text{PO}_2(\text{NH})_3(\text{CO})_2]_2$ ($M = \text{Ca}$) has been prepared by controlled hydrolysis of 1,1,3,5-tetrachloro-1-phospha-2,4,6-*s*-triazine ($M = \text{K}, \text{Rb}, \text{Cs}$) (Scheme 1) and by ion-exchange reaction ($M = \text{Li},$

Ca). The crystal structures of these salts have been solved and refined by single-crystal diffraction data (crystallographic details can be

Table 1. Crystallographic details of the structure refinement for the alkali biuretooxophosphates $M[\text{PO}_2(\text{NH})_3(\text{CO})_2] \cdot x\text{H}_2\text{O}$ ($M = \text{Li}, \text{K}, \text{Rb}, \text{and Cs}; x = 1, 0, 0.5, 0$) and the alkaline earth biuretooxophosphate $\text{Ca}[\text{PO}_2(\text{NH})_3(\text{CO})_2]_2$.

cation	Li	K	Rb	Cs	Ca
space group	$P2_1/c$	$P2_1/c$	Cc	$P2_1/c$	$P2_1/c$
<i>a</i> [pm]	721.76(14)	585.42(12)	926.55(19)	679.16(14)	1010.8(2)
<i>b</i> [pm]	683.90(14)	1756.6(4)	3255.3(7)	1486.5(3)	527.45(1)
<i>c</i> [pm]	1551.5(4)	691.70(14)	670.34(13)	745.37(15)	1375.3(5)
β [°]	117.53(2)	109.65(3)	132.07(3)	93.08(3)	122.38(2)
<i>V</i> [10 ⁶ pm ³]	679.1(3)	669.9(2)	1500.9(9)	751.4(3)	619.2(3)
<i>Z</i>	4	4	8	4	2

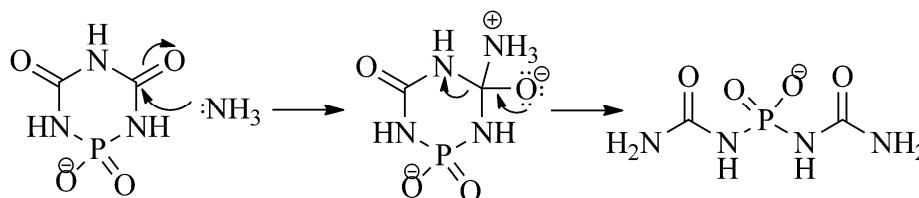
found in Table 1) and compared to the structures of the sodium and the ammonium salt known from literature. With the phosphorus atom maintaining its preferred (distorted) tetrahedral coordination, the biuretooxophosphate anions show slight deviations from a planar arrangement of the ring, thus exhibiting weakly pronounced twist, chair and half-chair conformations. The relative orientation of the rings changes with increasing cation size as well as the connectivity of the coordination polyhedra. Photoluminescence measurements of the colorless salts showed absorption and emission to occur in the UV region, thus being similar to *s*-triazine and tri-*s*-triazine derivatives. Decomposition of the biuretooxophosphates - examined by combined DTA/TG studies and temperature-dependent powder X-ray diffraction analysis - was proven to occur at slightly lower temperatures than for cyanurates (300-400 °C) and is accompanied by the formation of the corresponding phosphates (MPO₃)_x.

***N,N'*-Bis(aminocarbonyl)phosphorodiamidates**

(Chapter 5, published in *Eur. J. Inorg. Chem.* **2012**, 3296-3301)

According to Le Chatelier's principle, high-pressure conditions are necessary to impede the observed decomposition of biuretooxophosphates to metaphosphates at elevated temperatures and atmospheric pressure. Ammonothermal treatment of the corresponding alkali biuretooxophosphates at 350 °C and 120 – 150 bar yielded the so far unknown *N,N'*-bis(aminocarbonyl)-phosphorodiamidates Na[PO₂(NHCONH₂)₂] (*C2/c*, *a* = 875.2(2), *b* = 1191.2(2), *c* = 700.6(1) pm, *β* = 103.68(3)°, *V* = 709.7(2) 10⁶ pm³, *Z* = 4), K[PO₂(NHCONH₂)₂] (*Fdd2*, *a* = 1037.0(2), *b* = 1270.7(6), *c* = 1110.3(2) pm, *V* = 1463.1(8) 10⁶ pm³, *Z* = 8) and Rb[PO₂(NHCONH₂)₂] (*Fdd2*, *a* = 1272.6(6), *b* = 1058.6(2), *c* = 1127.0(2) pm, *V* = 1518.3(5) 10⁶ pm³, *Z* = 8).

By a ring-opening mechanism, induced by the nucleophilic attack of ammonia,



Scheme 2. Mechanism of the ammonolysis of biuretooxophosphates.

3D framework structures are formed in which *N,N'*-bis(aminocarbonyl)-phosphorodiamidate anions link the coordination polyhedra of the corresponding alkali cations (Scheme 2). These octahedral and cube-like bodies are interconnected, configuring 1D strands and a dense 3D

motif comprising interpenetrating *zweier* chains (Figure 4). Combined studies of DTA/TG measurements and temperature-dependent powder X-ray diffraction revealed the reversibility of the ammonolysis for the sodium and potassium salt at elevated temperatures before decomposing to the corresponding metaphosphates $(MPO_3)_x$ by the elimination of formamide $HCONH_2$ whereas the rubidium salt undergoes direct decomposition without ring condensation first.

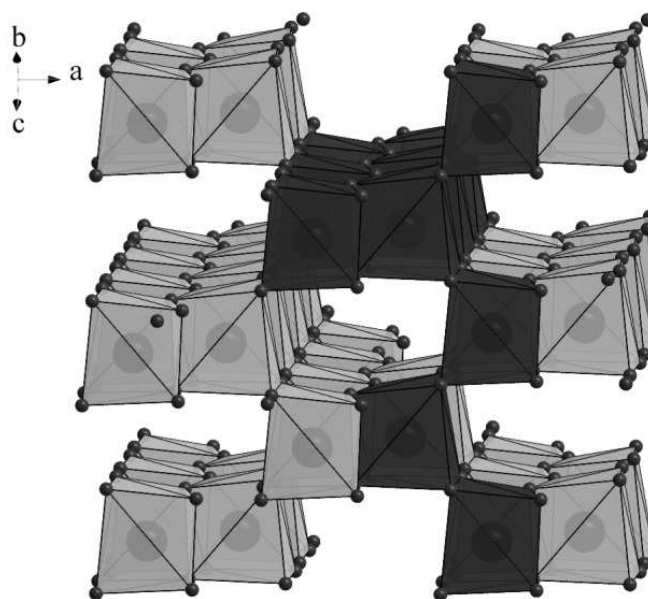


Figure 4. Interpenetrating *zweier* chains in $Rb[PO_2(NHCONH_2)_2]$, running in $[011]$ and $[0\bar{1}1]$ direction (highlighted in dark gray).

3. On the Formation and Solvothermal Treatment of Melam

Melam, a molecule formally accessible by condensation of two molecules melamine by elimination of ammonia is one of the first C/N/H compounds to be mentioned in literature. Nevertheless, the crystal structure as well as the synthesis of this “melamine-dimer” puzzled researchers for nearly one and a half century. With melam being an important intermediate on the way to g-C₃N₄, a multitude of experiments have been conducted to maintain this compound, mostly based on the addition of acids. Several melam derivatives are known in literature; however, melam itself was so far only synthesized in very little amounts by condensation of melamine, as the formation of melem is energetically favored. This chapter deals with a novel approach to synthesize melam in large amounts by autoclave synthesis. Reactions in supercritical and gaseous ammonia are compared and a new condensation intermediate accessible by heating dicyandiamide for nine days in gaseous ammonia at 450 °C is characterized. Furthermore, single crystals of melam hydrate, to date known as amorphous precursor for the synthesis of several melamium salts and solvates, were grown by hydrothermal treatment and rendered the structural characterization possible.

All NMR measurements in this subsection were carried out by Maria B. Mesch and Prof. Dr. J. Senker (University of Bayreuth) and will also be published as part of the PhD thesis of M. B. Mesch.

Formation and Characterization of Melam, Melam Hydrate and a Melam-Melem Adduct

Eva Wirnhier, Maria B. Mesch, Jürgen Senker and Wolfgang Schnick

published in: *Chem. Eur. J.* **2013**, *19*, 2041-2049. DOI: 10.1002/chem.201203340

Keywords: ammonia; hydrothermal synthesis, carbon nitrides, condensation reactions

Abstract: Until recently, melam $[\text{C}_3\text{N}_3(\text{NH}_2)_2]_2\text{NH}$ has been regarded as a short-lived intermediate in the condensation process of melamine, detectable only under special reaction conditions due to its high reactivity. A new synthetic approach allowed for a closer look into the formation and condensation behavior of melam by the use of elevated ammonia pressure in autoclaves. Whereas thermal treatment of dicyandiamide at 450 °C and 0.2 MPa NH_3 yielded melam in large amounts, longer treatment at such conditions (9 d) led to the formation of a melam-melem adduct phase, enabling first insights into the condensation process of melam to melem.

Hydrothermal treatment of melam at 300 °C (24 h) yielded melam hydrate $[\text{C}_3\text{N}_3(\text{NH}_2)_2]_2\text{NH} \cdot 2\text{H}_2\text{O}$ ($P2_1/c$, $a = 676.84(2)$, $b = 1220.28(4)$, $c = 1394.24(4)$ pm, $\beta = 98.372(2)^\circ$, $V = 1139.28(6) \cdot 10^6$ pm³, $Z = 4$) which crystallizes in a layered structure composed of nearly planar melam molecules, forming ellipsoidal rosette-like motifs. Resulting voids are filled with four water molecules, forming a dense network of hydrogen bonds.

3.1 Introduction

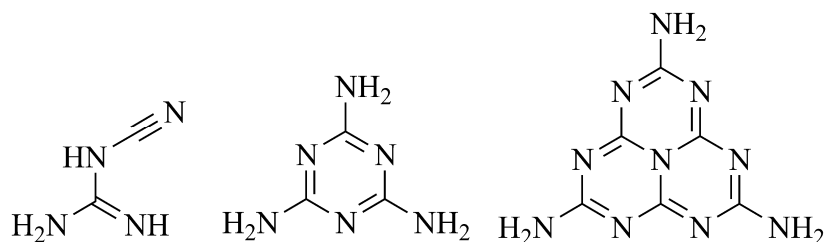
Since the “harder than diamond” fever has been evoked by the work of Liu and Cohen in 1989, carbon nitride-type materials have experienced significant interest due to their promising properties. Earlier work has concentrated mainly on synthesis of sp^3 -hybridized network phases of binary carbon nitride (C_3N_4) which was predicted to show extreme compressibility and superhardness.^[1-5] So far, the closest approach to binary carbon nitride has been carbon nitride imide $C_2N_2(NH)$ crystallizing in a defect wurtzite-type of structure, representing the first crystalline sp^3 -hybridized three-dimensional network structure of a carbon nitride presented to date.^[6] Recently, the focus of carbon nitride chemistry has shifted towards layer-like sp^2 -hybridized graphite-type carbon nitride type materials showing promising properties for catalytic applications (e.g. for water splitting and CO_2 reduction), for use in organic semiconductor science and as photoactive materials converting solar light into electricity.^[7-14] However, the

Table 1. Carbon nitride precursors, formally denominated as “ammonocarbonic acids” $x C_3N_4 \cdot y NH_3$.

ammonocarbonic acid	formula	$x C_3N_4 \cdot y NH_3$
cyanamide	H_2NCN	$\frac{1}{3} C_3N_4 \cdot \frac{2}{3} NH_3$
dicyanamide	$NH(CN)_2$	$\frac{2}{3} C_3N_4 \cdot \frac{1}{3} NH_3$
dicyandiamide	$(H_2N)_2C=NCN$	$\frac{2}{3} C_3N_4 \cdot 1\frac{1}{3} NH_3$
melamine	$C_3N_3(NH_2)_3$	$1 C_3N_4 \cdot 2 NH_3$
melam	$[C_3N_3(NH_2)_2]_2(NH)$	$2 C_3N_4 \cdot 3 NH_3$
melem	$C_6N_7(NH_2)_3$	$2 C_3N_4 \cdot 2 NH_3$
melon	$[C_6N_7(NH)(NH_2)]_n$	$2 C_3N_4 \cdot 1 NH_3$

synthesis of pure and crystalline g- C_3N_4 – being regarded as a possible precursor of superhard 3D C_3N_4 and predicted to be the most stable modification under ambient conditions^[5] – has not been reported so far.

Accordingly, chemical screening of potential precursors leading to this compound has been an ongoing quest in carbon nitride research.^[15-19] In the literature there has been a controversial discussion paralleled by theoretical calculations if g- C_3N_4 is made up of *s*-triazine or tri-*s*-triazine (“heptazine”) units.^[20-22] Regardless, g- C_3N_4 can be formulated as the final de-ammonation product of a series of “ammonocarbonic acids” ($x C_3N_4 \cdot y NH_3$) (Scheme 1, Table 1) like cyanamide and dicyandiamide containing alternating C and N atoms.^[23]



Scheme 1. The carbon nitride precursors dicyandiamide ($C_2N_4H_4$, left), melamine ($C_3N_6H_6$, middle) and melem ($C_6N_{10}H_6$, right).

Investigation of the thermolysis behavior of these precursors established relations with a class of historically important compounds first mentioned by Liebig (e. g. melamine, melam, melem and melon).^[24] In the literature, melamine (triamino-*s*-triazine, $C_3N_3(NH_2)_3$) and melem (triamino-tri-*s*-triazine, $C_6N_7(NH_2)_3$)^[15] have been assumed to be stable species in the condensation process leading finally to melon $[(C_6N_7(NH_2)(NH))]_n$ ^[16] since they have been invariably obtained by thermal treatment of carbon nitride precursors. The recent finding of three melamine-melem adducts phases in a temperature range of 620 – 660 K in closed ampoules^[25] added weight to a condensation mechanism based on gas-phase reactions including the sublimation of melamine and the rapid formation of melem with melam $[(C_3N_3(NH_2)_2)_2(NH)]$,^[19] an *s*-triazine-based dimer formed by condensation of two molecules of melamine, acting as a highly reactive intermediate phase. Pure melam was so far only obtained as a minor phase in form of few tiny crystals during the condensation of melamine in open crucibles (2d, 340 – 360 °C).^[19] Furthermore, only a small number of melam derivatives is known in the literature, whereas a multitude of publications can be found on derivatives of the energetically favored intermediates of melamine and melem.^[19,26,27]

This contribution is dealing with the so far often disregarded highly reactive intermediate melam and its role in the condensation process to melon. A new synthesis route allowing for the preparation of melam in high yields is presented, applying elevated ammonia pressure to inhibit further condensation of melam according to Le Chatelier's principle. This approach also affords the formation of a melam-melem adduct phase, shedding light on the condensation process from melam to melem for the first time. Furthermore, the accessibility of pure melam in sufficient amounts allowed for the synthesis of crystalline melam hydrate ($C_6N_{11}H_9 \cdot 2H_2O$) by hydrothermal treatment and for its structure elucidation from single-crystal data.

3.2 Results and Discussion

Melam: Bulk melam was synthesized by thermal treatment of dicyandiamide at 450 °C and 0.2 MPa NH₃ in an autoclave. With this synthesis method, large amounts of melam are now accessible, the yield merely being reduced by sublimated melamine at the top of the autoclave. At higher temperatures, melam is transformed into melem which is also present at 450 °C as side-phase as well as one of the melamine-melem adduct phases ($2C_3N_3(NH_2)_3 \cdot C_6N_7(NH_2)_3$) as proven by Rietveld refinement (Figure 1, Table 2).

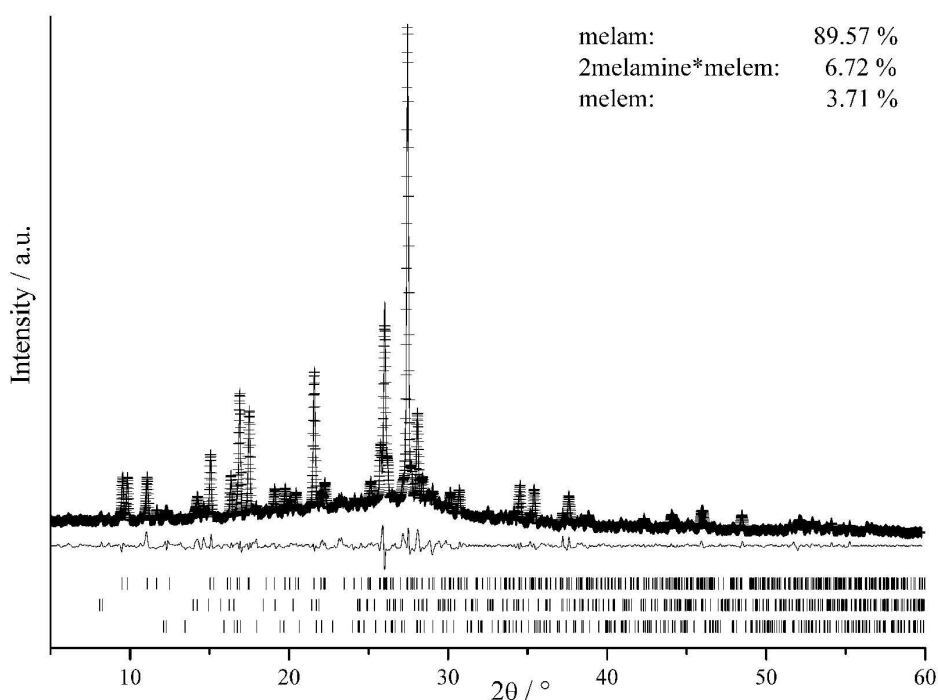


Figure 1. Rietveld refinement of the PXRD data of bulk melam (Cu-K_{α1} radiation). Measured data are indicated by crosses, refined data and the difference plot are given as solid lines. Bragg peaks are indicated by vertical bars (top: melam, middle: 2melamine*melem, bottom: melem).

Compared to the crystal data of melam which were determined at -143 °C from single-crystal XRD data, the cell parameters from the powder X-ray diffraction pattern taken at room temperature showed a significant deviation. Rietveld refinement proved nearly unchanged values for *a* and *b*, whereas the thermal expansion in *c*-direction leads to an enlargement of the corresponding parameter of 28 pm (from 1398 to 1426 pm). Although no pronounced π -stacking of the molecules is observed in the crystal structure of melam, the 3D screw-like

arrangement of mutually tilted melam units is elongated due to the weakened hydrogen bonds connecting the molecules in *c*-direction.

The thermal behavior of bulk melam was thoroughly investigated under different conditions (open/closed systems). Temperature-dependent X-ray powder diffraction measurements (TPXRD) in open quartz capillaries

Table 2. Crystallographic data of the Rietveld refinement of melam.

	melam	2melamine*melem	melem
Formula	C ₆ N ₁₁ H ₉	C ₁₂ N ₂₂ H ₁₈	C ₆ N ₁₀ H ₆
Space group	<i>C2/c</i>	<i>C2/c</i>	<i>P2₁/c</i>
<i>a</i> [pm]	1810.34(8)	2155.03(94)	738.43(40)
<i>b</i> [pm]	1085.45(4)	1267.00(95)	860.45(41)
<i>c</i> [pm]	1425.54(3)	684.51(14)	1329.97(99)
<i>V</i> [10 ⁶ pm ³]	2784.43(16)	1857.7(17)	835.66(88)
<i>Z</i>	12	4	4
Observed reflections	401	273	245
T[K]	293		
Diffraction range [°]	0 ≤ 2θ ≤ 60		
No. data points	5480		
GOF	1.474		
<i>R</i> indices (all data)	<i>R_p</i> = 0.04348, <i>wR_p</i> = 0.05934		

(to be referred to as a semi-closed system) indicated stability of melam up to 370 °C including a further elongation of the unit cell in *c*-direction visible by the shift of several intense reflections indexed as 113, 131 and 114 to smaller 2θ values (Figure 2) whereas no shift for the intense *hk0* reflection 310 was observed. Under slow heating conditions (heating rate of 1 °C min⁻¹), conversion into melem is observed at 380 °C without passing through an

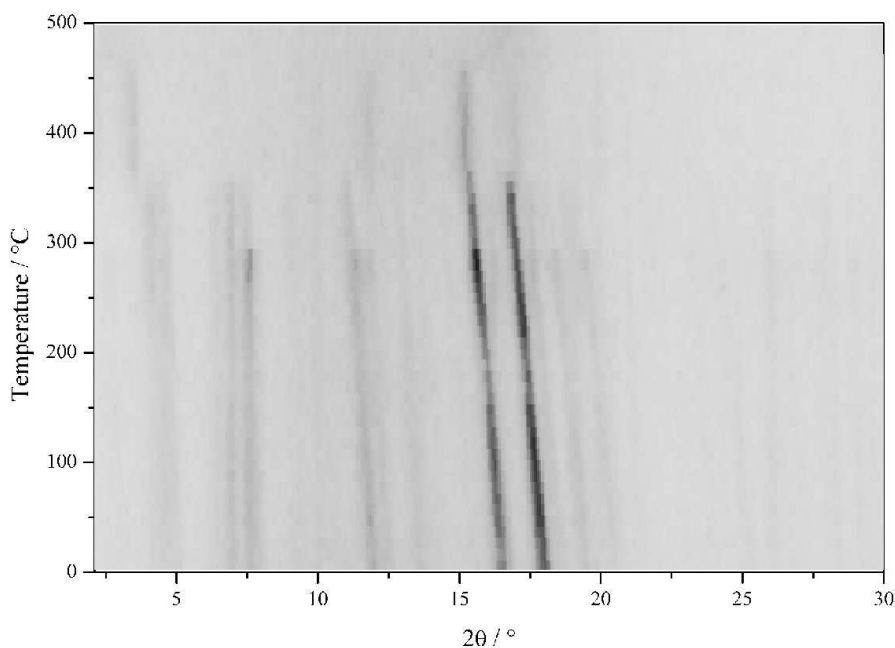


Figure 2. In situ temperature-programmed X-ray powder diffraction measurements (Mo-K_{α1} radiation) of bulk melam recorded between room temperature and 500 °C with a heating rate of 1 °C min⁻¹.

amorphous state. Pure melem was proven to be stable up to 460 °C.

Combined DTA/TG analysis (Figure 3) indicated the formation of two condensation products corresponding to two sharp endothermic signals at 374 and 403 °C accompanied by an observed overall mass loss of 22.6 % (3 mole NH₃: calculated 21.7 %). Whereas the formation of melem at around 370 °C upon thermal treatment of melam has been mentioned in literature,^[19] the second signal can probably be attributed to the formation of a new phase caused by the admixture of melem and a melamine-melem adduct phase in the bulk sample.

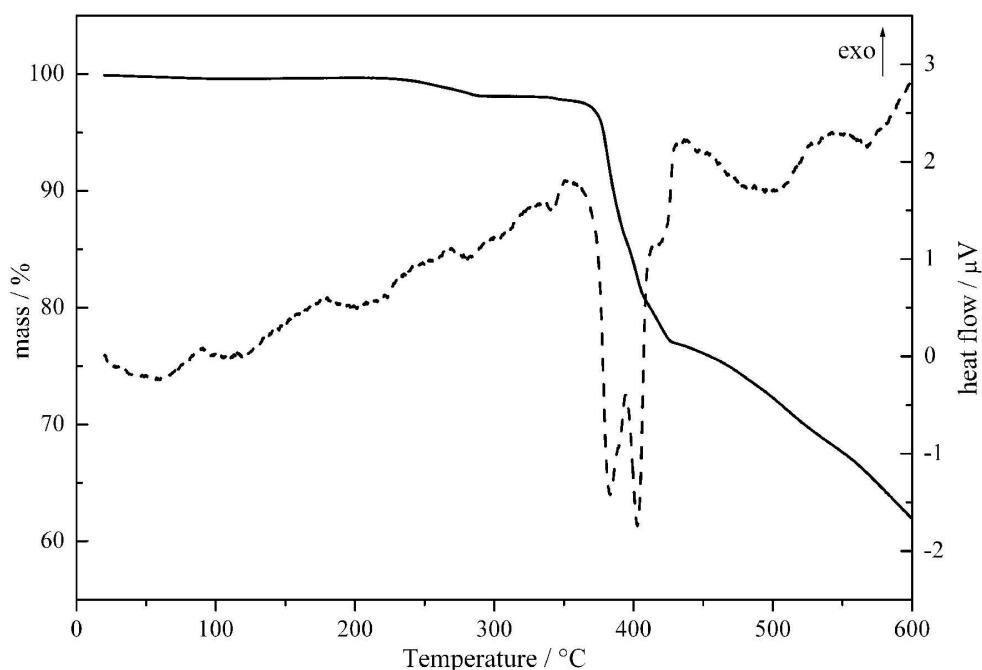


Figure 3. DTA/TG of bulk melam (24 mg) measured between room temperature and 600 °C with a heating rate of 5 °C min⁻¹.

As DTA/TG and TPXRD analysis yielded ambiguous results, further investigations in the interesting temperature range between 350 and 450 °C were conducted to isolate the above mentioned phase *ex situ*. In literature, it has been reported that melem is found within this temperature range (380 – 500 °C).^[15] However, a strong dependence not only of temperature and pressure but also of the reaction time has been revealed during investigation on thermal behavior of carbon nitride precursors. Whereas melem is formed at long reaction times (48h) at 380 °C and 400 °C in ampoules, shorter thermal treatment of melam (1h) yielded a mixture of melam, melem and a so far unknown phase which turned out to be a melam-melem adduct.

Melam-melem adduct phase: Similar to melam, the melam-melem adduct phase turned out to be a highly reactive intermediate stable only within a small temperature and time range. According to the synthesis of bulk melam, the adduct phase could therefore be isolated only by preventing further condensation using elevated ammonia pressure in an autoclave. Long reaction times (9-10 d) yielded samples of high crystallinity (Figure 4).

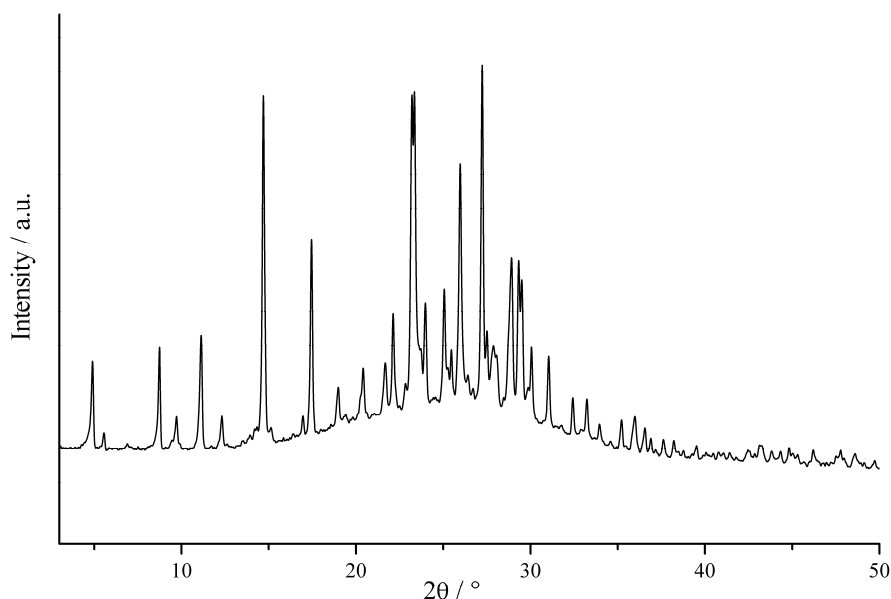


Figure 4. Powder X-ray diffraction pattern of phase I (Cu-K α_1 radiation).

To identify the building units of the adduct phase, mass spectrometry was carried out. Peaks at $m/z = 218$ and 235 were detected, corresponding exactly to the molecular mass of melem and melam, respectively, whereas no peaks at higher m/z values pointing out to more condensed products were found. The composition of the adduct phase was determined by elemental analysis. Observed and calculated results for various compositions are listed in Table 3.

Table 3. Elemental analysis data observed and calculated for different compounds and compositions.

Compound	sum formula	N[wt%]	C[wt%]	H[wt%]
phase I		64.31	32.28	3.25
melamine	[C ₃ N ₆ H ₆]	66.67	28.57	4.76
melam	[C ₆ N ₁₁ H ₉]	65.53	30.64	3.83
melem	[C ₆ N ₁₀ H ₆]	64.22	33.03	2.75
1:1 adduct ^[a]	[C ₆ N ₁₁ H ₉] [C ₆ N ₁₀ H ₆]	64.88	31.79	3.33
1:2 adduct ^[b]	[C ₆ N ₁₁ H ₉] [C ₆ N ₁₀ H ₆] ₂	64.66	32.19	3.15
2:3 adduct ^[c]	[C ₆ N ₁₁ H ₉] ₂ [C ₆ N ₁₀ H ₆] ₃	64.74	32.03	3.23

[a] melam/melem = 1:1; [b] melam/melem = 1:2; [c] melam/melem = 2:3.

As has been pointed out before, elemental analysis cannot be seen as an unambiguous proof of the formation of a certain adduct phase due to very similar compositions of the individual

compounds.^[19] However, with the building units of the adduct phase being verified to be melam and melam by mass spectrometry, and with the composition of the adduct matching neither melamine, melam nor melem, several different molar ratios assembling melam and melem into co-crystals were calculated. The best match was found for a 1:2 or a 2:3 adduct of melam and melem, with a small average deviation of 1.33 % and 0.69 %, respectively.

The FTIR spectrum of the melam-melem adduct phase is shown in Figure 5 (middle), together with the spectra of pure melam (top) and melem (bottom) for comparison. The similarity of the spectra becomes evident, especially regarding the NH stretching region above 3100 cm^{-1} and the characteristic sextant ring band around 800 cm^{-1} being split into two bands corresponding to the position of the absorption in the spectrum of melam (810 cm^{-1}) and melem (798 cm^{-1}).^[15,19] Also the fingerprint region of the adduct phase exhibits typical features of both spectra of the initial compounds. The several sharp and well-resolved absorption bands characteristic for C-N stretching and NH_2 bending vibrations visible for melam between 1640 and 1350 cm^{-1} are largely identical in the spectra of the adduct phase. However, the relative band intensities have changed showing a distribution closer related to that of melem. The most distinctive band of melam at 1583 cm^{-1} – absent in both the spectra

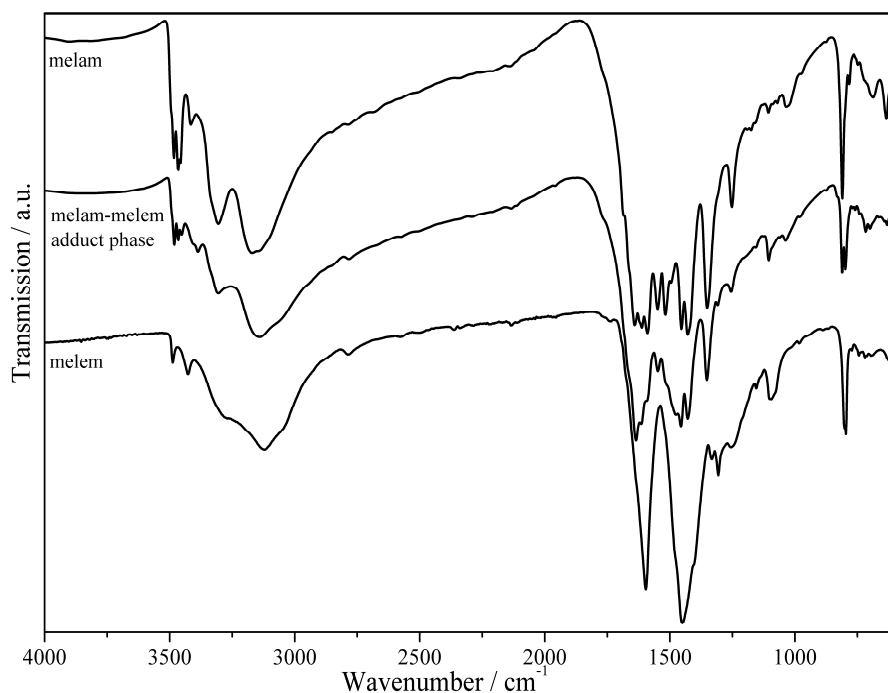


Figure 5. FTIR spectra of melam (top), melam-melem adduct phase (middle) and melem (bottom), measured as KBr pellets.

of melamine and melem – is found in the spectra of the adduct phase at 1590 cm^{-1} , as well as absorption below 1400 cm^{-1} (1350 and 1250 cm^{-1}) being characteristic of the C-NH-C unit found in melam and melon.^[16,19] These slight band shifts and the change in intensity exclude a simple superposition of the spectra of melam and melem, what was also discarded by PXRD results (Figure 4) and point out to a significantly altered hydrogen-bonding network. Although FTIR cannot supply the ultimate proof, the unambiguous similarity of the spectrum of the new phase with the ones of melam and melem clearly indicates the formation of an adduct phase of both compounds.

To gain further information on the nature of the adduct phase, ^{13}C and ^{15}N MAS NMR spectra have been recorded. The ^{13}C spectrum (Figure 6, top) exhibits characteristics of both the spectra of melam and melem. The signal at about 155.5 ppm can unambiguously be assigned to the CN_3 atoms of melem, whereas the markedly more intense group of signals between 162 and 170 ppm comprise signals of the CN_2NH_2 atoms of both substances.

A conventional ^{15}N CP MAS spectrum of the adduct phase could not be measured due to the long proton relaxation time.

However by introducing a flip-backsequence^[28,29] a significant gain in intensity could be reached by reducing the recycle delay to 2 s without a severe loss of intensity. Although the flip-back spectrum (Figure 6, bottom) still suffers from a low signal-to-noise ratio characteristic resonances for both melam and melem could be identified. The signals between -190 and -205 ppm are characteristic for

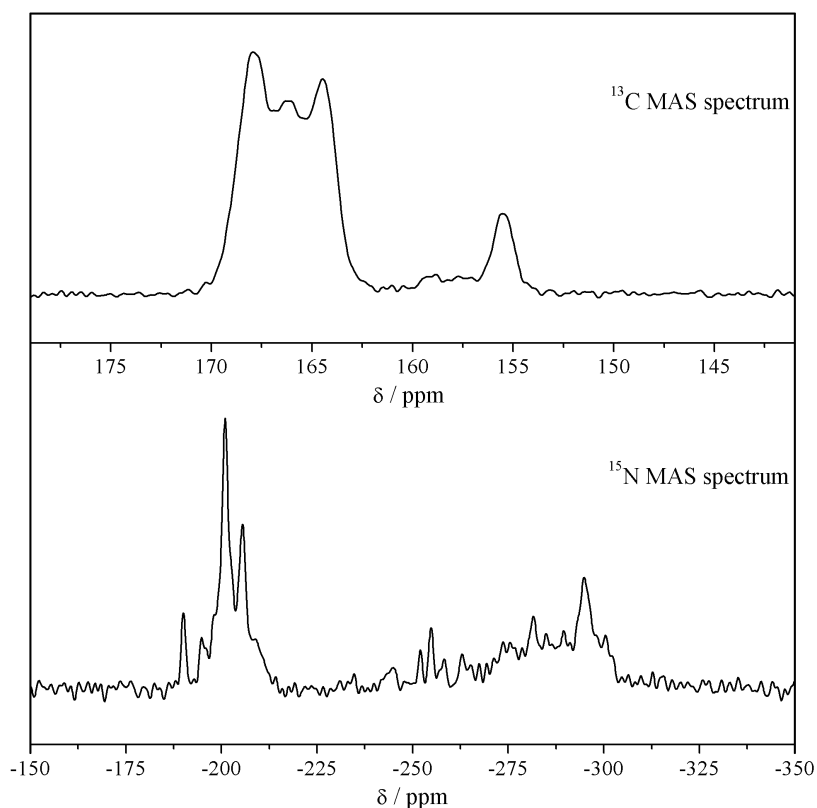


Figure 6. ^{13}C (top) and ^{15}N (bottom) MAS NMR spectra of the melam-melem adduct phase.

(outer) tertiary nitrogen atoms of triazine and tri-*s*-triazine units. The signal for the shielded central atom of melem which usually is the indicator for its presence can be found at -234.7 ppm. The signal has very low intensity which probably is a result of the measuring technique as CP experiments are not quantitative, especially if tertiary nitrogen atoms are in the vicinity of strongly coupled NH₂ groups. In the NH region, two signals at a chemical shift of -252 and -255 ppm are visible, therefore being in accordance with the split signal of the NH group in melam. The remaining signals between -270 and -300 ppm belong to NH₂ groups, with the tri-*s*-triazine nucleus of melem causing a low field shift (signals at -262 and -281 ppm) in comparison with the *s*-triazine rings of melam (signals between -282 and -300 ppm). The existence of few additional resonances (-194.8, -244.9, -258.2 and -262.9 ppm) strongly indicates a different hydrogen bond network as compared to pure melam and melem. This coincides the formation of an adduct phase of the building units melam and melem.

Both this and previous studies have shown that the choice of reaction conditions – especially pressure and temperature – is a critical factor for thermal condensation of these carbon nitride precursors.^[15,16,19,25] The tendency of melamine – the most stable intermediate - to sublime above 300 °C often leads to less defined products of low crystallinity (so-called raw melon, melem only with melamine as by-product) when condensation reactions are carried out in open systems. The partial elution of intermediates leads to rapid irreversible condensation. Accordingly, condensation reactions in ampoules (closed systems) which enable reversible gas phase reactions, usually lead to products of higher crystallinity.

Not only melem and melon can be synthesized in highly crystalline form in ampoules but also the structures of three so far unknown melamine-melem adducts have been elucidated recently from single crystals derived from such ampoule reactions.^[25] As expected the arising ammonia partial pressure seems to be the crucial factor for higher crystallinity as proven by the above presented autoclave reactions. Whereas the condensation of dicyandiamide beyond melamine is suppressed at supercritical conditions (20 MPa) even at 500 °C, reactions below 10 bar enabled condensation and ammonolysis reactions taking place at the same time, therefore inhibiting further condensation processes according to Le Chatelier. Correspondingly, by careful adjustment of the pressure, not only stable products like melamine and melem are formed but also further intermediates like melam and a melam-melem adduct phase can be isolated.

This synthesis strategy is furthermore in accordance with several routes to melam derivatives published so far. Both the synthesis of the melamium adduct $C_6N_{11}H_{10}Cl \cdot 0.5 NH_4Cl$ and the melamium-melamine adduct $C_6N_{11}H_{10}SCN \cdot 2 C_3N_3(NH_2)_3$ require elevated ammonia pressure in ampoules by usage of ammonium chloride (as additive for the pyrolysis of melamine) or ammonium thiocyanate (as single-source precursor), respectively.^[26]

Melam hydrate: Polycrystalline melam hydrate, which is used as starting material for the synthesis of melamium salts in solution due to the low solubility of melam, is commonly synthesized by treatment of melamium adducts like $C_6N_{11}H_{10}Cl \cdot 0.5 NH_4Cl$ with bases. Owing to the accessibility of bulk melam by the above presented autoclave method, single-crystals of melam hydrate were obtained for the first time by direct hydration applying hydrothermal conditions (300 °C / 24 h) and allowed for the determination of its crystal structure. Crystallographic data for melam hydrate and details of the structure refinement are summarized in Table 4.

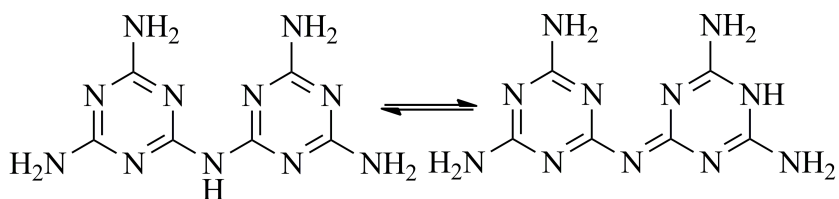
Melam hydrate crystallizes in space group $P2_1/c$ with four molecules in the monoclinic cell. The asymmetric unit contains one melam

Table 4. Crystallographic data and details of the structure refinement of melam hydrate.

	$C_6N_{11}H_9 \cdot 2 H_2O$
Molar mass [g·mol ⁻¹]	271.24
Crystal system	monoclinic
Space group	$P2_1/c$ (no. 14)
T [K]	293
Diffractometer	Nonius Kappa-CCD
Radiation, λ [pm]	Mo-K α , 71.073
<i>a</i> [pm]	676.84(2)
<i>b</i> [pm]	1220.28(4)
<i>c</i> [pm]	1394.24(4)
β [°]	98.372(2)
<i>V</i> [10 ⁶ pm ³]	1139.28(6)
<i>Z</i>	4
Calculated density [g·cm ⁻³]	1.582
Crystal size [mm ³]	0.25 x 0.15 x 0.09
Absorption coefficient [mm ⁻¹]	0.126
F(000)	568
Absorption correction	none
Diffraction range	$3.13^\circ \leq \theta \leq 25.35^\circ$
Index range	$-8 \leq h \leq 8,$ $-14 \leq k \leq 14$ $-16 \leq l \leq 16$
Parameters / restraints	211 / 0
Total no. of reflections	7590
No. of independent reflections	2087
No. of observed reflections	1766
Min./max. residual electron density [e·10 ⁻⁶ pm ⁻³]	-0.220 / 0.218
GooF	1.032
Final R indices [$I > 2\sigma(I)$]	$R1 = 0.0403, wR2 = 0.1083^{[a]}$
Final R indices (all data)	$R1 = 0.0490, wR2 = 0.1162^{[a]}$

[a] $w = [\sigma^2(F_0^2) + (0.0761P)^2 + 0.1753P]^{-1}$, with $P = (F_0^2 + 2 F_c^2)/3$.

molecule and two equivalents of water. As all hydrogen atoms have been found from difference Fourier syntheses the tautomeric form with



Scheme 2. The two tautomeric forms of melam discussed in literature.

conjugation between the triazine ring systems (Scheme 2, right) earlier discussed in the literature can be excluded,^[30-32] thus proving the “ditriazinylamine” form with two triazine units condensed through a bridging NH group, also corroborated by the crystal structure of melam

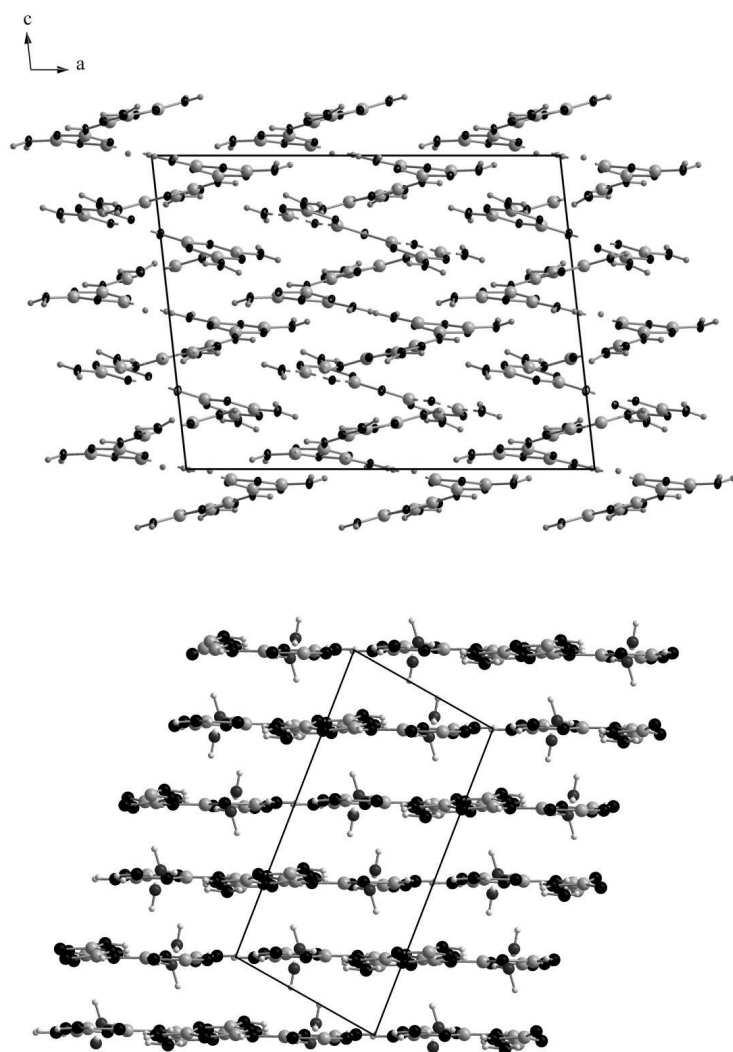


Figure 7. Top: Screw-like arrangement of the molecules in anhydrous melam (view along [010]). Bottom: layered structure of melam hydrate (view along [010]). Melam molecules are arranged coplanar, but show no π -stacking.

itself (Scheme 2, left).^[19,23,33-35] Compared to this structure, the molecules in melam hydrate show similar bond lengths and angles.

In anhydrous melam, a screw-like arrangement of slightly twisted melam molecules is observed, stabilized by a dense hydrogen bonding network.^[19] By hydrothermal treatment this network is broken up, therefore leading to a rearrangement of the now nearly planar melam molecules in a layered structure with an interlayer distance of 340 pm, thus slightly enlarged in comparison with other carbon nitride precursors like melem (327 pm) and melem hydrate (337 pm) (Figure 7).^[36,37]

Contrary to circular rosette-motifs known from melamine and melem derivatives,^[25,37-39] an ellipsoidal rosette-like motif is formed in melam hydrate according to – in comparison with

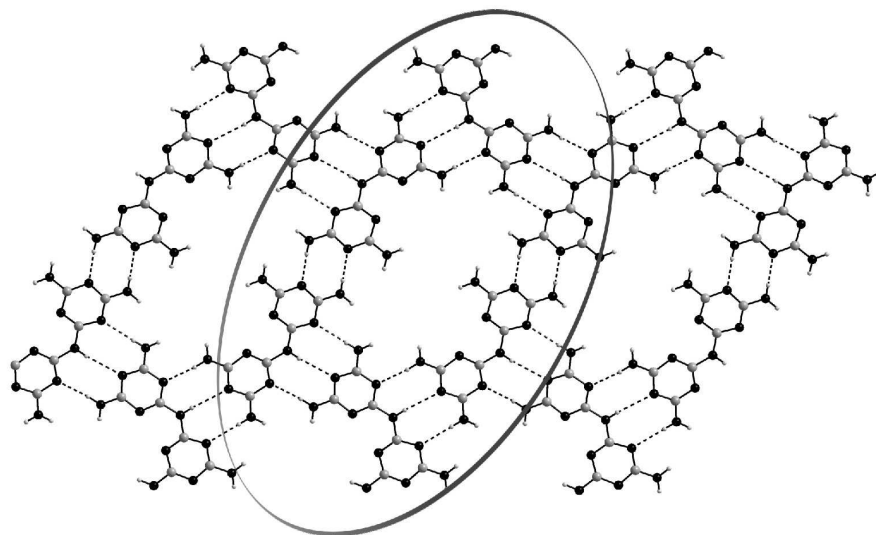


Figure 8. Arrangement of the melam molecules in a hydrogen-bonded ellipsoidal rosette-like motif in melam hydrate. Water molecules are omitted for clarity, carbon and hydrogen atoms are depicted in gray, nitrogen atoms in black; dashed lines represent hydrogen bonds.

melamine and melem - elongated building units. This structure is stabilized by a network of strong and medium strong hydrogen bonds with donor-acceptor distances ranging between 295 and 324 pm (Figure 8).

The oval voids within the rosettes show a transverse diameter of 8.3 Å and a conjugate diameter of 3.3 Å, values that are close to pore sizes found in melem hydrate (8.9 Å)^[37] and the 1:1 adduct of cyanuric acid and melamine (4 Å).^[38] Contrary to melem hydrate, the voids are not forming channels by AAA stacking but are arranged in a staggered fashion. The voids are filled with four water molecules, forming a dense network of hydrogen bonds (distances N-H...O = 300-355 pm, O-H...O = 277 pm, O-H...N = 296-297 pm) and probably acting as structure directing agents for the self-assembly of the melam molecules in solution (Figure 9).

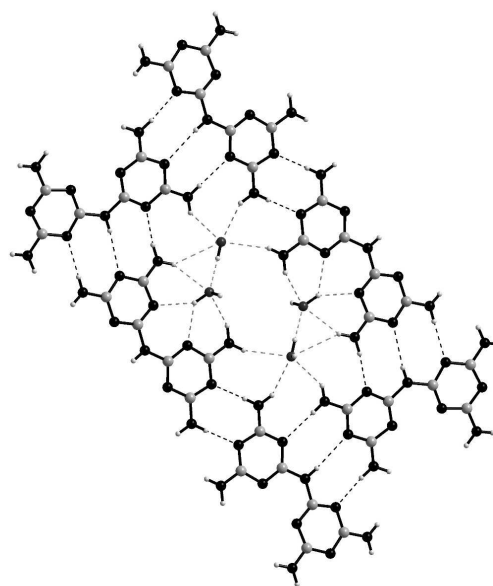


Figure 9. Representation of one ellipsoidal rosette filled with four templating water molecules, embedded in a dense hydrogen-bonded network.

The thermal behavior of melam hydrate was examined by combined thermogravimetry and differential thermal analysis to investigate the

strength of the non-covalent interactions between melam and water molecules. The obtained curves (Figure 10) show dehydration to take place between 100 and 150 °C. Elemental analysis has shown that the above presented hydrothermal treatment of melam leads to the formation of bulk samples with varying content of crystal water. Whereas further refinement of the oxygen occupancies in the single-crystal data yielded the formula $C_6N_{11}H_9 \cdot 1.93H_2O$, elemental analysis and combined DTA/TG measurements of several bulk samples synthesized at 300 °C point out to a lower content of water molecules per melam unit ($C_6N_{11}H_9 \cdot xH_2O$; $1 \leq x \leq 1.5$). Dehydrated melam is stable up to temperatures of 380 °C before rapidly decomposing, thus being in accordance with the thermal behavior of anhydrous melam.^[19]

In the case of melam hydrate temperature-dependent powder X-ray diffraction investigations

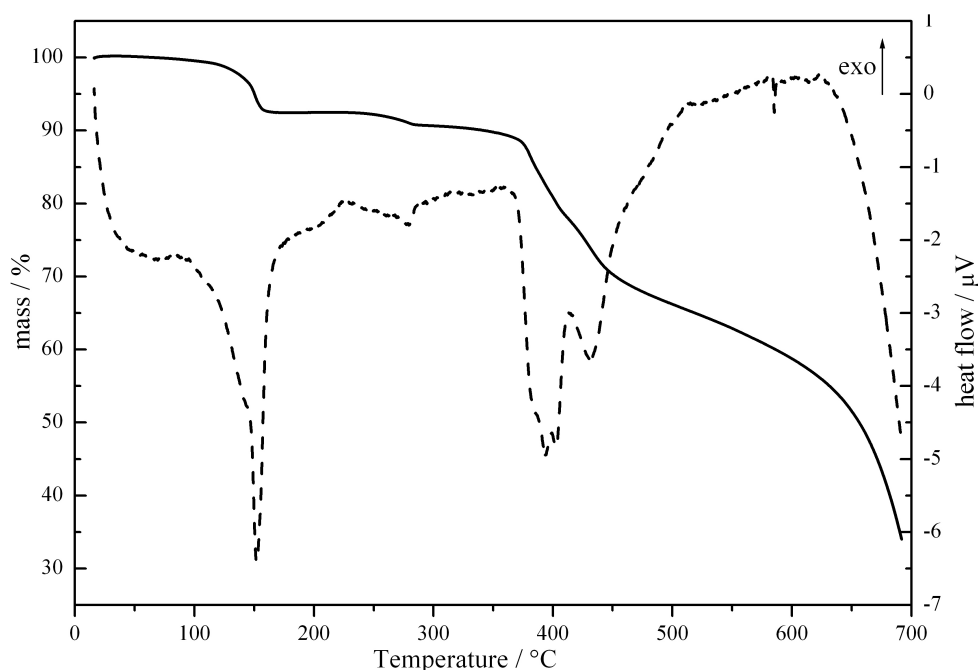


Figure 10. DTA/TG of melam hydrate (31 mg) measured between room temperature and 700 °C with a heating rate of 5 °C min⁻¹

have shown that dehydration leads to decreasing crystallinity of the sample as expected. Contrary to melam hydrate,^[37] the removal of crystal water is accompanied by rearrangement of the layered melam molecules in the screw-like formation of anhydrous melam, therefore proving the hydrogen bonding network including the water molecules to be the crucial factor for the stability of the planar arrangement of the molecules in melam hydrate.

The FTIR spectrum of melam hydrate is shown in Figure 11. All bending and stretching vibrations bear a clear resemblance with the signals for melam,^[19] however, some slight differences remain. In the OH and NH stretching region, the sharp signal at 3470 cm^{-1} observed for anhydrous melam is

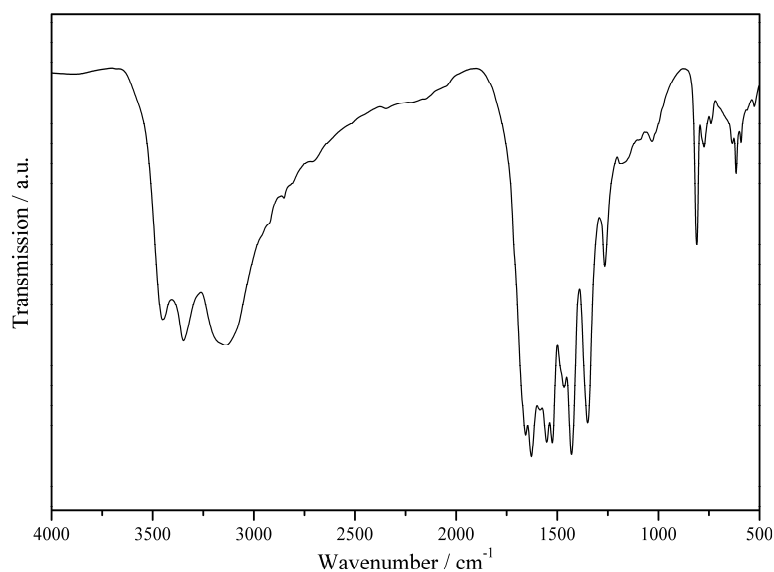


Figure 11. FTIR spectrum of melam hydrate (recorded as KBr pellet).

covered by a broad $\nu(\text{OH})$ signal in the spectrum of melam hydrate. Absorption at 810 cm^{-1} (the sextant ring band) and at 1350 and 1250 cm^{-1} characteristic for the C-NH-C unit in melam is in accordance with the data of anhydrous melam, whereas the bands between 1650 and 1430 cm^{-1} assigned to $\nu(\text{C}=\text{N})$ and $\delta(\text{NH}_2)$ vibrations are slightly changed in intensity and position due to the participation of the *s*-triazine rings and NH_2 groups in the hydrogen bonding network with the water molecules.

3.3 Conclusion

With the synthesis of bulk melam and a melam-melem adduct by thermal treatment of dicyandiamide under elevated ammonia pressure the influence not only of temperature but also of pressure adjustment for the condensation process of carbon nitrides has been proven. According to Le Chatelier's principle, ammonia pressure antagonizes the cleavage of ammonia which is the driving force of usually very fast condensation processes. To our present knowledge the formation of melam - which was long time thought to be a competitive reaction product of the condensation process of melamine to melem via the melamine-melem adduct phases - is in fact part of that condensation process, however most of the time not detectable due to the rapid further condensation of melam to melem (via at least one adduct phase). This fast transformation - leading to an always observed coexistence of the adduct

phase(s) with melam or melem – complicates a more detailed description of the adduct phase(s) regarding quantity, composition and structure. Local methods like advanced solid-state NMR spectroscopy or TEM investigations will be used to further study these compounds.

By careful adjustment of the reaction conditions the formation of further melam-melem adduct phases is conceivable as well. For investigations of further condensation processes (namely from melem to melon) special autoclaves with a maximal operation temperature of $>500\text{ }^{\circ}\text{C}$ are necessary, as up to $500\text{ }^{\circ}\text{C}$ and 2 bar NH_3 melem is the final de-ammonation product of melamine to be synthesized. However, reactions under elevated ammonia pressure might be a valuable tool for the synthesis of melem dimers or oligomers to further elucidate condensation processes up to polymeric carbon nitrides.

Hydrothermal treatment of melam up to $300\text{ }^{\circ}\text{C}$ did not induce condensation but led to the formation of melam hydrate $[\text{C}_3\text{N}_3(\text{NH}_2)_2]_2\text{NH} \cdot 2\text{H}_2\text{O}$. Melam hydrate, so far only known as polycrystalline multiphased compound was obtained in crystalline form for the first time, therefore proving the high reactivity of supercritical fluids and their good solvating properties. With melam now being accessible in large amounts and with the demonstrated possibility to enhance the solubility of melam by hydro- or solvothermal treatment, the prerequisites to explore the chemistry of melam in terms of acid-base-reactions or coordination chemistry are hence provided and recommend melam also for the synthesis of so-called “organic alloys”.^[40]

3.4 Experimental Section

Synthesis

Melam: Bulk melam was synthesized by heating dicyandiamide (1g, $11.9 \cdot 10^{-3}$ mol, $\geq 99\%$, Avocado) in a quartz inlay placed in an autoclave filled with gaseous NH_3 (2 bar) at $450\text{ }^{\circ}\text{C}$ with a heating rate of $2\text{ }^{\circ}\text{C min}^{-1}$. After a tempering time of 1-5 days, the autoclave was cooled down to room temperature at $1\text{ }^{\circ}\text{C min}^{-1}$ and opened carefully. Bulk melam is found at the bottom of the inlay, sublimated melamine at the top of the autoclave. Data for melam: IR (KBr): $\tilde{\nu} [\text{cm}^{-1}] = 3483\text{ (m)}, 3466\text{ (m)}, 3457\text{ (m)}, 3416\text{ (w)}, 3306\text{ (s)}, 3170\text{ (s)}, 1641\text{ (vs)}$,

1612 (vs), 1590 (vs), 1549 (vs), 1518 (vs), 1454 (vs), 1429 (vs), 1351 (vs), 1252 (m), 1175 (w), 1106 (w), 1070 (w), 1034 (w), 972 (vw), 811 (m), 783 (vw), 748 (vw), 687 (w), 634 (w).

Melam-melem adduct phase: The melam-melem adduct phase was synthesized by heating dicyandiamide (1g, $11.9 \cdot 10^{-3}$ mol, ≥ 99 %, Avocado) in a quartz inlay placed in an autoclave filled with gaseous NH_3 (2 bar) at 450 °C with a heating rate of 2 °C min^{-1} . After a tempering time of 9-10 days, the autoclave was cooled down to room temperature at 1 °C min^{-1} and opened carefully. The adduct is found at the bottom of the inlay, sublimated melamine at the top of the autoclave. Data for the melam-melem adduct phase: IR (KBr): $\tilde{\nu}$ [cm^{-1}] = 3482 (w), 3466 (w), 3452 (w), 3387 (w), 3306 (m), 3141 (s), 1635 (vs), 1592 (vs), 1548 (vs), 1475 (vs), 1456 (vs), 1428 (vs), 1352 (s), 1309 (m), 1255 (m), 1105 (w), 1037 (w), 811 (w), 798 (w), 769 (vw), 759 (vw), 741 (vw), 641 (vw), 717 (w), 700 (vw), 631 (vw), 610 (vw).

Melam hydrate: Single crystals of melam hydrate suitable for X-ray diffraction analysis were synthesized under hydrothermal conditions by heating a suspension of melam (100 mg, $0.36 \cdot 10^{-3}$ mol) in 30 mL H_2O in a quartz inlay placed in an autoclave. The autoclave was heated for 24 hours at 300 °C, then cooled down to room temperature at 0.05 °C min^{-1} . Data for melam hydrate: IR (KBr): $\tilde{\nu}$ [cm^{-1}] = 3451 (s), 3348 (s), 3139 (s), 1656 (vs), 1628 (vs), 1585 (vs), 1552 (vs), 1524 (vs), 1466 (s), 1430 (vs), 1350 (vs), 1265 (m), 1187 (w), 1031 (vw), 810 (m), 774 (w), 740 (vw), 635 (vw), 616 (w).

General techniques

Mass spectra were obtained using a Jeol MStation JMS-700 gas inlet system by using Direct insertion (DEI^+). Elemental analyses for C, H and N were performed with the elemental analyzer systems Vario EL and Vario Micro (Elementar Analysensysteme GmbH). FTIR measurements were carried out on a Bruker IFS 66v/S spectrometer. Spectra of the samples were recorded in an evacuated cell at ambient conditions between 400 and 4000 cm^{-1} after diluting the samples in KBr pellets (2 mg sample, 300 mg KBr, hand press with press capacity 10 kN). Thermoanalytical measurements were carried out under inert atmosphere (He) with a Thermoanalyzer TG-DTA92 (Setaram). The samples were heated in an alumina crucible from room temperature to 600 °C with a heating rate of 5 K \cdot min^{-1} .

X-ray diffraction: Powder X-ray diffraction data were collected on a Stoe STADI P diffractometer using Ge(111)-monochromated $\text{Cu-K}_{\alpha 1}$ radiation ($\lambda=154.06$ pm). High-

temperature in situ X-ray diffraction was carried out on a STOE Stadi P powder diffractometer (Ge(111)-monochromated Mo-K $_{\alpha 1}$ radiation, $\lambda = 70.093$ pm) with an integrated furnace using unsealed quartz capillaries (\varnothing 0.5 mm) as sample containers. The samples were measured from 298 K to temperatures around 773 K in steps of 10 K min $^{-1}$, using a heating rate of 1 K min $^{-1}$ between the scans.

Solid-state NMR spectroscopy: The 1D solid-state NMR experiments were carried out at ambient temperature on an Avance 500 NMR spectrometer (Bruker) with an external magnetic field of 11.7 T, operating at Larmor frequencies of 500.1 MHz, 125.7 MHz and 50.7 MHz for ^1H , ^{13}C and ^{15}N , respectively. The measurements were carried out in a 4 mm standard double resonance MAS probe (Bruker) at a spinning speed of 10 kHz. The chemical shifts of ^{13}C and ^{15}N were referenced relative to TMS and nitromethane. For the $^1\text{H}^{13}\text{C}$ and $^1\text{H}^{15}\text{N}$ cross-polarization (CP) MAS spectra a ramped-amplitude (RAMP) shape pulse on ^1H , centered on the $n = +1$ Hartmann-Hahn condition, with a nutation frequency ν_{nut} of 45 kHz (^{13}C) and 55 kHz (^{15}N) was used. The ^1H RF field varied linearly about 20% during a contact time of 1.5 ms (^{13}C) and 7 ms (^{15}N). During the acquisition of the FID ^1H continuous wave (CW) decoupling with a nutation frequency of ca 80 kHz (^{13}C experiment) and ca 70 kHz (^{15}N experiment) was performed. After the acquisition a flip-back (FB)^[28,29] pulse was applied on ^1H so that the recycle delay becomes less dependent of the ^1H T_1 relaxation time. The recycle delay was set to 20 s (^{13}C) and 2 s (^{15}N). About 2500 and 121000 transients were accumulated for the ^{13}C and ^{15}N experiments, respectively.

X-ray Structure Determination: Single-crystal X-ray diffraction data of melam hydrate was collected at 293 K with a Kappa CCD diffractometer using monochromated Mo-K $_{\alpha}$ radiation ($\lambda = 71.073$ pm). The diffraction intensities were scaled using the SCALEPACK software package.^[41] No additional adsorption correction was applied. The crystal structure was solved by direct methods using the software package SHELXS-97 and refined against F^2 by applying the full-matrix least-squares method (SHELXL-97).^[42-44] Hydrogen positions could be determined from difference Fourier syntheses and were refined isotropically. All non-hydrogen atoms were refined anisotropically. Crystallographic data for melam hydrate have been deposited with the Cambridge Crystallographic Data Centre, CCDC, 12 Union Road, Cambridge CB21EZ, UK. Data can be obtained free of charge on quoting the depository number CCDC-901046 (Fax: +44-1223-336-033; E-Mail: deposit@ccdc.cam.ac.uk, <http://www.ccdc.cam.ac.uk>).

Acknowledgements

We gratefully acknowledge financial support that was granted from the Deutsche Forschungsgemeinschaft (DFG) (project SCHN 377/15-1) and from the Fonds der Chemischen Industrie (FCI) (scholarship for E. Wirnhier). We furthermore gratefully acknowledge Dr. Charlotte Martineau and Dr. Francis Taulelle de Tectospin, Institut Lavoisier de Versailles, Université de Versailles Saint-Quentin-en-Yvelines for measurement time on their Avance 500 Bruker Spectrometer.

3.5 Bibliography

- [1] A. Y. Liu, M. L. Cohen, *Science* **1989**, *245*, 841-842.
- [2] A. Y. Liu, M. L. Cohen, *Phys. Rev. B* **1990**, *41*, 10727-10734.
- [3] A. Y. Liu, R. M. Wentzcovitch, *Phys. Rev. B* **1994**, *50*, 10362-10365.
- [4] C.-M. Sung, M. Sung, *Mater. Chem. Phys.* **1996**, *43*, 1-18.
- [5] D. M. Teter, R. J. Hemley, *Science* **1996**, *271*, 53-55.
- [6] E. Horvath-Bordon, R. Riedel, P. F. McMillan, P. Kroll, G. Miehe, P. A. van Aken, A. Zerr, P. Hoppe, O. Shebanova, I. McLaren, S. Lauterbach, E. Kroke, R. Boehler, *Angew. Chem.* **2007**, *119*, 1498-1502 *Angew. Chem. Int. Ed.* **2007**, *46*, 1476-1480.
- [7] A. Thomas, A. Fischer, F. Goettmann, M. Antonietti, J.-O. Müller, R. Schlögl, J. M. Carlsson, *J. Mater. Chem.* **2008**, *18*, 4893-4908.
- [8] F. Goettmann, A. Fischer, M. Antonietti, A. Thomas, *Chem. Commun.* **2006**, 4530-4532.
- [9] F. Goettmann, A. Fischer, M. Antonietti, A. Thomas, *New. J. Chem.* **2007**, *31*, 1455-1460.
- [10] F. Goettmann, A. Thomas, M. Antonietti, *Angew. Chem.* **2007**, *119*, 2773-2776 *Angew. Chem. Int. Ed.* **2007**, *46*, 2717-2720.
- [11] J. Zhang, X. Chen, K. Takanabe, K. Maeda, K. Domen, J. D. Epping, X. Fu, M. Antonietti, X. Wang, *Angew. Chem.* **2010**, *122*, 451-454; *Angew. Chem. Int. Ed.* **2010**, *49*, 441-444.
- [12] X. Wang, K. Maeda, A. Thomas, K. Takanabe, G. Xin, J. M. Carlsson, K. Domen, M. Antonietti, *Nat. Mater.* **2009**, *8*, 76-80.
- [13] Y. Zhang, A. Thomas, M. Antonietti, X. Wang, *J. Am. Chem. Soc.* **2009**, *131*, 50-51.
- [14] Y. Zhang, M. Antonietti, *Chem. Asian J.* **2010**, *5*, 1307-1311.
- [15] B. Jürgens, E. Irran, J. Senker, P. Kroll, H. Müller, W. Schnick, *J. Am. Chem. Soc.* **2003**, *125*, 10288-10300.
- [16] B. V. Lotsch, M. Döblinger, J. Sehnert, L. Seyfarth, J. Senker, O. Oeckler, W. Schnick, *Chem. Eur. J.* **2007**, *13*, 4969-4980.
- [17] B. V. Lotsch, W. Schnick, *Chem. Mater.* **2005**, *17*, 3976-3982.
- [18] B. V. Lotsch, W. Schnick, *Chem. Mater.* **2006**, *18*, 1891-1900.

- [19] B. V. Lotsch, W. Schnick, *Chem. Eur. J.* **2007**, *13*, 4956-4968.
- [20] D. T. Vodak, K. Kim, L. Iordanidis, P. G. Rasmussen, A. J. Matzger, O. M. Yaghi, *Chem. Eur. J.* **2003**, *9*, 4197-4201.
- [21] E. Kroke, M. Schwarz, E. Horvath-Bordon, P. Kroll, B. Noll, A. D. Norman, *New. J. Chem.* **2002**, *26*, 508-512.
- [22] J. Sehnert, K. Baerwinkel, J. Senker, *J. Phys. Chem. B* **2007**, *111*, 10671-10680.
- [23] E. C. Franklin, *J. Am. Chem. Soc.* **1922**, *44*, 486-509.
- [24] J. Liebig, *Ann. Pharm.* **1834**, *10*, 1.
- [25] A. Sattler, S. Pagano, M. Zeuner, A. Zurawski, D. Gunzelmann, J. Senker, K. Müller-Buschbaum, W. Schnick, *Chem. Eur. J.* **2009**, *15*, 13161-13170.
- [26] N. E. Braml, A. Sattler, W. Schnick, *Chem. Eur. J.* **2012**, *18*, 1811-1819.
- [27] S. Tragl, K. Gibson, H.-J. Meyer, *Z. Anorg. Allg. Chem.* **2004**, *630*, 2373-2376.
- [28] J. Tegenfeldt, U. Haeberlen, *J. Magn. Reson.* **1979**, *36*, 453-457.
- [29] K. Saito, C. Martineau, G. Fink, F. Taulelle, *Solid State Nucl. Magn. Reson.* **2011**, *40*, 66-71.
- [30] A. I. Finkel'shtein, *Russ. J. Gen. Chem.* **1961**, *31*, 1046-1049.
- [31] M. Takimoto, *Nippon Kagaku Zasshi* **1964**, *85*, 168-176.
- [32] N. V. Spiridonova, A. I. Finkel'shtein, *Khim. Geterotsykl. Soedin.* **1966**, *1*, 126-129.
- [33] C. E. Redemann, H. J. Lucas, *J. Am. Chem. Soc.* **1940**, *62*, 842-846.
- [34] P. Klason, *J. Prakt. Chem.* **1886**, *33*, 285-289.
- [35] B. Bann, S. A. Miller, *Chem. Rev.* **1958**, *58*, 131-172.
- [36] A. Sattler, W. Schnick, *Z. Anorg. Allg. Chem.* **2006**, *632*, 238-242.
- [37] S. J. Makowski, P. Köstler, W. Schnick, *Chem. Eur. J.* **2012**, *18*, 3248-3257.
- [38] A. Ranganathan, V. R. Pedireddi, C. N. R. Rao, *J. Am. Chem. Soc.* **1999**, *121*, 1752-1753.
- [39] G. M. Whitesides, E. E. Simanek, J. P. Mathias, C. T. Seto, D. N. Chin, M. Mammen, D. M. Gordon, *Acc. Chem. Res.* **1995**, *28*, 37-44.
- [40] T. Hasell, S. Y. Chong, M. Schmidtman, D. J. Adams, A. I. Cooper, *Angew. Chem.* **2012**, *124*, 7266-7269; *Angew. Chem. Int. Ed.* **2012**, *51*, 7154-7157.
- [41] Z. Otwinowski, W. Minor, *Methods Enzymol.* **1997**, *276*, 307-326.
- [42] G. M. Sheldrick, *SHELXS-97*, Program for the Solution of Crystal Structures, Universität Göttingen, **1997**.

- [43] G. M. Sheldrick, *SHELXL-97*, Program for the Refinement of Crystal Structures, Universität Göttingen **1997**.
- [44] G. M. Sheldrick, *Acta Crystallogr., Sect. A* **2008**, *64*, 112-122.

4. Polytriazine Imide – Structure, Properties and Possible Applications

As has been shown in the previous chapter, the utilization of ammonia and water as solvent or gaseous admixture can decelerate condensation reactions and allows for the synthesis of crystalline molecular carbon nitride intermediates. However, at the maximum temperatures permitted by the autoclave technique used in this work (500 °C), the formation of highly condensed networks is inhibited by ammonia pressure slowing down reaction kinetics. Accordingly, a different approach is necessary for the synthesis of highly condensed carbon nitride networks.

Salt melts have been known for a long time as high-temperature inorganic solvents with good solvating properties regarding for instance nitrides, carbides and cyanates. With the melting point of a multitude of salt melts being located below the formation temperature of carbon nitride networks (< 500 – 600 °C), their utilization overcomes the immobility of larger condensation intermediates and should therefore enable the synthesis of crystalline carbon nitride networks.

In this chapter, the synthesis of poly(triazine imide) with LiCl intercalation by the above mentioned salt melt method (using a LiCl/KCl flux) is described. The structure of this crystalline network is elucidated by a complementary approach using different diffraction techniques like electron and powder X-ray diffraction as well as NMR and IR spectroscopy. Furthermore, the effect of LiCl intercalation regarding structural and electronic properties is investigated. With XAS/XES and VEELS, two modern methods for band gap measurements are applied to carbon nitrides for the first time, enabling a very exact and – in the case of EELS - also local band gap determination which is compared to theoretical calculations. In the last part of this chapter, the photocatalytic activity of PTI/LiCl towards visible-light driven hydrogen evolution is examined and compared to several less crystalline and carbon-doped derivatives.

4.1 Poly(triazine Imide) with LiCl Intercalation (PTI/LiCl)

All NMR measurements in this subsection were carried out by Daniel Gunzelmann and Prof. Dr. J. Senker (University of Bayreuth) and will also be published as part of the PhD thesis of D. Gunzelmann.

Poly(triazine imide) with Intercalation of Lithium and Chloride Ions [(C₃N₃)₂(NH_xLi_{1-x})₃·LiCl]: A Crystalline 2D Carbon Nitride Network

**Eva Wirnhier, Markus Döblinger, Daniel Gunzelmann, Jürgen Senker,
Bettina V. Lotsch, and Wolfgang Schnick**

published in: *Chem. Eur. J.* **2011**, *17*, 3213 – 3221. DOI: 10.1002/chem.201002462

Keywords: carbon nitrides; electron diffraction; intercalations; layered compounds; NMR spectroscopy

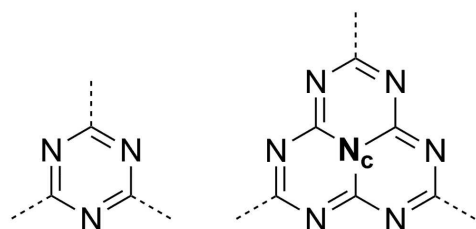
Abstract: Poly(triazine imide) with intercalation of lithium and chloride ions (PTI/Li⁺Cl⁻) was synthesized by temperature-induced condensation of dicyandiamide in a eutectic mixture of lithium chloride and potassium chloride as solvent. By using this ionothermal approach the well-known problem of insufficient crystallinity of carbon nitride (CN) condensation products could be overcome. The structural characterization of PTI/Li⁺Cl⁻ resulted from a complementary approach using spectroscopic methods as well as different diffraction techniques. Due to the high crystallinity of PTI/Li⁺Cl⁻ a structure solution from both powder

X-ray and electron diffraction patterns using direct methods was possible; this yielded a triazine-based structure model, in contrast to the proposed fully condensed heptazine-based structure that has been reported recently. Further information from solid-state NMR and FTIR spectroscopy as well as high-resolution TEM investigations was used for Rietveld refinement with a goodness-of-fit (χ^2) of 5.035 and $wRp=0.05937$. $\text{PTI/Li}^+\text{Cl}^-$ ($P6_3cm$ (no. 185); $a=846.82(10)$, $c=675.02(9)$ pm) is a 2D network composed of essentially planar layers made up from imide-bridged triazine units. Voids in these layers are stacked upon each other forming channels running parallel to [001], filled with Li^+ and Cl^- ions. The presence of salt ions in the nanocrystallites as well as the existence of sp^2 -hybridized carbon and nitrogen atoms typical of graphitic structures was confirmed by electron energy-loss spectroscopy (EELS) measurements. Solid-state NMR spectroscopy investigations using ^{15}N -labeled $\text{PTI/Li}^+\text{Cl}^-$ proved the absence of heptazine building blocks and NH_2 groups and corroborated the highly condensed, triazine-based structure model.

4.1.1 Introduction

Over the last few decades, main-group nitrides have significantly gained importance in the field of high-performance functional materials due to their exceptional chemical stability and properties.^[1–3] With the spotlight focused on light element-based nitrides qualified for a multitude of technological applications by their structural variety and strong covalence, carbon nitrides have boomed owing to their specific chemical properties. Since the “harder than diamond” fever has been evoked by the work of Liu and Cohen, much effort has been made to synthesize dense 3D phases of binary carbon nitride, C_3N_4 , which was predicted to show very low compressibility and superhardness.^[4–8] Carbon nitride imide ($C_2N_2(NH)$), presented in 2007, was the first described crystalline 3D carbon nitride network and showed a defect wurtzite-type structure.^[9] Recently, low-density 2D carbon nitrides have also been attracting interest owing to their manifold optical and electronic properties. Not only graphitic carbon nitride (g- C_3N_4), which is considered to be a precursor for high-pressure conversion into 3D C_3N_4 and computed as the most stable modification under ambient conditions,^[8] but also hydrogen-richer samples seem to be promising new materials for organic semiconductor science, catalytic applications, and as photoactive materials for converting solar light into electricity.^[10–17]

In the case of 2D graphitic carbon nitrides, a class of compounds that was already known in 1834 has regained interest. The pioneering work of Berzelius, Liebig, and Franklin included



Scheme 1. Triazine core (C_3N_3) (left) and heptazine core (C_6N_7) (right). For the heptazine core, two types of nitrogen atoms are distinguishable: the outer nitrogen atoms and the central nitrogen atom (“ N_c ”).

the first synthesis of melon [$C_6N_7(NH_2)(NH)$]_n and other deamination products of so-called “ammonocarbonic acids” ($x C_3N_4 \cdot y NH_3$) such as cyanamide or melamine.^[18,19] Due to the amorphous character and undefined composition of melon, its structure was an object of discussion for a long time, which resulted in several structural models based on both heptazine or triazine cores (see Scheme 1), respectively.^[18,20–23] Recently, a structure solution by

combination of several analytical techniques comprising electron diffraction and solid-state

NMR spectroscopy yielded a heptazine-based 2D network.^[24] With melon regarded as an important intermediate towards g-C₃N₄, its structure solution adds weight to theoretically favored heptazine-based structure models for this carbon nitride (CN) modification.^[25] However, triazine-based structure predictions according to N-substituted graphite layers have not been completely ruled out.^[6, 8, 26–28] A plethora of experimental efforts has been made using chemical and physical vapor deposition techniques as well as bulk synthesis routes to elucidate the crystal structure of g-C₃N₄. Mostly, kinetic problems such as condensation being too fast and the immobility of the condensation intermediates have inhibited a complete reaction and yielded nonstoichiometric, amorphous products.^[1, 28–37] Recently, Antonietti et al. reported a novel approach to increase crystallinity by using salt melts as solvents for CN condensation reactions. The reaction product was claimed to be g-C₃N₄ and a structural model was proposed based on staggered sheets of 2D condensed heptazine building blocks as predicted previously for graphitic carbon nitride.^[1, 38]

With their high thermal stability and their good solvating properties regarding nitrides, carbides, cyanides, cyanates, and thiocyanates, salt melts were already known as good solvents in the 1960s.^[39–42] In particular, a eutectic mixture of LiCl and KCl with its melting point below the condensation temperature of melon C₆N₇(NH₂)₃ exhibits promising capability for CN condensation reactions.

Herein we report on the synthesis and the first unambiguous structure solution by powder X-ray diffraction methods for a 2D carbon nitride network with high crystallinity due to the usage of a LiCl/KCl salt melt. High-resolution (HR) TEM investigations and electron diffraction as well as solid-state NMR and FTIR spectroscopy data corroborated the triazine-based structure model and clarified the occupation of voids within the structure.

4.1.2 Results and Discussion

Synthesis and characterization

Heating intimate mixtures of dicyandiamide and a eutectic mixture of lithium chloride and potassium chloride in sealed silica glass ampoules at 600 °C according to the literature^[38] yielded a brownish product. After removing excess amounts of salt with boiling distilled

water a brown powder, later identified as poly(triazine imide) with intercalation of lithium and chloride ions (PTI/Li⁺Cl⁻), was obtained. Elemental analysis yielded an approximate composition of C₁₂N_{17.5}H_{6.3}Cl_{1.5}Li_{3.2} with a molar ratio C/N=0.69 being closer to carbon nitride networks such as melon (0.68)^[24] or poly(heptazine imide) (PHI; 0.65)^[43] than to fully condensed C₃N₄ (theoretical: 0.75). The color of the obtained material is probably due to the onset of carbonization at temperatures between 550 and 600 °C. Whereas at temperatures above 600 °C rapidly increasing carbonization and decomposition occur, temperatures below 600 °C lead to a significant decrease of crystallinity.

Solid-state NMR spectroscopy

Because solid-state NMR spectroscopy is independent of the long-range order of a material it is a valuable tool for further investigations of micro- and nanocrystalline samples on local and intermediate length scales. Both ¹³C and ¹⁵N magic-angle-spinning (MAS) NMR spectra have been recorded. However, in the past especially high-resolution ¹⁵N NMR spectroscopy has proven to be very sensitive for the determination of the characteristic chemical building units (see Scheme 1).^[24, 43–46] The ¹⁵N cross-polarization (CP) MAS NMR spectrum of PTI/Li⁺Cl⁻, a ¹⁵N cross-polarization with polarization inversion (CPPI) experiment with attenuation of NH_x signals, and the curve fits of the time-dependent polarization inversion dynamics of the different ¹⁵N building units in a CPPI experiment are displayed in Figure 1.

The nanocrystallinity of the material leads to a comparatively high resolution of the spectra. For a reliable signal assignment ¹⁵N CPPI experiments with and without attenuation of NH_x signals were carried out. The number of protons covalently bound to different N atoms can be determined by evaluating the time dependence of the polarization inversion dynamics of the corresponding ¹⁵N nuclei (Figure 1, bottom). From these investigations two types of signals are distinguishable. Signals between $\delta=-185$ and -200 ppm exhibit a marginal intensity loss with a continuous, slow decrease of polarization that is diagnostic of tertiary (tert) nitrogen atoms in condensed CN networks.^[24, 47] In addition, these signals can be observed in the attenuated ¹⁵N CPPI experiment whereby no protons can be directly related to these ¹⁵N nuclei. In contrast, two signals between $\delta=-240$ and -255 ppm with an intensity ratio of 1:2 exhibit a two-step evolution as a function of t_{inv} with a turning point around zero. The number

of covalently bonded protons is accessible from polarization at the crossover according to the formula $(2/(n+1))^{-1}$ ($n=0, 1, 2$) in which n is the number of bonded protons. This allows the assignment of these signals to NH.^[45] Based on a direct excitation the intensity ratio for both types is estimated to be 3.6 (N_{tert}):1 (NH). Signals for NH_2 nitrogen nuclei (with a theoretical crossover at $-1/3$), indicating an only partially condensed network, could not be detected.

Additionally, ^{15}N solid-state NMR spectroscopy investigations are a helpful tool for further information on the nature of the building blocks of condensed CN networks. A differentiation between the two most discussed building blocks, triazine and heptazine cores, is possible by means of the signal for the central nitrogen atom (“ N_c ”) in heptazine units (see Scheme 1). In essentially all heptazine-based compounds studied so far, this N_c atom exhibits an up-field

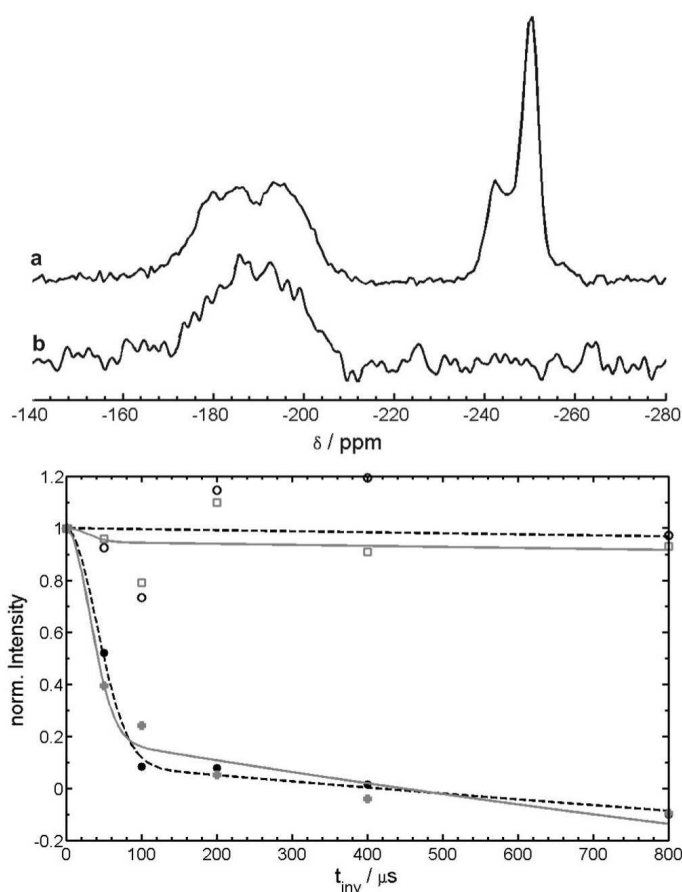


Figure 1. Top: ^{15}N CP-MAS NMR spectrum of PTI/ Li^+Cl^- (a) and a ^{15}N CPPI experiment with attenuation of NH_x signals (b). Bottom: Curve fits of the time-dependent polarization inversion dynamics of the different ^{15}N building units in a CPPI experiment. Open symbols denote the signals at $\delta=-187$ and -195 ppm, filled symbols denote the signals at $\delta=-243$ and -250 ppm.

shift relative to the outer N atoms of the ring to values between $\delta=-225$ and -235 ppm.^[24,44,48] As the signal for the N_c atom could be covered by the broad signals of the NH nitrogen nuclei in the ^{15}N CPPI experiment, the NH_x attenuated spectra is needed for clarity. In this spectra ^{15}N nuclei with covalently bound protons are damped almost completely, through which nuclei without a direct proton environment appear more intense. Missing signals for N_c atoms even in this attenuated ^{15}N CPPI experiment exclude the presence of heptazine units in PTI/ Li^+Cl^- and corroborate a triazine-based structure model, contrary to recent investigations that favored corrugated heptazine units to be the most likely building blocks of

highly condensed carbon nitride networks.^[1,24,43,49,50]

The ^{13}C MAS NMR spectra (Figure 2) exhibit three resonances in a region typical for both heptazine and triazine units.^[24,45,51,52] Thus, based on the results of the ^{15}N data an assignment to the carbon atoms in the triazine building blocks of $\text{PTI}/\text{Li}^+\text{Cl}^-$ can be made. Whereas two resonances ($\delta=162.6$ and 157.9 ppm) are well developed already for short CP contact times (τ_c), a third resonance ($\delta=168.0$ ppm) evolves for $\tau_c=10$ ms (Figure 2c). In direct excitation (Figure 2a) all three signals show an intensity ratio of 1:1:1, which demonstrates that two thirds of the C entities

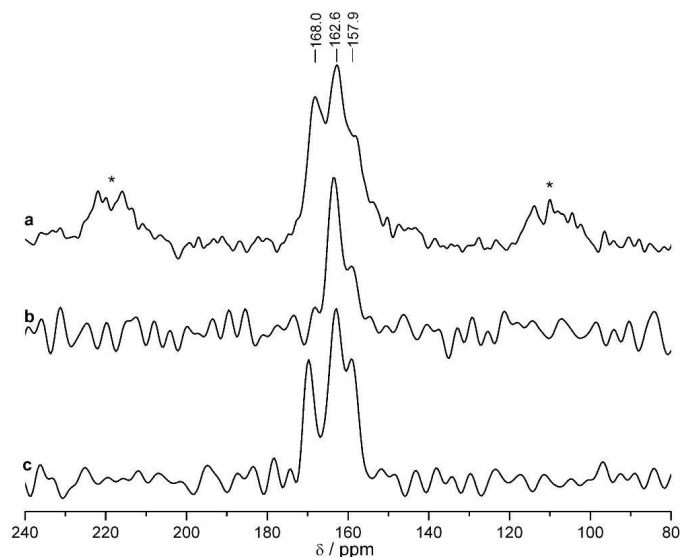


Figure 2. a) ^{13}C direct excitation spectrum of $\text{PTI}/\text{Li}^+\text{Cl}^-$ (spinning side bands are marked by asterisks); and ^{13}C CP-MAS NMR spectra recorded with contact times (τ_c) of b) 0.5 and c) 10 ms.

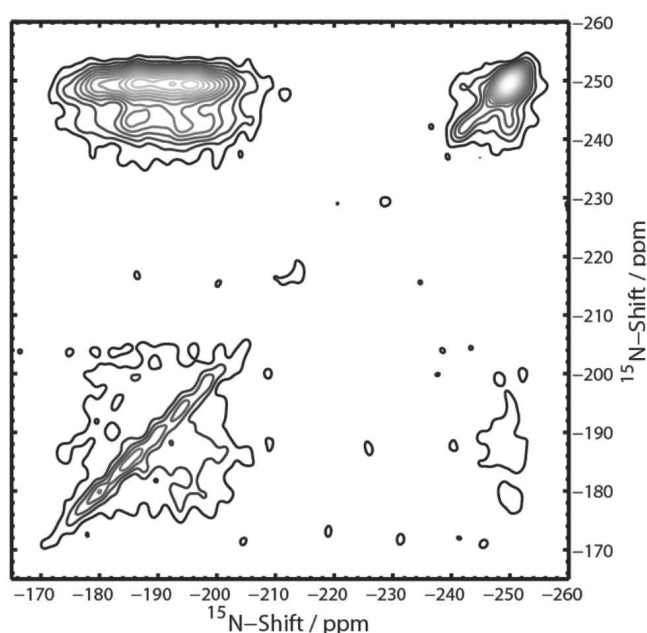


Figure 3. ^{15}N 2D-fp-RFDR experiment for a mixing time of 80 ms to probe the spatial proximity of the NH and NC_2 building units by means of homonuclear spin diffusion.

have significantly closer contact to protons. The splitting of the NH resonances in the ^{15}N MAS (Figure 1) as well in the ^{13}C MAS (Figure 2) NMR spectra is consistent with the Li^+/H^+ ion disorder observed in the channels of the $\text{PTI}/\text{Li}^+\text{Cl}^-$ structure model (see below). From derivation of the intensity ratio of the ^{15}N MAS measurement with direct excitation, the disorder seems to involve a partial deprotonation of imide units (roughly one of three NH groups). While the ^{13}C resonances at $\delta=162.6$ and 157.9 ppm with the faster polarization buildup

would belong to C nuclei located next to the protonated triazine N atoms differentiated only by their Li^+ environment, C species adjacent to nonprotonated ring N atoms would exhibit the resonance at $\delta=168$ ppm.

To probe the homogeneity of $\text{PTI/Li}^+\text{Cl}^-$ on the nanometer scale, a ^{15}N 2D-fp-RFDR (finite pulse radio-frequency-driven dipolar recoupling) experiment with a mixing time of 80 ms was collected (Figure 3). It allows the analysis of the spatial proximity of ^{15}N nuclei based on radio-frequency-driven homonuclear spin diffusion. In a ^{15}N fp-RFDR spectrum of a ^{15}N -enriched compound, cross intensities (off-diagonal signals) develop when the nuclei are sufficiently close to each other (5–10 Å). In Figure 3, cross peaks are observed between all nitrogen resonances depicted in the 1D MAS spectrum (Figure 1), which is a strong indication of the homogeneity of the sample. Whereas the cross correlation between the NH groups and the NC_2 units of the triazine rings is already well developed for a mixing time of 80 ms, the cross peaks between both NH signals just start emerging (Figure 3). This suggests that the mean NH–NH distance is significantly longer (by roughly 40 to 50 %) than the average NC_2 –NH distance. Since the splitting of the NH resonances is caused by Li^+/H^+ disorder, this allows the characteristic length scale for the disorder to be placed below 4 Å.

IR spectroscopy

The FTIR spectrum of the product is displayed in Figure 4. The width of the bands is characteristic of networks as single absorptions are difficult to resolve. Nevertheless, the resolution of the IR spectra is high enough to be indicative of an at least partially ordered material. Due to the sharp band at about 810 cm^{-1} that can be assigned to ring-sextant out-of-plane bending vibrations, triazine or heptazine units are likely to be the elementary building blocks of this material.^[24,45,53,54]

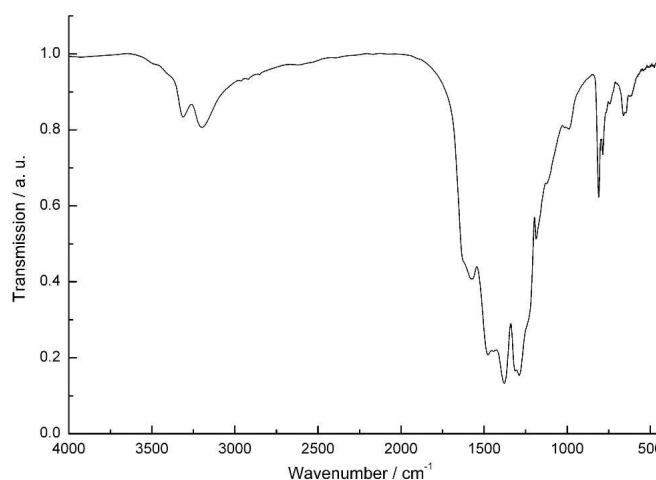


Figure 4. FTIR spectrum of $\text{PTI/Li}^+\text{Cl}^-$ recorded as a KBr pellet between 400 and 4000 cm^{-1} .

Although a differentiation between both ring systems cannot be made by FTIR spectroscopy, the exclusion of heptazine units by solid-state NMR spectroscopy relates this signal to triazine building blocks. The linkage of these ring systems by NH groups is proven by the presence of the prominent absorption bands in the $1200\text{--}1400\text{ cm}^{-1}$ region that have been shown to be characteristic for the C-NH-C unit in melam and melon.^[24,55–59] According to the ^{15}N NMR spectroscopy data, absorptions found in the N—H stretching region near 3310 and 3200 cm^{-1} were exclusively assigned to NH groups, with the splitting (with an intensity ratio of the two bands of approximately 1:2 being consistent with ^{15}N NMR spectroscopic data) being evoked by Li^+/H^+ ion disorder in the channels of the $\text{PTI}/\text{Li}^+\text{Cl}^-$ structure (see below). The broadness of the signals as well as the absence of NH_2 groups corroborate the existence of a highly condensed network.

Electron microscopy

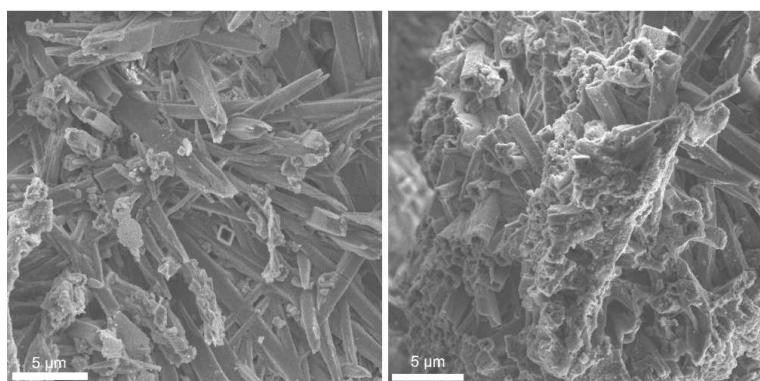


Figure 5. Characteristic SEM images of $\text{PTI}/\text{Li}^+\text{Cl}^-$ taken from various sample regions. The images reveal the microcrystalline character of the sample in the form of hollow tubes.

Scanning electron microscopy images (Figure 5) gave a deeper insight into the morphology of the product. Its micro- and nanocrystalline character is shown by the formation of hollow tubes with a diameter of about $1\text{ }\mu\text{m}$ and a length of several micrometers. Energy dispersive X-ray analysis

(EDX) investigations for semiquantitative analysis proved the equal distribution of the molar ratio C/N as well as the ubiquitous presence of chlorine.

The small crystallite size apparent from SEM images excludes a structure elucidation by single-crystal X-ray diffraction. For such materials, transmission electron microscopy (TEM) and electron diffraction (ED) are valuable tools to provide structural insights. TEM images (Figure 6) reveal the microtubules as an oriented assembly of hexagonal prismatic crystallites (diameter about 50 nm , in agreement with estimated crystallite sizes from the powder XRD

results) with the hexagonal axis of the crystallites being parallel to the long axis of the microtubules.

HRTEM images (Figure 7, left) suggest a hexagonal symmetry of the prisms.

Electron diffraction (Figure 7, right) confirmed the hexagonal

symmetry with a hexagonal lattice parameter $a=855$ pm. Despite the arrangement of most hexagonal prisms along a preferred orientation, diffraction patterns of different orientations

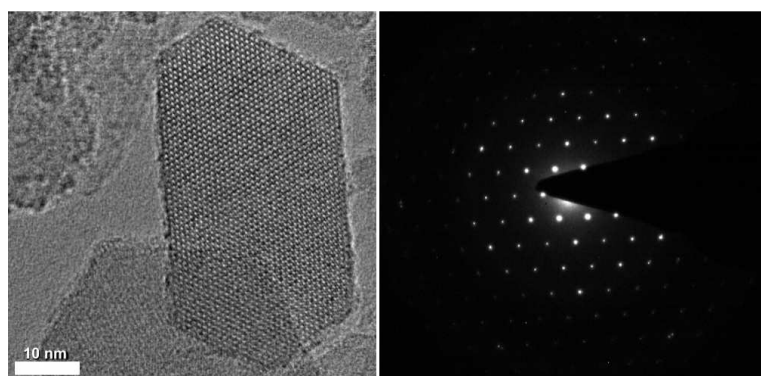


Figure 7. Left: HRTEM image of PTI/Li⁺Cl⁻; right: SAED pattern of the $h0l$ plane, both showing the hexagonal array of lattice planes in $[001]$ orientation.

The SAED pattern of the $h0l$ plane shows the well-defined stacking of layers perpendicular to the hexagonal axis with an interplanar layer distance of 330 pm being typical for a graphite-like stacking. Together with the hexagonal intensity distribution along the $[001]$ zone axis this feature allows the classification of the material as a member of the wide class of

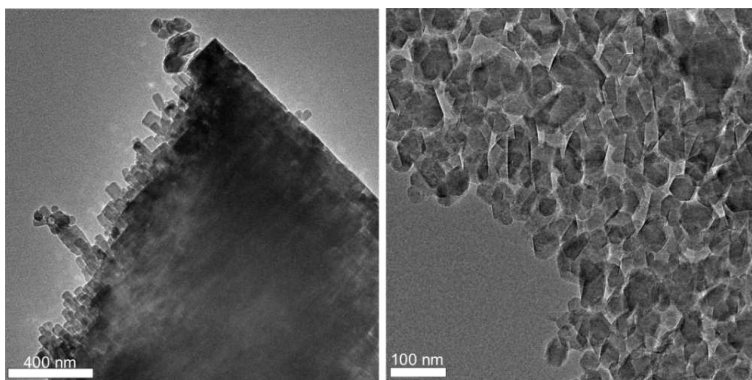


Figure 6. TEM images of PTI/Li⁺Cl⁻ showing hexagonal prisms on the nanometer length scale.

were recorded (Figure 8). The broadening of reflections observed in the $h0l$ plane is caused by rotational disorder because of slightly tilted domains. However, most diffraction patterns show very sharp symmetric peaks that render disordered structures quite unlikely.

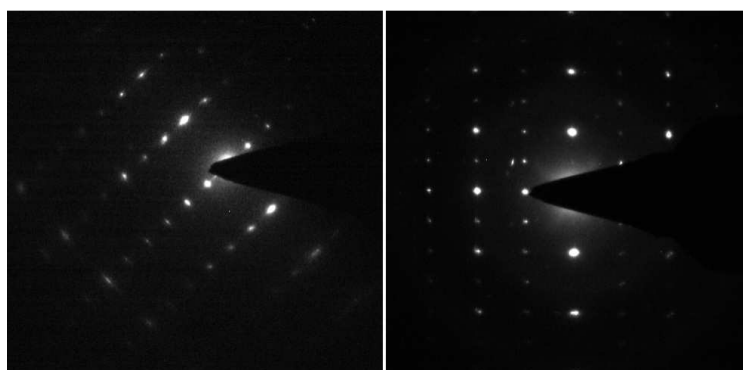


Figure 8. SAED patterns of the $h0l$ plane (left) and the hhl plane (right), both showing the systematic absence $00l: l=2n+1$.

graphite-like CN compounds considered as intermediates on the way to graphitic carbon nitride.^[24,28,36,43]

Evaluation of the observed systematic absences in the $h0l$ and the hhl plane ($00l$: $l=2n+1$, Figure 8) suggests the presence of a 6_3 axis, which renders a heptazine-based structure model quite unlikely. The 6_3 -symmetry operation and the determined hexagonal lattice parameter cannot be aligned with the metric of a heptazine-based structure model with appropriate CN distances of 120–140 pm. No evidence for corrugated layers (as recently predicted for graphitic carbon nitride networks)^[47,60] that could allow the presence of heptazine units has been obtained from HRTEM images, nor from electron diffraction (ED) patterns.

By taking into account some promotive factors (i.e., the light atom structure and the planarity of the layers), a structure solution based on electron diffraction data (52 independent reflections) was possible. Although the kinematical approximation $I_{hkl} \propto |F_{hkl}|^2$ could only be used with constraints due to the sample thickness, a triazine-based structure model analogous to PHI^[43] with a figure of merit of 24% was elucidated by using SIR-97.^[61] All carbon and nitrogen atoms could be located with reasonable bond angles and lengths. In conjunction with information from ED data (lattice parameters, symmetry operations) this structure model made important contributions to the structure solution from powder XRD data.

Electron energy-loss spectroscopy (EELS) provides the capability to examine the presence of light elements on the nanometer scale. EELS spectra of hexagonal nanoprisms (Figure 9) confirm the presence of lithium and chlorine in these nanocrystals with ionization edges at an energy loss of 60 eV (Li_K) and 200–240 eV ($Cl_{L_{2,3}}$), respectively. Therefore, the very existence of the ions as residual salt in the bulk can be excluded; both the lithium and chloride ions have to be part of the crystal structure as they were found in the nano-

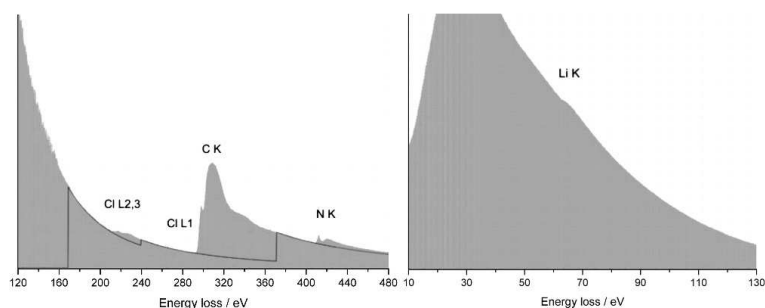


Figure 9. EELS spectra of a hexagonal prism, showing lithium-, carbon-, and nitrogen-K ionization edges as well as chlorine-L ionization edges.

crystals. Carbon- and nitrogen-K ionization edges at 290 and 410 eV are consistent with the triazine-based structure model from ED data as both regions show sharply defined π^* and σ^*

fine structural features that are characteristic for sp^2 -hybridized carbon and nitrogen atoms in graphite-like structures.^[62–65]

Structure solution and refinement

Figure 10 displays the powder X-ray diffraction pattern (PXRD) of PTI/Li⁺Cl⁻. With its strongest reflection indexed as 002 by analogy to graphite it is indicative of a layered

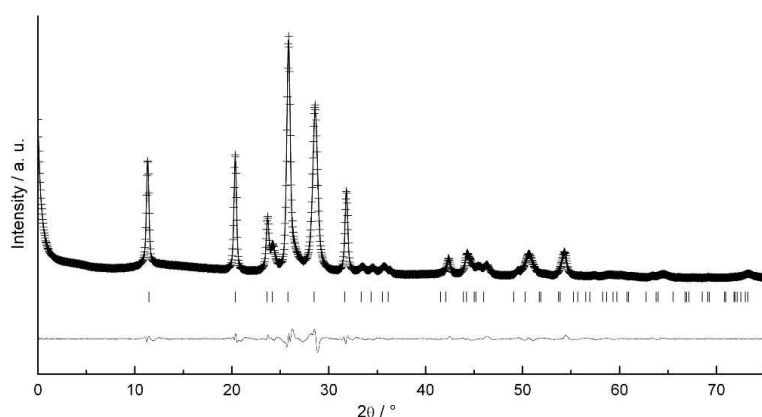


Figure 10. Rietveld refinement of the X-ray diffraction data for PTI/Li⁺Cl⁻. Measured data are indicated by crosses, refined data and the difference profile are given as solid lines. Bragg peaks are indicated by vertical bars.

compound with an interlayer spacing of 3.36 Å.^[1,31,33,36,53,54] Contrary to almost all CN condensation products obtained so far, PTI/Li⁺Cl⁻ exhibits a number of well-resolved and intense X-ray reflections, thereby indicating the high crystallinity induced by the salt melt technique. The broadening of single reflections can be assigned to the nanocrystalline character of the sample. An evaluation of the PXRD data using the Scherrer equation yielded crystallite sizes between 30 and 60 nm.^[66]

The high crystallinity of PTI/Li⁺Cl⁻ allowed for a structure solution by direct methods from the X-ray diffraction pattern, which yielded a layered, triazine-based structure model corroborating the structure solution from ED data for the bulk material. After introducing further information from solid-state NMR and FTIR spectroscopy as well as electron diffraction and HRTEM investigations, a Rietveld refinement of the X-

Table 1. Crystallographic data of the structure solution and refinement of PTI/Li⁺Cl⁻.

space group	$P6_3cm$ (No. 185)
T [K]	293
a [Å]	8.4684(10)
c [Å]	6.7502(9)
V [Å ³]	419.21(9)
diffraction range	$0^\circ \leq 2\theta \leq 75^\circ$
no. data points	1726
observed reflections	52
independent parameters	92
GOF	5.035
R indices (all data) [%]	$R_p = 4.177$, $wR_p = 5.937$

ray diffraction pattern was carried out (Figure 10). Details regarding the data collection and refinement are summarized in Table 1.

Poly(triazine imide) (PTI), a structural analogue to poly(heptazine imide),^[43] comprises an infinite 2D network of triazine units that are condensed by means of NH bridges (Figure 11). With its triazine-based structure corroborated by solid-state NMR spectroscopy, PTI forms a contrast to many other high-temperature condensation CN networks built up from heptazine units.^[24,36,43] We assume that the utilization of salt melts destabilizes or even decomposes heptazine units at higher temperatures, since even the use of heptazine-based precursors like melem^[45] leads to the formation of triazine-based PTI at 600 °C.

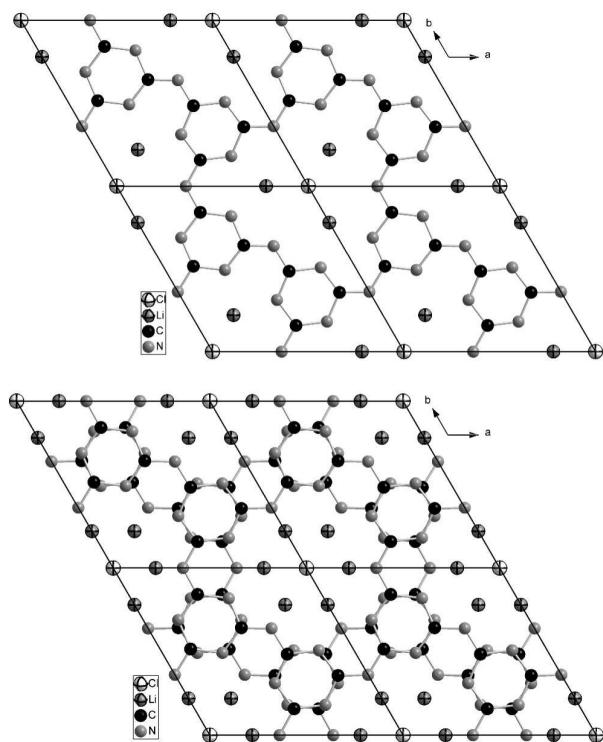


Figure 11. Parallel projection of the structure of PTI/Li⁺Cl⁻. Top: One layer with lithium, carbon, and nitrogen atoms in a plane and chlorine atoms shifted by (001/4). The depicted Li⁺ positions have an occupancy of 1/3. Bottom: Projection of layers with ABA stacking, leading to the formation of channels along the *c* axis.

Regarding the 2D organization of its C/N/H network, PTI bears a clear resemblance to C₆N₉H₃·HCl.^[28] However, the stacking order of the latter Li-free compound results in an overlap of the Cl⁻-containing voids, whereas the voids of the layers of PTI/Li⁺Cl⁻ are stacked upon each other forming channels along the *c* axis by ABA stacking, which yields a zeolite-like porous motif. Due to its smaller pore size than PHI, the channels in PTI are filled with Li⁺ and Cl⁻ ions according to elemental analysis, ICP, and EELS measurements. In parallel projection, resemblance with the NPO zeolite structure type is apparent. Accordingly, Cl⁻ ions are placed in the center of the channels and Li⁺ ions surrounded by two Cl⁻ and two N atoms in a tetrahedral arrangement occupy the inner walls of the channels.^[67] Figure 11 displays a 2D projection of the crystal structure of PTI with Li⁺ and Cl⁻ intercalation (PTI/Li⁺Cl⁻). We assume that the almost planar arrangement of the layers (Figure 12) confirmed by ED data arises from

conjugation within the layers and the intercalation of salt ions. Additionally, the interlayer spacing of 3.36 Å determined from the strongest reflection in the PXRD indexed as 002 by analogy with graphite is significantly higher than in other graphite-like CN condensation products. Compared with melon (3.19 Å), PHI (3.20 Å), and C₆N₉H₃·HCl (3.21 Å)^[24,28,43] this enlargement can be attributed to the incorporation of Cl⁻ ions, the effective ionic radii (3.34 Å) of which require a widening by more than 0.1 Å. Owing to spatial reasons the Cl⁻ ions are shifted by (00 1/4) to the CN layers as Li⁺ ions occupy the voids coplanar with the C and N atoms.

An exact determination of the Li⁺ positions turned out to be difficult due to the elusive nature of Li regarding most crystallographic and analytical methods. By taking into account appropriate distances of Li–N and Li–Cl the position at the inner walls of the channels is the most reasonable localization for the Li⁺ ions. A difference Fourier synthesis after refinement of the CN network and the Cl⁻ atoms corroborated this consideration by showing blurred electron density along the channels with maxima at the height of the CN layers. This implies a partial occupancy of the Li⁺ sites that was corroborated by structure refinement. Full occupancy of the Li⁺ positions shown in Figure 11 is not possible with respect to charge compensation.

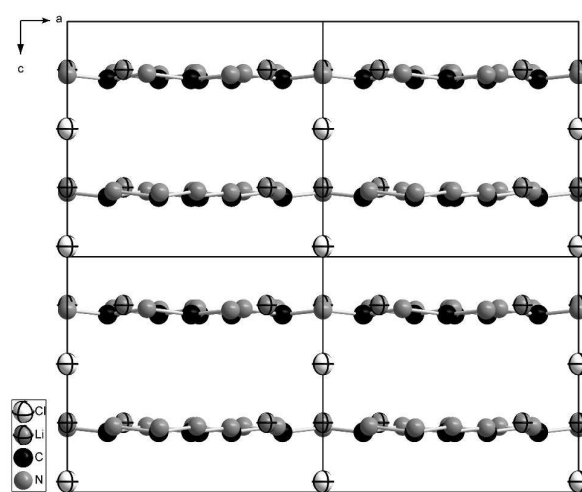


Figure 12. ABA stacking of layers in PTI/Li⁺Cl⁻ along the *c* axis with a nearly planar arrangement.

As shown above, PTI/Li⁺Cl⁻ provides another example of a successful structure solution including complementary diffraction and spectroscopic methods. Whereas the structure of the triazine-based CN “backbone” and the stacking order as well as the position of the chloride ions were clearly determined, the position and distribution of H and Li atoms is not yet unequivocal. Both NMR and IR spectroscopic data suggest Li⁺/H⁺ ion disorder in the channels of the PTI/Li⁺Cl⁻ structure model involving partial deprotonation of imide units. The ratio N_{tert}/NH of 3.6:1 as determined by ¹⁵N direct excitation measurements indicates the deprotonation of two imide groups per unit cell, which yields approximately the molar ratio

$N_{\text{tert}}/\text{NH}$ given above. Substitution of the protons by Li^+ causes a certain phase width, which results in the formula $[(\text{C}_3\text{N}_3)_2(\text{NH}_x\text{Li}_{1-x})_3\cdot\text{LiCl}]$. By combination of the Li^+/H^+ disorder and the partial occupancy of the Li^+ sites the signal splitting and the intensity ratio in both ^{15}N and ^{13}C MAS NMR spectra and the FTIR spectrum are consistent with the structure model presented. Based on the fp-RFDR experiments (Figure 3), the proximity of the individual NH groups was estimated to be smaller than 4 \AA , which suggests a local disorder within the channels in contrast to the formation of small domains. The disorder pattern will be the subject of further investigations including advanced NMR spectroscopy experiments and theoretical calculations.

4.1.3 Conclusion

With poly(triazine imide) we present a triazine-based CN network, the high crystallinity of which enabled a structure solution by X-ray diffraction methods. Prepared from dicyandiamide condensed in a eutectic mixture of LiCl and KCl, brownish PTI/ Li^+Cl^- crystallizes in the hexagonal space group $P6_3cm$ with cell parameters of $a=846.82(10)$ and $c=675.02(9)$ pm, as determined by HRTEM investigations and electron and powder X-ray diffraction. As proved by solid-state NMR and FTIR spectroscopy, the 2D layered compound is composed of imide-bridged triazine units yielding a partly condensed 2D network with triangular voids, thereby excluding the heptazine-based structure model recently proposed for the same compound that was assumed to be $g\text{-C}_3\text{N}_4$.^[38] The 3D examination of PTI/ Li^+Cl^- exhibits a zeolite-like porous motif as the Li^+ - and Cl^- -filled voids of these layers are stacked upon each other forming channels along the c axis. The intercalation of ions results in an augmented CN layer distance of 336 pm and an almost planar arrangement of the layers.

The fact that PTI, contrary to most other CN compounds synthesized at high temperatures,^[24,36,43] is not built up from heptazine building blocks, raises the question as to the unexpected stability of triazine units under these synthetic conditions, since even the use of heptazine-based precursors like melem^[45] leads to the formation of triazine-based PTI. Just recently, investigations regarding the stability of the heptazine-based compound melon in potassium and sodium cyanate melts have shown the same decomposition behavior, thereby yielding the corresponding tricyanomelaminat ions;^[68] this renders the temperature-

dependence of the degradation of heptazine units and the stabilization of triazine units in salt melts important research topics for the future.

As CN networks gain more and more attention for their catalytic and electronic properties^[15,69–71] an investigation of the potential of this material is highly desirable. The intercalation of ions in CN compounds holds the key for tunable bandgap sizes to create promising candidates for organic semiconductors. In this context, disorder phenomena, concerning the H/Li distribution in the channels and the insertion of other ions by ion exchange, for instance, will be studied. Other investigations will focus on ion conductivity of these systems or their application in optoelectronics. Beyond that, the structural investigation of this material that has the same composition as melon with regard to the C/N/H framework sheds new light on the old discussion of heptazine or triazine units being the building blocks of highly condensed CN networks. Providing a better understanding and control of condensation processes, ionothermal synthetic strategies and their products such as PTI/Li⁺Cl⁻ represent important intermediate steps on the way to the still hypothetical graphitic carbon nitride.

4.1.4 Experimental Section

Synthesis of PTI/Li⁺Cl⁻

Dicyandiamide (0.200 g, 2.38 mmol) and a eutectic mixture of lithium chloride (59.2 mol %, 0.904 g, 21.33 mmol) and potassium chloride (40.8 mol %, 1.096 g, 14.70 mmol) were ground together in a glovebox. The reaction mixture was transferred into a dried thick-walled silica glass tube ($\phi_{\text{ext.}}=15$ mm, $\phi_{\text{int.}}=11$ mm). The tube was placed in a vertical tube furnace and heated under atmospheric argon pressure at 6 K min⁻¹ to 400 °C. This temperature was held for 12 h and afterwards the sample was cooled to room temperature at 6 K min⁻¹. After this procedure the tube was evacuated and sealed at a length of 120 mm with a hydrogen–oxygen burner. The resulting ampoule was again placed in a vertical tube furnace and heated at 10 K min⁻¹ to 600 °C at which temperature the sample was held for 48 h. After being cooled down to room temperature (8 K min⁻¹) the ampoule was carefully broken, and the sample was

isolated and washed twice with boiling water to remove residual salt. The resulting material was dried at 200 °C/5×10⁻⁴ mbar to yield PTI/Li⁺Cl⁻ as a brown powder (60–80 mg, 37-50 %).

IR (KBr): $\tilde{\nu}$ = 3312 (w), 3198 (w), 1574 (m), 1479 (m), 1378 (s), 1314 (s), 1289 (s), 1187 (w), 810 (w), 786 (w), 660 cm⁻¹ (vw); elemental analysis calcd (%) for [(C₃N₃)₂(NH)₃·LiCl]: C 29.59, H 1.24, N 51.76, Cl 14.56, Li 2.85; found: C 29.6, H 1.3, N 50.4, Cl 11.0, Li 4.6.

General techniques

Elemental analyses were performed on a commercial C, H, N, Cl Vario EL elemental analyzer system (Elementar Analysensysteme GmbH). Lithium quantification was performed by atomic emission spectrophotometry with inductively coupled plasma (ICP-AES) on a Varian-Vista simultaneous spectrometer. FTIR measurements were carried out on a Bruker IFS 66v/S spectrometer. Spectra of the samples were recorded in an evacuated cell at ambient conditions between 400 and 4000 cm⁻¹ after diluting the samples in KBr pellets (2 mg sample, 300 mg KBr, hand press with press capacity 10 kN). Scanning electron microscopy was performed on a JEOL JSM-6500F equipped with a field emission gun at an acceleration voltage of 4 kV. Samples were prepared by putting the powder specimen on adhesive conductive pads and subsequently coating them with a thin conductive carbon film.

Powder X-ray diffraction data were collected in Bragg–Brentano geometry on a Bruker D8 Discover diffractometer (Göbel mirrors, Cu_{Kα1} radiation, λ =154.18 pm). The structure was solved by direct methods with the EXPO program package^[72] and refined in space group *P*6₃*cm* using the program TOPAS.^[73] Further details of the crystal structure investigations can be obtained from the Fachinformationszentrum Karlsruhe, 76344 Eggenstein-Leopoldshafen, Germany (fax: (+49) 7247-808-666; e-mail: crysdata@fiz-karlsruhe.de, http://www.fiz-karlsruhe.de/request_for_deposited_data.html) on quoting the depository number CSD-422088.

Solid-state NMR spectroscopy

¹³C and ¹⁵N MAS solid-state NMR spectra were recorded at ambient temperature on the conventional impulse spectrometer Avance II 300 (Bruker) operating at proton resonance frequencies of 75.5 (¹³C) and 30.4 MHz (¹⁵N). The samples were contained in 3.2, 4, and 7 mm ZrO₂ rotors that were mounted in standard double-resonance MAS probes (Bruker). The

^{13}C signals were referenced with respect to TMS and ^{15}N signals were referenced relative to nitromethane. For all experiments broadband proton decoupling using the SPINAL64 sequence was applied. The CP experiments were conducted with a ramped cross-polarization sequence by decreasing the ^1H pulse power linearly by 50 %. The ^{15}N CPPI experiment was made at a rotation frequency of 3.9 kHz and an initial contact time of 12 ms, whereas for the ^{15}N fp-RFDR experiment the rotation frequency was 22.222 kHz and the contact time was 20 ms. During the mixing time of 79.92 ms, 180° pulses on the ^{15}N channel were applied at every middle third of a rotation period to recouple the dipolar interaction between ^{15}N nuclei. The ratio of tertiary nitrogen atoms to NH atoms was calculated by means of a ^{15}N measurement with direct excitation. To ensure equilibrium conditions the ^{15}N -enriched sample was measured with a recycle delay of 7200 s and 8 scans.

Electron diffraction/transmission electron microscopy/EELS measurements

ED and TEM measurements were carried out on a FEI Titan 80-300 equipped with a field emission gun operating at 300 kV. The images were recorded using a Gatan UltraScan 1000 (2k \times 2k) camera. EELS was performed in diffraction mode at 300 kV on a post-column filter (GIF Tridiem 863). The sample was finely dispersed by sonication in a ethanol suspension, and a small amount of the suspension was subsequently dispersed on a copper grid coated with carbon film. The grids were mounted on a double-tilt holder with a maximum tilt angle of 30° and subsequently transferred to the microscope. Reflection intensities were extracted using the ELD program package.^[74,75] The observed absence $00l$: $l=2n+1$ indicates the presence of a 6_3 axis. The most probable solution as found by SIR-97^[61] had a figure of merit of 24 %.

Acknowledgements

We gratefully acknowledge financial support that was granted from the Deutsche Forschungsgemeinschaft (DFG) (project SCHN 377/12 and SE 1417/2) and from the Fonds der Chemischen Industrie (FCI) (scholarship for E.W.) The authors thank the Center for Nanoscience and the Cluster of excellence Nanosystems Initiative Munich (NIM) for financial support.

4.1.5 Bibliography

- [1] E. Kroke, M. Schwarz, *Coord. Chem. Rev.* **2004**, *248*, 493-532.
- [2] W. Schnick, *Angew. Chem.* **1993**, *105*, 846-858; *Angew. Chem. Int. Ed. Engl.* **1993**, *32*, 806-818.
- [3] W. Schnick, *Angew. Chem.* **1999**, *111*, 3511-3512; *Angew. Chem. Int. Ed.* **1999**, *38*, 3309-3310.
- [4] A. Y. Liu, M. L. Cohen, *Science* **1989**, *245*, 841-842.
- [5] A. Y. Liu, M. L. Cohen, *Phys. Rev. B* **1990**, *41*, 10727-10734.
- [6] A. Y. Liu, R. M. Wentzcovitch, *Phys. Rev. B* **1994**, *50*, 10362-10365.
- [7] C.-M. Sung, M. Sung, *Mater. Chem. Phys.* **1996**, *43*, 1-18.
- [8] D. M. Teter, R. J. Hemley, *Science* **1996**, *271*, 53-55.
- [9] E. Horvath-Bordon, R. Riedel, P. F. McMillan, P. Kroll, G. Miehe, P. A. van Aken, A. Zerr, P. Hoppe, O. Shebanova, I. McLaren, S. Lauterbach, E. Kroke, R. Boehler, *Angew. Chem.* **2007**, *119*, 1498-1502; *Angew. Chem. Int. Ed.* **2007**, *46*, 1476-1480.
- [10] A. Thomas, A. Fischer, F. Goettmann, M. Antonietti, J.-O. Müller, R. Schlögl, J. M. Carlsson, *J. Mater. Chem.* **2008**, *18*, 4893-4908.
- [11] F. Goettmann, A. Fischer, M. Antonietti, A. Thomas, *Chem. Commun.* **2006**, 4530-4532.
- [12] F. Goettmann, A. Fischer, M. Antonietti, A. Thomas, *New. J. Chem.* **2007**, *31*, 1455-1460.
- [13] F. Goettmann, A. Thomas, M. Antonietti, *Angew. Chem.* **2007**, *119*, 2773-2776; *Angew. Chem. Int. Ed.* **2007**, *46*, 2717-2720.
- [14] J. Zhang, X. Chen, K. Takanabe, K. Maeda, K. Domen, J. D. Epping, X. Fu, M. Antonietti, X. Wang, *Angew. Chem.* **2010**, *122*, 451-454; *Angew. Chem. Int. Ed.* **2010**, *49*, 441-444.
- [15] X. Wang, K. Maeda, A. Thomas, K. Takanabe, G. Xin, J. M. Carlsson, K. Domen, M. Antonietti, *Nat. Mater.* **2009**, *8*, 76-80.
- [16] Y. Zhang, A. Thomas, M. Antonietti, X. Wang, *J. Am. Chem. Soc.* **2009**, *131*, 50-51.
- [17] Y. Zhang, M. Antonietti, *Chem. Asian J.* **2010**, *5*, 1307-1311.

- [18] E. C. Franklin, *J. Am. Chem. Soc.* **1922**, *44*, 486-509.
- [19] J. Liebig, *Ann. Chem. Pharm.* **1834**, *10*, 1.
- [20] C. E. Redemann, H. J. Lucas, *J. Am. Chem. Soc.* **1940**, *62*, 842-846.
- [21] H. May, *J. Appl. Chem.* **1959**, *9*, 340-344.
- [22] L. Costa, G. Camino, G. Martinasso, *Polym. Prepr. (Am. Chem. Soc., Div. Polym. Chem.)* **1989**, *30*, 531-533.
- [23] L. Pauling, J. H. Sturdivant, *Proc. Natl. Acad. Sci. U.S.A.* **1937**, *23*, 615-620.
- [24] B. V. Lotsch, M. Döblinger, J. Sehnert, L. Seyfarth, J. Senker, O. Oeckler, W. Schnick, *Chem. Eur. J.* **2007**, *13*, 4969-4980.
- [25] E. Kroke, M. Schwarz, E. Horvath-Bordon, P. Kroll, B. Noll, A. D. Norman, *New. J. Chem.* **2002**, *26*, 508-512.
- [26] D. Foy, G. Demazeau, P. Florian, D. Massiot, C. Labrugère, G. Goglio, *J. Solid State Chem.* **2009**, *182*, 165-171.
- [27] J. Ortega, O. F. Sankey, *Phys. Rev. B* **1995**, *51*, 2624-2627.
- [28] Z. Zhang, K. Leinenweber, M. Bauer, L. A. J. Garvie, P. F. McMillan, G. H. Wolf, *J. Am. Chem. Soc.* **2001**, *123*, 7788-7796.
- [29] G. Goglio, D. Foy, G. Demazeau, *Mater. Sci. Eng. R* **2008**, *58*, 195-227.
- [30] H. Montigaud, B. Tanguy, G. Demazeau, I. Alves, S. Courjault, *J. Mater. Sci.* **2000**, *35*, 2547-2552.
- [31] I. Alves, G. Demazeau, B. Tanguy, F. Weill, *Solid State Commun.* **1999**, *109*, 697-701.
- [32] M. C. dos Santos, F. Alvarez, *Phys. Rev. B* **1998**, *58*, 13918-13924.
- [33] M. Kawaguchi, K. Nozaki, *Chem. Mater.* **1995**, *7*, 257-264.
- [34] Q. Guo, Y. Xie, X. Wang, S. Lu, T. Hou, X. Liu, *Chem. Phys. Lett.* **2003**, *380*, 84-87.
- [35] S. Muhl, J. M. Mendez, *Diamond Relat. Mater.* **1999**, *8*, 1809-1830.
- [36] T. Komatsu, *J. Mater. Chem.* **2001**, *11*, 802-805.
- [37] T. Malkow, *Mater. Sci. Eng. A* **2001**, *302*, 311-324.
- [38] M. J. Bojdys, J.-O. Müller, M. Antonietti, A. Thomas, *Chem. Eur. J.* **2008**, *14*, 8177-8182.
- [39] J. Stenzel, W. Sundermeyer, *Chem. Ber.* **1967**, *100*, 3368-3370.
- [40] W. Sundermeyer, *Z. Anorg. Allg. Chem.* **1961**, *313*, 290-295.

- [41] W. Sundermeyer, *Angew. Chem.* **1965**, *77*, 241-258; *Angew. Chem. Int. Ed. Engl.* **1965**, *4*, 222-238.
- [42] W. Verbeek, W. Sundermeyer, *Angew. Chem.* **1967**, *79*, 860-861; *Angew. Chem. Int. Ed. Engl.* **1967**, *6*, 871-872.
- [43] M. Döblinger, B. V. Lotsch, J. Wack, J. Thun, J. Senker, W. Schnick, *Chem. Commun.* **2009**, 1541-1543.
- [44] A. Sattler, L. Seyfarth, J. Senker, W. Schnick, *Z. Anorg. Allg. Chem.* **2005**, *631*, 2545-2554.
- [45] B. Jürgens, E. Irran, J. Senker, P. Kroll, H. Müller, W. Schnick, *J. Am. Chem. Soc.* **2003**, *125*, 10288-10300.
- [46] L. Seyfarth, J. Sehnert, N. El-Gamel, W. Milius, E. Kroke, J. Breu, J. Senker, *J. Mol. Struct.* **2008**, *889*, 217-228.
- [47] J. Sehnert, K. Baerwinkel, J. Senker, *J. Phys. Chem. B* **2007**, *111*, 10671-10680.
- [48] A. Sattler, Diploma thesis, Ludwig-Maximilians-University Munich (Germany), **2005**.
- [49] J. Gracia, P. Kroll, *J. Mater. Chem.* **2009**, *19*, 3013-3019.
- [50] J. R. Holst, E. G. Gillan, *J. Am. Chem. Soc.* **2008**, *130*, 7373-7379.
- [51] B. Jürgens, Ph. D. thesis, Ludwig-Maximilians-University Munich (Germany), Shaker, Aachen, **2004**.
- [52] G. C. Levy, R. L. Lichter, G. L. Nelson, in *Carbon-13 Nuclear Magnetic Resonance Spectroscopy*, John Wiley & Sons Ltd., New York, Chichester, Brisbane, Toronto, **1980**.
- [53] B. V. Lotsch, W. Schnick, *Chem. Mater.* **2006**, *18*, 1891-1900.
- [54] B. V. Lotsch, W. Schnick, *Chem. Mater.* **2005**, *17*, 3976-3982.
- [55] A. I. Finkel'shtein, *Opt. i Spekr.* **1959**, *6*, 33-37.
- [56] A. I. Finkel'shtein, N. V. Spiridonova, *Russ. Chem. Rev.* **1964**, *33*, 400-405.
- [57] B. V. Lotsch, W. Schnick, *Chem. Eur. J.* **2007**, *13*, 4956-4968.
- [58] M. Takimoto, *Kogyo Kagaku Zasshi* **1961**, *64*, 1452-1455.
- [59] M. Takimoto, *Nippon Kagaku Zasshi* **1964**, *85*, 168-176.
- [60] D. T. Vodak, K. Kim, L. Iordanidis, P. G. Rasmussen, A. J. Matzger, O. M. Yaghi, *Chem. Eur. J.* **2003**, *9*, 4197-4201.

- [61] A. Altomare, M. C. Burla, M. Camalli, G. L. Cascarano, C. Giacovazzo, A. Guagliardi, A. G. G. Moliterni, G. Polidori, R. Spagna, *J. Appl. Crystallogr.* **1999**, *32*, 115-119.
- [62] C. Cao, F. Huang, C. Cao, J. Li, H. Zhu, *Chem. Mater.* **2004**, *16*, 5213-5215.
- [63] H. L. Chang, C. M. Hsu, C. T. Kuo, *Appl. Phys. Lett.* **2002**, *80*, 4638-4640.
- [64] M. Terrones, N. Grobert, H. Terrones, *Carbon* **2002**, *40*, 1665-1684.
- [65] P. Moreau, F. Boucher, G. Goglio, D. Foy, V. Mauchamp, G. Ouvrard, *Phys. Rev. B* **2006**, *73*, 195111/1-195111/11.
- [66] A. Guinier, in *X-Ray Diffraction in Crystals, Imperfect Crystals, and Amorphous Bodies*, Dover Publications, New York, **1994**, pp. 121-125.
- [67] S. Correll, O. Oeckler, N. Stock, W. Schnick, *Angew. Chem.* **2003**, *115*, 3674-3677; *Angew. Chem. Int. Ed.* **2003**, *42*, 3549-3552.
- [68] A. Sattler, W. Schnick, *Eur. J. Inorg. Chem.* **2009**, 4972-4981.
- [69] D. Mitoraj, H. Kisch, *Angew. Chem.* **2008**, *120*, 10123-10126; *Angew. Chem. Int. Ed.* **2008**, *47*, 9975-9978.
- [70] D. Mitoraj, H. Kisch, *Chem. Eur. J.* **2010**, *16*, 261-269.
- [71] X. Wang, K. Maeda, X. Chen, K. Takanabe, K. Domen, Y. Hou, X. Fu, M. Antonietti, *J. Am. Chem. Soc.* **2009**, *131*, 1680-1681.
- [72] A. Altomare, M. C. Burla, M. Camalli, B. Carrozzini, G. L. Cascarano, C. Giacovazzo, A. Guagliardi, A. G. G. Moliterni, G. Polidori, R. Rizzi, *J. Appl. Crystallogr.* **1999**, *32*, 339-340.
- [73] A. Coelho, TOPAS Academic, v4.1, Coelho Software, Brisbane, **2007**.
- [74] X. Zou, Y. Sukharev, S. Hovmöller, *Ultramicroscopy* **1993**, *49*, 147-158.
- [75] X. Zou, Y. Sukharev, S. Hovmöller, *Ultramicroscopy* **1993**, *52*, 436-444.

4.2 Bandgap Determination of PTI/LiCl

All bandgap calculations and XAS/XES measurements in this subsection were carried out by Eamon McDermott (University of Saskatchewan, Canada, advisor: Prof. Dr. A. Moewes) and were also published as part of his master thesis.

EELS measurements were conducted by Kulpreet S. Viridi (LMU Munich, advisor: Prof. Dr. C. Scheu) and Yaron Kauffmann and Wayne D. Kaplan (Technion – Israel Institute of Technology, Haifa, Israel).

Band gap tuning in poly(triazine imide) - a nonmetallic photocatalyst

Eamon McDermott, Eva Wirnhier, Wolfgang Schnick, Kulpreet Singh Viridi, Christina Scheu, Yaron Kauffmann, Wayne D. Kaplan, Ernst Z. Kurmaev and Alexander Moewes

published in: *J. Phys. Chem. C* **2013**, *117*, 8806-8812; DOI: 10.1021/jp4002059

Keywords: carbon nitrides; water splitting; X-ray spectroscopy; DFT; layered compounds

Abstract: We have used a combination of X-ray and electron energy-loss spectroscopies along with DFT calculations to investigate the electronic structure of PTI/LiCl, a graphitic carbon nitride-type material with LiCl intercalation shown to photocatalyze the water-splitting reaction. The material is shown to have a band gap that is tunable with LiCl loading, with a minimum gap of 2.2 eV when fully loaded. This suggests that PTI/LiCl may be further optimized through control of their LiCl loading, and shows that graphitic carbon nitride-type materials can be chemically tuned to improve their photocatalytic activity.

4.2.1 Introduction

Graphitic carbon nitride-type materials are an emerging class of functional semiconductors which have recently drawn considerable attention due to variety of their potential applications, including metal-free catalysis,^[1] serving as mesoporous templates for metal-nitride synthesis,^[2] optical sensing for metalions^[3] and photocatalysis.^[4,5] The physical properties of these materials are well-suited for use as a water-splitting photocatalyst as they are insoluble, as well as physically, photo and thermally stable.^[4,6,7] Additionally, graphitic carbon nitride-type materials have been shown to enable metal-free photocatalysis, enabling hydrogen reduction in water using naturally abundant elements along with light from the visible spectrum.^[4,5,8] This is in contrast to traditional inorganic photocatalysts, such as TiO₂, which primarily absorb UV radiation due to their high intrinsic band gap.^[9,10]

Modifying the chemical composition and morphology of non-metallic catalysts offers considerable flexibility in tuning their physical parameters.^[7] For example, theoretical predictions show that a heptazine-based graphitic carbon nitride-type structure should be more stable than triazine-based structures.^[11] However, a highly crystalline triazine-based structure, poly(triazine imide) (PTI/LiCl), has been synthesized by condensation of dicyandiamide in a eutectic LiCl / KCl salt mixture.^[12] As a result of this synthesis route, Li⁺ and Cl⁻ ions are incorporated into the triazine imide network. This raises the possibility of modifying the electronic structure of this graphitic carbon nitride-type material by tuning the loading of these ions, which may serve to donate or withdraw charge from the primary polymer matrix.

PTI/LiCl as synthesized is a dark brown-colored powder, and exhibits photocatalytic activity as measured by H₂ evolution.^[5] It has also been shown to have a small improvement in photoactivity compared to yellow-colored polymeric melon.^[13] Practical photocatalytic water splitting has to date been limited by a lack of materials having an appropriate conduction band edge energy to allow hydrogen reduction, as well as a low enough band gap to generate a reasonable photocurrent from the available solar spectrum.^[10,14] Therefore a study of the band gap and band edge positions of PTI/LiCl is important in understanding this improvement in performance.

In this work we probe the valence band electronic structure of PTI/LiCl using X-ray Emission Spectroscopy (XES) and its conduction band structure using X-ray Absorption Near-Edge Spectroscopy (XANES) and electron energy-loss spectroscopy (EELS). XES measures a core-hole lifetime broadened ground-state valence band partial density of states (DOS), while XANES measures a conduction band partial density of states in an excited state caused by the transition of a core-level electron to an unoccupied state. By interpreting these experimental probes using an electronic structure model, produced using a linearized augmented plane wave plus local orbital (LAPW+lo) density functional theory (DFT) code,^[15] we estimate the band gap of PTI at different levels of LiCl loading.

In the past, characterization of carbon nitrides has been performed by XES and XANES for plasma sputtered films.^[16,17] These measurements were notable for having much sharper spectral features than other carbon-based solids such as graphene or diamond. In addition, XES measurements of ion sputtered CN_x films demonstrate the dominance of sp² hybridized carbon in these graphitic carbon nitride-type materials, as well as demonstrated the sensitivity of XES to the two inequivalent, bulk N sites in these systems (as first demonstrated by XPS^[18]). The high quality of X-ray spectra for this material class supports the use of these techniques in studying related materials such as PTI/LiCl.

The elementally specific band gap derived from X-ray spectroscopy is compared to a band gap determined using valence electron energy-loss spectroscopy (VEELS) performed in a monochromated transmission electron microscope (TEM). This method has been used to determine the band gaps of semiconductors such as Si and GaN^[19] and insulators such as SiO₂.^[20] In general, EELS uses a spectrometer to analyze electrons transmitted through a sample, and is able to resolve energy losses occurring due to both core and valence level electrons being excited into higher energy unoccupied states. By analysing the electron energy loss near edge structure (ELNES) associated with elementally-specific absorption edges, a wealth of chemical information can be extracted from a sample, such as its oxidation state^[21,22] and site coordination.^[23] Experimental conditions are usually chosen such that dipole allowed transitions are probed and dipole forbidden transitions are minimized, resulting in measurements that are comparable to XANES.

4.2.2 Experimental Section

For the synthesis of PTI/LiCl, dicyandiamide (0.200 g, 2.38 mmol) and a eutectic mixture of lithium chloride (59.2 mol%, 0.904 g, 21.33 mmol) and potassium chloride (40.8 mol%, 1.096 g, 14.70 mmol) were ground together in a glovebox. The reaction mixture was transferred into a thick-walled silica glass tube. The tube was heated in a vertical furnace under argon atmosphere at a rate of 6 K·min⁻¹ to 400 °C where they were held for 12h. After heating, the samples were returned to room temperature at 6 K·min⁻¹. The tube was then evacuated and sealed with a hydrogen-oxygen burner at a length of 120 mm. The sealed tube was then heated to 600 °C at a rate of 10 K·min⁻¹ and held at this temperature for 48h. The sealed tube was again returned to room temperature (8 K·min⁻¹) and the contents washed twice with boiling water to remove any residual salt mixture. Finally, the material was dried at 200 °C under 5 x 10⁻⁴ mbar, resulting in 60-80 mg of dark brown powder. Elemental analysis of the resulting product is summarized in Table 1.

Table 1. Elemental Analysis Results of PTI samples.

Sample	(wt.-%)	C	N	H	Li	Cl
PTI/LiCl		29.58	50.35	1.30	4.59	10.99
PTI/(LiCl) _{0.5}		31.25	51.15	2.04	2.08	5.97
PTI/(LiCl) _{0.25}		31.22	52.23	2.42	1.01	3.00
PTI/(LiCl) ₀		32.21	53.72	2.45	0.35	0.00

PTI/LiCl with reduced LiCl content was prepared by Soxhlet extraction of 500 mg PTI/LiCl with 200 ml water for 20, 24 and 72h, giving molecular formulas of

PTI/(LiCl)_{0.5}, PTI/(LiCl)_{0.25} and PTI/(LiCl)₀, respectively. The resulting samples were dried at 200 °C, 5 x 10⁻⁴ mbar to yield brown powders (430 mg to 470 mg (20h) and 400 mg to 435 mg (72h)). Results from elemental analysis of the products after extraction are also summarized in Table 1.

X-ray emission spectroscopy was performed at Beamline 8.0.1 at the Advanced Light Source at the Lawrence Berkeley National Laboratory. Beamline 8.0.1 uses a spectrometer with a Rowland-circle geometry to resolve X-rays emitted by a sample undergoing excitation by synchrotron radiation, achieving a resolving power of $E/\Delta E = 1000$. Measured samples were mounted at a 30° angle with respect to the incident radiation, while the spectrometer is mounted at a 90° angle. The spectrometer entrance and monochromator exit slits were

oriented to open and shut in a line perpendicular to the plane of the horizontally polarized synchrotron radiation. Non-resonant emission spectra were collected using X-ray beam excitation energies above the associated absorption edge of the element in question (C, 320 eV; N, 420 eV; O, 550 eV). Resonantly excited emission measurements were also performed to differentiate between different N sites in the PTI/LiCl samples. The powdered samples were mounted using carbon tape to a conductive plate; additional test measurements with samples mounted on indium foil showed no contribution from carbon tape to the measurements.

X-ray absorption spectroscopy was performed at the spherical grating monochromator (SGM) beamline at the Canadian Light Source located at the University of Saskatchewan, Canada. Samples were oriented with the incident synchrotron radiation along the surface normal and grounded using carbon tape. Absorption total fluorescence yield (TFY) was measured using a channel plate detector. Total electron yield (TEY) was measured using an ammeter connected to the sample ground as X-ray generated secondary electrons left the sample surface.

Transmission electron microscopy was performed on the fully loaded PTI/LiCl powder, which was dissolved in ethanol and drop coated onto lacey C coated Cu grids (Plano GmbH, Germany). An FEI TITAN 80-300 scanning TEM equipped with a field emission source, Gatan Tridiem 866 energy filter, and a Wien-type monochromator was used to perform the measurements. The EELS data were acquired in TEM mode using a collection angle of 9.5 mrad. A dispersion of 0.01 eV/channel was used for VEELS and 0.2 eV/channel was used for core-loss measurements of C and N K edges. An energy resolution of 0.19 eV was determined using the full width at half maximum of the zero-loss peak (ZLP). A power-law function was used to fit the tail of the ZLP for subtraction as used by Erni and Browning.^[24] The onset of the sample conduction band was determined using two methods: from the observed onset after ZLP subtraction and from a linear extrapolation.^[20] In addition, for core loss excitations, the background of the C and N K edges was subtracted using a power law fitting.^[25]

4.2.3 DFT modeling

Because of the complexity of the physical structure of PTI/LiCl, a model of its electronic structure is useful in deconvoluting our experimental measurements. DFT modeling was performed using the generalized gradient approximation (GGA) as formulated by Perdew, Burke and Ernzerhof as the exchange functional^[26] and ignoring van-der-Waals interactions. The N K XES measurements in particular have a number of features that originate from the inequivalent sites within the crystal unit that are more easily differentiated by using a model. Since the occupation scheme of Li and H within the pores of PTI was not known in advance from the crystal structure refined from powdered X-ray diffraction (PXRD), it was necessary to attempt a number of possible orientations to determine the most stable configuration. As the Li average positions were known and FTIR spectroscopy indicated the presence of imide linkages between triazine units within, several arrangements of Li⁺ and H⁺ could be tested. Candidate structures were force-optimized within the constraints of the PXRD lattice parameters and the resulting structure was compared to the original PXRD refinement to determine fitness. Fitness was also assessed by the ability of the calculation to reproduce a band gap lower than our experimental result (as DFT calculations generally underestimate the band gap of a semiconductor^[27]) as well as to reproduce the valence band features experimentally observed in PTI/LiCl. The resulting partial DOS for model low and high LiCl-loaded structures are shown in Figure 2.

From the PXRD structure, PTI/LiCl is expected to have two inequivalent N sites: sites within the triazine ring (N-1) and the imide linkage sites (N-2) that bind to H, as depicted in Figure 1a. Previous study of PTI/LiCl using NMR^[12] also indicates that partial substitution of Li⁺ for H⁺ in the imide units occurs in the sample at high loading. This substitution is therefore the expected method for Li loading above the basic unit cell structure of PTI/LiCl refined from PXRD. To model this requires the introduction of two Li per Cl atom in the pores of the model and the removal of a H to maintain charge balance. However, there are several possible arrangements of this additional Li, and the structural candidate that best balances the repulsive forces within the pore was found to be two adjacent Li ions opposed by two NH groups on the opposite side of the pore; this arrangement is then reversed on the adjacent PTI layer. As a result of this H substitution, an additional inequivalent N site is introduced into the model (denoted N-3).

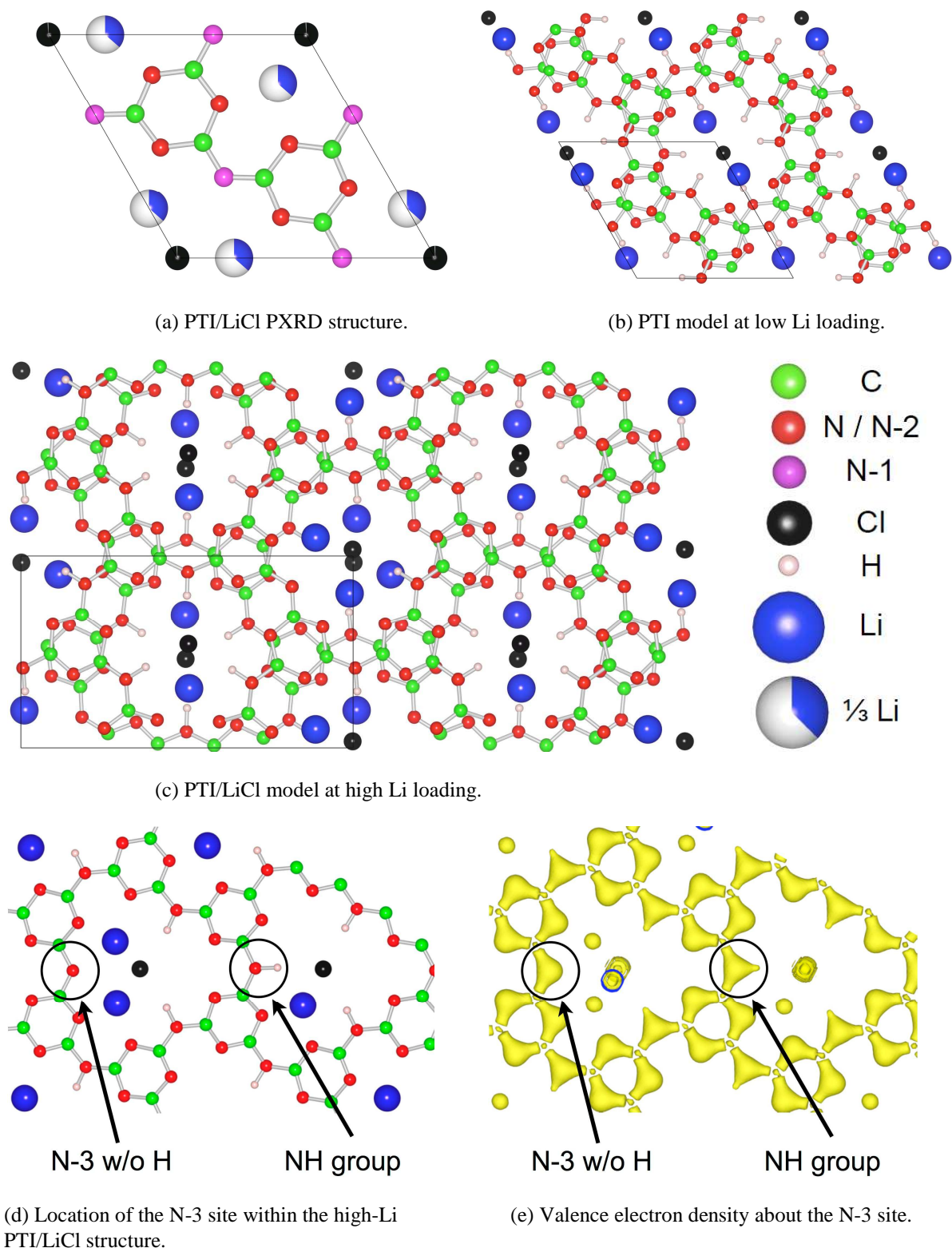


Figure 1. (a) PTI/LiCl structure derived from PXRD.^[12] The inequivalent N-1 and N-2 sites are in magenta and red respectively, C in green, Cl in black and Li in blue. (b,c) Structural candidates used for DFT calculations, with H in pink. The high Li loading structure (c) was found to agree well with experiment and is used as a model for PTI/LiCl at full loading. The structures observe the same AB layer stacking perpendicular to the graphitic plane as the PXRD-derived structure. (d,e) In the high-Li loading model, an N-3 site with two neighboring Li atoms displays a unique valence electron density.

Since the high-loading DFT model contains three inequivalent N sites in different local chemical environments, it becomes important to consider the binding energy shift of their 1s levels, relative to which we measure valence band X-ray emission. While it would be most appropriate to determine this splitting with an XPS measurement, this is precluded by the lack of a macroscopic crystal to measure; however our all-electron DFT model can also provide relative binding energies between the sites. In the high-Li model, the core level for the N-2 site has the highest binding energy, followed by the N-1 site 1.3 eV below it, with the N-3 site at lowest a binding energy 1.9 eV below the N-1 site. These core level shifts, combined with the valence band density of states contributed by each sites, are then responsible for the energy position of each N site's contribution to the measured X-ray spectra.

Of particular interest in the calculated results are the highest-energy N states, which should be strongly responsible for photoabsorption, as N 2p sites are also a component of the conduction

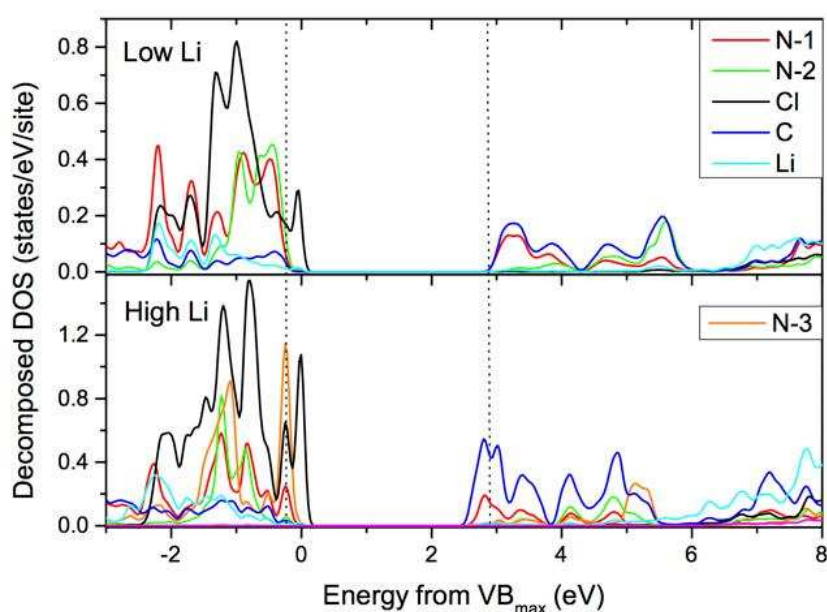


Figure 2. Comparison of the broadened total DOS broken down by element for the low Li (top) and high Li (bottom) DFT models. The contribution of N states is further split by site, and the Cl contribution is scaled by 1/5 for clarity. In both high and low Li loading there is a sharp Cl 2p feature at the valence band maximum that weakly hybridizes with C and N 2p states. The conduction band minimum consists of hybridized C and N 2p states, with C dominating. At high Li loading the conduction band minimum lowers in energy by 0.4 eV while the valence band maximum remains essentially unchanged. However, the N 2p states split, with N-3 states being pulled to higher valence band energy, in agreement with the XES measurements, by an apparent hybridization with the higher-energy Cl sites. The dashed lines are provided as a visual aid.

band minimum. The N-3 site in the high Li structural model is an imide linkage that has had its bonded H removed, and is instead coordinated with two Li sites. The charge density about this position becomes unique in the DFT model, causing a splitting of the N 2p states and a sharp contribution of states just below the valence band maximum, as shown in Figure 2. The existence of the N-3 site is therefore predicted to

contribute to an increase in the energy of the valence band maximum of PTI/LiCl versus samples with lower LiCl loading, as observed in the XES measurements. More importantly, the absolute energy position of the closed shell Cl should be largely insensitive to other modifications in the PTI structure, suggesting that Cl loading would serve to pin the valence band maximum at a constant energy.

Because of their low binding energy, Cl 2p electrons will occupy the highest energy states in the valence band. However, these states are not expected to participate significantly in photoabsorption as they will be highly spatially localized at the Cl site, which should have a filled 2p shell due to charge transfer from a neighbouring Li site. The Cl site will also not have localized unoccupied states at low enough energy to participate in optical transitions, as can be observed in Figure 2 where there is negligible contribution of Cl states until orbital energy significantly above the conduction band minimum. The presence of these Cl valence states at energies above those contributed by the C-N matrix could explain the broad onset of optical absorption in PTI.^[13]

4.2.4 Experimental Discussion

Soft X-ray emission spectroscopy measures the fluorescence produced by valence band electrons transitioning to X-ray excited core holes on a sample under study. By tuning the energy of the exciting X-ray, it is possible to excite specific sites within the sample, for example by creating a 1s core hole on a C or N site. The 1s levels for the three inequivalent N sites are sufficiently separated in energy that the N-3 site can be resonantly excited with an X-ray energy of 401.5 eV. Excitations below this energy will primarily excite the N-1 site due to the structure of the conduction band. The resulting N K resonant emission spectra (RXES, as shown in Figure 3), which measure transitions from N 2p \rightarrow 1s states, therefore probe the local projected density of valence band states at these two sites, while non-resonant spectra probe all N sites simultaneously. The resonantly excited spectra enhance valence band features specific to an individual site, particularly at lower binding energies where N and C 2p states hybridize to form bonding states. There is additionally a strong resonance feature at 393.5 eV that emerges when PTI/LiCl is resonantly excited at 401.5 eV, corresponding to a maximum in N-3 conduction band states. This resonance feature corresponds to a DOS at the

same energy as the N-1 peak at 395 eV; however, the lower binding energy of the N-3 site 1s orbital causes this emission to be shifted to lower energy. At reduced LiCl loading the unique charge density of the N-3 site is no longer expected to be present in the structure (as NH units are more stable), and this is observed in the XES measurement of PTI/LiCl_{0.5}, where this

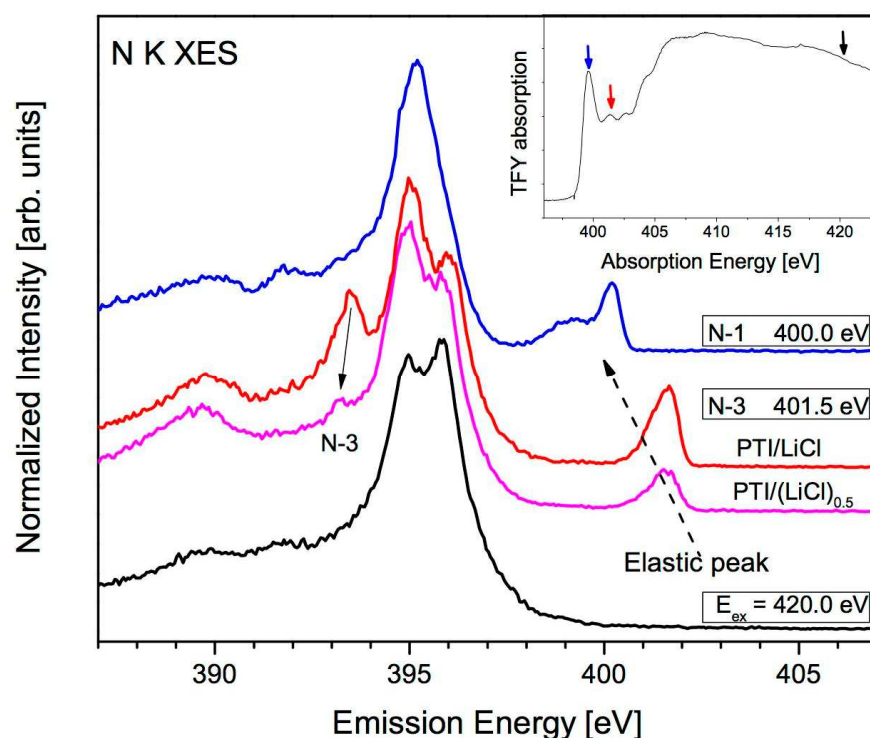


Figure 3. Resonantly excited XES of the PTI/LiCl N-1 site (blue) and N-3 site (red) as compared to the non-resonant spectrum (black). The inset shows the features in the N absorption spectrum that were excited at specific energies, depicted using arrows of the same color. Resonant excitation of the N-1 site no longer shows emission from the feature at 395.8 eV. Resonant excitation of the N-3 site reveals a feature at 393.5 eV associated with full Li loading at the N-3 site; the feature is greatly diminished in the PTI/(LiCl)_{0.5} measurement (magenta).

feature is largely extinguished. The presence of this feature is a good indicator of the agreement between our high-loading DFT model and the experimental measurements. Since the C and N K XES measurements of PTI/LiCl display good hybridization features, they can be aligned on a common energy scale in order to show the energy position of each element's contribution to the valence band, as shown in Figure 4. In this case we have chosen a binding energy scale with zero energy coinciding with the experimentally determined valence band maximum. The N K XES spectrum extends to the high-energy side of the valence band, indicating N contributes more states than C to the valence band maximum. C and N K XAS spectra can similarly be aligned to this common energy scale, giving an overview of the electronic structure of PTI/LiCl in the vicinity of its band gap. XANES spectra are typically shifted downwards in X-ray energy by the presence of the core-hole in the final state of the XANES measurement. It has been shown that DFT models can accurately estimate this excitonic shift in a single particle approximation by the introduction

feature is largely extinguished. The presence of this feature is a good indicator of the agreement between our high-loading DFT model and the experimental measurements.

Since the C and N K XES measurements of PTI/LiCl display good hybridization features, they can be aligned on a common energy scale in order to show the energy position of each

of a core vacancy in the calculation,^[28] necessitating our DFT model as discussed above. The resulting shift (found to be approximately 0.4 eV in our high-Li loading model of PTI/LiCl) can then be added to the position of the fully loaded PTI/LiCl XANES spectrum onset to determine a band gap. As the core-hole shift depends on the physical structure used to model it, this shift is appropriate only for the fully loaded PTI/LiCl measurement. Though this core-hole shift is not expected to vary significantly between the samples measured, determining it

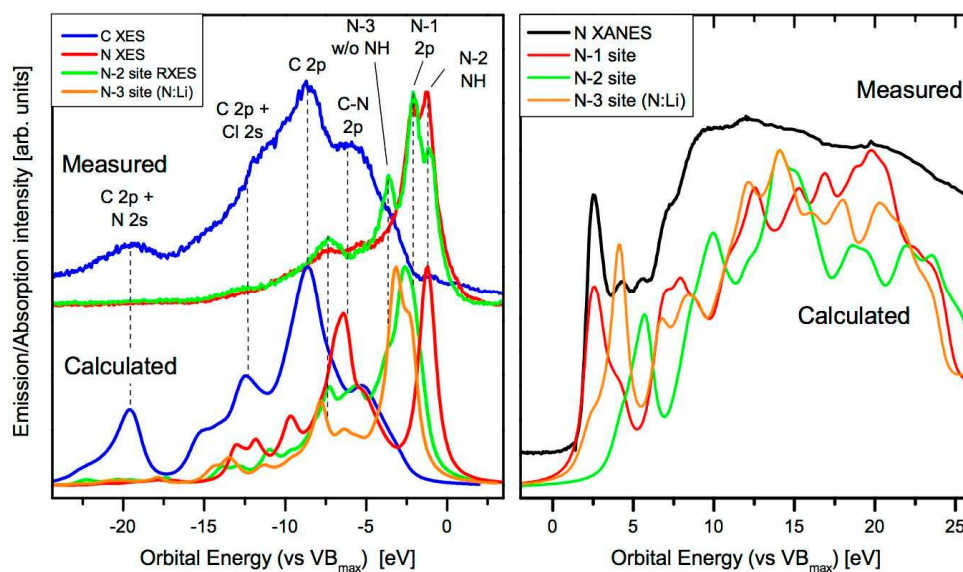


Figure 4. Comparison of the PTI/LiCl XES and XAS measurements with calculated emission spectra for the high Li loading model structure (left). The calculated C emission spectrum reproduces the experiment well, with all major features accounted for, including an appropriate amount of splitting between the C 2p valence states and the lower energy C 2p/N 2s sub-band. The N-3 resonant emission spectrum (in green) shows similar feature splitting as the calculated emission spectra below. The calculated N-1/N-2/N-3 site splitting also reproduces the features of the N XANES measurement (right).

depends on the accuracy of the structural model used to calculate it, and the PTI samples with lower LiCl loading are not understood well enough to fully model at the present time.

At maximum Li loading, two features (at 401.4 eV and 402.7 eV) are discernible in the N K XANES measurement that correspond to unoccupied states contributed by the N-3 and N-2 sites, respectively. However, as Li is extracted from the samples these features are quickly extinguished with a corresponding shift in the onset peak, suggesting that changes in Li concentration can control splitting of the low-lying conduction band states. While the samples in this study had Li and Cl removed in tandem, the closed shell of a Cl⁻ ion is not expected to contribute unoccupied states near the band edge, suggesting that changes in Li concentration

may be sufficient to control the conduction band minimum. Such a tuning capability could be used to align the CB minimum with the hydrogen reduction redox level to improve H_2 evolution. Choosing band onsets from the spectra was performed by taking the positive second derivative peak in the region of the measured signal onset as indicative of the energy at which the partial DOS begins to contribute to the spectrum and overcomes the effects of experimental and core-hole lifetime broadening. This method has been found to be a useful metric in measuring the band gap of post-transition metal oxides^[29] where there is a sharp onset in states at a band edge, as is the case with the PTI/LiCl measurements. The results of choosing these onset positions (shown in Figure 5) produce a band gap of 2.2 eV for PTI with full LiCl loading. This

compares with the established band gap of melon of 2.7 eV,^[4] showing a 0.5 eV band gap decrease. As LiCl is removed from the system the band gap apparently increases, as observed in the DFT models and the shifting of XANES features; however, this does not appear to affect the onset point of the N-edge exciton induced during the XANES measurement (which should sit on the lowest-energy N-1 site that is not adjacent to Li^+). Instead, the sharpness of

the onset decreases, and the lowest energy N absorption peak (also caused by the N-1 site) shifts upwards in energy approximately 0.4 eV. A similar shift of 0.34 eV of the conduction

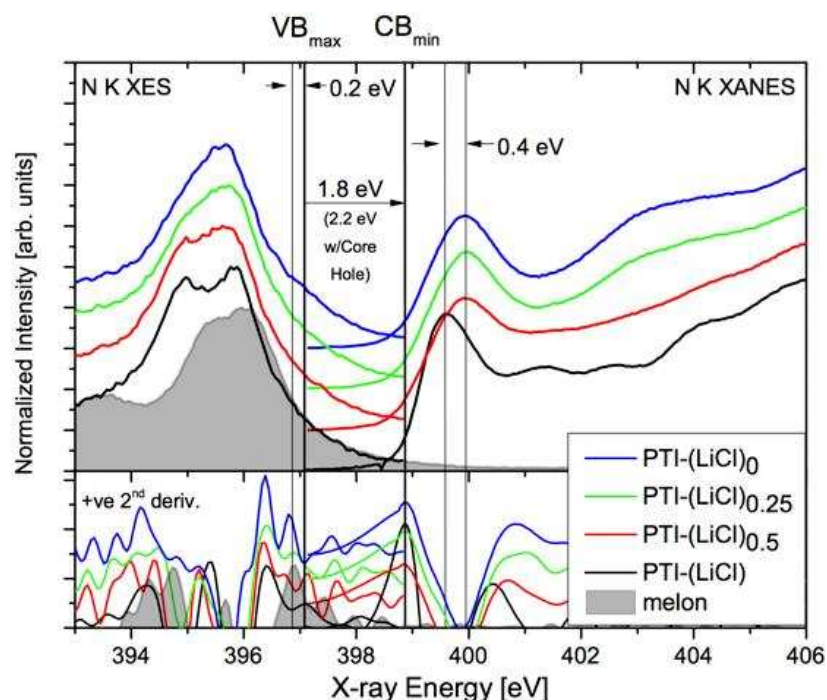


Figure 5. Comparison of different LiCl loadings of PTI with the valence band onset position of polymeric melon. The band gap of PTI increases as LiCl is removed through the loss of a high energy feature (expected to be N-Cl 2p state hybridization); simultaneously N peak splitting at the VB maximum is reduced. The VB maximum of PTI/LiCl shows a 0.2 eV increase above that of melon and the reduced-loading PTI/LiCl samples, indicating the remaining band gap decreased of PTI/LiCl must be caused by a decrease in the conduction band minimum. Although this shift in conduction band onset is obscured by the effect of the XANES core hole, the onset peak maximum of N absorption shifts downwards by 0.4 eV when comparing the low to high-loaded LiCl measurement because of the introduction of the N-3 site.

band onset between high and low Li loading is also seen in the DOS in Figure 2. However, a peak position is not indicative of the onset of states in a solid system,^[30] thus, it is only possible to estimate a band gap of ~ 2.8 eV for PTI-(LiCl)₀, with a lower gap for the intermediate loadings.

The complementary EELS band gap measurement serves to support the choice of band onsets in the X-ray spectra. In a semiconducting material, an energy-loss in a transmitted electron beam may occur due to the transition of electrons from the valence band into the conduction band. For determining the band gap of PTI/LiCl, the contribution of the zero-loss peak (ZLP) was subtracted from the VEEL spectrum (using a power-law fit to the tail of the ZLP) and a linear fit was made with the observed onset as shown in Figure 6c; this linear fit intersects the

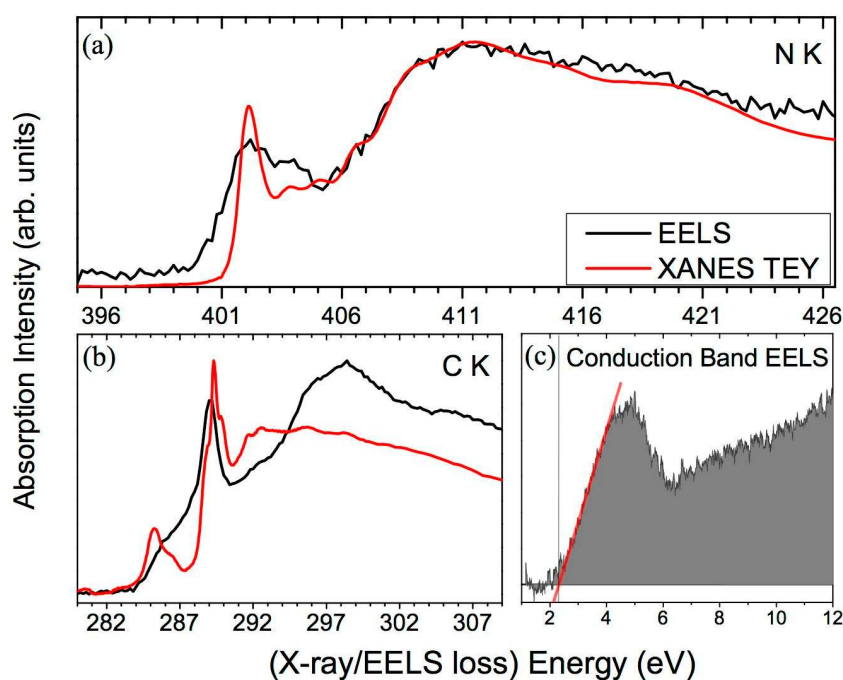


Figure 6. Comparison of the EELS core-level edges versus the XANES TEY measurements. The N K edge (a) shows good agreement in terms of feature position and peak ratio after the XANES measurement has been aligned with EELS (shifted upwards by 2.5 eV), indicating that the conduction band of PTI is dominated by 2p states. The broadening of EELS at the C K edge (b) is more pronounced than at the N K edge but shows contribution from 2s anti-bonding states at energies above 295 eV that are not probed by the XANES measurement. (c) VEELS band gap determination of 2.2 eV using a linear fit to the onset of the first energy-loss feature.

noise floor at 2.2 eV.

The VEELS probe of PTI/LiCl was performed on a single crystallite and agrees with the X-ray band gap. A high-energy electron beam will also cause core-level transitions to occur, and the observed ELNES of these edges are similar to those measured by XANES. Because EELS is measured from electrons transmitted through thin samples, it is mostly comparable to XANES measured by total

electron yield (TEY), which is highly surface sensitive.^[31] Comparing the C and N K edge

measurements of XANES TEY versus the ELNES data in Figure 6 shows good agreement, allowing us to confirm that the sample is receiving little damage during the EELS measurement that would affect the measured band gap.

4.2.5 Conclusions

Through EELS and X-ray spectra, we have shown that PTI/LiCl displays a decreased band gap (~ 2.2 eV) with respect to polymeric melon (2.7 eV) as well as to PTI samples with reduced loading of Li^+ and Cl^- . The mechanism for this band gap decrease is 2-fold:

1. A reduction in the conduction band minimum energy caused by splitting of inequivalent unoccupied N states by an interaction with loaded Li^+ , which substitutes for H^+ in the imide links between triazine units.
2. A similar splitting of N 2p states at the valence band maximum, allowing increased hybridization between the Li^+ substituted imide links with low binding energy Cl 2p states.

We have constructed a DFT model that demonstrates a high degree of qualitative agreement with the measured X-ray spectral features and quantitative agreement with the observed band edge shifts. We have demonstrated by resonant X-ray Emission Spectroscopy a sensitive probe for the Li substituted imide N presented in PTI/LiCl at high LiCl loading. We propose that the contribution of Li^+ and Cl^- loading to the band edge shifts may be independent of each other, suggesting that the hydrogen evolution performance of PTI/LiCl could be further improved by independent control of the valence and conduction band edges achieved by removal of Li^+ while maintaining full Cl^- loading.

Acknowledgements

We gratefully acknowledge support from the Natural Sciences and Engineering Research Council of Canada (NSERC) and the Canada Research Chair program. Measurements described in this work were performed at the Canadian Light Source, which is supported by NSERC, the National Research Council Canada, the Canadian Institutes of Health Research,

the Province of Saskatchewan, Western Economic Diversification Canada, and the University of Saskatchewan. The Advanced Light Source is supported by the Director, Office of Science, Office of Basic Energy Sciences of the US Department of Energy under Contract DE-AC02-05CH11231. Computing resources were provided by WestGrid and Compute/Calcul Canada. We gratefully acknowledge financial support that was granted from the Deutsche Forschungsgemeinschaft (DFG) (project SCHN 377/15-1) and from the Fonds der Chemischen Industrie (FCI) (scholarship for E.W.). K.S.V. gratefully acknowledges the Elite Network of Bavaria and the Nanosystems Initiative Munich for financial endowment.

4.2.6 Bibliography

- [1] A. Thomas, A. Fischer, F. Goettmann, M. Antonietti, J.-O. Müller, R. Schlögl, J. M. Carlsson, *J. Mater. Chem.* **2008**, *18*, 4893–4908.
- [2] A. Fischer, M. Antonietti, A. Thomas, *Adv. Mater.* **2007**, *19*, 264–267.
- [3] E. Z. Lee, Y.-S. Jun, W. H. Hong, A. Thomas, M. M. Jin, *Angew. Chem. Int. Ed.* **2010**, *49*, 9706–9710.
- [4] X. Wang, K. Maeda, A. Thomas, K. Takanebe, G. Xin, J. M. Carlsson, K. Domen, M. Antonietti, *Nat. Mater.* **2009**, *8*, 76–80.
- [5] Y. Ham, K. Maeda, D. Cha, K. Takanebe, K. Domen, *Chem. Asian J.* **2012**, 1–8.
- [6] A. Liu, R. Wentzcovitch, *Phys. Rev. B* **1994**, *50*, 10362–10365.
- [7] J. Zhang, X. Chen, K. Takanebe, K. Maeda, K. Domen, J. D. Epping, X. Fu, M. Antonietti, X. Wang, *Angew. Chem. Int. Ed.* **2010**, *49*, 441–444.
- [8] K. Maeda, X. Wang, Y. Nishihara, D. Lu, M. Antonietti, K. Domen, *J. Phys. Chem. C* **2009**, *113*, 4940–4947.
- [9] A. Fujishima, K. Honda, *Nature* **1972**, *238*, 37–38.
- [10] M. D. Archer, J. R. Bolton, *J. Phys. Chem.* **1990**, *94*, 8028–8036.
- [11] E. Kroke, M. Schwarz, E. Horath-Bordon, P. Kroll, B. Noll, A. D. Norman, *New J. Chem.* **2002**, *26*, 508–512.
- [12] E. Wirnhier, M. Döblinger, D. Gunzelmann, J. Senker, B. V. Lotsch, W. Schnick, *Chem. Eur. J.* **2011**, *17*, 3213–3221.
- [13] K. Schwinghammer, B. Tuffy, M. B. Mesch, E. Wirnhier, C. Martineau, F. Taulelle, W. Schnick, J. Senker, B. V. Lotsch, *Angew. Chem. Int. Ed.* **2013**, *52*, 2435–2439.
- [14] A. J. Nozik, *Ann. Rev. Phys. Chem.* **1978**, *29*, 189–222.
- [15] P. Blaha, K. Schwarz, G. Madsen, D. Kvasnicka, J. Luitz, *WIEN2k, an augmented plane wave + local orbitals program for calculating crystal properties*; Karlheinz Schwarz, Techn. Universität Wien, Austria, **2001**.
- [16] Y. Muramatsu, Y. Tani, Y. Aoi, E. Kamijo, T. Kaneyoshi, M. Motoyama, J. J. Delaunay, T. Hayashi, M. M. Grush, T. A. Callcott, D. L. Ederer, C. Heske, J. H. Underwood, R. C. C. Perera, *Jpn. J. Appl. Phys.* **1999**, *38*, 5143–5147.

- [17] E. Kurmaev, A. Moewes, R. Winarski, S. Shamin, D. Ederer, J. Feng, S. Turner, *Thin Solid Films* **2002**, *402*, 60–64.
- [18] D. Marton, K. Boyd, A. Al-Bayati, S. Todorov, J. Rabalais, *Phys. Rev. Lett.* **1994**, *73*, 118–121.
- [19] L. Gu, V. Srot, W. Sigle, C. Koch, P.A. van Aken, F. Scholz, S. Thapa, C. Kirchner, M. Jetter, M. Rühle, *Phys. Rev. B* **2007**, *75*, 195214.
- [20] J. Park, S. Heo, J.-G. Chung, H. Kim, H. Lee, K. Kim, G.-S. Park, *Ultramicroscopy* **2009**, *109*, 1183–1188.
- [21] J. H. Rask, B. A. Miner, P. R. Buseck, *Ultramicroscopy* **1987**, *21*, 321–326.
- [22] P. A. van Aken, B. Liebscher, V. Styrsa, *J. Phys. Chem. Miner.* **1998**, *25*, 323–327.
- [23] R. Brydson, L. A. J. Garvie, A. J. Craven, H. Sauer, F. Hofer, G. Cressey, *J. Phys.: Condens. Matter* **1993**, *5*, 9379–9392.
- [24] R. Erni, N. D. Browning, *Ultramicroscopy* **2007**, *107*, 267–273.
- [25] R. F. Egerton, *Electron Energy-Loss Spectroscopy in the Electron Microscope, Third Edition*; Springer Science + Business Media, New York, **2011**.
- [26] J. P. Perdew, K. Burke, M. Ernzerhof, *Phys. Rev. Lett.* **1996**, *77*, 3865–3868.
- [27] J. P. Perdew, M. Levy, *Phys. Rev. Lett.* **1983**, *51*, 1884–1887.
- [28] L. Triguero, L. G. M. Pettersson, *Phys. Rev. B* **1998**, *58*, 8097–8110.
- [29] J. A. McLeod, R. G. Wilks, N. A. Skorikov, L. D. Finkelstein, M. Abu-Samak, E. Z. Kurmaev, A. Moewes, *Phys. Rev. B* **2010**, *81*, 245123.
- [30] S. J. Kang, Y. Yi, C. Y. Kim, C. N. Whang, T. A. Callcott, K. Krochak, A. Moewes, G. S. Chang, *Appl. Phys. Lett.* **2005**, *86*, 232103.
- [31] B. H. Frazer, B. Gilbert, B. R. Sonderegger, G. De Stasio, *Surf. Sci.* **2003**, *537*, 161–167.

4.3 Photocatalytic Activity of PTI/LiCl

All “doping” experiments and photocatalytic measurements in this subsection were conducted by Katharina Schwinghammer and Brian Tuffy (Max Planck Institute for Solid State Research, Stuttgart, advisor: Prof. Dr. B. Lotsch) and will also be published as part of their PhD theses.

All NMR measurements were carried out by Maria B. Mesch (University of Bayreuth, advisor: Prof. Dr. J. Senker) and Charlotte Martineau and Francis Taulelle (Tectospin, Institut Lavoisier de Versailles, France) and will also be published as part of the PhD thesis of M. B. Mesch.

Triazine-based Carbon Nitrides for Visible-Light Driven Hydrogen Evolution

Katharina Schwinghammer, Brian Tuffy, Maria B. Mesch, Eva Wirnhier, Charlotte Martineau, Francis Taulelle, Wolfgang Schnick, Jürgen Senker and Bettina V. Lotsch

published in: *Angew. Chem.* **2013**, 125, 2495-2499; *Angew. Chem. Int. Ed.* **2013**, 52, (2435-2439); DOI: 10.1002/anie.201206817

Keywords: Carbon nitrides; copolymerization; photocatalysis; triazines; water splitting

Abstract: A new dimension: The doping of amorphous poly(triazine imide) (PTI) through ionothermal copolymerization of dicyandiamide with 4-amino-2,6-dihydroxypyrimidine (4AP) results in triazine-based carbon nitrides with increased photoactivity for water splitting compared to crystalline poly(triazine imide) (PTI/Li⁺Cl⁻, see picture) and melon-type carbon nitrides. This family of carbon nitride semiconductors has potential as low-cost, environmentally clean photocatalysts for solar fuel production.

The development of catalysts that enable the direct conversion of solar energy into chemical energy has been defined as one of the major challenges of modern materials chemistry. Hydrogen generated by photochemical water splitting has been identified as a promising energy carrier that offers a high energy density while being environmentally clean.^[1] Nevertheless, to realize a light-driven hydrogen-based economy, the exploration of new materials for highly efficient, stable, economically viable, and environmentally friendly photocatalysts is required.

To date, numerous inorganic semiconductors have been developed for water splitting, most of them being transition metal compounds containing heavy metals such as La, Bi, Ta, or Nb, which impede scalability, increase cost, and add complexity.^[2] Recently, attention has been attracted to a new class of metal-free photocatalysts, comprising polymeric melon-type carbon nitrides (CNs) based on imide-bridged heptazine units (see Figure 1 a).^[3] CNs are readily accessible, lightweight, stable, and low-cost compounds that offer an attractive alternative to metal-rich catalysts while still maintaining efficient photoactivity.^[4]

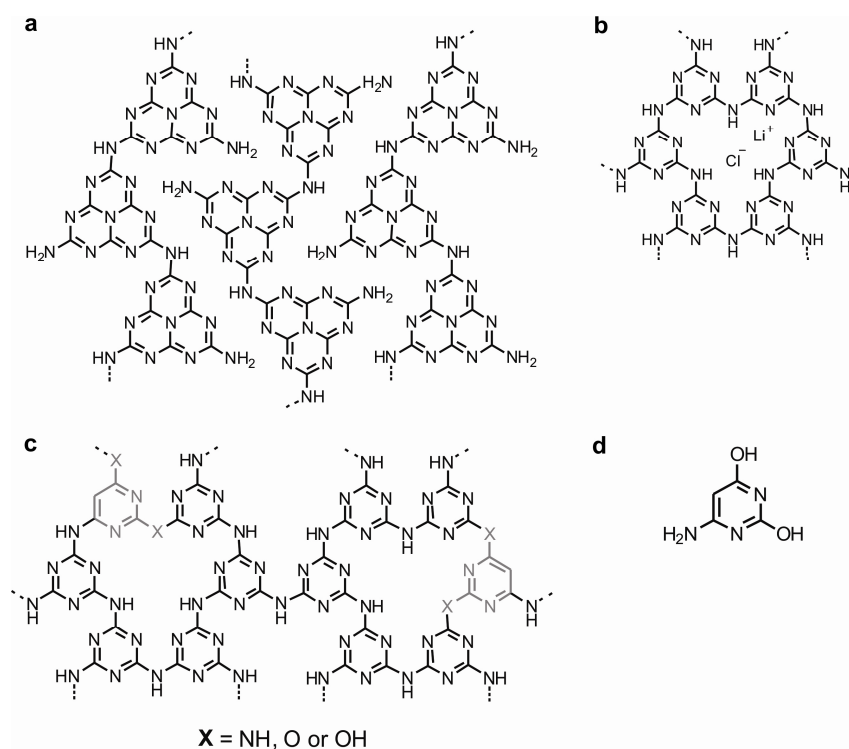


Figure 1. Chemical structures of a) melon, b) PTI/Li⁺Cl⁻ (idealized structure), c) aPTI_4AP_{16%} (proposed structure), and d) the dopant 4AP.

Thermal condensation of CNs forms a wide variety of chemical species that differ substantially with respect to their degree of condensation, hydrogen content, crystallinity, and morphology.^[5,6] The chemical modification of CNs by molecular “dopants” has resulted in a number of CN materials with improved photocatalytic activity.^[7] Although the evidence is largely empirical, the property enhancement presumably originates from subtle modifications

of the parent structures by incorporation of heteroatoms as well as structural defects, to give rise to enhanced absorption in the visible light range and a more complete exploitation of the solar energy spectrum.

In contrast to all known CN photocatalysts, which are composed of heptazine building blocks, poly(triazine imide)(PTI/Li⁺Cl⁻) is the only structurally characterized 2D CN network featuring imide-linked triazine units (see Figure 1b).^[8,9] Owing to its high level of crystallinity, PTI/Li⁺Cl⁻ lends itself as an excellent model system to study photocatalytic activity towards water splitting as a function of the number of building blocks, the composition, and the degree of structural perfection of the system. Herein, we present a new generation of CN photocatalysts based on triazine building blocks and demonstrate their enhanced photocatalytic activity in comparison to heptazine-based CNs. Moreover, we show that their performance can be amplified by small-molecule doping, thus rendering them the most active nonmetal photocatalysts for the hydrogen evolution reaction that have been reported to date.

As a starting point, we synthesized crystalline PTI/Li⁺Cl⁻ as a model structure for triazine-based CNs in a two-step ionothermal synthesis according to the procedure of Wirnhier et al.^[8,9] To study the effect of crystallinity on the photocatalytic activity, we also synthesized an amorphous variant of PTI (aPTI), through a one-step ionothermal synthesis involving a LiCl/KCl salt melt. We used 4-amino-2,6-dihydroxypyrimidine (4AP; Figure 1d) as the dopant because of its structural similarity to melamine and higher carbon and oxygen content. The photocatalytic activity of the as-prepared CNs was compared with that of crystalline PTI/Li⁺Cl⁻ and of heptazine-based raw melon (see the Supporting Information).

The XRD patterns of the aPTI samples confirm their amorphous character by the absence of sharp reflections (see the Supporting Information, Figure S1), which are present in the XRD patterns of crystalline PTI/Li⁺Cl⁻. However, the FTIR spectra of the synthesized aPTI CNs are still largely similar to that of PTI/Li⁺Cl⁻^[8] (Figure 2d and Figures S2–5 in the Supporting Information), as they contain a band at 810 cm⁻¹ (ring sextant out of plane bending) and a fingerprint region between 1200 and 1620 cm⁻¹ that is dominated by $\nu(\text{C-NH-C})$ and $\nu(\text{C=N})$ stretching vibrations.^[5,10] Doping with 4AP gives rise to less well-defined IR bands, thereby indicating a decrease in the structural order. In addition, in the spectra of 16% and 32% doped PTI there is a band at 914 cm⁻¹ that can be assigned to aromatic C-H bending vibrations of the

dopant (see the Supporting Information, Figure S5). Interestingly, the bands at 2160 cm^{-1} , 1730 cm^{-1} , and around 1200 cm^{-1} , which are seen in the spectrum of aPTI and partially in those of the doped samples, point to the presence of terminal nitrile groups as well as oxygen-containing functionalities, such as C=O and C-O.

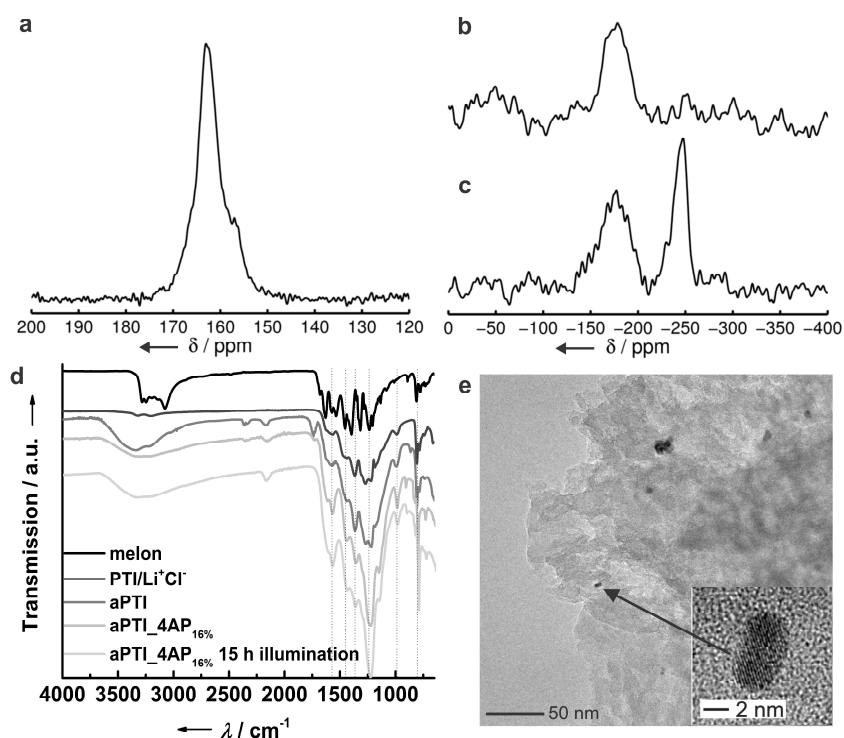


Figure 2. a) ^{13}C CP-MAS NMR spectrum (10 kHz), b) ^{15}N CPPI MAS NMR spectrum (6 kHz, inversion time=400 ms) and c) ^{15}N CP-MAS NMR spectrum (10 kHz) of aPTI_4AP_{16%}. d) FTIR spectra of aPTI_4AP_{16%} synthesized at $550\text{ }^\circ\text{C}$ before and after 15 h illumination, compared to crystalline PTI/Li⁺Cl⁻, aPTI_{500 °C}, and melon. e) A typical image of 2.3 wt% Pt-loaded aPTI_4AP_{8%} after illumination for 3 h under visible light ($\lambda > 420\text{ nm}$) and at higher magnification (inset).

Elemental analysis (EA) indicates the atomic ratio $\text{C/N} = 0.68$ for PTI/Li⁺Cl⁻, whereas the C/N ratios of the aPTI samples are slightly increased for those synthesized at elevated temperatures, indicating either a higher degree of condensation or an increase of oxygen incorporation (see the Supporting Information, Table S1). Notably, the amount of Li and Cl is lower in doped and non-

doped aPTI than in crystalline PTI/Li⁺Cl⁻, whereas the oxygen content is significantly higher, consistent with the IR results. This finding is worth noting as the amount of carbon and oxygen atoms in CNs is likely to play an essential role in the activity of CN photocatalysts.^[11] By increasing the amount of 4AP incorporated in the doped PTI from 2% to 64% the C/N ratio increases from 0.69 to 1.13, respectively (see the Supporting Information, Table S2). In summary, the EA and IR results suggest that both carbon and oxygen atoms are incorporated into the amorphous materials, most likely through replacement of one of the ring or bridging nitrogen atoms, as proposed in Figure 1c.

The ^{13}C and ^{15}N cross-polarization magic-angle spinning (CP-MAS) NMR spectra (Figure 2 a and c) for aPTI doped with 16% 4AP and synthesized at 550 °C (aPTI_4AP16%) provide additional information about the structural composition of the material derived from copolymerization with 4AP. Both spectra are similar to those of PTI/Li⁺Cl⁻ (see the Supporting Information, Figure S6),^[8,9] albeit with significantly increased line width (full width at half maximum (FWHM)) of 1.5 kHz compared to 600 Hz) owing to the less ordered character of the materials (see the Supporting Information, Figure S1). The ^{15}N CP-MAS spectrum shows two broad signal groups centered around -175 and -245 ppm. The former group is typical for tertiary ring nitrogen atoms (N_{tert} ; from the outer ring nitrogen atoms of heptazine or triazine rings), whereas the latter is characteristic of bridging NH groups. A very weak signal around -280 ppm indicates that only a small amount of terminal NH₂ groups is present, hence a melon-type structure seems very unlikely. However, to further corroborate this hypothesis and identify the type of heterocycle formed under the conditions used—triazine versus heptazine—we recorded a ^{15}N cross polarization polarization inversion (CPPI)^[12] NMR spectrum of aPTI_4AP16% (Figure 2b) with an inversion time of 400 ms. Under such conditions, resonances of the NH groups are reduced to zero intensity whereas signals of NH₂ units will be inverted. In contrast, the ^{15}N signals of tertiary nitrogen atoms are expected to remain largely unaffected. Hence, the unique signal for the central nitrogen atom, N_{c} , of a heptazine ring between -220 and -240 ppm can unequivocally be identified.^[5] The absence of any signals in the ^{15}N CPPI spectrum (Figure 2b) in the region between -200 and -300 ppm therefore strongly suggests the absence of heptazine units within the detection limit of roughly 10–15%. The markedly different intensity ratios in the ^{13}C CP-MAS spectrum of aPTI_4AP16% (Figure 2a) compared to those in the ^{13}C CP-MAS spectrum of PTI/Li⁺Cl⁻, and the broad asymmetric high-field flank of the signal between -140 and -170 ppm in the ^{15}N CP-MAS spectrum (Figure 2c) may indicate partial incorporation of pyrimidine into the PTI framework during copolymerization, which is not observed for PTI/Li⁺Cl⁻.^[8,9]

The brown color of crystalline PTI/Li⁺Cl⁻ indicates substantial absorption in the visible range of the spectrum. More specifically, the material absorbs largely in the UV region, yet additional absorption takes place in the blue part of the visible region and there is a gradual decrease in absorption toward higher wavelengths (Figure 3 and Figure S7 in the Supporting Information). The absorption spectra of aPTI synthesized at 400–600 °C show bands that are comparable to those in the spectrum of melon, thus rendering the color of the materials similar to that of melon (see the Supporting Information, Figures S7 and S10). When the reaction temperature is increased, the color of aPTI changes from cream (400 °C) to yellow (500 °C), suggesting enhanced absorption in the visible region. The absorption of aPTI_{500°C}, which is synthesized at a reaction temperature of 500 °C, is strongly red-shifted compared to that of crystalline PTI/Li⁺Cl⁻, thereby representing further improvement in the visible-light absorption (see the Supporting Information, Figure S7 (1)). With increasing amounts of

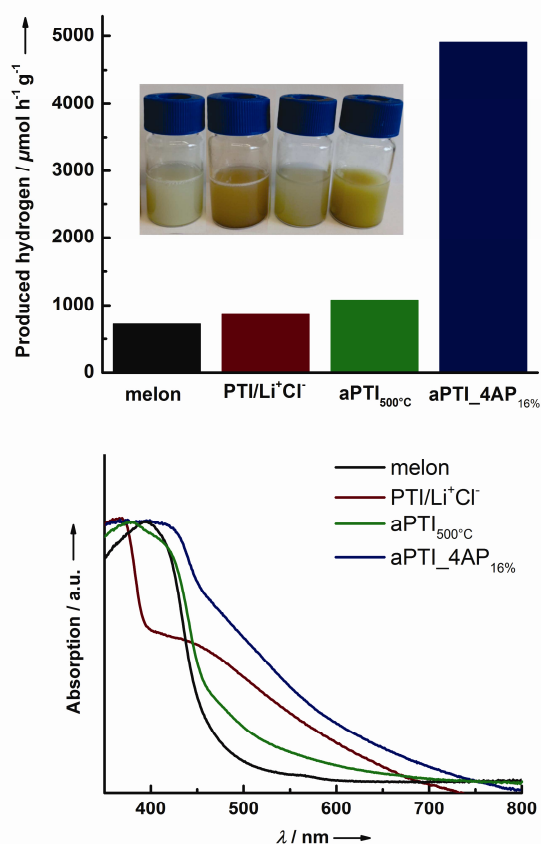


Figure 3. Photocatalytic activity towards hydrogen production (a). UV/Vis spectra (b) and color of the water/TEoA suspensions (inset in a) of aPTI_{4AP}_{16%} synthesized at 550 °C compared to crystalline PTI/Li⁺Cl⁻, aPTI synthesized at 500 °C, and melon.

dopant the color of the 4AP-doped CNs gets darker, changing from yellow (2%) to red-brown (64%); this color change correlates well with the red-shift observed in the absorption spectra (see the Supporting Information, Figure S8).

The inherent 2D architecture of crystalline PTI/Li⁺Cl⁻ gives rise to an expanded π -electron system, lower band-gap, and enhanced absorption as compared to the 1D polymer melon, and thus renders PTI/Li⁺Cl⁻ a promising photocatalyst that may even outperform the heptazine-based semiconductors. In fact, hydrogen production of 864 mmol h⁻¹ g⁻¹ (ca. 15% error) was measured for crystalline PTI/Li⁺Cl⁻ in the presence of a Pt co-catalyst and triethanolamine (TEoA) as sacrificial electron donor; this result equates to an

enhancement of approximately 20% compared to synthesized raw melon (see the Experimental Section; $722 \text{ mmol h}^{-1} \text{ g}^{-1}$) and is comparable to “g-C₃N₄” synthesized at 600 °C (synthesis according to Zhang et al.,^[7a] $844 \text{ mmol h}^{-1} \text{ g}^{-1}$). The photocatalytic activity of the amorphous CNs synthesized in an open system in the temperature range 400–600 °C showed that the highest activity was achieved for the CN synthesized at a reaction temperature of 500 °C ($1080 \text{ mmol h}^{-1} \text{ g}^{-1}$); this activity corresponds to an approximately 50% enhancement compared to that of raw melon (see Table 1).

Table 1. Physicochemical properties and photocatalytic activity of different Pt/CN_x species for the hydrogen evolution reaction driven by visible light.

Catalyst	Surface area [m ² g ⁻¹]	C/N molar ratio	Hydrogen evolution rate [$\mu\text{mol h}^{-1} \text{ g}^{-1}$]	Quantum efficiency [%]
PTI/Li ⁺ Cl ⁻	37	0.68	864	0.60
Melon	18	0.67	722	0.50
aPTI _{500°C}	122	0.69	1080	0.75
aPTI_4AP _{16%}	60	0.82	4907	3.40

Although the above results show a moderate improvement of the photocatalytic activity of PTI-derived materials compared to melon-based ones, when PTI is doped with 4AP the increase in the photoactivity

of PTI is a function of the doping level and synthesis temperature. By increasing the temperature from 400 to 600 °C, an optimum photocatalytic activity was measured for the material synthesized at 550 °C (see the Supporting Information, Figure S13). When the content of 4AP was increased from 2 to 64%, the highest photocatalytic activity of $4907 \text{ mmol h}^{-1} \text{ g}^{-1}$ (3.4% quantum efficiency) was detected for 16% doped aPTI, synthesized at 550 °C (aPTI_4AP16%; Figure S14 in the Supporting Information and Table 1). In essence, the photocatalytic activity of PTI/Li⁺Cl⁻ can be enhanced by 5–6 times upon doping with 4AP in a simple one-pot reaction. 4AP doping of crystalline PTI/Li⁺Cl⁻ leads to no apparent photocatalytic activity. Also, as a control experiment, pure 4AP was shown to be photocatalytically inactive by itself and under ionothermal or thermal treatment. Water oxidation experiments in which O₂ evolution was measured, carried out in the presence of a Co₃O₄ co-catalyst, did not yield substantial amounts of oxygen, thus suggesting that either water oxidation is thermodynamically unfeasible or that the reaction conditions need to be further optimized.

A typical TEM micrograph shows that the surface morphology of doped aPTI is layered and platelet-like (Figure 2d and S11 in the Supporting Information). The crystallite size and

composition of the platinum nanoparticles deposited on the carbon nitride catalyst in situ were studied by TEM and EDX. The results reveal that the photoinduced reduction of the co-catalyst results in well-dispersed nanoparticles roughly 5 nm in diameter.

N₂ sorption measurements allow us to quantify the impact of the surface area (SA) of the catalysts on the photocatalytic activity. In Table 1, the measured specific Brunauer–Emmett–Teller (BET) SAs indicate a weak correlation between SA and activity, but the increased photoactivity in the doped species cannot be rationalized by an increased SA alone.

As seen in Figure 3, the aPTI_4AP16% photocatalyst yields an orange-brown suspension and its diffuse reflectance spectrum spans across the visible region. It is therefore instructive to examine the wavelength-specific hydrogen production to determine which wavelengths actively contribute to the H₂ evolution. In the wavelength dependence graph (Figure 4), the absorption is overlaid with the wavelength-specific hydrogen evolution. The hydrogen production rate falls off at 450–500 nm, thus indicating that the majority of photons contributing to the hydrogen production are at $\lambda < 500$ nm. It is suggested that the active absorption follows the band edge observed between 430 and 440 nm. This band is similar to that seen for the other PTI compounds although red-shifted by the 4AP doping. The broad absorption profile suggests the existence of intra band-gap electronic states at various energies, which could

arise from the incorporated 4AP (see the Supporting Information, Figure S4 and S5). However, as Figure 4 infers, not all electronic states – especially those associated with absorption at higher wavelengths – contribute to the hydrogen evolution but may rather act as traps

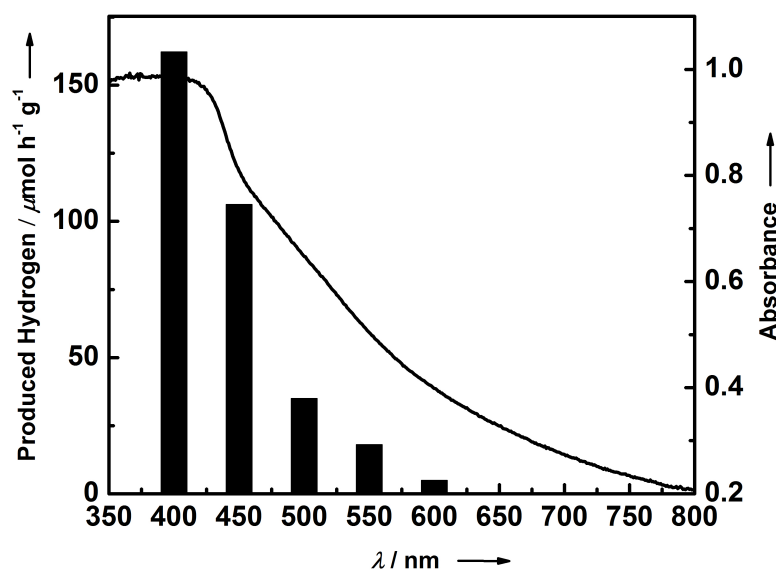


Figure 4. Overlay of UV-VIS spectrum and wavelength-specific hydrogen production (black bars) of aPTI_4AP_{16%} using 40 nm FWHM band-pass filters.

and quenching sites for excitons. We therefore envision that through active control of the number and position of defects in the material, photocatalysts with further enhanced activity can rationally be designed. Nevertheless, the increased visible-light activity up to approximately 500 nm in doped PTI results in a significant improvement over its undoped or crystalline counterparts and is a contributing factor to its high photoactivity.

In conclusion, we have reported a new family of 2D triazine-based carbon nitrides that shows substantial visiblelight-induced hydrogen production from water, and in this regard rivals the benchmark heptazine-derived photocatalysts. With external quantum efficiencies as high as 3.4%, the amorphous carbon- and oxygen-enriched poly(triazine imide) species not only outperform melon-type photocatalysts, but also crystalline PTI by 5 to 6 times. Consistent with previous results,^[13] we have demonstrated that a rather low level of structural definition and the introduction of defects up to a certain doping level (16% for 4-amino-2,6-dihydroxypyrimidine) tend to enhance the photoactivity of the catalysts.

We believe that the diverse range of available organic and inorganic dopants will allow the rational design of a broad set of triazine-based CN polymers with controlled functions, thus opening new avenues for the development of light-harvesting semiconductors. The easily adjustable structural and electronic properties of CN polymers render them particularly versatile for solar energy applications.

Bibliography

- [1] X. Chen, S. Shen, L. Guo, S. S. Mao, *Chem. Rev.* **2010**, *110*, 6503–6570.
- [2] H. Tong, S. Ouyang, Y. Bi, N. Umezawa, M. Oshikiri, J. Ye, *Adv. Mater.* **2012**, *24*, 229-251.
- [3] a) X. Wang, K. Maeda, A. Thomas, K. Takanabe, G. Xing, J. M. Carlsson, K. Domen, M. Antonietti, *Nat. Mater.* **2009**, *8*, 76-80; b) E. Kroke, M. Schwarz, E. Horath-Bordon, P. Kroll, B. Noll, A. D. Norman, *New J. Chem.* **2002**, *26*, 508-512.
- [4] a) Y. Wang, X. Wang, M. Antonietti, *Angew. Chem.* **2012**, *124*, 70 – 92; *Angew. Chem. Int. Ed.* **2012**, *51*, 68 – 89; b) Y. Zheng, J. Liu, J. Liang, M. Jaroniec, S. Z. Qiao, *Energy Environ. Sci.* **2012**, *5*, 6717 – 6731.
- [5] a) B. V. Lotsch, M. Döblinger, J. Sehnert, L. Seyfarth, J. Senker, O. Oeckler, W. Schnick, *Chem. Eur. J.* **2007**, *13*, 4969 – 4980; b) L. Seyfarth, J. Seyfarth, B. V. Lotsch, W. Schnick, J. Senker, *Phys. Chem. Chem. Phys.* **2010**, *12*, 2227 – 2237; c) B. Jürgens, E. Irran, J. Senker, P. Kroll, H. Müller, W. Schnick, *J. Am. Chem. Soc.* **2003**, *125*, 10288 – 10300.
- [6] a) D. Mitoraj, H. Kisch, *Chem. Eur. J.* **2010**, *16*, 261 – 269; b) E. Kroke, M. Schwarz, *Coord. Chem. Rev.* **2004**, *248*, 493 – 532; c) G. Goglio, D. Foy, G. Demazeau, *Mater. Sci. Eng. R* **2008**, *58*, 195 – 227; d) X. Li, J. Zhang, L. Shen, Y. Ma, W. Lei, Q. Cui, G. Zou, *Appl. Phys. A* **2009**, *94*, 387 – 392.
- [7] a) J. Zhang, X. Chen, K. Takanabe, K. Maeda, K. Domen, J. D. Epping, X. Fu, M. Antonietti, X. Wang, *Angew. Chem.* **2010**, *122*, 451 – 454; *Angew. Chem. Int. Ed.* **2010**, *49*, 441 – 444; b) Q. Li, B. Yue, H. Iwai, T. Kako, J. Ye, *J. Phys. Chem. C* **2010**, *114*, 4100 – 4105; c) Y. Zhang, A. Thomas, M. Antonietti, X. Wang, *J. Am. Chem. Soc.* **2009**, *131*, 50 – 51; d) H. Yan, Y. Huang, *Chem. Commun.* **2011**, *47*, 4168 – 4170.
- [8] E. Wirnhier, M. Döblinger, D. Gunzelmann, J. Senker, B. V. Lotsch, W. Schnick, *Chem. Eur. J.* **2011**, *17*, 3213 – 3221.
- [9] M. J. Bojdys, J.-O. Müller, M. Antonietti, A. Thomas, *Chem. Eur. J.* **2008**, *14*, 8177 – 8182.

- [10] a) B. V. Lotsch, W. Schnick, *Chem. Mater.* **2006**, *18*, 1891 – 1900; b) A. I. Finkel'shtein, *Opt. Spektrosk.* **1959**, *6*, 33; c) M. Takimoto, *Kogyo Kagaku Zasshi* **1961**, *64*, 1452 – 1454; d) M. Takimoto, *Nippon Kagaku Zasshi* **1964**, *85*, 159 – 168; e) D. A. Long, *J. Raman Spectrosc.* **2004**, *35*, 905 – 905; f) B. V. Lotsch, W. Schnick, *Chem. Eur. J.* **2007**, *13*, 4956 – 4968.
- [11] a) P. Niu, G. Liu, H.-M. Cheng, *J. Phys. Chem. C* **2012**, *116*, 11013 – 11018; b) A. Thomas, A. Fischer, F. Goettmann, M. Antonietti, J.-O. Müller, R. Schlögl, J. M. Carlsson, *J. Mater. Chem.* **2008**, *18*, 4893 – 4908; c) A. V. Semencha, L. N. Blinov, *Glass Phys. Chem.* **2010**, *36*, 199 – 208; d) X. Q. Gong, A. Selloni, M. Batzill, U. Diebold, *Nat. Mater.* **2006**, *5*, 665 – 670; e) M. K. Nowotny, L. R. Sheppard, T. Bak, J. Nowotny, *J. Phys. Chem. C* **2008**, *112*, 5275 – 5300.
- [12] a) X. Wu, K. W. Zilm, *J. Magn. Reson. Ser. A* **1993**, *102*, 205 – 213; b) C. Gervais, F. Babonneau, J. Maquet, C. Bonhomme, D. Massiot, E. Framery, M. Vaultier, *Magn. Reson. Chem.* **1998**, *36*, 407 – 414.
- [13] a) X. Chen, L. Liu, P. Y. Yu, S. S. Mao, *Science* **2011**, *331*, 746 – 750; b) M. Alvaro, E. Carbonell, V. Fornés, H. García, *ChemPhysChem* **2006**, *7*, 200 – 205; c) G. Zhang, J. Zhang, M. Zhang, X. Wang, *J. Mater. Chem.* **2012**, *22*, 8083 – 8091.
- [14] While this paper was in review, complementary data on the photocatalytic water splitting of crystalline PTI were published: Y. Ham, K. Maeda, D. Cha, K. Takanabe, K. Domen, *Chem. Asian J.* **2013**, *8*, 218–224.

5. Phosphorus-doped Carbon Nitride Precursors

Both methods described in the last chapter (XAS/XES and EELS) offer the possibility of a very exact determination of the band gap, especially in comparison with the wide-spread standard method diffuse reflectance spectroscopy. Moreover, with EELS being a very local method, the band gaps of multiphase compounds can be measured simultaneously and distinguished contrary to bulk methods averaging over the whole sample. Using the example of PTI/LiCl, this combination of methods could be established, yielding a band gap of 2.2 eV, thus being lowered in comparison with melon (2.7 eV) by “doping” with LiCl. Another approach to lower the band gap and to shift the absorption more into the visible region (and to enhance the effectiveness for possible photocatalytic applications) is the replacement of carbon atoms by phosphorus atoms, to be interpreted as n-doping.

Despite several attempts, no crystalline phosphorus-doped carbon nitride network was reported so far, enabling a direct comparison of structure and properties. In this chapter, synthesis and crystal structures of a number of phosphorus-doped carbon nitride precursors (alkali biuretooxophosphates and the new class of *N,N'*-bis(aminocarbonyl)-phosphorodiamidates) are presented. Furthermore, the suitability of these precursors for the synthesis of crystalline phosphorus-doped carbon nitride networks is investigated by examining their thermal stability and their behavior applying high-pressure high-temperature conditions.

5.1 Biuretooxophosphates

5.1.1 Lithium, Potassium, Rubidium and Cesium Biuretooxophosphate

A Systematic Approach to Alkali Biuretooxophosphates

Eva Wirnhier and Wolfgang Schnick

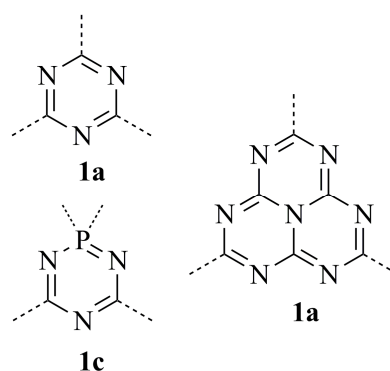
published in: *Eur. J. Inorg. Chem.* **2012**, 1840-1847. DOI: 10.1002/ejic.201101317

Keywords: Structure elucidation; Biuretooxophosphates; Photoluminescence spectroscopy; Alkali metals

Abstract: Biuretooxophosphates represent a link between carbon nitride and phosphorus (oxo)nitride precursor chemistry being closely related to cyanurates and trimetaphosphimates. The group of alkali biuretooxophosphates has been complemented by the synthesis of four salts $M[\text{PO}_2(\text{NH})_3(\text{CO})_2] \cdot x\text{H}_2\text{O}$ in which $M = \text{Li, K, Rb, and Cs}$ ($x = 1, 0, 0.5, 0$, respectively). The structures were solved by single-crystal X-ray diffraction and compared with the corresponding ammonium and sodium salts. For all of the salts, the 1-phospha-2,4,6-*s*-triazine ring exhibits a nearly planar conformation with the phosphorus atom being slightly deflected. In the sequence Li to Cs, the crystal structures show a significant change in orientation leading from a parallel to a perpendicular arrangement of the rings, the latter being bridged by N–H \cdots O bonds. The thermal behavior of the biuretooxophosphates was examined by means of temperature-dependent powder X-ray diffraction measurements and combined thermogravimetric analysis (TGA) and differential thermal analysis (DTA). Moreover, the FTIR and photoluminescence spectra of the salts are discussed.

5.1.1.1 Introduction

Graphite-type carbon nitride networks have recently gained significant interest regarding their exceptional chemical stability and their manifold properties. Among others, the ability to act as heterogeneous metal-free catalyst for CO₂ reduction and water splitting as well as the photovoltaic effect have been shown for melon,^[1–5] the most prominent representative of this class of compounds. However, with an optical band gap of approximately 2.7 eV, resulting in absorption only of blue light up to 450 nm, pure melon is not efficient enough for solar-energy conversion for application in photovoltaic devices.^[3,5,6] Several attempts have been made to modify the electronic structure of graphite-like carbon nitrides including chemical doping to alter the band gap.^[5,7–11] In particular, the replacement of carbon atoms by phosphorus, interpreted in the literature as n-doping, seems to be a promising strategy to lower the band gap and shift the absorption more into the visible region, therefore enhancing the performance of such organic semiconductors. Previous attempts based on the copolymerization of dicyandiamide and 1-butyl-3-methylimidazolium hexafluorophosphate indeed showed a shift in the band gap to lower energies accompanied by a change in color from yellow to brown.^[5] However, no well-defined product was obtained and the different possible doping sites led to a UV/Vis absorption spectrum that was hard to interpret.



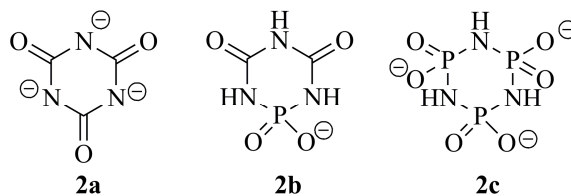
Scheme 1. The *s*-triazine (**1a**), tri-*s*-triazine (**1b**), and 1-phospha-2,4,6-*s*-triazine core (**1c**).

With both *s*-triazine (**1a**) and tri-*s*-triazine (**1b**) cores (the building units of carbon nitride networks) being very stable, the targeted partial exchange of C by P during the condensation process seems to be rather improbable. A different approach to obtain well-defined phosphorus carbon nitride compounds is the use of suitable precursors containing preorganized C-N-P motifs. Recently, *Kroke et al.* reported on several *s*-heptazine-based iminophosphoranes C₆N₇(N=PR₃)₃ (R = methyl, ethyl, etc.), which can be seen as exocyclic doped carbon nitride precursors.^[12]

Exchanging one carbon ring atom in *s*-triazine-based compounds by phosphorus may lead to precursor molecules with a defined atomic ratio C/N/P = 2:3:1 (i.e., endocyclic doping). Such

compounds with this 1-phospha-2,4,6-*s*-triazine (**1c**) core were already synthesized in 1962 (Scheme 1).^[13]

Biuretooxophosphates establish a link between precursor compounds of carbon nitride and phosphorus (oxo)nitride chemistry or on a molecular level between cyanurates (**2a**) and trimetaphosphimates (**2c**) (Scheme 2), the salts of the latter



Scheme 2. The cyanurate anion (**2a**), biuretooxophosphate anion (**2b**), and trimetaphosphimate anion (**2c**).

compound being systematically investigated recently.^[14–19]

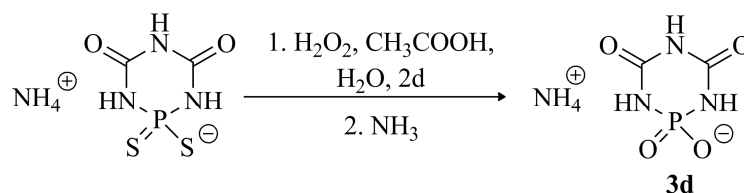
The first biuretooxophosphate, namely $\text{NH}_4[\text{PO}_2(\text{NH})_3(\text{CO})_2]$ (**3d**), was described in 1986 by Neels.^[20,21] We are now targeting a thorough characterization of biuretooxophosphates as possible precursors for the synthesis of new C/P/O/N-containing compounds.

In this contribution we report on a new approach towards the preparation of biuretooxophosphates in crystalline form. We have complemented the group of alkali biuretooxophosphates and compare their structural and spectroscopic properties as well as the thermal behavior of these air-stable and water-soluble salts.

5.1.1.2 Results and Discussion

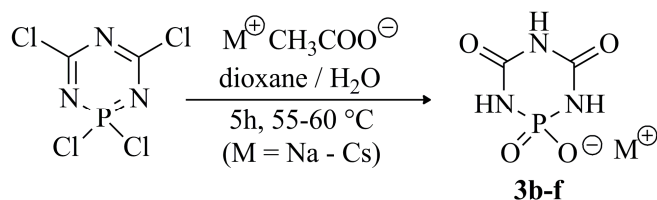
NH_4^+ -biuretooxophosphate

(**3d**) was first synthesized by oxidation of NH_4^+ -biuretodithiophosphate (Scheme 3), which was obtained as a byproduct of the synthesis of COS from P_4S_{10} with urea.^[20,21]



Scheme 3. Previous synthesis of **3d** by oxidation of NH_4^+ -biuretodithiophosphate.^[20]

The corresponding sodium salt (**3b**) was synthesized by ion exchange in aqueous solution.^[22]



Scheme 4. New synthesis route to alkali biuretooxophosphates by the controlled hydrolysis of 1,1,3,5-tetrachloro-1-phospha-2,4,6-*s*-triazine.

(according to the synthesis of the alkali trimetaphosphimates, Scheme 4).^[24,25] After evaporation of the solvents, large colorless blocklike crystals of Li[PO₂(NH)₃(CO)₂]·H₂O (**3a**), Na[PO₂(NH)₃(CO)₂] (**3b**), K[PO₂(NH)₃(CO)₂] (**3c**), NH₄[PO₂(NH)₃(CO)₂] (**3d**), Rb[PO₂(NH)₃(CO)₂]·0.5H₂O (**3e**), and Cs[PO₂(NH)₃(CO)₂] (**3f**) could be isolated.

Crystal structures

All alkali biuretooxophosphates crystallize in space group $P2_1/c$ except for the rubidium salt (**3e**), which crystallizes in the monoclinic space group Cc forming an inversion twin. Crystallographic data and details of the structure refinements for **3a**, **3c**, **3e**, and **3f** are summarized in Table 6. For detailed investigation of the crystal structure of the remaining salts, single-crystal X-ray diffraction of **3b**^[22] and **3d**^[20] was reproduced. The comparison of simulated and experimental powder X-ray diffraction patterns of the bulk phase is shown in

Table 1. Angles of torsion for the alkali biuretooxophosphates **3a–3f**.

3a ^[a]	3b ^[b]	3c ^[a]	3d ^[a]	3e (Rb1) ^[a]	3e (Rb2) ^[a]	3f ^[c]
5.87	13.58	-6.03	-6.28	8.33	13.06	-8.97
-6.18	-11.08	4.53	4.69	-3.77	-11.62	8.81
-13.90	-1.34	13.98	9.73	-14.89	0.55	-5.69
26.16	7.65	-23.51	-17.22	22.28	5.85	2.82
-26.50	-4.89	21.92	15.71	-17.85	-4.27	-2.89
14.57	-3.81	-10.57	-6.94	5.84	-3.55	5.96

[a] ideal sign sequence for half-chair conformation: $x/-x/-x/x/-x/x$.

[b] ideal sign sequence for twist conformation: $x/-x/-x/x/-x/-x$.

[c] ideal sign sequence for chair conformation $x/-x/x/-x/x/-x$.

We have developed a novel approach to synthesize alkali biuretooxophosphates [except the lithium salt (**3a**), which was obtained by ion exchange] in crystalline form by the controlled hydrolysis of 1,1,3,5-tetrachloro-1-phospha-2,4,6-*s*-triazine^[23] in the presence of the corresponding acetate

Figure S1 (Supporting Information). Besides phase purity, the diffractograms show that all reflections could be indexed with the known cell parameters and their observed intensities were in very good agreement with the calculated diffraction patterns based on single-crystal diffraction data.

Table 2. Puckering parameters for the alkali biuretooxophosphates **3a** – **3f**.

	3a ^[a]	3b ^[b]	3c ^[a]	3d ^[a]	3e (Rb1) ^[a]	3e (Rb2) ^[a]	3f ^[a]
q_2	0.239(2)	0.123(1)	0.208(1)	0.159(1)	0.645(10)	1.169(22)	0.032(2)
q_3	0.127(2)	-0.007(1)	-0.111(1)	-0.074(1)	-1.743(9)	2.968(38)	0.047(2)
$\Phi / ^\circ$	0.7(4)	-11.6(6)	175.0(5)	174.9(4)	-76.6(6)	-111.7(4)	178.5(47)
Q_T	0.270(1)	0.123(1)	0.236(1)	0.175(1)	1.858(8)	3.190(42)	0.057(2)
$\theta / ^\circ$	61.9(4)	93.4(6)	118.1(4)	114.9(4)	159.7(3)	21.5(2)	33.9(18)

[a] ideal puckering parameters for half-chair conformation: $q_2 = Q_T \sin\theta$, $q_3 = Q_T \cos\theta$, $Q_T = (q_2^2 + q_3^2)^{1/2}$.

[b] ideal puckering parameters for twist conformation: $q_2 \neq 0$, $q_3 = 0$, $Q_T = q_2$, $\theta = 90^\circ$.

Whereas the potassium salt is isotopic with the ammonium salt, the other alkali biuretooxophosphates exhibit different crystal structures. In contrast to most trimetaphosphimates that adopt almost a regular chair, twist, or boat conformation,^[15,19,26–29] the biuretooxophosphates are nearly planar. Evaluation of the torsion angles^[30] (Table 1) as well

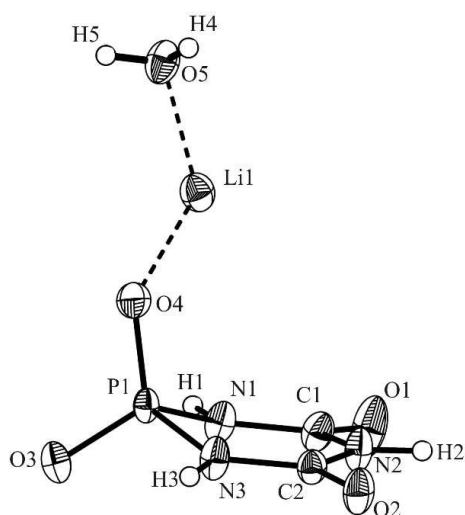


Figure 1. View of the half-chair ring conformation of **3a** showing 50% probability displacement ellipsoids. H atoms are drawn as

as the puckering parameters (amplitude and phase coordinates that describe the geometry of the ring puckering relative to the plane)^[31] (Table 2) suggest a weak pronounced twist and chair or half-chair conformation for **3b** and **3f**, respectively, while the other biuretooxophosphates exhibit a half-chair conformation due to the fact that the phosphorus atom maintains its preferred (distorted) tetrahedral coordination, whereas all C/N-ring atoms show more or less the typical coplanar alignment for *s*-triazine cores (Figure 1). For **3e**, a second type of half-chair conformation, with the nitrogen atom instead of the phosphorus atom deflected, appears.

The bond lengths P–O and P–N (148–150 and 166–169 pm, respectively) and the angles O–P–O (115–118°) and O–P–N (108–112°) are in the typical range of trimetaphosphimates, whereas the angles N–P–N (98–99°) are smaller due to the biuretooxophosphate anion being more planar than the trimetaphosphimate anion.^[26–28] The bond lengths C–O and C–N (120–124 and 133–139 pm, respectively) are comparable to the distances observed in cyanurates and cyamelurates with the C–N(–P) bonds being 2–3 pm shorter than the C–N(–C) bonds, but both in the range of C–N single bonds. For the angles, the N–C–O (118–124°) and N–C–N

angles ($115\text{--}119^\circ$) are also in typical ranges relative to cyanurates and cyamelurates, whereas the distortion of the almost planar ring by the phosphorus atom becomes more apparent by the appearance of larger C–N–C angles ($127\text{--}129^\circ$).^[32–36]

A systematic change in the relative orientation of the anionic rings is observed with increasing cation size. Whereas the rings of **3a** and **3b** show a nearly parallel arrangement without building a hydrogen-bonding network (Figure 2 and Figure 3), a slight zig-zag orientation for the rings appears

for **3c** and **3d** (Figure 3). N–H \cdots O (N \cdots O 278–295 pm) bonds are bridging the rings, forming interconnected zig-zag strands. One half of the rings in **3e** linked by N–H \cdots O bonds (N \cdots O 281 pm) shows a more pronounced zig-zag orientation, whereas the other half is aligned vertically, also connected by N–H \cdots O bonds (N \cdots O 279–288 pm) (Figure 3e). A 3D network is formed by the connections of both types of rings by two further N–H \cdots O bonds (N \cdots O 281–

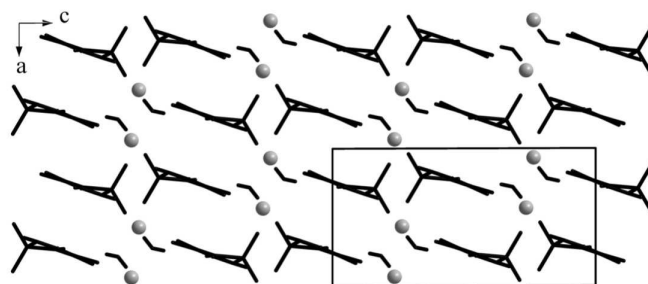


Figure 2. Crystal structure of **3a**.

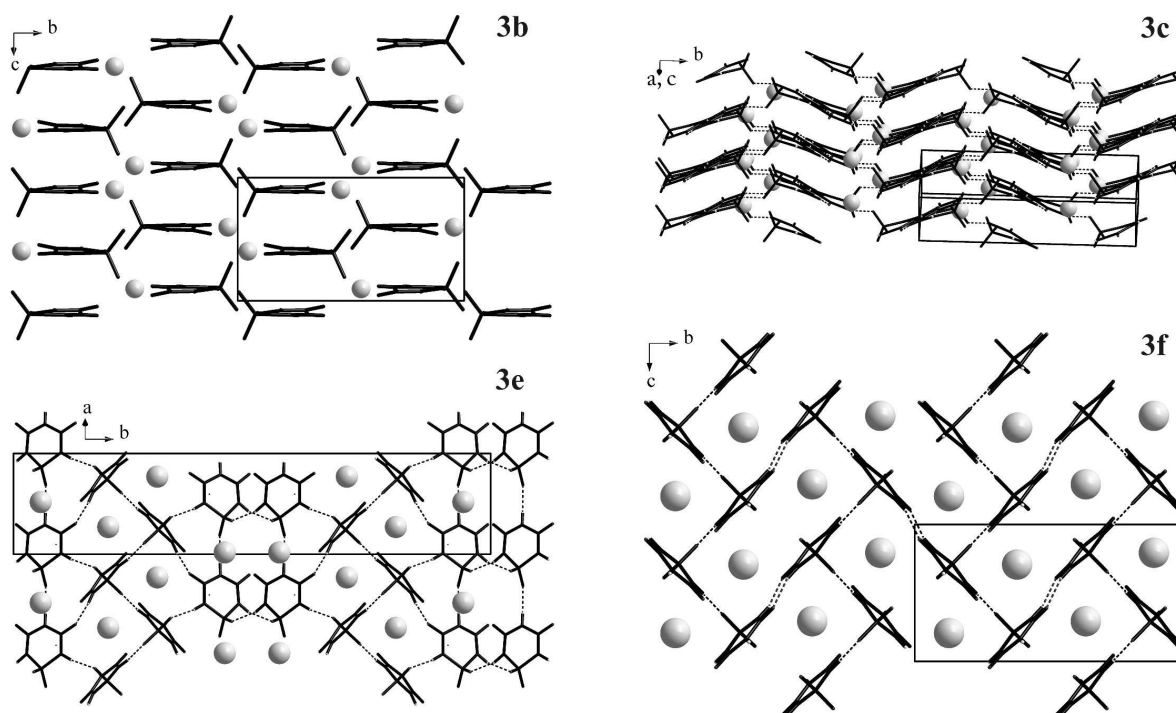


Figure 3. Crystal structures of **3b**, **3c**, **3e**, and **3f**.

284 pm). For **3f**, the vertically aligned rings form a wire-mesh fence-like network by N–H···O bonds (N···O 273–285 pm) (Figure 3).

The coordination number of the alkali ions increases with the ionic radii of the cations, thereby causing an increasing connectivity of the coordination polyhedra. In **3a**, the lithium ions exhibit a coordination number of four, which results in

isolated, slightly distorted tetrahedrons (103–120°). The sixfold and (5+1)-fold coordination of the Na⁺, K⁺, and NH₄⁺ ions configuring edge-sharing distorted octahedrons leads to 1D twisted strands along *a* (**3b**) and *c* (**3c**, **3d**), respectively. The rubidium salt exhibits two distinct Rb sites, once sevenfold coordinated (Rb1), showing edge-shared strands along *a* and once sixfold coordinated (Rb2), building corner-shared strands in the *a,c* plane. For **3f**, the only 2D motif arises by edge-sharing heptagons in the *b,c* plane. In the case of **3a** and **3e**, a solvent water molecule is incorporated to complete the coordination sphere, which is otherwise built up from both oxygen species of the PO₂(NH)₃(CO)₂ ring. The rings act as monodentate and partially bridging (μ^2) ligands for the corresponding cations with an

increasing number of ligand functionalities with increasing cationic size (Table 3).

The distances M–O are comparable with those of the alkali trimetaphosphates and cyanmelurates and are in accordance with the sums of the ionic radii [Li: 192–197 pm; Na: 230–252 pm; NH₄: 275–291(369) pm; K:

Table 3. Number and type of ligand functionalities of the PO₂(NH)₃(CO)₂-ring.

	3a	3b	3c/d	3e	3f
O1 (CO)	---	μ^1	μ^1	μ^1 / μ^2	μ^2
O2 (CO)	μ^1	μ^2	μ^1	μ^2 / μ^2	μ^2
O3 (PO ₂)	μ^1	μ^1	μ^2	μ^1 / μ^2	μ^1
O4 (PO ₂)	μ^1	μ^2	μ^2	μ^1 / μ^1	μ^2
Σ	3	6	6	5 / 7	7

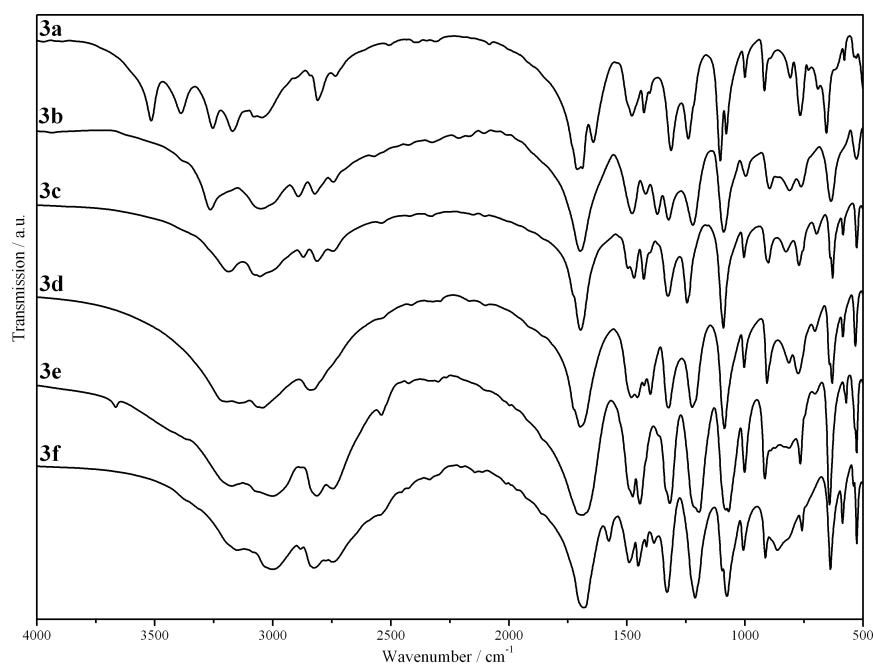


Figure 4. FTIR spectra of the alkali biuretooxophosphates **3a–f**.

260–307 pm; Rb: 283–315 pm; Cs: 308–336 pm].^[32–36]

FTIR Spectroscopy

The FTIR spectra of the alkali biuretooxophosphates are represented in Figure 4. They exhibit features of both alkali trimetaphosphimates and alkali cyanurates. Accordingly, the assignment of the bands (Table 4) was accomplished by comparison with both compound classes.^[14,37] For all biuretooxophosphates, strong absorption in the N–H stretching region (3300–3000 cm⁻¹) occurs. The broadness of the signals may be due to the participation of the NH groups in hydrogen

bonding, also resulting in weak (for the smaller cations) and strong (for the bigger cations) bands between 3050 and 2730 cm⁻¹. These effects are in accordance with the results from the crystal structure analysis, which show intermolecular hydrogen bonds only between the rings of the salts of the heavier alkali elements. The bending and wagging modes of the NH groups are also assigned in Table 4. As for the cyanurates, strong absorption due to C=O and C–N stretching vibrations occurs around 1700 cm⁻¹ and between

Table 4. Vibrational frequencies (cm⁻¹) observed in the FTIR spectra of the alkali biuretooxophosphates and their assignment.

3a	3b	3c	3d	3e	3f	Assignment
3515 s				3472 w		v(H ₂ O)
3389 s				3410 w		v(H ₂ O)
3254 s	3266 s					v(NH)
3171 s		3188 m		3175 m	3156 m	v(NH)
			3143 vs			v(NH ₄ ⁺)
3047 s	3053 m	3054 m	3044 vs	3068 vs	3045 m	v(NH)
	2891 m	2871 m				v(N–H...O)
2810 m	2825 m	2813 m	2841 s	2814 vs	2826 s	v(N–H...O)
2735 w	2745 w	2746 m		2745 s	2748 s	v(N–H...O)
1711 vs	1699 vs	1696 vs	1698 vs	1694 vs	1684 vs	v(C=O)
1643 s		1496 m			1491 s	v(C–N)
1479 m	1477 m	1470 m	1481 s	1476 vs	1452 s	v(C–N)
			1456 s			v(NH ₄ ⁺)
1428 m	1425 m	1429 m	1428 s	1445 vs	1417 m	v(C–N)
			1401 s			v(NH ₄ ⁺)
	1372 s				1386 m	δ(NH)
1313 vs	1326 s	1326 s	1323 vs	1319 vs	1330 vs	δ(NH)
1240 s	1216 s	1245 s	1224 vs	1194 vs	1211 vs	v _{as} (PO ₂)/ δ(NH)
1105 vs						v _s (PO ₂)
1079 s	1087 s	1091 vs	1087 vs	1082 vs	1097 s	v _s (PO ₂)
				1069 vs	1076 vs	v _s (PO ₂)
1000 w	1001 w	1005 m	1004 m	1002 s	1007 m	v _{as} (P–NH)
918 m	899 m	901 m	907 s	916 s	914 s	δ(C–N)
808 w	810 w	827 m	814 m	814 m	815 m	v _s (P–NH)
766 m	757 w	772 m	775 m	766 s	758 m	ω(NH)
		697 w		703 vw		ω(NH)
655 s	636 m	629 m	631 s	642 vs	638 s	δ(PO ₂)
579 vw	577vw	585 w	585 w	572 w	587 w	v(MO)
529 vw	530 w	527 m	532 w	527 m	527 m	δ(C=O)
481 s	467 w	470 m	468 s	461 s	467 s	δ(NCO)
416 w	417 vw	426 w	432 w	407 s	422 m	δ(NCO)

1500 and 1420 cm^{-1} , respectively. The corresponding bending modes in the biuretooxophosphates are observed around 900 (C–N) and 503 cm^{-1} (C=O), respectively. Very strong absorption bands are also visible for the symmetric and asymmetric PO_2 stretching vibrations (1100–1070 and 1250–1200 cm^{-1}). In accordance with trimetaphosphimates, the symmetric and asymmetric P–N stretching vibrations appear between 1000 and 800 cm^{-1} .

Photoluminescence Spectroscopy

The excitation and emission spectra of the alkali biuretooxophosphates in aqueous solution ($c = 2 \times 10^{-3} \text{ mol L}^{-1}$) are displayed in Figure S2 (Supporting Information). Excitation and emission maxima are summarized in Table 5.

Table 5. Excitation and emission maxima of the alkali biuretooxophosphates in solution (solvent = H_2O , $c = 2 \cdot 10^{-3} \text{ mol}\cdot\text{L}^{-1}$).

substance	3a	3b	3c	3d	3e	3f	4a	4b
$\lambda_{\text{ex,max}}$ [nm]	264/344	269/333	260/329	253/290/327	267/354	252/324	253/288/326	289/334
$\lambda_{\text{em,max}}$ [nm]	390	374	371	369	403	365	379	366

The excitation spectra of the alkali biuretooxophosphates – recorded at the wavelength of the emission maximum – show two maxima in the UV region (252–269 and 324–354 nm, respectively) with the second signal being less intense. Emission occurs close to the UV/Vis transition (365–403 nm). For comparison, spectra of the sodium salts of the cyanurates and trimetaphosphimates [$\text{NaH}_2\text{C}_3\text{N}_3\text{O}_3\cdot\text{H}_2\text{O}$ (**4a**) and $\text{Na}_3(\text{PO}_2\text{NH})_3\cdot\text{H}_2\text{O}$ (**4b**)] were measured. Excitation and emission maxima of these two compounds (Table 5) are in the same range as those for the alkali biuretooxophosphates, with the maxima of the sodium biuretooxophosphate being located in between. Further comparison with the excitation and emission maxima of tri-*s*-triazine-based compounds like melem (2,5,8-triamino-*s*-heptazine; $\lambda_{\text{ex,max}} = 288 \text{ nm}$, $\lambda_{\text{em,max}} = 366 \text{ nm}$),^[38] 2,5,8-triazido-*s*-heptazine ($\lambda_{\text{em,max}} = 430 \text{ nm}$),^[39] and 2,5,8-trichloro-*s*-heptazine ($\lambda_{\text{ex,max}} = 310 \text{ nm}$, $\lambda_{\text{em,max}} = 468 \text{ nm}$)^[40] provides an indication that the ring substituents have more influence on the luminescent properties than the cations, thus changing the electronic properties of the ring systems. Showing a significant shift compared to the other tri-*s*-triazine based compounds, the excitation and emission maxima of melem are therefore closer to the biuretooxophosphates due to similar electron-donating strengths of NH_2 and OH .

Thermal Analysis

The thermal behavior of the alkali biuretooxophosphates was examined by combined thermogravimetric analysis (TGA) and differential thermal analysis (DTA) measurements (Figure S3 in the Supporting Information) and temperature-dependent powder X-ray

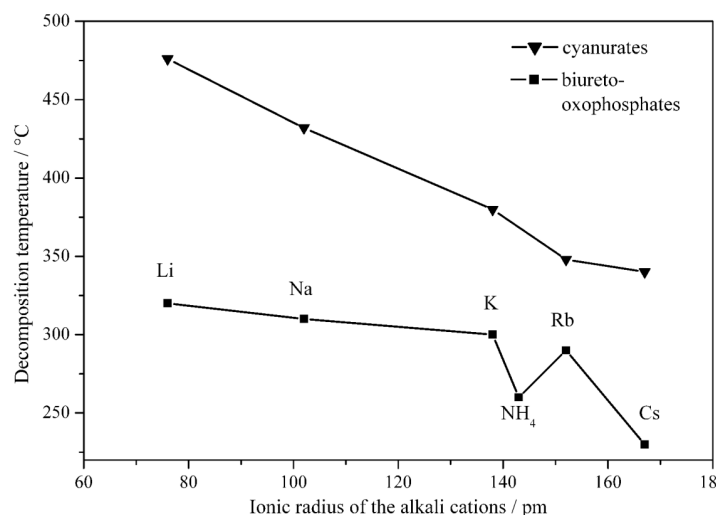


Figure 5. Decomposition temperatures of alkali cyanurates and alkali biuretooxophosphates (**3a–f**).^[37]

diffraction analysis. For the monohydrated lithium salt and the semihydrated rubidium salt the release of crystal water is visible at 190 °C (mass loss observed: 10.2 %, calculated: 9.5 %) and 170 °C (mass loss observed: 5.0 %, calculated: 3.5 %), respectively. The resulting dehydrated lithium biuretooxophosphate is stable up to 320 °C; the thermal stability of the other salts decreases with increasing atomic mass of the alkali cation (Figure 5); an analogous observation has been reported for the cyanurates.^[37]

The decomposition of the alkali biuretooxophosphates is accompanied by a continuous mass loss and endothermic signals, which presumably indicate the release of gaseous byproducts like CO₂, HNCO, and NH₃. The formation of the corresponding cyclic and linear metaphosphates (MPO₃)_x as intermediates can be observed by temperature-dependent powder X-ray diffraction patterns, accompanied by an endothermic signal in the DTA curves of the less heavier cations (**3a**: 354 °C; **3b**: 357 °C; **3c**: 329 °C; **3e**: 296 °C).

4.1.1.3 Conclusion

In this contribution, we have presented a novel approach to the alkali biuretooxophosphates $M[\text{PO}_2(\text{NH})_3(\text{CO})_2] \cdot x\text{H}_2\text{O}$ (in which $M = \text{Li, Na, K, NH}_4, \text{Rb, Cs}$ and $x = 1, 0, 0, 0, 0.5, 0$, respectively) with detailed investigation of crystal structures, FTIR and PL spectroscopic properties, as well as the thermal behavior. From a structural point of view, the biuretooxophosphates can be interpreted as intermediates between precursor compounds in carbon nitride and phosphorus (oxo)nitride chemistry, the cyanurates and the trimetaphosphimates. Temperature-dependent powder X-ray diffraction analysis as well as combined DTA/TG measurements showed the stability of the 1-phospha-2,4,6-*s*-triazine ring up to temperatures of at least 200 °C. The decomposition of the ring at higher temperatures is accompanied by the formation of the corresponding metaphosphates $(\text{MPO}_3)_x$, therefore indicating a breakup of the ring next to the phosphorus atom and to a release of the remaining ring in the form of gaseous byproducts like CO_2 , HNCO , and NH_3 . To use the biuretooxophosphates as precursors for the synthesis of crystalline C(O)NP networks it is essential to keep the preorganized C-N-P motif intact or at least to prevent the disappearance of the CN parts of the ring. According to Le Chatelier's principle, future work will focus on pyrolysis of the biuretooxophosphates under elevated pressure (for example, in an autoclave or by using a high-pressure apparatus) to avoid the complete decomposition of the preorganized C-N-P motif and to enable the synthesis of well-defined phosphorus-doped carbon nitride networks.

4.1.1.4 Experimental Section

Syntheses

1,1,3,5-Tetrachloro-1-phospha-2,4,6-*s*-triazine was synthesized according to the literature^[23] by reacting sodium dicyanamide (17.6 g, 0.20 mol, Fluka, 96 %) with phosphorus pentachloride (41.6 g, 0.20 mol, Fluka, 98 %) in dichloroethane (600 mL; reflux, 12–14 h). The byproduct NaCl was removed by filtration and the filtrate was evaporated to a concentrated solution of 200 mL. At 4 °C the product was obtained as large colorless crystals.

Table 6. Crystallographic data and details of the structure refinement for **3a**, **3c**, **3e** and **3f**.

	3a	3c	3e	3f
Formula	Li[PO ₂ (NH) ₃ (CO) ₂] \cdot H ₂ O	K[PO ₂ (NH) ₃ (CO) ₂]	Rb[PO ₂ (NH) ₃ (CO) ₂] \cdot 0.5H ₂ O	Cs[PO ₂ (NH) ₃ (CO) ₂]
Molar mass [g mol ⁻¹]	189.00	203.14	258.51	296.95
Crystal system	monoclinic	monoclinic	monoclinic	monoclinic
Space group	<i>P</i> 2 ₁ / <i>c</i> (no. 14)	<i>P</i> 2 ₁ / <i>c</i> (no. 14)	<i>Cc</i> (no. 9)	<i>P</i> 2 ₁ / <i>c</i> (no. 14)
<i>a</i> [pm]	721.76(14)	585.42(12)	926.55(19)	679.16(14)
<i>b</i> [pm]	683.90(14)	1756.6(4)	3255.3(7)	1486.5(3)
<i>c</i> [pm]	1551.5(4)	691.70(14)	670.34(13)	745.37(15)
β [°]	117.53(2)	109.65(3)	132.07(3)	93.08(3)
<i>V</i> [10 ⁶ pm ³]	679.1(3)	669.9(2)	1500.9(9)	751.4(3)
<i>Z</i>	4	4	8	4
Calculated density [g \cdot cm ⁻³]	1.849	2.014	2.279	2.625
Crystal size [mm ³]	0.12 x 0.10 x 0.09	0.31 x 0.16 x 0.12	0.15 x 0.12 x 0.11	0.12 x 0.10 x 0.06
Absorption coefficient [mm ⁻¹]	0.389	0.999	6.791	5.112
F(000)	384	408	992	552
Absorption correction	none	none	multi-scan	multi-scan
Min. / max. transmission			0.2704 / 0.3730	0.3820 / 0.6644
Diffraction range [°]	3.13 $\leq \theta \leq$ 27.49	3.34 $\leq \theta \leq$ 27.42	3.03 $\leq \theta \leq$ 27.49	3.30 $\leq \theta \leq$ 27.49
Index range	-9 $\leq h \leq$ 9 -8 $\leq k \leq$ 8 -20 $\leq l \leq$ 20	-7 $\leq h \leq$ 7 -22 $\leq k \leq$ 22 -8 $\leq l \leq$ 8	-12 $\leq h \leq$ 12 -42 $\leq k \leq$ 42 -8 $\leq l \leq$ 8	-8 $\leq h \leq$ 8 -19 $\leq k \leq$ 19 -9 $\leq l \leq$ 8
Parameters / restraints	129 / 5	112 / 3	228 / 8	112 / 3
Total reflections	5357	5661	6178	12375
Independent reflections	1548	1531	3258	1727
Observed reflections	1364	1369	2820	1573
Min./max. resid. electron density [e ⁻ 10 ⁻⁶ pm ⁻³]	-0.395 / 0.260	-0.409 / 0.326	-1.159 / 1.161	-1.412 / 0.473
GooF	1.045	1.076	1.035	1.190
Final R indices [<i>I</i> > 2 σ (<i>I</i>)]	<i>R</i> 1 = 0.0279, <i>wR</i> 2 = 0.0745 ^[a]	<i>R</i> 1 = 0.0269, <i>wR</i> 2 = 0.0702 ^[b]	<i>R</i> 1 = 0.0581, <i>wR</i> 2 = 0.1429 ^[c]	<i>R</i> 1 = 0.0211, <i>wR</i> 2 = 0.0539 ^[d]
Final R indices (all data)	<i>R</i> 1 = 0.0333, <i>wR</i> 2 = 0.0783 ^[a]	<i>R</i> 1 = 0.0323, <i>wR</i> 2 = 0.0740 ^[b]	<i>R</i> 1 = 0.0668, <i>wR</i> 2 = 0.1471 ^[c]	<i>R</i> 1 = 0.0239, <i>wR</i> 2 = 0.0558 ^[d]

[a] $w = [\sigma^2(F_0^2) + (0.0385P)^2 + 0.0388P]^{-1}$, [b] $w = [\sigma^2(F_0^2) + (0.0375P)^2 + 0.3991P]^{-1}$, [c] $w = [\sigma^2(F_0^2) + (0.0997P)^2 + 0.0000P]^{-1}$, [d] $w = [\sigma^2(F_0^2) + (0.0286P)^2 + 0.5402P]^{-1}$, for all with $P = (F_0^2 + 2 F_c^2)/3$.

According to the synthesis of the trimetaphosphimates M₃[PO₂NH]₃ (M⁺ = Na⁺, K⁺),^[24,25] the alkali biuretooxophosphates **3b–f** were obtained by reaction of 1,1,3,5-tetrachloro-1-phospha-2,4,6-triazine (300 mg, 1.26 mmol) in dioxane (5 mL) with the corresponding acetate M(OOCCH₃) [15.12 mmol; M = Na (Merck, 99 %), NH₄ (Merck, 98 %), K (Grüssing, 99 %), Rb (Alfa Aesar, 99.8 %), Cs (Alfa Aesar, 99.9 %)] in H₂O (5 mL). A temperature of 55–60 °C

was maintained, first by cooling with an ice bath, later by heating in an oil bath. After cooling down to room temperature and evaporation of the solvent, the product was obtained as colorless blocklike crystals. The corresponding alkali chlorides can be removed by stirring the precipitate in methanol (50 mL).

Lithium biuretooxophosphate monohydrate (**3a**) was obtained by an ion-exchange reaction in aqueous solution at room temperature. An aqueous solution of LiCl (75 mL; 9.7 g, 0.228 mol, Sigma–Aldrich, 99.9%) was poured onto a column (ion-exchange capacity: 76 mmol) containing a strongly acidic ion-exchange resin (15 mL; Amberlyst 15, Fluka). After thoroughly washing the column with deionized water (3 L), NH_4^+ -biuretooxophosphate (**3d**; 546.3 mg, 2.5 mmol) in water (30 mL) was poured onto the column. The eluate was collected and crystallized by evaporation of the solvent.

Elemental analysis (wt.-%): **3a**: calcd. C 12.71, H 2.67, Li 3.67, N 22.23, P 16.39; found C 12.45, H 2.75, Li 3.55, N 21.73, P 16.07; **3b**: calcd. C 12.84, H 1.62, N 22.47, Na 12.3, P 16.56; found C 12.71, H 1.88, N 21.71, Na 12.7, P 14.70; **3c**: calcd. C 11.83, H 1.49, K 19.3, N 20.69, P 15.25; found C 11.81, H 1.66, K 18.90, N 19.86, P 13.31; **3d**: calcd. C 13.19, H 3.88, N 30.77, P 17.01; found C 11.39, H 4.04, N 29.08, P 13.60; **3e**: calcd. C 9.29, H 1.56, N 16.25, P 11.98, Rb 33.10; found C 9.44, H 1.45, N 16.33, P 11.85, Rb 31.28; **3f**: calcd. C 8.09, H 1.02, N 14.15, P 10.43; found C 7.84, H 1.19, N 12.33, P 8.62.

X-ray Structure Determination

Single-crystal X-ray diffraction data were collected at 293 K (**3a**, **3e**) and 173 K (**3b**, **3c**, **3d**, **3f**) with a Nonius Kappa CCD diffractometer (**3a–d**, **3f**) and a STOE IPDS I diffractometer (**3e**), both using monochromated Mo- K_α radiation ($\lambda = 71.073$ pm; Table 6). The diffraction intensities were scaled using the SCALEPACK software package.^[41] For **3a–d** no additional adsorption correction was applied, whereas for **3e** and **3f** an absorption correction was performed using the programs XPREP and SADABS, respectively.^[42,43] The crystal structures were solved by direct methods using the software package SHELXS-97 and refined against F^2 by applying the full-matrix least-squares method (SHELXL-97).^[44–46] Except for **3e**, the hydrogen positions could be determined from difference Fourier syntheses and were refined isotropically using restraints for oxygen–hydrogen and nitrogen–hydrogen distances. All non-hydrogen atoms were refined anisotropically.

CCDC-854273 (for **3a**), CCDC-854274 (for **3c**), CCDC-854276 (for **3e**), and CCDC-854275 (for **3f**) contain the supplementary crystallographic data for this paper. These data can be obtained free of charge from The Cambridge Crystallographic Data Centre via www.ccdc.cam.ac.uk/data_request/cif.

Powder X-ray diffraction data were collected on a Stoe STADI P diffractometer using Cu- $K_{\alpha 1}$ radiation (for **3a–e**) and Mo- $K_{\alpha 1}$ radiation (for **3f**).

General Techniques

FTIR measurements were carried out on a Bruker IFS 66v/S spectrometer. Spectra of the samples were recorded in an evacuated cell at ambient conditions between 400 and 4000 cm^{-1} after diluting the samples in KBr pellets (2 mg sample, 300 mg of KBr, hand press with press capacity 10 kN).

PL measurements were performed on a Photon Technology International (PTI) fluorescence system featuring a PTI 814 photomultiplier detector and a PTI A1010B xenon arc lamp driven by a PTI LPS-220B lamp power supply.

Thermoanalytical measurements were carried out under an inert atmosphere (He) with a Thermoanalyzer TG-DTA92 (Setaram). The samples were heated in an alumina crucible from room temperature to 600 $^{\circ}\text{C}$ with a heating rate of 5 K min^{-1} .

Elemental analyses for C, H, and N were performed with the elemental analyzer systems Vario EL and Vario Micro (Elementar Analysensysteme GmbH). Alkali metal and phosphorus quantification was performed by atomic emission spectrophotometry with inductively coupled plasma (ICP-AES) on a Varian-Vista simultaneous spectrometer.

Supporting Information (see footnote on the first page of this article): Figure S1 with the experimental and simulated powder X-ray diffraction patterns for **3a–f**, Figure S2 with the photoluminescence spectra of **3a–f**, and Figure S3 with the DTA/TG curves of **3a–f**.

Acknowledgements

We gratefully acknowledge financial support that was granted from the Deutsche Forschungsgemeinschaft (DFG) (project SCHN377/15-1) and from the Fonds der Chemischen Industrie (FCI) (scholarship for E. Wirnhier). We like to thank Dr. Peter Mayer

and Thomas Miller for single-crystal data collection as well as Christian Argyo (all Department Chemie, LMU München) for help with the photoluminescence measurements.

4.1.1.5 Bibliography

- [1] B. V. Lotsch, M. Döblinger, J. Sehnert, L. Seyfarth, J. Senker, O. Oeckler, W. Schnick, *Chem. Eur. J.* **2007**, *13*, 4969-4980.
- [2] F. Goettmann, A. Thomas, M. Antonietti, *Angew. Chem.* **2007**, *119*, 2773-2776; *Angew. Chem. Int. Ed.* **2007**, *46*, 2717-2720.
- [3] X. Wang, K. Maeda, A. Thomas, K. Takanae, G. Xin, J. M. Carlsson, K. Domen, M. Antonietti, *Nat. Mater.* **2009**, *8*, 76-80.
- [4] Y. Zhang, M. Antonietti, *Chem. Asian J.* **2010**, *5*, 1307-1311.
- [5] Y. Zhang, T. Mori, J. Ye, M. Antonietti, *J. Am. Chem. Soc.* **2010**, *132*, 5294-5295.
- [6] J.-L. Brédas, J. E. Norton, J. Cornil, V. Coropceanu, *Acc. Chem. Res.* **2009**, *42*, 1691-1699.
- [7] B. Yue, Q. Li, H. Iwai, T. Kako, J. Ye, *Sci. Technol. Adv. Mater.* **2011**, *12*, 034401/1-034401/7.
- [8] D. Portehault, C. Giordano, C. Gervais, I. Senkowska, S. Kaskel, C. Sanchez, M. Antonietti, *Adv. Funct. Mater.* **2010**, *20*, 1827-1833.
- [9] G. Liu, P. Niu, C. Sun, S. C. Smith, Z. Chen, G. Q. Lu, H.-M. Cheng, *J. Am. Chem. Soc.* **2010**, *132*, 11642-11648.
- [10] Y. Wang, H. Li, J. Yao, X. Wang, M. Antonietti, *Chem. Sci.* **2011**, *2*, 446-450.
- [11] Y. Zhang, A. Thomas, M. Antonietti, X. Wang, *J. Am. Chem. Soc.* **2009**, *131*, 50-51.
- [12] T. Saplinova, C. Lehnert, U. Böhme, J. Wagler, E. Kroke, *New J. Chem.* **2010**, *34*, 1893-1908.
- [13] H. Beyer, T. Pyl, H. Lemke, *J. Prakt. Chem.* **1962**, *16*, 137-144.
- [14] A. John, D. Philip, N. Stock, W. Schnick, S. Devanarayanan, *Spectrochim. Acta, Part A* **2001**, *57*, 959-969.
- [15] N. Stock, E. Irran, W. Schnick, *Z. Anorg. Allg. Chem.* **1999**, *625*, 555-561.
- [16] N. Stock, W. Herrendorf, J. Beck, W. Schnick, *Eur. J. Inorg. Chem.* **1998**, 469-476.
- [17] N. Stock, W. Schnick, *Z. Naturforsch., B: J. Chem. Sci.* **1997**, *52*, 251-255.
- [18] S. Correll, N. Stock, W. Schnick, *Solid State Sci.* **2004**, *6*, 953-965.
- [19] S. Correll, S. J. Sedlmaier, W. Schnick, *Solid State Sci.* **2005**, *7*, 1261-1271.
- [20] J. Neels, K.-H. Jost, M. Meisel, *Z. Anorg. Allg. Chem.* **1986**, *540/541*, 307-318.

- [21] J. Neels, M. Meisel, R. Moll, *Z. Chem.* **1984**, *24*, 389-390.
- [22] K. K. Palkina, S. I. Maksimova, N. T. Chibiskova, J. Neels, B. Valis, *Izv. Akad. Nauk SSSR, Neorganicheskie Materialy* **1991**, *27*, 340-346.
- [23] M. Becke-Goehring, D. Jung, *Z. Anorg. Allg. Chem.* **1970**, *372*, 233-247.
- [24] M. L. Nielsen, T. J. Morrow, *Inorg. Synth.* **1960**, *6*, 99.
- [25] M. L. Nielsen, T. J. Morrow, *Inorg. Synth.* **1960**, *6*, 97-98.
- [26] H. Jacobs, R. Nymwegen, *Z. Anorg. Allg. Chem.* **1998**, *624*, 199-204.
- [27] N. Stock, W. Schnick, *Acta Crystallogr., Sect. C: Cryst. Struct. Commun.* **1996**, *C52*, 2645-2647.
- [28] N. Stock, W. Schnick, *Acta Crystallogr., Sect. C: Cryst. Struct. Commun.* **1997**, *53*, 532-534.
- [29] S. J. Sedlmaier, D. Johrendt, O. Oeckler, W. Schnick, *Z. Anorg. Allg. Chem.* **2007**, *633*, 2217-2222.
- [30] R. Bucourt, *Topics in Stereochemistry*, Wiley, New York, **1974**, *8*, 159-224.
- [31] D. Cremer, J. A. Pople, *J. Am. Chem. Soc.* **1975**, *97*, 1354-1358.
- [32] A. Sattler, W. Schnick, *Z. Anorg. Allg. Chem.* **2006**, *632*, 531-533.
- [33] E. Horvath-Bordon, E. Kroke, I. Svoboda, H. Fuess, R. Riedel, S. Neeraj, A. K. Cheetham, *Dalton Trans.* **2004**, 3900-3908.
- [34] F. Belaj, E. Nachbaur, *Monatsh. Chem.* **1987**, *118*, 1077-1085.
- [35] K. Sivashankar, *Proc. Indian Acad. Sci., Chem. Sci.* **2000**, *112*, 607-614.
- [36] N. E. A. El-Gamel, J. Wagler, E. Kroke, *J. Mol. Struct.* **2008**, *888*, 204-213.
- [37] G. B. Seifer, *Russ. J. Coord. Chem.* **2002**, *28*, 301-324.
- [38] B. Jürgens, E. Irran, J. Senker, P. Kroll, H. Müller, W. Schnick, *J. Am. Chem. Soc.* **2003**, *125*, 10288-10300.
- [39] D. R. Miller, D. C. Swenson, E. G. Gillan, *J. Am. Chem. Soc.* **2004**, *126*, 5372-5373.
- [40] E. Kroke, M. Schwarz, E. Horvath-Bordon, P. Kroll, B. Noll, A. Norman, *New J. Chem.* **2002**, *26*, 508-512.
- [41] Z. Otwinowski, W. Minor, *Methods Enzymol.* **1997**, *276*, 307-326.
- [42] G. M. Sheldrick, *SADABS*, Version 2, Universität Göttingen, **2001**.
- [43] Bruker-AXS, *XPREP*, Reciprocal Space Exploration, Version 6.12, **2001**.
- [44] G. M. Sheldrick, *SHELXS-97*, Program for the Solution of Crystal Structures, Universität Göttingen, **1997**.

- [45] G. M. Sheldrick, *SHELXL-97*, Program for the Refinement of Crystal Structures, Universität Göttingen **1997**.
- [46] G. M. Sheldrick, *Acta Crystallogr., Sect. A* **2008**, *64*, 112-122.

5.1.2 Calcium Biuretooxophosphate

Ca[PO₂(NH)₃(CO)₂]₂ – The First Biuretooxophosphate with a Divalent Cation

Eva Wirnhier and Wolfgang Schnick

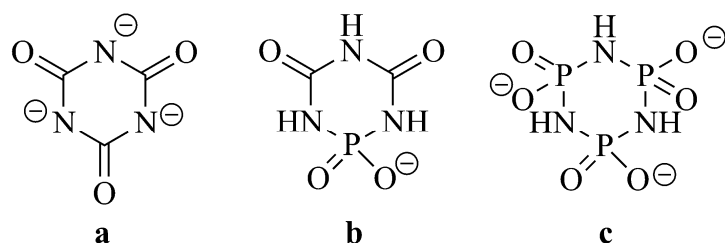
published in: *Z. Anorg. Allg. Chem.* **2012**, 638, 920-924. DOI: 10.1002/zaac.201200068

Keywords: Biuretooxophosphates; Crystal structure; Calcium; 1-Phospha-2, 4, 6-*s*-triazine core

Abstract: Calcium biuretooxophosphate Ca[PO₂(NH)₃(CO)₂]₂ was synthesized by ion exchange reaction in aqueous solution. The crystal structure of the salt was elucidated by single-crystal X-ray diffraction. Anionic 1-phospha-2, 4, 6-*s*-triazine rings exhibiting a half-chair conformation act as monodentate ligands for the calcium ions. A 3D network is formed by the resulting CaO₆ octahedrons together with the anionic rings interconnected by hydrogen bonds. Beside the crystal structure, FTIR and photoluminescence spectra of calcium biuretooxophosphate are discussed. The thermal behavior of the salt is examined by means of temperature-dependent powder X-ray diffraction measurements and combined TG and DTA analyses.

5.1.2.2 Introduction

Over the last decades, both carbon nitrides and (oxo)nitridophosphates have significantly gained interest due to their outstanding chemical properties. Whereas carbon nitride networks were proven – among others – to act as thermally rather stable metal-free catalysts for CO₂ reduction and water splitting,^[1,2] (oxo)nitridophosphates are known for their broad structural variety and the formation of zeolite and clathrate structures with various pore sizes.^[3,4] Biuretooxophosphates represent a link between carbon nitride and phosphorus nitride networks in terms of precursor chemistry. Built up from a six-membered PC₂N₃ ring they can be regarded as intermediates between triazine-based cyanurates and trimetaphosphimates, the latter consisting of P₃N₃ rings (Scheme 1).^[5] Both rings were proven to be building blocks of 2D and 3D network structures like poly(triazine imide)*LiCl/HCl^[6-8] or the first two nitridic zeolites NPO and NPT.^[3,9,10]



Scheme 1. The *s*-triazine-based cyanurate anion (a), the biuretooxophosphate anion (b) and the trimetaphosphimate anion (c).

Whereas cyanurates and trimetaphosphimates were first mentioned in the 19th century,^[11-14] biuretooxophosphates are a relatively new class of compounds. The ammonia salt was described by *Neels* in 1986 as by-product of the synthesis of COS starting from urea and P₂S₅, the corresponding sodium salt was synthesized by ion-exchange.^[15-17] Only recently, a detailed structural and spectroscopic characterization of all alkali biuretooxophosphates has been given.^[18] While alkali cyanurates and trimetaphosphimates are also well characterized, the salts of the alkaline earth elements were hardly described in detail. Except for two hydrates of calcium and barium cyanurate {Ca[H₂C₃N₃O₃]₂·7H₂O, Ba[H₂C₃N₃O₃]₂·2H₂O}^[19] whose structures were examined by single-crystal X-ray diffraction, alkaline earth cyanurates are only investigated regarding their spectroscopic and thermal properties. Alkaline earth trimetaphosphimates are discussed in the literature but no comprehensive study including structural characterization was done so far.^[5,20]

In this contribution we report on the first biuretooxophosphate with a divalent metal ion, namely $\text{Ca}[\text{PO}_2(\text{NH})_3(\text{CO})_2]_2$, its structural and spectroscopical properties as well as its thermal behavior.

4.1.2.2 Results and Discussion

Calcium biuretooxophosphate was synthesized by ion exchange in aqueous solution, using a similar approach recently described for the synthesis of lithium biuretooxophosphate

Table 1. Crystallographic data and details of the structure refinement for $\text{Ca}[\text{PO}_2(\text{NH})_3(\text{CO})_2]_2$.

	$\text{Ca}[\text{PO}_2(\text{NH})_3(\text{CO})_2]_2$
Molar mass /g·mol ⁻¹	368.17
Crystal system	monoclinic
Space group	$P2_1/c$ (no. 14)
T /K	173
Diffractometer	Nonius Kappa-CCD
Radiation, λ /pm	Mo- K_{α} , 71.073
a /pm	1010.8(2)
b /pm	527.45(11)
c /pm	1375.3(5)
β /°	122.38(2)
V /10 ⁶ pm ³	619.2(3)
Z	2
Calculated density /g·cm ⁻³	1.975
Crystal size /mm ³	0.18 x 0.13 x 0.09
Absorption coefficient /mm ⁻¹	0.820
F(000)	372
Absorption correction	none
Diffraction range	$3.13^\circ \leq \theta \leq 27.49^\circ$
Index range	$-13 \leq h \leq 13,$ $-6 \leq k \leq 6$ $-17 \leq l \leq 17$
Parameters / restraints	109 / 3
Total no. of reflections	5029
No. of independent reflections	1426
No. of observed reflections	1233
Min./max. residual electron density /e·10 ⁻⁶ pm ⁻³	-0.522 / 0.356
Goof	1.023
Final R indices [$I > 2\sigma(I)$]	$R1 = 0.0298, wR2 = 0.0828$ ^[a]
Final R indices (all data)	$R1 = 0.0360, wR2 = 0.0863$ ^[a]

[a] $w = [\sigma^2(F_0^2) + (0.0476P)^2 + 0.3418P]^{-1}$, with $P = (F_0^2 + 2 F_c^2)/3$

monohydrate.^[18] After evaporation of the solvent, large colorless block-like crystals of $\text{Ca}[\text{PO}_2(\text{NH})_3(\text{CO})_2]_2$ were isolated.

Crystal Structure

Calcium biuretooxophosphate crystallizes in the monoclinic space group $P2_1/c$. Crystallographic data and details of the structure refinement are summarized in Table 1. The comparison of simulated and experimental powder X-ray diffraction patterns of the bulk

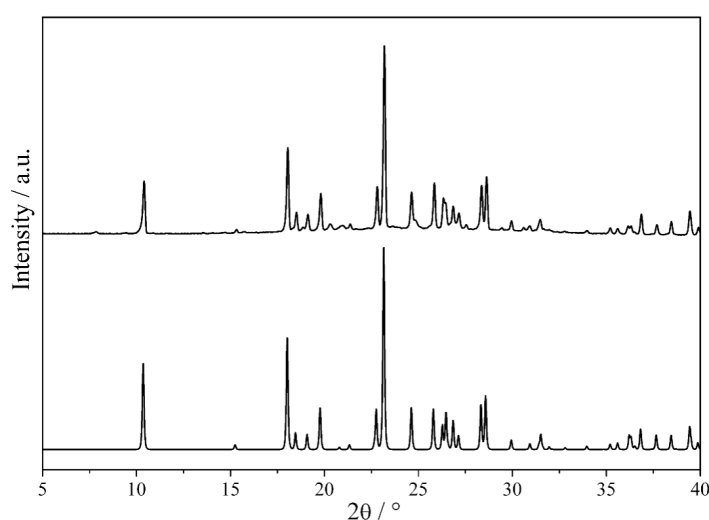


Figure 1. Powder X-ray diffraction patterns ($\text{Cu-K}\alpha_1$) of $\text{Ca}[\text{PO}_2(\text{NH})_3(\text{CO})_2]_2$ (top: experimental, bottom: simulated).

phase is shown in Figure 1. The observed intensities are in good agreement with the calculated diffraction pattern based on single-crystal data.

Similar to most alkali biureto-oxophosphates,^[18] the anionic $\text{PO}_2(\text{NH})_3(\text{CO})_2$ ring in the calcium salt exhibits a half-chair conformation with the phosphorus maintaining its preferred (distorted) tetrahedral coordination (Figure 2), proven by the torsion

angles ($-12.1, 13.0, 16.1, -35.1, 36.1, -17.9$; ideal sign sequence $-x/x/x/-x/x/-x$)^[21] and the

puckering parameters (amplitude and phase coordinates that describe the geometry of the ring puckering relative to the plane) $q_2 = 0.353(2)$, $q_3 = 0.161(2)$, $\Phi = 178.5(3)^\circ$, $Q_T = 0.388(2)$, $\theta = 114.5(3)$ [ideal

puckering parameters for half-chair conformation: $q_2 = Q_T \sin\theta$, $q_3 = Q_T \cos\theta$, $Q_T = (q_2^2 + q_3^2)^{1/2}$].^[22]

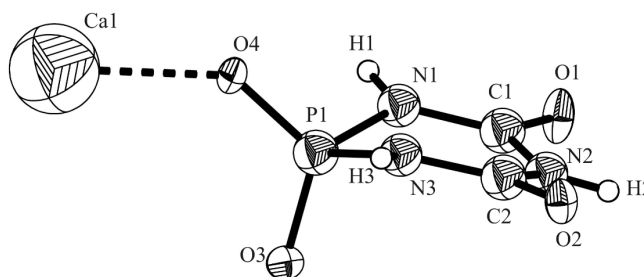
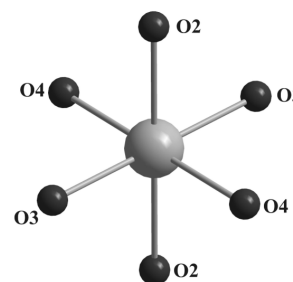
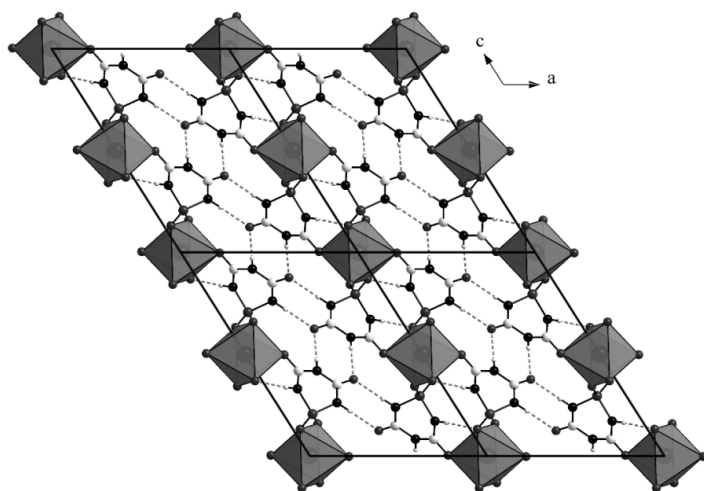


Figure 2. View of the half-chair ring conformation of $\text{Ca}[\text{PO}_2(\text{NH})_3(\text{CO})_2]_2$, showing 50% probability displacement ellipsoids. H atoms are drawn as small circles of arbitrary size.

Table 2. Selected interatomic distances /pm and angles /° in $\text{Ca}[\text{PO}_2(\text{NH})_3(\text{CO})_2]_2$.

Ca-O	227.3 (1), 232.6(8) 234.7(1)		
P-O	147.4(1), 148.9(1)	O-P-O	118.50 (7)
P-N	168.2(2), 168.3(2)	N-P-N	97.99(9)
		O-P-N	108.75(8), 109.05(8), 110.25(9), 110.37(8)
C-O	122.4(3), 123.3 (3)	C-N-C	128.11(20)
C-N	135.4(3), 134.6(2), 137.1(3), 138.6(4)	N-C-N	116.16(17), 117.20(16) 123.83(16), 118.98(19), 124.29 (19), 119.53(21)

The bond lengths P–O and P–N as well as the angles O–P–O and O–P–N (Table 2) are comparable with the values observed in trimetaphosphimates.^[23–26] Furthermore, the angles N–C–O and N–C–N as well as the bond lengths C–O and C–N are in the same range as the angles N–C–O and N–C–N and the C=O double and C–N single bonds in cyanurates^[19,27–30] and cyamelurates^[30,31] (the salts of the cyanuric acid $\text{H}_3\text{C}_3\text{N}_3\text{O}_3$ and the cyameluric acid $\text{H}_3\text{C}_6\text{N}_7\text{O}_3$) with the C–N(–P) bonds being slightly shorter than the C–N(–C) bonds. The distortion of the planar conformation of cyanurate rings by introducing tetrahedral coordinated phosphorus instead of carbon is visible most clearly in the larger C–N–C angles owing to a not completely planar N–C–N–C–N half ring. Furthermore, smaller N–P–N angles compared to trimetaphosphimates appear.

**Figure 3.** Coordination sphere of Ca^{2+} in $\text{Ca}[\text{PO}_2(\text{NH})_3(\text{CO})_2]_2$ (Ca: light gray, O: dark gray).**Figure 4.** Representation of the three-dimensional network of $\text{Ca}[\text{PO}_2(\text{NH})_3(\text{CO})_2]_2$. CaO_6 octahedrons and H-bonds (indicated by dotted lines) are interconnecting anionic biuretooxophosphate rings.

The rings act as monodentate ligands for the Ca^{2+} ions, thus resulting in coordination number 6 of the cations with nearly regular, isolated octahedrons (Figure 3, Figure 4). The distances Ca–O are in the range of the sum of the respective ionic radii.^[32] Altogether, a three-dimensional network is formed by connection of the anionic

biuretooxophosphate rings by CaO_6 octahedrons as well as $\text{N-H}\cdots\text{O}$ hydrogen bonds [2.830(2), 3.056(3) pm].

FTIR Spectroscopy

The FTIR spectrum of $\text{Ca}[\text{PO}_2(\text{NH})_3(\text{CO})_2]_2$ is displayed in Figure 5. Strong absorption occurs in the N–H stretching region between 3300 and 3000 cm^{-1} due to the imide groups in the anionic ring. The broadness of the signals as well as the band at 2883 cm^{-1} arise from the participation of the nitrogen atoms in $\text{N-H}\cdots\text{O}$ hydrogen bonds. Very strong and sharp absorption bands can be observed in the fingerprint region ($1700\text{--}500\text{ cm}^{-1}$). An assignment of the observed frequencies was carried out in comparison with cyanurates and trimetaphosphimates and is presented in Table 3.

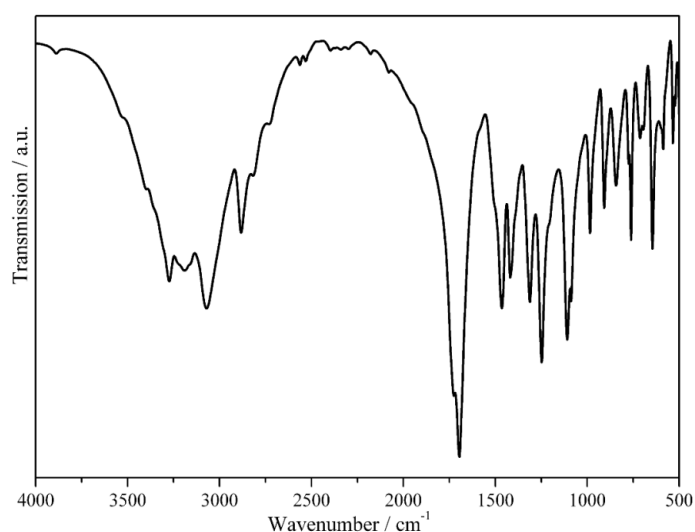


Figure 5. FTIR spectrum of $\text{Ca}[\text{PO}_2(\text{NH})_3(\text{CO})_2]_2$ (KBr pellet).

Table 3. Vibrational frequencies (cm^{-1}) observed in the FTIR spectrum of $\text{Ca}[\text{PO}_2(\text{NH})_3(\text{CO})_2]_2$ and their assignment.

observed frequencies	assignment	observed frequencies	assignment
3273m	$\nu(\text{NH})$	1087s	$\nu_s(\text{PO}_2)$
3191m	$\nu(\text{NH})$	985m	$\nu_{\text{as}}(\text{P-NH})$
3070s	$\nu(\text{NH})$	908m	$\delta(\text{C-N})$
2883m	$\nu(\text{N-H}\cdots\text{O})$	844w	$\nu_s(\text{P-NH})$
1696vs	$\nu(\text{C=O})$	762m	$\omega(\text{NH})$
1465s	$\nu(\text{C-N})$	713w	$\omega(\text{NH})$
1419m	$\nu(\text{C-N})$	646m	$\delta(\text{PO}_2)$
1312s	$\delta(\text{NH})$	587w	$\nu(\text{MO})$
1247s	$\nu_{\text{as}}(\text{PO}_2) / \delta(\text{NH})$	534w	$\delta(\text{C=O})$
1109s	$\nu_s(\text{PO}_2)$	480m	$\delta(\text{NCO})$

Photoluminescence Spectroscopy

As the structurally related class of cyamelurates was proven to show interesting luminescent properties possibly useful for applications as brighteners or UV-stabilizers,^[33] photoluminescence spectra of $\text{Ca}[\text{PO}_2(\text{NH})_3(\text{CO})_2]_2$ were recorded (Figure 6). The excitation spectrum shows two maxima in the UV region ($\lambda_{\text{ex, max}} = 265$ and 340 nm) with the second signal being less intense. Emission occurs close to the UV/Vis transition ($\lambda_{\text{em, max}} = 385$ nm) and is therefore similar to the emission of alkali cyamelurates (370–400 nm). No significant shift is observed in comparison with the alkali biuretooxophosphates, due to similar electronic properties of the anionic 1-phospha-2,4,6-*s*-triazine ring in all salts.^[18]

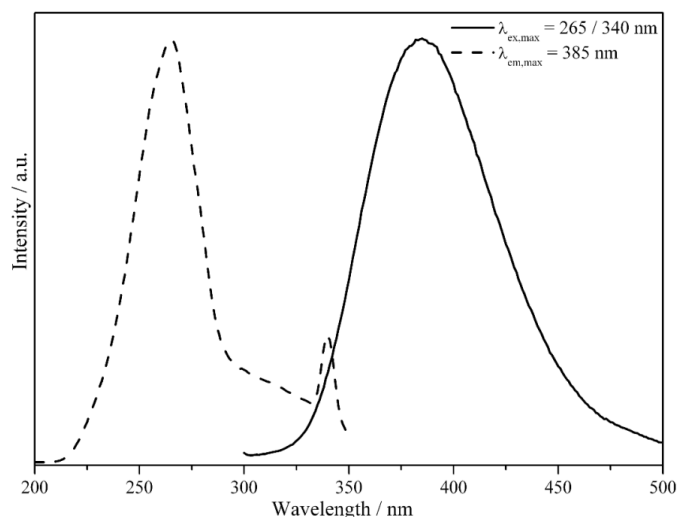


Figure 6. Photoluminescence spectra (dashed line: excitation, solid line: emission) of a solution of $\text{Ca}[\text{PO}_2(\text{NH})_3(\text{CO})_2]_2$ ($c = 2 \cdot 10^{-3} \text{ mol} \cdot \text{L}^{-1}$, solvent: water).

Differential Thermal Analysis and Thermogravimetry

With regards to the possible applicability of $\text{Ca}[\text{PO}_2(\text{NH})_3(\text{CO})_2]_2$ as precursor for the synthesis of well-defined CNP(O) networks, the thermal behavior of the title compound was examined. TG and DTA curves of $\text{Ca}[\text{PO}_2(\text{NH})_3(\text{CO})_2]_2$ recorded between room temperature and 600 °C are shown in Figure 7. Accompanied by a strong endothermic signal, the decomposition of $\text{Ca}[\text{PO}_2(\text{NH})_3(\text{CO})_2]_2$ starts at 376 °C. The thermal stability of the calcium salt is therefore slightly higher than for the alkali biuretooxophosphates which start to decompose below 350 °C. The thermal behavior beyond this temperature is characterized by a continuous mass loss, suggesting the release of gaseous by-products like CO_2 , HNCO , and NH_3 . A second endothermic signal is caused by the formation of the corresponding phosphate $\text{Ca}(\text{PO}_3)_2$ at 440 °C, proven by temperature-dependent powder X-ray diffraction analysis.

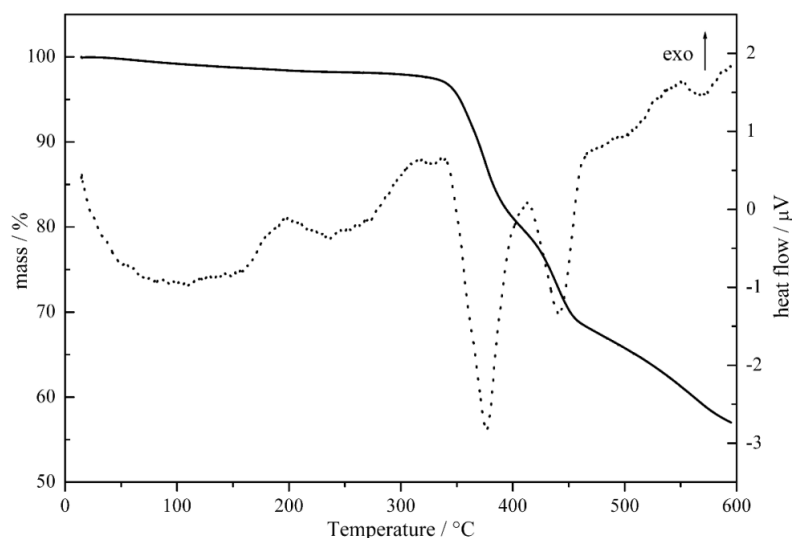


Figure 7. TG (solid) and DTA (dotted) curves of $\text{Ca}[\text{PO}_2(\text{NH})_3(\text{CO})_2]_2$, (24.2 mg), recorded with a heating rate of $5\text{ °C}\cdot\text{min}^{-1}$.

5.1.2.3 Conclusions

In this contribution we have reported on synthesis and crystal structure as well as FTIR and photoluminescent spectroscopic properties, and thermal behavior of the first biuretooxophosphate with a divalent cation $\text{Ca}[\text{PO}_2(\text{NH})_3(\text{CO})_2]_2$. Being structurally related to cyanurates and trimetaphosphimates, the applicability of biuretooxophosphates as precursors for the synthesis of crystalline CNP(O) networks will be in the focus of further investigations. Analysis of the thermal behavior shows a cleavage of the 1-phospha-2,4,6-*s*-triazine ring at temperatures around 370 °C accompanied by the release of gaseous by-products like CO_2 , NH_3 , and HNCO . Hence, future work will focus on pyrolysis under elevated pressure (for example in an autoclave under ammonothermal conditions or by using a high-pressure apparatus) according to le Chatelier's principle to avoid the decomposition of the preorganized C–N–P motif. Furthermore, $\text{Ca}[\text{PO}_2(\text{NH})_3(\text{CO})_2]_2$ may also serve as a potential biomaterial being a water-soluble precursor for the synthesis of porous $\text{Ca}(\text{PO}_3)_2$, which serves as artificial bone graft.^[34,35]

5.1.2.4 Experimental Section

Syntheses

Ammonium biuretooxophosphate was synthesized according to reference [12,13] from urea (Riedel-de Hën, 99.5%) and P₂S₅ (Fluka, 98%).

Calcium biuretooxophosphate was obtained by ion exchange reaction in aqueous solution at room temperature. An aqueous solution of CaCl₂·2H₂O (75 mL, 22.3 g, 0.152 mol, Merck, 99.5%) was poured onto a column containing 15 mL (ion exchange capacity: 76 mmol) of a strongly acidic ion exchange resin (Amberlyst 15, Fluka). After thoroughly washing the column with deionized water (3 L), NH₄⁺-biuretooxophosphate (285.9 mg, 1.57 mmol) in water (20 mL) was poured onto the column. The eluate was collected and crystallized by evaporation of the solvent (212.7 mg, 73.6 %). Elemental analysis: N 22.71 (calcd. 22.83), C 12.90 (calcd. 13.05), H 1.81 (calcd. 1.64), P 15.85 (calcd. 16.83), Ca 10.41 % (calcd. 10.89 %). ¹H NMR (400 MHz, D₂O): $\delta = 9.6$ ppm. ¹³C NMR (400 MHz, D₂O): $\delta = 152.9$ ppm. ³¹P NMR (400 MHz, D₂O): $\delta = -9.6$ ppm.

X-ray Structure Determination

Single-crystal X-ray diffraction data was collected at 173 K with a Kappa CCD diffractometer using monochromated Mo-*K*_α radiation ($\lambda = 71.073$ pm). The diffraction intensities were scaled using the SCALEPACK software package.^[36] No additional adsorption correction was applied. The crystal structures were solved by direct methods using the software package SHELXS-97 and refined against F^2 by applying the full-matrix least-squares method (SHELXL-97).^[37–39] The hydrogen positions could be determined from difference Fourier syntheses and were refined isotropically using restraints for nitrogen–hydrogen distances. All non-hydrogen atoms were refined anisotropically.

Crystallographic data (excluding structure factors) for the structure in this paper have been deposited with the Cambridge Crystallographic Data Centre, CCDC, 12 Union Road, Cambridge CB21EZ, UK. Copies of the data can be obtained free of charge on quoting the depository number CCDC-857517 (Fax: +44-1223-336-033; E-Mail: deposit@ccdc.cam.ac.uk, <http://www.ccdc.cam.ac.uk>).

General Techniques

Powder X-ray diffraction data was collected using capillaries with a Stoe STADI P diffractometer using Cu- $K_{\alpha 1}$ radiation with a germanium monochromator and a linear PSD detector. FTIR measurements were carried out with a Bruker IFS 66v/S spectrometer. Spectra of the sample were recorded in an evacuated cell at ambient conditions between 400 and 4000 cm^{-1} after diluting the sample in a KBr pellet (2 mg sample, 300 mg KBr, hand press with press capacity 10 kN). Photoluminescence measurements were performed with a Photon Technology International (PTI) fluorescence system featuring a PTI 814 photomultiplier detector and a PTI A1010B xenon arc lamp driven by a PTI LPS-220B lamp power supply. Thermoanalytical measurements were performed in an inert atmosphere (helium) with a Thermoanalyzer TG-DTA92 (Setaram). The sample was heated in an alumina crucible from room temperature to 600 °C with a heating rate of 5 $\text{K}\cdot\text{min}^{-1}$. Elemental analyses for C, H and N were performed with the elemental analyzer systems Vario EL and Vario Micro (Elementar Analysensysteme GmbH). Ca and P quantification was performed by atomic emission spectrophotometry with inductively coupled plasma (ICP-AES) with a Varian-Vista simultaneous spectrometer.

Acknowledgement

We gratefully acknowledge financial support that was granted from the Deutsche Forschungsgemeinschaft (DFG) (project SCHN377/15-1 and from the Fonds der Chemischen Industrie (FCI) (scholarship for *E. Wirnhier*). We like to thank *Dr. Peter Mayer* for single-crystal diffraction data collection as well as *Christian Argyo* (both Department Chemie, LMU München) for help with the photoluminescence measurements.

5.1.2.5 Bibliography

- [1] F. Goettmann, A. Thomas, M. Antonietti, *Angew. Chem.* **2007**, *119*, 2773-2776; *Angew. Chem. Int. Ed.* **2007**, *46*, 2717-2720.
- [2] X. Wang, K. Maeda, A. Thomas, K. Takanabe, G. Xin, J. M. Carlsson, K. Domen, M. Antonietti, *Nat. Mater.* **2009**, *8*, 76-80.
- [3] S. Correll, N. Stock, O. Oeckler, W. Schnick, *Angew. Chem.* **2003**, *115*, 3674-3677; *Angew. Chem. Int. Ed.* **2003**, *42*, 3549-3552.
- [4] F. Karau, W. Schnick, *Angew. Chem.* **2006**, *118*, 4617-4620; *Angew. Chem. Int. Ed.* **2006**, *45*, 4505-4508.
- [5] R. Marchand, W. Schnick, N. Stock, *Adv. Inorg. Chem.* **2000**, *50*, 193-233.
- [6] E. Wirnhier, M. Döblinger, D. Gunzelmann, J. Senker, B. V. Lotsch, W. Schnick, *Chem. Eur. J.* **2011**, *17*, 3213-3221.
- [7] P. F. McMillan, V. Lees, E. Quirico, G. Montagnac, A. Sella, B. Reynard, P. Simon, E. Bailey, M. Deifallah, F. Corà, *J. Solid State Chem.* **2009**, *182*, 2670-2677.
- [8] Z. Zhang, K. Leinenweber, M. Bauer, L. A. J. Garvie, P. F. McMillan, G. H. Wolf, *J. Am. Chem. Soc.* **2001**, *123*, 7788-7796.
- [9] S. J. Sedlmaier, M. Döblinger, O. Oeckler, J. Weber, J. Schmedt auf der Günne, W. Schnick, *J. Am. Chem. Soc.* **2011**, *133*, 12069-12078.
- [10] S. J. Sedlmaier, M. Döblinger, O. Oeckler, J. Weber, J. Schmedt auf der Günne, W. Schnick, *Database of Zeolite Structures*: <http://www.iza-structure.org/databases/>, accessed February 2012.
- [11] A. Hantzsch, *Ber. Dtsch. Chem. Ges.* **1906**, *39*, 139-153.
- [12] F. Wöhler, *Justus Liebigs Ann. Chem.* **1844**, *35*, 241.
- [13] H. N. Stokes, *Am. Chem. J.* **1895**, *17*, 275-290.
- [14] H. N. Stokes, *Am. Chem. J.* **1896**, *18*, 629-663.
- [15] J. Neels, K.-H. Jost, M. Meisel, *Z. Anorg. Allg. Chem.* **1986**, *540/541*, 307-318.
- [16] J. Neels, M. Meisel, R. Moll, *Z. Chem.* **1984**, *24*, 389-390.
- [17] K. K. Palkina, S. I. Maksimova, N. T. Chibiskova, J. Neels, B. Valis, *Izv. Akad. Nauk SSSR, Neorganicheskie Materialy* **1991**, *27*, 340-346.
- [18] E. Wirnhier, W. Schnick, *Eur. J. Inorg. Chem.* **2012**, DOI: 10.1002/ejic.201101317.

- [19] C.-Z. Chen, Z.-B. Lin, J.-Q. Shi, X.-Y. Huan, D.-S. Gao, D. Li, H.-Y. Jiang, *Jiegou Huaxue* **1994**, *13*, 468-471.
- [20] M. Sakurai, Y. Ebata, H. Suzuki, M. Maeda, M. Watanabe, *Phos. Res. Bull.* **1999**, *10*, 758-763.
- [21] R. Bucourt, *Topics in Stereochemistry*, Wiley, New York, **1974**, *8*, 159-224.
- [22] D. Cremer, J. A. Pople, *J. Am. Chem. Soc.* **1975**, *97*, 1354-1358.
- [23] H. Jacobs, R. Nymwegen, *Z. Anorg. Allg. Chem.* **1998**, *624*, 199-204.
- [24] N. Stock, W. Schnick, *Acta Crystallogr., Sect. C: Cryst. Struct. Commun.* **1996**, *C52*, 2645-2647.
- [25] N. Stock, W. Schnick, *Acta Crystallogr., Sect. C: Cryst. Struct. Commun.* **1997**, *53*, 532-534.
- [26] S. J. Sedlmaier, D. Johrendt, O. Oeckler, W. Schnick, *Z. Anorg. Allg. Chem.* **2007**, *633*, 2217-2222.
- [27] A. N. Chekhlov, *Zh. Neorg. Khim.* **2006**, *51*, 799-803.
- [28] F. Belaj, E. Nachbaur, *Monatsh. Chem.* **1987**, *118*, 1077-1085.
- [29] K. Sivashankar, *Proc. Indian Acad. Sci., Chem. Sci.* **2000**, *112*, 607-614.
- [30] N. E. A. El-Gamel, J. Wagler, E. Kroke, *J. Mol. Struct.* **2008**, *888*, 204-213.
- [31] A. Sattler, W. Schnick, *Z. Anorg. Allg. Chem.* **2006**, *632*, 531-533.
- [32] R. D. Shannon, C. T. Prewitt, *Acta Crystallogr., Sect. B* **1969**, *25*, 925-946.
- [33] E. Horvath-Bordon, E. Kroke, I. Svoboda, H. Fuess, R. Riedel, S. Neeraj, A. K. Cheetham, *Dalton Trans.* **2004**, 3900-3908.
- [34] Y. Ota, T. Iwashita, T. Kasuga, Y. Abe, A. Seki, *J. Mater. Sci. Mater. Med.* **2002**, *13*, 895-900.
- [35] H. R. R. Ramay, M. Zhang, *Biomaterials* **2004**, *25*, 5171-5180.
- [36] Z. Otwinowski, W. Minor, *Methods Enzymol.* **1997**, *276*, 307-326.
- [37] G. M. Sheldrick, *SHELXS-97*, Program for the Solution of Crystal Structures, Universität Göttingen, **1997**.
- [38] G. M. Sheldrick, *SHELXL-97*, Program for the Refinement of Crystal Structures, Universität Göttingen **1997**.
- [39] G. M. Sheldrick, *Acta Crystallogr., Sect. A* **2008**, *64*, 112-122.

5.2 *N,N'*-Bis(aminocarbonyl)phosphorodiamidates

Ammonothermal Synthesis of Alkali *N,N'*- Bis(aminocarbonyl)phosphorodiamidates $M[PO_2(NHCONH_2)_2]$ ($M = Na, K, Rb$)

Eva Wirnhier, Ruth Deborah Boller and Wolfgang Schnick

published in: *Eur. J. Inorg. Chem.* **2012**, 3296-3301, DOI: 10.1002/ejic.201200209

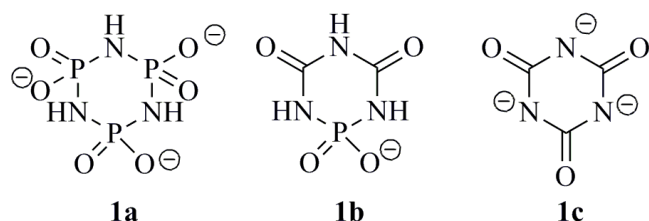
Keywords: Ammonothermal synthesis; Alkali metals; High-pressure chemistry; X-ray diffraction; Thermal behavior

Abstract: Compounds $M[PO_2(NHCONH_2)_2]$ with $M = Na, K,$ and Rb , which are the salts of *N,N'*-bis(aminocarbonyl)phosphorodiamidic acid, were synthesized by ammonolysis of the corresponding alkali biuretooxophosphates $M[PO_2(NH)_3(CO)_2]$ ($M = Na, K, Rb$) at 350 °C and 120–150 bar in an autoclave. The structures were solved by single-crystal X-ray diffraction and exhibit 3D frameworks in which *N,N'*-bis(aminocarbonyl)phosphorodiamidate ions connect the corresponding alkali ions. The thermal behavior was investigated by combined thermogravimetric (TG) and differential thermal analysis (DTA) as well as temperature-dependent powder X-ray diffraction to evaluate applicability of the alkali *N,N'*-bis(aminocarbonyl)phosphorodiamidates as precursors for the synthesis of CNP(O) networks. In this context, the concept of Le Chatelier's principle for the hindrance of premature decomposition by applying elevated pressure was examined

5.2.1 Introduction

Hydrothermal reactions have long been known as a powerful approach for the synthesis of oxides and related compounds as well as the growth of extremely pure large single crystals (e.g., quartz crystals used as wafers, or zeolites).^[1-3] In general, all solvothermal methods (hydrothermal, ammonothermal syntheses) use solvents heated above their boiling point at high vapor pressure (sometimes even beyond the critical point) to crystallize compounds with poor solubility and high melting point by chemical transport reactions. Whereas hydrothermal reactions in supercritical water are mainly used for the crystal growth of oxidic materials like SiO₂, ZnO, CrO₂, and zeolites, the ammonothermal method is particularly suitable for the growth of nitridic single crystals such as GaN.^[4-9] As ammonia can react as a tribasic acid, not only nitridic materials arise from ammonothermal syntheses. A multitude of binary and ternary amides were synthesized by Jacobs et al. in the 1970s; they intensely investigated the behavior of inorganic compounds when applying supercritical ammonia.^[10] Furthermore, these authors investigated the ammonolysis of P₃N₅, which results in the synthesis of diamidooxophosphates and trimetaphosphimates by addition of the corresponding alkali metal hydroxides.^[11,12]

The P₃N₃ ring found in the trimetaphosphimate anion (**1a**) as well as its CN-based analogue, the *s*-triazine ring found in cyanurate anions (**1c**) (Scheme 1), were proven to be building blocks of 2D and 3D network structures like poly(triazine imide)·LiCl/HCl^[13-15] or the first two nitridic zeolites, oxonitridophosphate-1 (NPO) and oxonitridophosphate-2 (NPT).^[16-18]



Scheme 1. Trimetaphosphimate ion (**1a**), biuretooxophosphate ion (**1b**) and *s*-triazine-based cyanurate ion (**1c**).

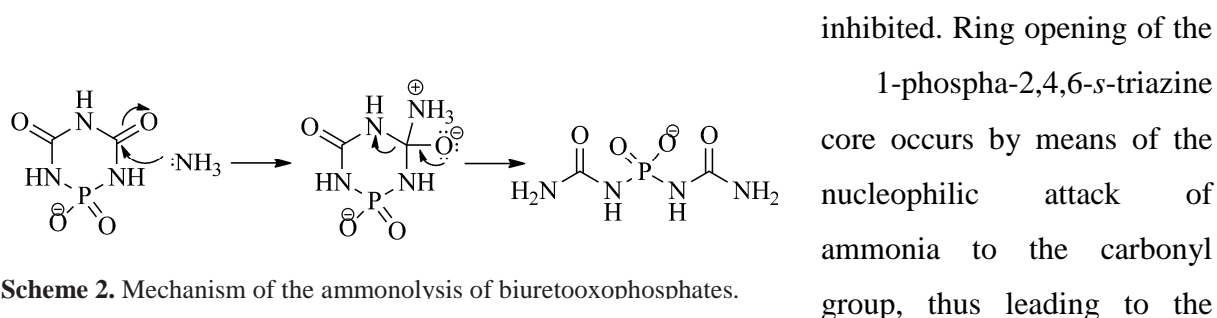
Recently, biuretooxophosphates (**1b**) with a 1-phospha-2,4,6-*s*-triazine core, which are intermediates between cyanurates and trimetaphosphimates, were investigated with regards to their structure, spectroscopic properties, and thermal behavior in light of their

possible applications as precursors.^[19] Thermal treatment at temperatures >200 °C led to the

cleavage of the anionic ring accompanied by release of gaseous byproducts like HNCO and NH₃. The replacement of C by P in an *s*-triazine core, maintaining its preferred (distorted) tetrahedral coordination, lowers the thermal stability of the biuretooxophosphates relative to the related class of cyanurates,^[20] as stabilization from the π - π stacking found for planar *s*-triazine cores is missing. Furthermore, the formation of corresponding stable metaphosphates (MPO₃)_x as decomposition products acts as a driving force for the comparatively low decomposition temperatures. With regards to the applicability of biuretooxophosphates as precursors for the synthesis of CNP(O) networks, pyrolysis needs to be conducted under elevated pressure to avoid the decomposition of the preorganized CNP motif according to Le Chatelier's principle. In this context, investigations on the behavior of the alkali biuretooxophosphates in supercritical ammonia at high temperatures were performed. Ammonolysis of the biuretooxophosphates at 350 °C yielded alkali *N,N'*-bis(aminocarbonyl)phosphorodiamidates M[PO₂(NHCONH₂)₂] (M = Na, K, Rb), which are characterized thoroughly in this contribution in terms of their structural and spectroscopic properties as well as their thermal behavior.

5.2.2 Results and Discussion

The alkali *N,N'*-bis(aminocarbonyl)phosphorodiamidates M[PO₂(NHCONH₂)₂] with M = Na (**2a**), K (**2b**), and Rb (**2c**) were synthesized by ammonolysis of the alkali biuretooxophosphates M[PO₂(NH)₃(CO)₂] (M = Na, K, Rb) in an autoclave at 350 °C. Due to the generated autogenous pressure of about 120–150 bar, an elimination of gaseous byproducts as observed for the thermal treatment of biuretooxophosphates under ambient pressure was



Scheme 2. Mechanism of the ammonolysis of biuretooxophosphates.

formation of the symmetric *N,N'*-bis(aminocarbonyl)phosphorodiamidate anion (Scheme 2). At higher temperatures (>400 °C), the nucleophilic attack of two further molecules of

ammonia leads to the cleavage of urea and the formation of $\text{NaPO}_2(\text{NH}_2)_2$, which decomposes to $\text{NaHPO}_3\text{NH}_2$ in air.

Crystal Structures

The sodium salt of *N,N'*-bis(aminocarbonyl)phosphorodiamidic acid (**2a**) crystallizes in the monoclinic space group $C2/c$, and the isotypic potassium (**2b**) and rubidium (**2c**) salts in the orthorhombic space group $Fdd2$. Crystallographic data and details of the structure refinements for **2a**, **2b**, and **2c** are summarized in Table 1. The comparison of simulated and experimental powder X-ray diffraction patterns of the bulk phases is shown in Figure S1 in the Supporting Information. In addition to phase purity, the diffractograms show that all reflections could be indexed with the known cell parameters, and their observed intensities were in good agreement with the calculated diffraction patterns based on single-crystal diffraction data.

The title compounds exhibit three-dimensional framework structures in which *N,N'*-bis(aminocarbonyl)phosphorodiamidate anions link the corresponding alkali ions. The anion provides four potential coordination sites ($2 \times \text{C}=\text{O}$, $1 \times \text{PO}_2$), which all participate in the coordination of the cations in **2a**, **2b**, and **2c**. However, with the P atom maintaining its

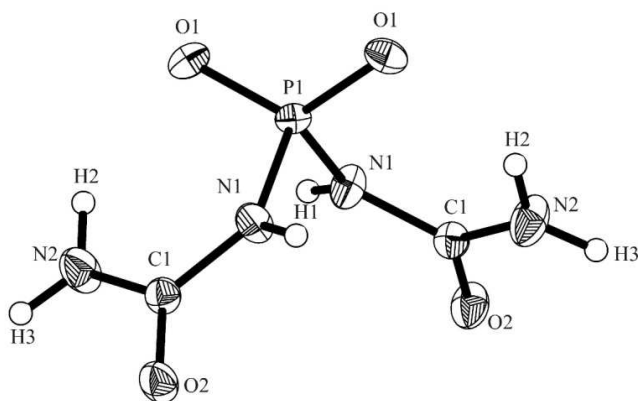


Figure 1. View of the *N,N'*-bis(aminocarbonyl)phosphorodiamidate anion (**2a**) showing 50% probability displacement ellipsoids. Hydrogen atoms are drawn as small circles of arbitrary size.

preferred (distorted) tetrahedral coordination and the resulting twisted conformation of the anion (Figure 1), a tetradentate coordination of the cations is excluded. For **2a**, the sodium cation is coordinated by six anions that act as monodentate ligands. By means of the bridging function of the μ_2 -carbonyl groups in the a,c plane, this sixfold coordination of the cations configures

edge-sharing regular octahedrons, therefore leading to the formation of 1D strands along the c axis (Figure 2). Additionally, the octahedrons are connected through the PO_2 groups of *N,N'*-

Table 1. Crystallographic data and details of the structure refinement for **2a**, **2b** and **2c**.

	2a	2b	2c
Empirical formula	C ₂ H ₆ N ₄ NaO ₄ P	C ₂ H ₆ KN ₄ O ₄ P	C ₂ H ₆ N ₄ O ₄ PRb
Formula mass [g mol ⁻¹]	204.07	220.18	266.55
Crystal system	monoclinic	orthorhombic	orthorhombic
Space group	<i>C2/c</i> (no. 15)	<i>Fdd2</i> (no. 43)	<i>Fdd2</i> (no. 43)
<i>T</i> /K	293	173	293
Diffractometer	Nonius Kappa-CCD	Oxford Sapphire CCD	Nonius Kappa-CCD
Radiation, λ [pm]	Mo-K α , 71.073	Mo-K α , 71.073	Mo-K α , 71.073
<i>a</i> [pm]	875.2(2)	1037.0(2)	1272.6(6)
<i>b</i> [pm]	1191.2(2)	1270.7(6)	1058.6(2)
<i>c</i> [pm]	700.6(1)	1110.3(2)	1127.0(2)
β [°]	103.68(3)	90	90
<i>V</i> [10 ⁶ pm ³]	709.7(2)	1463.1(8)	1518.3(5)
<i>Z</i>	4	8	8
D _{calcd.} [g cm ⁻³]	1.910	1.999	2.332
Crystal size [mm ³]	0.20 x 0.20 x 0.13	0.25 x 0.20 x 0.08	0.34 x 0.30 x 0.27
μ [mm ⁻¹]	0.429	0.927	6.716
F(000)	416	896	1040
Absorption correction	none	multi-scan	multi-scan
Min. / max. transmission	-	0.6765 / 1.0000	0.2356 / 0.4145
Diffraction range [°]	3.42 ≤ θ ≤ 30.03	4.88 ≤ θ ≤ 30.49	4.83 ≤ θ ≤ 27.45
Index range	-12 ≤ <i>h</i> ≤ 12, -16 ≤ <i>k</i> ≤ 16 -9 ≤ <i>l</i> ≤ 9	-10 ≤ <i>h</i> ≤ 14, -18 ≤ <i>k</i> ≤ 17 -15 ≤ <i>l</i> ≤ 15	-16 ≤ <i>h</i> ≤ 16, -13 ≤ <i>k</i> ≤ 13 -14 ≤ <i>l</i> ≤ 14
Parameters / restraints	69 / 3	61 / 2	57 / 1
Total no. of reflections	3466	3150	6382
No. of independent reflections	1041	1056	803
No. of observed reflections	987	1011	791
Min./max. residual electron density [e 10 ⁻⁶ pm ⁻³]	-0.312 / 0.312	-0.423 / 0.320	-0.670 / 0.459
GoF	1.049	1.107	1.035
Final R indices [<i>I</i> > 2 σ (<i>I</i>)]	<i>R</i> 1 = 0.0251, <i>wR</i> 2 = 0.0650 ^[a]	<i>R</i> 1 = 0.0294, <i>wR</i> 2 = 0.0848 ^[b]	<i>R</i> 1 = 0.0341, <i>wR</i> 2 = 0.1010 ^[c]
Final R indices (all data)	<i>R</i> 1 = 0.0265, <i>wR</i> 2 = 0.0663 ^[a]	<i>R</i> 1 = 0.0313, <i>wR</i> 2 = 0.0869 ^[b]	<i>R</i> 1 = 0.0347, <i>wR</i> 2 = 0.1016 ^[c]

[a] $w = [\sigma^2(F_o^2) + (0.0274P)^2 + 0.7971P]^{-1}$, [b] $w = [\sigma^2(F_o^2) + (0.0528P)^2 + 0.6972P]^{-1}$, [c] $w = [\sigma^2(F_o^2) + (0.0489P)^2 + 17.6549P]^{-1}$, for all with $P = (F_o^2 + 2 F_c^2)/3$.

bis(aminocarbonyl)phosphordiamidate anions, which bridge by turns the remaining two axial vertices of the octahedrons. To complete the coordination sphere of the cations in **2b** and **2c**, which resembles the diamond structure, seven *N,N'*-bis(aminocarbonyl)phosphordiamidate anions are necessary, the latter acting as bidentate ligands for one cation at a time with their PO₂ group. An eightfold coordination of the cations appears, thus forming irregular polyhedrons that significantly resemble distorted cubes. Each polyhedron is built from four

oxygen atoms from a carbonyl group and four oxygen atoms from a PO_2 group. With both oxygen species having a μ_2 -bridging function a new and rather dense 3D motif that comprises interpenetrating zweier chains formed by edge-sharing RbO_8 polyhedrons is formed (Figure 3). The chains run in $[011]$ and $[0\bar{1}1]$ direction with each polyhedron being part of both chains and sharing four edges with neighboring polyhedrons in two directions. The motif of edge-sharing cubelike polyhedrons has hitherto only been known in layered structures like EuKNaTaO_5 ^[21] with four parallel edges shared in EuO_8 cubes or for structures that contain trigonal units of triply edge-sharing cubes in three directions like $\text{Li}_{24}[\text{MnN}_3]_3\text{N}_2$ with NMnLi_7 cubes.^[22]

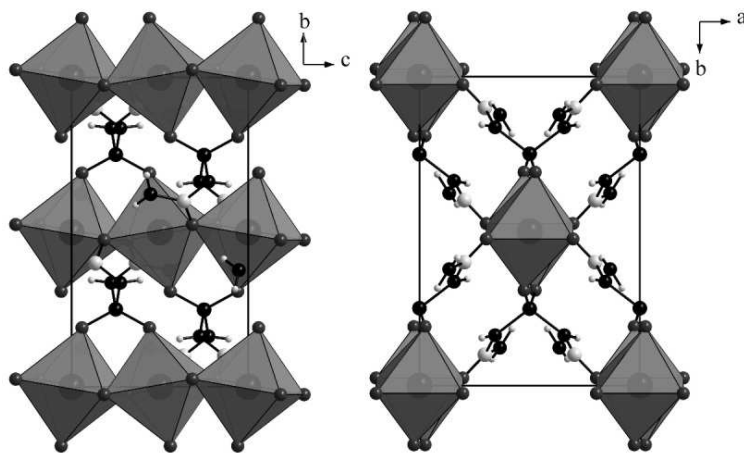


Figure 2. Crystal structure of **2a**, showing 1D strands of edge-sharing NaO_6 octahedrons along the c axis interconnected by N,N' -bis(aminocarbonyl)phosphorodiamidate anions.

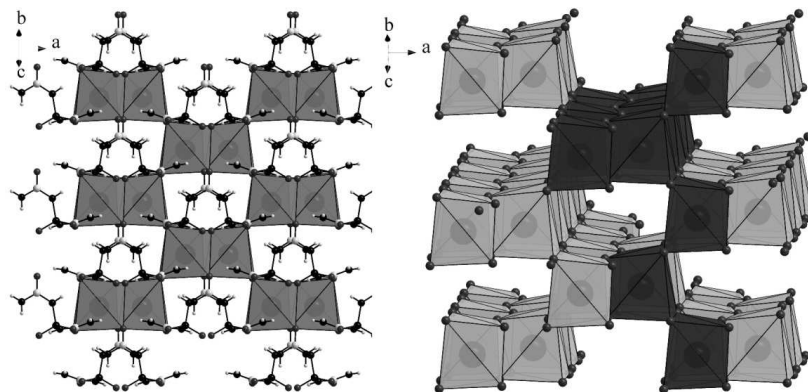


Figure 3. Crystal structure of **2c** showing a 3D framework of edgesharing RbO_8 polyhedrons interconnected by N,N' -bis(aminocarbonyl)phosphorodiamidate anions. Interpenetrating zweier chains run in $[011]$ and $[0\bar{1}1]$ direction (exemplarily highlighted in dark gray on the right side).

The framework structures of **2a**, **2b** and **2c** are complemented by the formation of H-bonding networks interconnecting the N,N' -bis(aminocarbonyl)phosphorodiamidate anions. Both NH and NH_2 groups are acting as donors, forming $\text{NH}\cdots\text{O}$ bonds with the oxygen

atoms of the carbonyl and the phosphate group. With distances $\text{N}\cdots\text{O}$ of 290–299 ppm the H-bonds in **2b** and **2c** are slightly shorter than in **2a** (303–316 pm), thus causing a denser network. The interatomic P–O, P–N, C–O, and C–N distances (Table 2) are nearly the same in **2a**, **2b**, and **2c** and do not differ significantly from the bond lengths in the corresponding

Table 2. Selected interatomic distances [pm] and angles [°] in **2a**, **2b** and **2c**.

	2a	2b	2c
M-O	233.2(1), 239.9(1), 248.2(1)	282.8(2), 296.9(2), 301.4(2), 308.1(2)	291.3(3), 301.6(4), 305.0(4), 316.2(5)
P-O	148.6(1)	149.4(4)	149.3(4)
P-N	168.8(1)	169.1(2)	169.3(4)
C-O	124.4(1)	124.8(3)	124.5(6)
C-N	133.9(2), 137.0(2)	133.9(3), 137.2(3)	134.4(6), 136.9(6)
O-P-O	122.69(5)	120.77(9)	120.97(21)
N-P-N	105.39(5)	106.34(9)	105.86(20)
O-P-N	104.71(5), 109.11(5)	104.99(9), 109.50(9)	105.37(20), 109.20(20)

biuretooxophosphates. Due to the ring opening, the N–P–N angles are larger than for biuretooxophosphates and approach the ideal tetrahedral angle of 109.47° as do the O–P–N angles. Only the O–P–O angles cause a slight distortion of the PO_2N_2 tetrahedrons. The M–O distances are comparable with the ones found for biuretooxophosphates and in accordance with the sum of the ionic radii.^[23]

FTIR Spectroscopy

The FTIR spectra of **2a**, **2b**, and **2c** are displayed in Figure 4; an assignment of the bands is given in Table 3. Strong absorption occurs in the N–H stretching region ($3450\text{--}3200\text{ cm}^{-1}$) due to the presence of NH and NH_2 groups in the N,N' -bis(aminocarbonyl)phosphorodiamidate anion. In comparison with urea and biuret, the two bands at higher wavenumbers are assigned to NH_2 groups, whereas the band at around 3200 cm^{-1} that is clearly visible only for **2b** and **2c** results from the NH groups. The difference between the spectra arises probably from a different hydrogen-bonding network with both NH and NH_2 groups acting

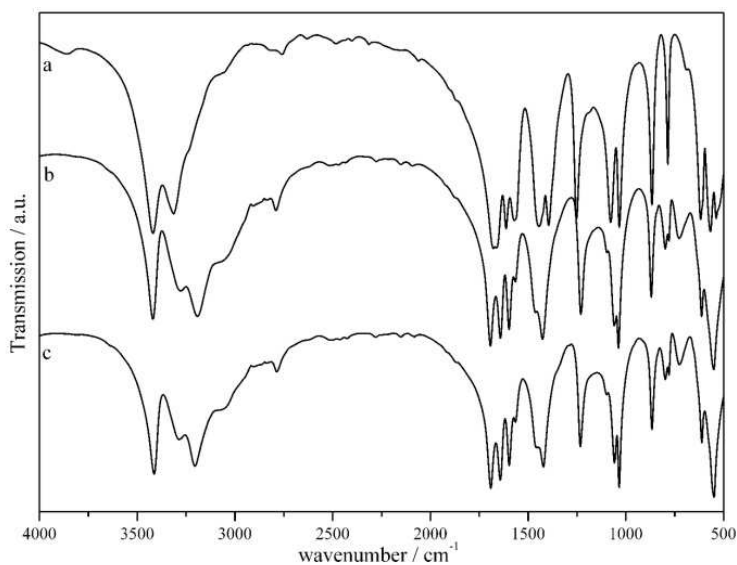
**Figure 4.** FTIR spectra of **2a**, **2b**, and **2c**.

Table 3. Vibrational frequencies [cm^{-1}] observed in the FTIR spectra of **2a**, **2b** and **2c** with assignment.

Urea ^[24]	2a	2b	2c	
3447	3420 (vs)	3420 (vs)	3414 (vs)	$\nu(\text{NH}_2)$
3347	3315 (vs)	3277 (s)	3286 (s)	$\nu(\text{NH}_2)$
		3193 (vs)	3205 (vs)	$\nu(\text{NH})$
	2760 (vw)	2791 (w)	2786 (w)	$\nu(\text{N-H}\cdots\text{O})$
1683	1678 (vs)	1693 (vs)	1691 (vs)	$\delta(\text{NH}_2)$
1631	1613 (vs)	1642 (vs)	1643 (vs)	$\delta(\text{NH}_2)$
1603	1571 (vs)	1598 (vs)	1597 (vs)	$\nu(\text{C=O})$
1468	1444 (vs)	1426 (vs)	1422 (vs)	$\nu(\text{C-N})$
	1395 (vs)			$\delta(\text{NH})$
	1252 (vs)	1230 (s)	1233 (s)	$\nu_{\text{as}}(\text{PO}_2)$
1166				$\rho(\text{NH}_2)$
	1078 (vs)	1060 (s)	1058 (s)	$\nu_{\text{s}}(\text{PO}_2)$
1061	1033 (vs)	1038 (vs)	1034 (vs)	$\rho(\text{NH}_2)$
	866 (s)	870 (m)	866 (m)	$\nu(\text{P-NH})$
	785 (m)	798 (w)	798 (w)	$\omega(\text{NH})$
		780 (w)	779 (w)	$\omega(\text{NH})$
	618 (vs)	613 (s)	611 (s)	$\delta(\text{PO}_2)$
	568 (vs)	550 (vs)	549 (vs)	$\delta(\text{C=O})/\nu(\text{MO})$

as donor. Bending and wagging modes of NH and NH_2 groups are also assigned in Table 3 and cause strong absorption in the fingerprint region. As for urea, C=O and C–N stretching vibrations are visible at 1600 cm^{-1} and around 1450 to 1420 cm^{-1} . Strong absorption is also observed for the symmetric and asymmetric PO_2 stretching vibrations ($1080\text{--}1050\text{ cm}^{-1}$ and $1250\text{--}1230\text{ cm}^{-1}$).

Thermal Behavior

The thermal behavior of **2a–c** was examined by means of combined thermogravimetric (TG) and differential thermal analysis (DTA) (Figure S1 in the Supporting Information) and temperature-dependent powder X-ray diffraction. The alkali N,N' -bis(aminocarbonyl)phosphorodiamidates are stable up to 150 (**2a** and **2b**) and 250 °C (**2c**), respectively. For **2c** the decomposition process is initiated by the elimination of formamide HCONH_2 , accompanied by a strong endothermic signal (mass loss observed: 17.4%, calculated: 16.9 %). The TG curves of **2a** and **2b** show a slow mass loss starting at 150 °C due to a partial transformation of **2a** and **2b** into the corresponding biuretooxophosphates (proven by temperature-dependent powder X-ray diffraction) associated with the elimination of ammonia. At 250 and 226 °C, complete decomposition starts, accompanied by a mass loss of 14.5 (**2a**) and 15.5% (**2b**), respectively, probably due to the elimination of formamide from residual N,N' -bis(aminocarbonyl)phosphorodiamidate ions. At higher temperatures a continuous mass loss is observed, which leads to the formation of the corresponding metaphosphates (MPO_3)_x.

5.2.3 Conclusion

In this contribution we have reported the first investigation of the behavior of CNP-based compounds under ammonothermal conditions. By means of ammonolysis of the alkali biuretooxophosphates at temperatures >350 °C, the alkali N,N' -bis(aminocarbonyl)-phosphorodiamidates $M[\text{PO}_2(\text{NHCONH}_2)_2]$ with $M = \text{Na, K, and Rb}$ were prepared. Structural investigations based on single-crystal X-ray diffraction data showed the formation of 3D frameworks in which N,N' -bis(aminocarbonyl)phosphorodiamidate anions link the corresponding alkali ions. A new 3D motif that comprised interpenetrating zweier chains formed by edge-sharing MO_8 polyhedrons was observed for $M = \text{K, Rb}$. Temperature-dependent powder X-ray diffraction analysis as well as combined DTA/TG measurements showed a low thermal stability of the title compounds up to 150 °C at ambient conditions compared to the synthesis temperature of 350 °C at 120–150 bar. Accordingly, the reaction behavior is in accordance with Le Chatelier's principle, because the breakup of the biuretooxophosphate ring next to the P atom and the release of the residual ring in the form of gaseous C/N/O/H-containing byproducts could be shifted to higher temperatures under elevated pressure. Further investigations will focus on the pyrolysis of appropriate CNPO precursors like biuretooxophosphates and alkali N,N' -bis(aminocarbonyl)phosphorodiamidates under higher pressure, for instance, by using the multianvil technique to enable the synthesis of well-defined CNP(O) networks.

5.2.4 Experimental Section

Syntheses

The title compounds **2a**, **2b**, and **2c** were synthesized by reaction of the corresponding biuretooxophosphates $M[\text{PO}_2(\text{NH})_3(\text{CO})_2] \cdot x\text{H}_2\text{O}$ ($x = 0/0/0.5$) with liquid ammonia in a high-pressure vessel. The starting material was introduced into a Parr autoclave (Type 4740CH) with a Parr gage block (Type 4316) and connected to a vacuum/inert gas line. After evacuation of the vessel, a sufficient amount of ammonia was condensed by cooling the vessel to -80 °C. The vessel was closed and slowly warmed to room temperature, then heated to 350 °C in two steps (at 2 °C·min $^{-1}$ to 200 °C, then at 1 °C·min $^{-1}$ to 350 °C). A pressure of

120–150 bar was observed during the reaction. After 60 h, the vessel was cooled to room temperature at $1\text{ }^{\circ}\text{C}\cdot\text{min}^{-1}$, and the residual pressure was released by carefully opening the valve of the gage block. The product (quantitative yield) was obtained as finely dispersed white powder. Single crystals were grown by recrystallization from water.

Compound **2a**: calcd. C 11.77, H 2.96, N 27.46, Na 11.27, P 15.18; found, C 11.30, H 2.96 N 26.57, Na 11.72, P 15.24. Compound **2b**: calcd. C 10.91, H 2.75, K 17.76, N 25.45, P 14.07; found C 10.74, H 3.32, K 14.26, N 27.01, P 14.36. Compound **2c**: calcd. C 9.01, H 2.27, N 21.02, P 11.62, Rb 32.07; found C 8.47, H 2.42, N 20.8, P 11.57, Rb 28.8.

^1H NMR (270 MHz, D_2O ; **2a–2c**): $\delta = 6.3$ (s, 2 H, NH_2), 9.7 (s, 2 H, NH). ^{13}C NMR (67.9 MHz, D_2O ; **2a–2c**): $\delta = 159.7$ ppm. ^{31}P NMR (109 MHz, D_2O ; **2a–2c**): $\delta = -9.2$ ppm.

X-ray Structure Determination

Single-crystal X-ray diffraction data for compounds **2a** and **2c** were collected at 293 K with a Kappa CCD diffractometer by using monochromated Mo- $K\alpha$ radiation ($\lambda = 71.073$ pm). The diffraction intensities were scaled by using the SCALEPACK software package.^[25] For **2a** no additional adsorption correction was applied, whereas for **2c** an absorption correction was performed by using the program SADABS.^[26] Single-crystal X-ray diffraction data for compound **2b** were collected at 173 K with an Oxford XCalibur3 diffractometer by using an enhanced optic with Mo- $K\alpha$ radiation ($\lambda = 71.073$ pm). Data collection and reduction were carried out by using the CrysAlisPro software package.^[27] An absorption correction was performed by using the program SCALE3 ABSPACK.^[28] The crystal structures were solved by direct methods using the software package SHELXS-97 and refined against F^2 by applying the full-matrix least-squares method (SHELXL-97).^[29–31] The hydrogen positions could be determined from difference Fourier syntheses and were refined isotropically by using restraints for N–H distances. All non-hydrogen atoms were refined anisotropically. Further details of the crystal structure investigation may be obtained from Fachinformationszentrum Karlsruhe, 76344 Eggenstein-Leopoldshafen, Germany (Fax: +49-7247-808-666; E-mail: crysdata@fiz-karlsruhe.de, http://www.fiz-karlsruhe.de/request_for_deposited_data.html) on quoting the depository numbers CSD-424129 (for **2a**), -424131 (for **2b**) and -424130 (for **2c**), respectively. Powder X-ray diffraction data were collected with a Stoe STADI P

diffractometer by using Cu- $K_{\alpha 1}$ radiation. In addition to phase purity, the diffractograms show that all reflections could be indexed with the known cell parameters, and their observed intensities were in very good agreement with the calculated diffraction patterns based on single-crystal data.

General Techniques

FTIR measurements were carried out with a Bruker IFS 66v/S spectrometer. Spectra of the samples were recorded in an evacuated cell at ambient conditions between 400 and 4000 cm^{-1} after diluting the samples in KBr pellets (2 mg sample, 300 mg KBr, hand press with a pressure of 10 kN). Thermoanalytical measurements were carried out under He with a Thermoanalyzer TG-DTA92 (Setaram). The samples were heated in an alumina crucible from room temperature to 600 °C with a heating rate of 5 $\text{K}\cdot\text{min}^{-1}$. Elemental analyses for C, H, and N were performed with Vario EL and Vario Micro (Elementar Analysensysteme GmbH) elemental analyzer systems. Alkali metal and phosphorus quantification was performed by atomic emission spectrophotometry and inductively coupled plasma (ICP-AES) with a Varian-Vista simultaneous spectrometer.

Supporting Information (see footnote on the first page of this article): Figure S1 with the experimental and simulated powder X-ray diffraction patterns for **2a–c**, and Figure S2 with the DTA/TG curves of **2a–2c**.

Acknowledgements

We gratefully acknowledge financial support that was granted from the Deutsche Forschungsgemeinschaft (DFG) (project SCHN377/15-1) and from the Fonds der Chemischen Industrie (FCI) (scholarship for E. W.). We would like to thank Dr. Peter Mayer (Department Chemie, LMU München) for single-crystal data collection.

5.2.5 Bibliography

- [1] A. Rabenau, *Angew. Chem.* **1985**, *97*, 1017-1032; *Angew. Chem. Int. Ed. Engl.* **1985**, *24*, 1026-1040.
- [2] R. A. Laudise, *Chem. Eng. News* **1987**, *65*, 30-43.
- [3] C. S. Cundy, P. A. Cox, *Chem. Rev.* **2003**, *103*, 663-701.
- [4] H. Jacobs, J. Bock, *J. Less-Common Met.* **1987**, *134*, 215-220.
- [5] U. Zachwieja, H. Jacobs, *J. Less-Common Met.* **1990**, *161*, 175-184.
- [6] H. Jacobs, C. Stueve, *J. Less-Common Met.* **1984**, *96*, 323-329.
- [7] A. Denis, G. Goglio, G. Demazeau, *Mater. Sci. Eng., R* **2006**, *R50*, 167-194.
- [8] T. F. Kuech, S. Gu, R. Wate, L. Zhang, J. Sun, J. A. Dumesic, J. M. Redwing, *Mater. Res. Soc. Symp. Proc.* **2001**, *639*, G1.1/1-G1.1/11.
- [9] T. Fukuda, D. Ehrentraut, *J. Cryst. Growth* **2007**, *305*, 304-310.
- [10] H. Jacobs, D. Schmidt, *Curr. Top. Mater. Sci.* **1982**, *8*, 381-427.
- [11] H. Jacobs, R. Nymwegen, *Z. Anorg. Allg. Chem.* **1997**, *623*, 1786-1790.
- [12] H. Jacobs, R. Nymwegen, *Z. Anorg. Allg. Chem.* **1998**, *624*, 199-204.
- [13] E. Wirnhier, M. Döblinger, D. Gunzelmann, J. Senker, B. V. Lotsch, W. Schnick, *Chem. Eur. J.* **2011**, *17*, 3213-3221.
- [14] P. F. McMillan, V. Lees, E. Quirico, G. Montagnac, A. Sella, B. Reynard, P. Simon, E. Bailey, M. Deifallah, F. Corà, *J. Solid State Chem.* **2009**, *182*, 2670-2677.
- [15] Z. Zhang, K. Leinenweber, M. Bauer, L. A. J. Garvie, P. F. McMillan, G. H. Wolf, *J. Am. Chem. Soc.* **2001**, *123*, 7788-7796.
- [16] S. Correll, N. Stock, O. Oeckler, W. Schnick, *Angew. Chem.* **2003**, *115*, 3674-3677; *Angew. Chem. Int. Ed.* **2003**, *42*, 3549-3552.
- [17] S. J. Sedlmaier, M. Döblinger, O. Oeckler, J. Weber, J. Schmedt auf der Günne, W. Schnick, *Database of Zeolite Structures*: <http://www.iza-structure.org/databases/>, accessed February **2012**.
- [18] S. J. Sedlmaier, M. Döblinger, O. Oeckler, J. Weber, J. Schmedt auf der Günne, W. Schnick, *J. Am. Chem. Soc.* **2011**, *133*, 12069.
- [19] E. Wirnhier, W. Schnick, *Eur. J. Inorg. Chem.* **2012**, 1840-1847.
- [20] G. B. Seifer, *Russ. J. Coord. Chem.* **2002**, *28*, 301-324.

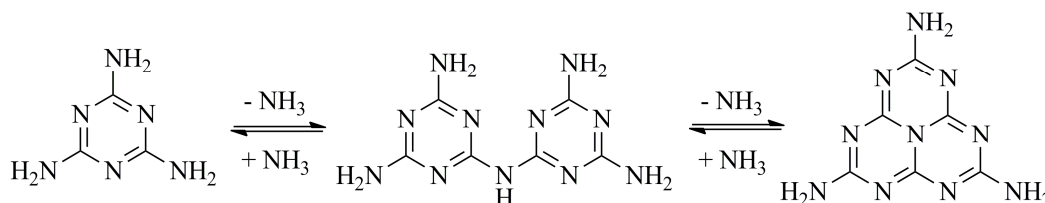
- [21] I. P. Roof, M. D. Smith, S. Park, H.-C. zur Loye, *J. Am. Chem. Soc.* **2009**, *131*, 4202-4203.
- [22] R. Niewa, F. R. Wagner, W. Schnelle, O. Hochrein, R. Kniep, *Inorg. Chem.* **2001**, *40*, 5215-5222.
- [23] R. D. Shannon, C. T. Prewitt, *Acta Crystallogr., Sect. B* **1969**, *25*, 925-946.
- [24] J. Grdadolnik, Y. Maréchal, *J. Mol. Struct.* **2002**, *615*, 177-189.
- [25] Z. Otwinowski, W. Minor, *Methods Enzymol.* **1997**, *276*, 307-326.
- [26] G. M. Sheldrick, *SADABS*, Version 2, Universität Göttingen, **2001**.
- [27] CrysAlisPro, Version 171.33.41, Oxford Diffraction, Oxford, **2009**.
- [28] SCALE3 ABSPACK (1.0.4,gui: 1.0.3) (C), Oxford Diffraction, Oxford, **2005**.
- [29] G. M. Sheldrick, *SHELXS-97*, Program for the Solution of Crystal Structures, Universität Göttingen, **1997**.
- [30] G. M. Sheldrick, *SHELXL-97*, Program for the Refinement of Crystal Structures, Universität Göttingen **1997**.
- [31] G. M. Sheldrick, *Acta Crystallogr., Sect. A* **2008**, *64*, 112-122.

6. Discussion and Outlook

6.1 On the Formation and Solvothermal Treatment of Melam

Since the first pioneering investigations by Liebig in 1834 who reported on the synthesis of melamine, melam, melem, ammeline and ammelide by pyrolysis of ammonium thiocyanate, questions on the existence and structure of melam have occupied researchers for one and a half century.^[1] Not until 2007 these questions were answered by the determination of melam's structure by single-crystal X-ray diffraction.^[2] However, marginal yields as well as the low solubility of this molecule spoiled further efforts to extend melam chemistry.

As melam is regarded a very short-lived and highly reactive intermediate in the condensation process of melamin to melem and only achievable in a narrow temperature and time range as by-product of other condensation intermediates, this thesis developed the idea of slowing down condensation rates by applying elevated ammonia pressure. According to Le Chatelier's principle, the raise of pressure shifted the equilibrium to the reactant side (Scheme 1), allowing for the isolation of nearly phase-pure bulk melam from reactions of dicyandiamide at 450 °C and 0.2 MPa ammonia pressure (4-5 days).



Scheme 1. Condensation of melamine to melam and melem by elimination of ammonia.

Together with the synthesis of melam-melem adduct phase(s) at longer reaction times of 9-12 days, which allowed insights into the condensation process from melam to melem for the first

time, the formation of melam can be regarded as a “proof of principle” of this synthesis strategy. By a very carefully adjustment of reaction conditions, also the synthesis of further melam-melem adduct phases is conceivable. The use of elevated ammonia pressure may as well permit investigations on the condensation process from melem to melon if reactions are conducted at higher temperatures. However, special autoclaves with maximal operation temperatures of $> 500\text{ }^{\circ}\text{C}$ are needed for these reactions as the condensation of melem to melon occurs not until $\sim 620\text{ }^{\circ}\text{C}$ in ampoules.^[3]

For closer insights into the nature of the herein presented melam-melem adduct phase(s) regarding quantity, composition and structure, local methods like advanced solid-state NMR spectroscopy or TEM investigations will be the methods of choice, though being very time-intensive. First attempts to solve the structure of the adduct phase(s) by ADT measurements in cooperation with Tobias Rosenthal (LMU Munich) and Dr. Tatiana Gorelik (University of Mainz) yielded a large unknown unit cell with the parameters $a = 18.97$, $b = 4.53$, $c = 21.57$ and $\beta = 105^{\circ}$. By evaluating symmetry operations and extinctions, the space group $P2_1/c$ was determined. Further investigations are in progress.

Due to the low solubility of melam in common solvents, melam chemistry was so far nearly completely restricted to solid-state syntheses. Except for melamium diperchlorate ($\text{C}_6\text{N}_{11}\text{H}_{11}(\text{ClO}_4)_2 \cdot 2\text{H}_2\text{O}$), a salt that was synthesized by reaction of melam with HClO_4 in solution,^[2] all residual completely characterized melam compounds (two melamium adducts ($\text{C}_6\text{N}_{11}\text{H}_{10}\text{Cl} \cdot 0.5\text{NH}_4\text{Cl}$, $\text{C}_6\text{N}_{11}\text{H}_{10}\text{SCN} \cdot 2\text{C}_3\text{N}_3(\text{NH}_2)_3$)^[4] and the complex $\text{Zn}[\text{C}_6\text{N}_{11}\text{H}_9]\text{Cl}_2$)^[2] were formed in ampoule reactions. However, as the synthesis of crystalline melam hydrate ($\text{C}_6\text{N}_{11}\text{H}_9 \cdot 2\text{H}_2\text{O}$) - which was so far only accessible as polycrystalline multiphased compound - has proven, the solubility of melam can be improved by hydrothermal conditions using an autoclave. Hence, new pathways for melam chemistry have developed. Both investigations on the acid-base-behavior of melam according to similar investigations on melem^[5,6] as well as the synthesis of coordination networks by reaction with transition metals in solution are feasible, extending the knowledge about this historically compound.

6.2 Polytriazine Imide – Structure and Properties

The synthesis and characterization of PTI/LiCl has enlarged the rather small field of well-defined carbon nitride networks by its so far most crystalline representative. By ionothermal synthesis in a LiCl/KCl salt melt the well-known issue of rapid condensation leading to amorphous products has been overcome, therefore allowing for an ab initio structure solution for PTI/LiCl from powder and electron diffraction for the first time in polymeric carbon nitride chemistry. Furthermore, the incorporation of Li^+ and Cl^- ions in channel-like voids is influential for increased crystallinity and should probably allow for a variation of the network for example by ion exchange or by the utilization of other salt melts. However, the

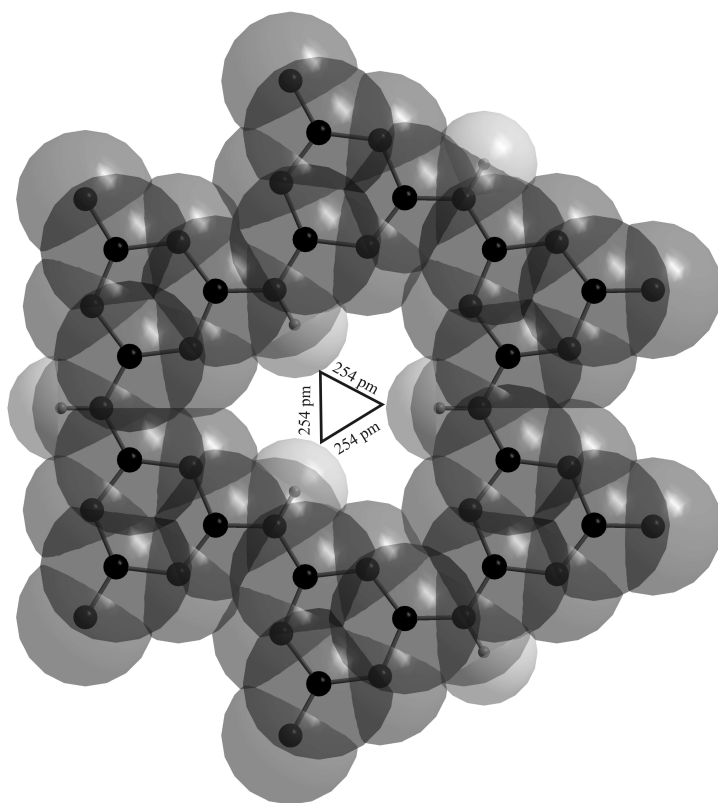


Figure 1: Space-filling model of PTI/LiCl, showing a small diameter of the voids of 254 pm after subtraction of the van der Waals radii.

insolubility of PTI/LiCl in all common solvents impedes any ion exchange reaction by solution chemistry. By reacting dicyandiamide in other salt melts (containing NaCl, KCl, ZnCl_2 e.g.), only the formation of amorphous products is observed, probably due to the small diameter of the voids (254 pm, cf. Figure 1) which allows only for the incorporation of very small cations like Li^+ or H^+ . Despite the insolubility of PTI/LiCl, soxhlet extraction with water enabled the successive extraction of Li^+ and Cl^- ions while keeping the structure of this carbon nitride imide polymer intact. Furthermore, samples with HCl incorporation and a different stacking order of the poly(triazine imide) network were presented by *McMillan* et al.^[7,8] Hence, these modification of PTI/LiCl enable both

investigations on the properties of these crystalline networks as well as their structural correlations.

Further examination of the structure of PTI/LiCl points out to the existence of Li^+/H^+ disorder phenomena regarding the occupation of the voids. Appropriate Li-N and Li-Cl distances as well as a difference Fourier synthesis were taken into account to localize Li^+ ions; however, an exact determination of the Li^+ positions by Rietveld refinement turned out to be difficult due to the elusive nature of Li. By yielding a ratio $N_{\text{tert}}/\text{NH}$ of 3.6:1 and an increased Li content, both elemental analysis and solid-state NMR investigations indicate partial deprotonation of the bridging imide units and substitution of H^+ with Li^+ , resulting in the empirical formula of $[(\text{C}_3\text{N}_3)_2(\text{NH}_x\text{Li}_{1-x})_3\cdot\text{LiCl}]$. For a more detailed description of the disorder, theoretical calculations and elaborated solid-state NMR investigations may serve, the latter probing the short-range order and the local environment of parts of the structure. Via REDOR (rotational echo double resonance) and REAPDOR (rotational echo adiabatic passage double resonance) measurements the strength of heteronuclear dipolar couplings can be examined, yielding for instance H-H, H-Li or N-Li distances which facilitate the evaluation of various theoretical models.

Band gap measurements for PTI/LiCl and samples with reduced LiCl content were conducted by means of X-ray absorption/emission spectroscopy (XAS/XES) on bulk samples and by valence electron energy loss spectroscopy (VEELS). They show strong dependence on the LiCl content and the band gap ranges from 2.2 eV to 2.9 eV by gradually reducing the amount of LiCl incorporated, explicable by theoretical calculations on the band structure. They show hybridization of the N 2p and Cl 2p states as well as a strong influence of the charge density of the hydrogen-stripped imide sites below the top of the valence band which change the N 2p \rightarrow N/C 2p transition determining the band gap. With the combination of local and bulk experimental methods on the one side and theoretical calculations on the other side a pool of methods has now been established which allows for a very exact (and explainable) determination of the band gap and the electronic structure and could now be transferred to other graphite-type carbon nitride networks like melon^[3] or PTI/HCl.^[7,8]

Hence, with a tunable band gap, PTI(LiCl) represents a promising organic semiconductor with high thermal and electrochemical stability, therefore being an auspicious candidate for photocatalytic activity not only towards water splitting. Furthermore, due to its continuous 2D

connectivity and the absence of strong interlayer forces a graphite- (and graphene?) like chemistry may be expected. Both for further investigations on various properties of PTI/LiCl (conductivity, HOMO/LUMO level) as well as for possible (opto-)electronical applications as coatings, membranes or sensors the processability of this compound needs to be extended. The deposition of thin films is advantageous in many respects and may be accessible by various spin, dip or spray coating methods or by layer-by-layer (LbL) deposition.

6.3 Phosphorus-doped Carbon Nitride Precursors

Since the first use of carbon nitride type materials as metal-free heterogeneous catalysts in 2006,^[9,10] this class of compounds has attracted much attention owing to medium-bandgap semiconducting properties leading to a high efficiency in photocatalytical applications. As chemical doping is regarded as a capable strategy for tuning physicochemical properties of the mother compounds, several attempts to improve the attributes of carbon nitrides by introducing sulfur,^[11] boron,^[12] fluorine^[13] and phosphorus have been reported.^[14] Although no structure elucidation is given for these examples, structure models based on *s*-heptazine units with single nitrogen or carbon atoms replaced by foreign atoms are proposed for these compounds, which were synthesized by copolymerization or post-functionalization of carbon nitride networks.

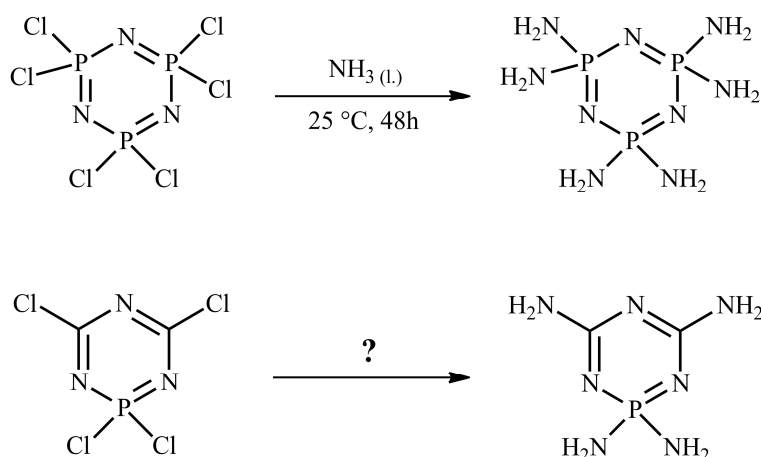
Within this thesis, another approach towards phosphorus-doped carbon nitride materials was persecuted. As the intermediates melamine and melem as well as the final condensation product melon are very stable thermodynamical drains in the condensation process to carbon nitrides, the synthesis of well-defined C/N/P-networks by a targeted exchange of several atoms by the methods outlined above seems rather improbable. By contrast, precursor molecules exhibiting the 1-phospha-2,4,6-*s*-triazine core are promising candidates for the synthesis of crystalline networks and were examined regarding functionalization and thermal behavior. With the phosphorus atom embedded in the *s*-triazine ring (“endocyclic doping”), the synthesis of well-defined networks with evenly distributed phosphorus according to the synthesis of “pure” C/N/H polymers was considered meaningful.

With the alkali and alkaline earth biuretooxophosphates presented in Chapter 5, a first class of compounds consisting of an 1-phospha-2,4,6-*s*-triazine core was examined with regards to their applicability as precursors for the synthesis of well-defined C/N/P/(O) networks. Being intermediates between carbon nitride and phosphorus nitride precursors (cyanurates and trimetaphosphimates), investigations on the thermal treatment of these precursors yielded valuable information on the stability of C/N/P/(O) compounds. At ambient conditions, biuretooxophosphates were proven to be stable up to at most 375 °C before decomposing into the corresponding metaphosphates (MPO₃)_x, indicating a breakup of the ring next to the phosphorus atom. The residual ring components are released in form of gaseous byproducts like CO₂, HNCO and NH₃. Hence, regarding the stability of the generated phosphates and byproducts, the formation of phosphorus-doped carbon nitride networks by condensation (or copolymerization) reactions under ambient conditions and in air can rather be excluded. However, especially the formation of gaseous byproducts leads to the assumption that – according to Le Chatelier’s principle – the use of elevated pressure may be the method of choice to impede the decomposition of the preorganized CNP ring at higher temperatures which are necessary for the formation of networks. The same also applies for a second class of precursors, the *N,N'*-bis(aminocarbonyl)-phosphorodiamidates which were synthesized by ammonolysis of the corresponding biuretooxophosphates and decompose to metaphosphates at elevated temperatures as well.

Reactions under elevated pressure can be realized by various methods. One way are solvothermal syntheses by the usage of supercritical fluids combined with autoclave technique. Established solvents are water, carbon dioxide or ammonia, the latter one leading to the formation of the *N,N'*-bis(aminocarbonyl)-phosphorodiamidates by high-temperature treatment of the biuretooxophosphates as presented in Chapter 5.2. Good solvating properties and a low viscosity are important advantages provided by supercritical fluids, probably leading to the formation of more new interesting and crystalline C/N/P/(O) compounds. For the synthesis of networks, however, reaction temperatures achievable in autoclaves are not high enough. Most commercialized autoclaves are designed for temperatures up to 300 °C; a maximum temperature of 500 °C is accessible for the autoclaves used in this work. Although amorphous carbon nitride networks are already formed at 500 °C in open systems, even the ammonia partial pressure arising from condensation reactions in ampoules increases the temperature necessary for the formation of networks to at least 600 °C. As the pressure in

autoclaves is much higher than in ampoules, temperatures significantly above 600 °C are probably needed for the formation of networks in autoclave reactions.

Another method to achieve high pressure and high temperature conditions simultaneously is the multianvil technique. Pressure is generated mechanically, thus excluding reactions of the precursor with the solvent. First attempts in a low pressure range (up to 5 GPa) indicate that the stability of the formed phosphates may be the crucial factor impeding the formation of C/N/P/(O) networks. A comparison of the binding energies of P-O and P-N bonds^[15] leads to the assumption, that a precursor consisting only of the elements C, N, P (and H) may rather enable the formation of a stable C/N/P network than a oxygen containing one. Keeping the idea of the 1-phospha-2,4,6-*s*-triazine core being the most promising candidate for the formation of such networks, a probably very convenient precursor for this approach is, in



Scheme 2. Top: synthesis of hexaaminocyclotriphosphazene from hexachlorocyclotriphosphazene by reaction with liquid ammonia in an autoclave according to [16]. Bottom: 1,1,3,5 tetrachloro-1-phospha-2,4,6-*s*-triazine as possible starting material for the synthesis of 1,1,3,5 tetraamino-1-phospha-2,4,6-*s*-triazine.

(according to the synthesis of hexaaminocyclotriphosphazene from hexachlorocyclotriphosphazene^[16]) led to the decomposition of the CNP ring and spoiled therefore subsequent condensation reactions. However, further experiments adjusting reaction conditions or using other amination reagents should allow for the synthesis of this promising precursor and enable the preparation of crystalline C/N/P networks.

analogy with melamine for the synthesis of carbon nitride networks, 1,1,3,5 tetraamino-1-phospha-2,4,6-*s*-triazine (Scheme 1).

According to database research, this compound has not been synthesized yet. First attempts to prepare this precursor by reaction of 1,1,3,5 tetrachloro-1-phospha-2,4,6-*s*-triazine with ammonia

6.4 Bibliography

- [1] J. Liebig, *Ann. Pharm.* **1834**, *10*, 1.
- [2] B. V. Lotsch, W. Schnick, *Chem. Eur. J.* **2007**, *13*, 4956-4968.
- [3] B. V. Lotsch, M. Döblinger, J. Sehnert, L. Seyfarth, J. Senker, O. Oeckler, W. Schnick, *Chem. Eur. J.* **2007**, *13*, 4969-4980.
- [4] N. E. Braml, A. Sattler, W. Schnick, *Chem. Eur. J.* **2012**, *18*, 1811-1819.
- [5] A. Sattler, L. Seyfarth, J. Senker, W. Schnick, *Z. Anorg. Allg. Chem.* **2005**, *631*, 2545-2554.
- [6] A. Sattler, W. Schnick, *Z. Anorg. Allg. Chem.* **2008**, *634*, 457-460.
- [7] P. F. McMillan, V. Lees, E. Quirico, G. Montagnac, A. Sella, B. Reynard, P. Simon, E. Bailey, M. Deifallah, F. Corà, *J. Solid State Chem.* **2009**, *182*, 2670-2677.
- [8] Z. Zhang, K. Leinenweber, M. Bauer, L. A. J. Garvie, P. F. McMillan, G. H. Wolf, *J. Am. Chem. Soc.* **2001**, *123*, 7788-7796.
- [9] F. Goettmann, A. Fischer, M. Antonietti, A. Thomas, *Angew. Chem.* **2006**, *118*, 4579-4583; *Angew. Chem. Int. Ed.* **2006**, *45*, 4467-4471.
- [10] F. Goettmann, A. Fischer, M. Antonietti, A. Thomas, *Chem. Commun.* **2006**, 4530-4532.
- [11] G. Liu, P. Niu, C. H. Sun, S. C. Smith, Z. G. Chen, G. X. Lu, H. M. Cheng, *J. Am. Chem. Soc.* **2010**, *132*, 11642-11648.
- [12] Y. Wang, H. R. Li, J. Yao, X. C. Wang, M. Antonietti, *Chem. Sci.* **2011**, *2*, 446-450.
- [13] Y. Wang, Y. Di, M. Antonietti, H. R. Li, X. F. Chen, X. C. Wang, *Chem. Mater.* **2010**, *22*, 5119-5121.
- [14] Y. Zhang, T. Mori, J. Ye, M. Antonietti, *J. Am. Chem. Soc.* **2010**, *132*, 6294-6295.
- [15] E. Riedel, *Anorganische Chemie*, 6th Ed., de Gruyter, **2004**, 119.
- [16] D. B. Sowerby, L. F. Audrieth, *Chem. Ber.* **1961**, *94*, 2670-2675.

7. Appendix

7.1 Supporting Information

7.1.1 Supporting information for Chapter 4.3

Experimental Section

Photocatalysis. 1 mg mL⁻¹ aqueous solutions of carbon nitride catalyst were prepared and dispersed with an ultrasonic bath for 30 min. Triethanolamine (TEoA) was used as a sacrificial electron donor and H₂PtCl₆ (8 wt% in H₂O) was used as the Pt co-catalyst precursor which was photo-reduced during the reaction. Suspensions with 10 vol% TEoA and 6 μL H₂PtCl₆ (2.3 wt% Pt) were illuminated in 24 mL glass vials in an argon atmosphere with PTFE/Teflon septa. Samples were side-illuminated with a 300 W Xenon lamp with a water filter and dichroic mirror blocking wavelengths < 420 nm. The evolved gas was measured by gas chromatography with an online injection system and using a thermal conductivity detector with argon as carrier gas.

Synthesis of PTI/Li⁺Cl⁻ according to Wirnhier et al.^[S1,S2] Dicyandiamide (0.20 g, 2.38 mmol) and an eutectic mixture of lithium chloride (59.2 mol%, 0.90 g, 21.33 mmol) and potassium chloride (40.8 mol%, 1.01 g, 14.70 mmol) were ground together in a glovebox. The reaction mixture was transferred into a dried thick-walled silica glass tube ($\phi_{\text{ext.}}$ 15 mm, $\phi_{\text{int.}}$ 11 mm). The tube was placed in a vertical tube furnace and heated under atmospheric argon pressure at 6°C min⁻¹ to 400°C. This temperature was held for 12 h and afterwards the sample was cooled to room temperature at 20°C min⁻¹. After this procedure, the tube was evacuated and sealed at a length of 120 mm. In a second step the ampoule was placed in a vertical tube furnace and heated at 1°C min⁻¹ to 600°C at which the sample was held for 24 h. After

cooling down to room temperature the ampoule was broken and the sample was isolated and washed with boiling water to remove residual salt. The resulting material $\text{PTI}/\text{Li}^+\text{Cl}^-$ was obtained as a brown powder (80 mg, 50%).

Synthesis of aPTI using a modified procedure reported by Wirnhier et al.^[S1,S2] Dicyandiamide (1.00 g, 11.90 mmol) and an eutectic mixture of lithium chloride (59.2 mol%, 2.26 g, 53.56 mmol) and potassium chloride (40.8 mol%, 2.74 g, 39.88 mmol) were ground together in a glovebox. The reaction mixture was transferred in open porcelain crucibles which were heated either in an argon-purged tube- or muffle furnace at $12^\circ\text{C min}^{-1}$ to 400 – 600°C. The temperature was held for 6 h and afterwards the samples were cooled down to room temperature. The samples were isolated and washed with boiling water to remove residual salts. The resulting materials yielded beige (0.70 g, 88%) to yellow colored powders (0.30 g, 38%).^[a]

Synthesis of doped amorphous PTI using a modified procedure reported by Wirnhier et al.^[S1,S2] Dicyandiamide (0.50 g, 5.95 mmol), an eutectic mixture of lithium chloride (59.2 mol%) and potassium chloride (40.8 mol%) and 4AP as doping agent (2, 8, 16, 32 or 64%) were ground and transferred in open porcelain crucibles, which were heated in a muffle furnace at 400 – 600°C for 6 hours. The syntheses yielded yellow (0.30 g, 75%) to dark orange colored products (0.16 g, 40%).^[a]

^[a] Yields in percentage are based on crystalline PTI and can be considered as an approximate value.

Synthesis of raw melon according to Sattler et al.^[S3] A porcelain crucible was loaded with melamine (20 g) and covered with a porcelain lid. The crucible was placed in a muffle furnace and maintained at 490°C for 4 days. The product was ground to a powder and homogenized after the first day.

Synthesis of “g-C₃N₄” according to Zhang et al.^[S4] A porcelain crucible was loaded with dicyandiamide and heated in a muffle furnace at 600°C for 4 hours. The synthesis yielded a yellow colored powder.

Methods

X-ray powder diffraction. X-ray powder diffraction experiments were carried out on a Huber G670 diffractometer in Guinier geometry using Ge(111)-monochromatized Cu-K $_{\alpha 1}$ -radiation ($\lambda = 1.54051 \text{ \AA}$). The specimen was ground in a mortar and evenly spread between two chemplexfoils (Breitlänger GmbH).

IR-spectroscopy. FTIR spectra were recorded on a Perkin Elmer Spektrum BX II spectrometer with an attenuated total reflectance unit.

NMR-spectroscopy. The ^{13}C and ^{15}N MAS NMR spectra were recorded at ambient temperature on an Avance 500 solid-state NMR spectrometer (Bruker) with an external magnetic field of 11.7 T, operating at frequencies of 500.1 MHz, 125.7 MHz and 50.7 MHz for ^1H , ^{13}C and ^{15}N , respectively. The sample was contained in a 4 mm ZrO $_2$ rotor which was mounted in a standard double resonance MAS probe (Bruker). The ^{13}C and ^{15}N chemical shifts were referenced relative to TMS and nitromethane.

The $^1\text{H}^{15}\text{N}$ and $^1\text{H}^{13}\text{C}$ cross-polarization (CP) MAS spectra were recorded at a spinning speed of 10 kHz using a ramped-amplitude (RAMP) CP pulse on ^1H , centered on the $n = +1$ Hartmann-Hahn condition, with a nutation frequency ν_{nut} of 55 kHz (^{15}N) and 40 kHz (^{13}C). During a contact time of 7 ms the ^1H RF field was linearly varied about 20%.

The ^{15}N cross polarization combined with polarization inversion (CPPI) NMR spectrum was recorded at a spinning frequency of 6 kHz using a contact time of 7 ms and an inversion time of 400 μs . Constant amplitude CP pulses were applied on ^{15}N ($\nu_{\text{nut}} = 55 \text{ kHz}$) and ^1H ($\nu_{\text{nut}} = 50 \text{ kHz}$).

In all ^{15}N NMR experiments, a flip-back (FB)^[55] pulse was applied on ^1H after the acquisition of the FID, so that the recycle delay becomes less dependent of the ^1H T_1 relaxation time. ^1H continuous wave (CW) decoupling (ca 70 kHz RF field) was applied during the acquisition of the ^{15}N signal. The recycle delay was set to 1.5 s. About 47500 and 121000 transients were accumulated for the CP and CPPI experiments, respectively.

Diffuse reflectance measurements. Optical diffuse reflectance spectra were collected at room temperature with a UV/VIS diffuse reflectance spectrometer (Varian, Cary 500). Powders were prepared between two quartz discs at the edge of the integrating sphere with BaSO $_4$ as

the optical standard. Absorption spectra were calculated from the reflectance data with the Kubelka-Munk function.

TEM. HRTEM was performed with a Philips CM 30 ST microscope (LaB₆ cathode, 300 kV, CS = 1.15 mm). Images were recorded with a CCD camera (Gatan) and Digital Micrograph 3.6.1 (Gatan) was used as evaluation software. Chemical analyses (EDX) were performed with a Si/Li detector (Thermo Fisher, Noran System Seven).

Adsorption measurements. Nitrogen adsorption measurements were performed at 77 K with an Autosorb iQ instrument (Quantachrome Instruments, Boynton Beach, Florida, USA). Samples were outgassed in vacuum at 300°C for 12 h. For BET calculations pressure ranges were chosen with the help of the BET Assistant in the ASiQwin software (version 2.0). In accordance with the ISO recommendations multipoint BET tags equal or below the maximum in $V \cdot (1 - P/P_0)$ were chosen.

Quantum efficiency. The quantum efficiency was calculated according to $QE\% = (2 \times H)/P \times 100/1$, where H = number of evolved H₂ molecules and P = incident number of photons on the sample. The incident light was measured with a thermopile power meter with a constant efficiency response across the visible spectrum. Wavelength specific hydrogen evolution was measured with 40 nm FWHM light filters (Thor labs) and with the same incident light and filter transmission efficiency for each filter.

Elemental analysis. Elemental analysis of the elements C, H, N and S is accomplished by high temperature digestion coupled with dynamic gas components separation. The samples are burned explosively at 1150°C in a highly oxygenated helium atmosphere. The combustion products are CO₂, H₂O, H₂, NO, NO₂, SO₂ and SO₃. The detection of the gases is done by a thermal conductivity measurement cell. The accuracy is 0.30 %. Measurements were done on an Elementar vario EL. The determination of oxygen was done under inert conditions at high temperature (1200 – 1400°C).

Table S1. Elemental analysis of aPTI synthesized air (muffel) or inert atmosphere (Ar-tube) at 400 – 600°C compared to PTI/Li⁺Cl⁻ and melon. The arrow indicates an increasing C/N atomic ratio.

Sample	Oven	Temperature [°C]	C [wt%]	N [wt%]	H [wt%]	C/N/H	C/N
PTI/Li ⁺ Cl ⁻	tube	600	29.6	50.4	1.3	C _{3.0} N _{4.4} H _{1.6}	0.68
melon	muffel	490	33.2	62.7	1.8	C _{3.0} N _{4.9} H _{1.9}	0.62
aPTI _{400°C}	muffel	400	26.9	46.6	2.8	C _{3.0} N _{4.5} H _{3.7}	0.67
aPTI _{450°C}	muffel	450	27.1	46.6	3.0	C _{3.0} N _{4.4} H _{4.0}	0.68
aPTI _{500°C}	muffel	500	24.7	41.9	2.5	C _{3.0} N _{4.4} H _{3.6}	0.69
aPTI _{550°C}	muffel	550	22.0	36.6	2.8	C _{3.0} N _{4.3} H _{4.6}	0.70
aPTI _{400°C}	Ar-tube	400	27.9	50.8	3.2	C _{3.0} N _{4.7} H _{4.1}	0.64
aPTI _{450°C}	Ar-tube	450	21.6	36.5	2.6	C _{3.0} N _{4.3} H _{4.3}	0.69
aPTI _{500°C}	Ar-tube	500	25.9	43.8	2.4	C _{3.0} N _{4.4} H _{3.3}	0.69
aPTI _{550°C}	Ar-tube	550	26.5	45.3	2.0	C _{3.0} N _{4.4} H _{2.7}	0.68
aPTI _{600°C}	Ar-tube	600	26.8	45.4	2.1	C _{3.0} N _{4.4} H _{2.8}	0.69

Table S2. Elemental analysis of aPTI_4AP synthesized at 400 – 600°C compared to PTI/Li⁺Cl⁻ and melon. The arrows indicate an increasing C/N atomic ratio.

Sample	Temperature [°C]	4AP [%]	C [wt%]	N [wt%]	H [wt%]	C/N/H	C/N
PTI/Li ⁺ Cl ⁻	600	0	29.6	50.4	1.3	C _{3.0} N _{4.4} H _{1.6}	0.68
melon	490	0	33.2	62.7	1.8	C _{3.0} N _{4.9} H _{1.9}	0.62
aPTI_4AP _{16%}	400	16	28.7	46.7	2.6	C _{3.0} N _{4.2} H _{3.2}	0.72
aPTI_4AP _{16%}	450	16	30.3	47.4	2.5	C _{3.0} N _{4.0} H _{3.0}	0.74
aPTI_4AP _{16%}	500	16	29.8	46.3	2.4	C _{3.0} N _{4.0} H _{2.9}	0.75
aPTI_4AP _{16%}	550	16	30.5	43.5	2.6	C _{3.0} N _{3.7} H _{3.1}	0.82
aPTI_4AP _{16%} ^[a]	550	16	30.1	42.2	2.9	C _{3.0} N _{3.6} H _{3.5}	0.83
aPTI_4AP _{2%}	550	2	29.2	49.0	2.4	C _{3.0} N _{4.3} H _{2.9}	0.69
aPTI_4AP _{8%}	550	8	29.8	48.3	2.3	C _{3.0} N _{4.2} H _{2.8}	0.72
aPTI_4AP _{16%}	550	16	30.5	43.5	2.6	C _{3.0} N _{3.7} H _{3.1}	0.82
aPTI_4AP _{32%}	550	32	28.2	35.9	2.7	C _{3.0} N _{3.3} H _{3.4}	0.92
aPTI_4AP _{64%}	550	64	35.5	36.8	2.6	C _{3.0} N _{2.7} H _{2.6}	1.13

[a] after illumination for 15 hours.

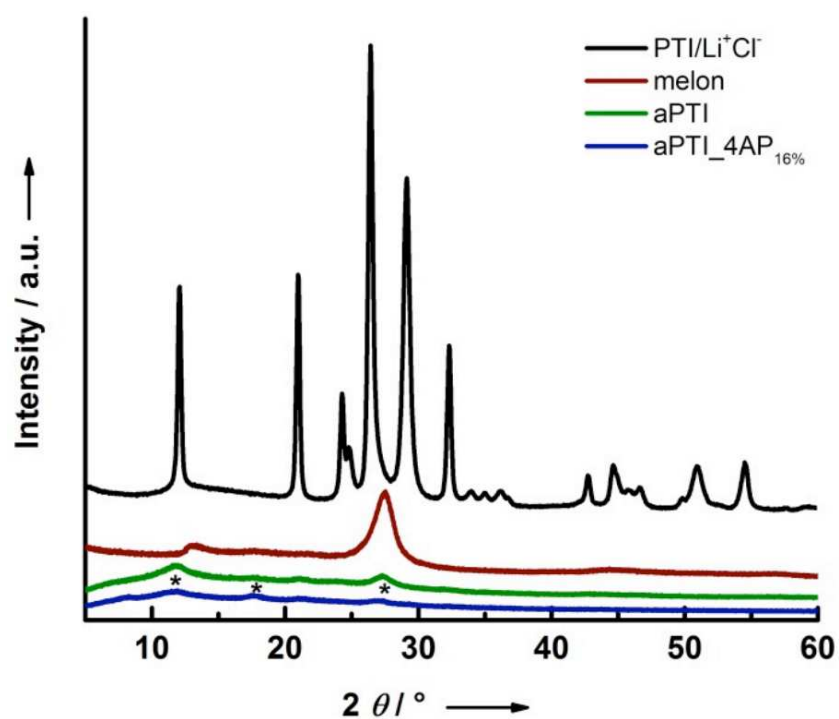


Figure S1. PXRD patterns of aPTI_{4AP}_{16%} synthesized at 550°C, compared to crystalline PTI/Li⁺Cl⁻, aPTI_{500°C} and melon. The reflections marked with an asterisk are assigned to artifacts caused by the plastic sample holder.

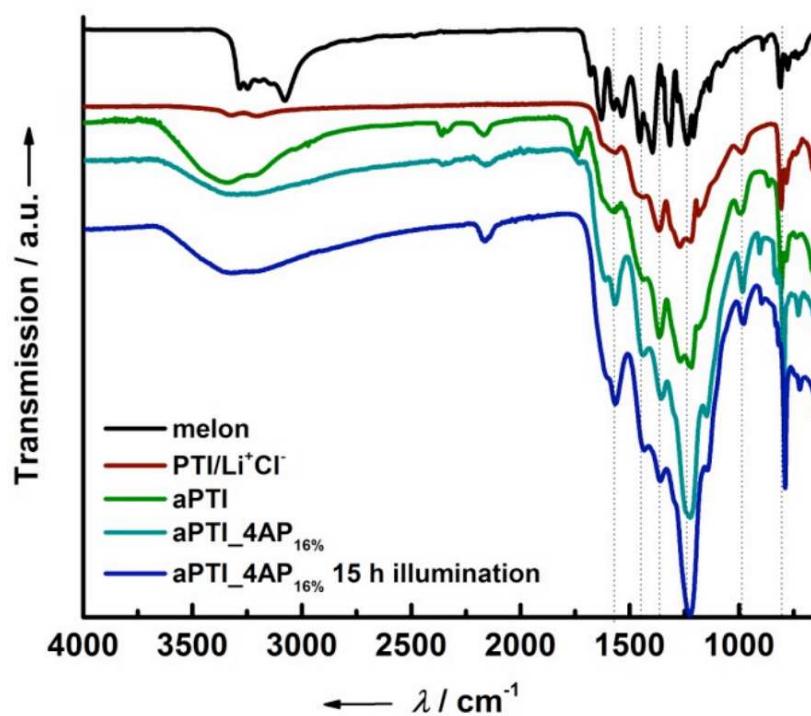


Figure S2. FTIR spectra of aPTI_{4AP}_{16%} synthesized at 550°C before and after 15 h illumination, compared to crystalline PTI/Li⁺Cl⁻, aPTI_{500°C} and melon.

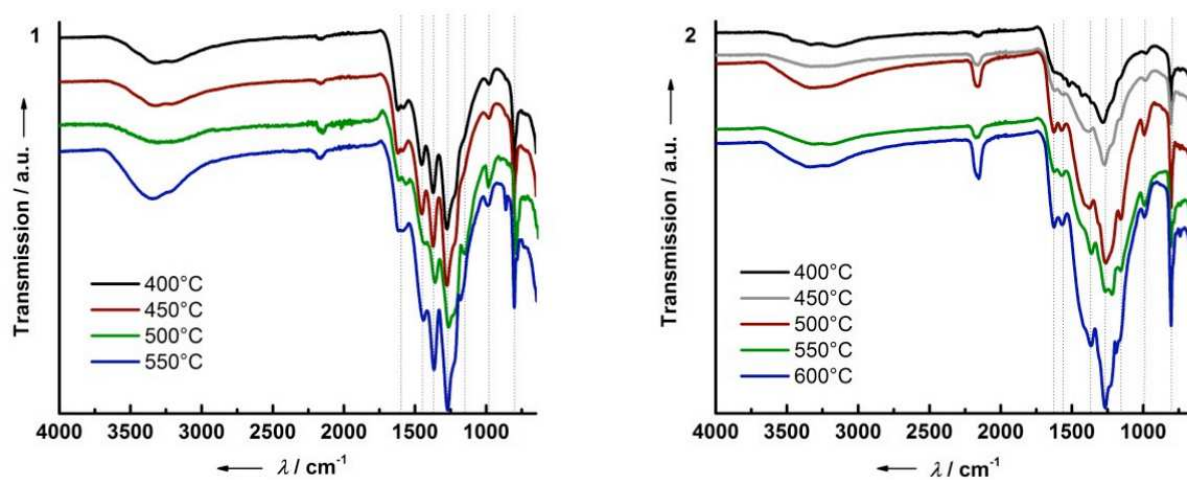


Figure S3. FTIR spectra of aPTI synthesized at 400 – 600°C in 1) air and 2) inert atmosphere.

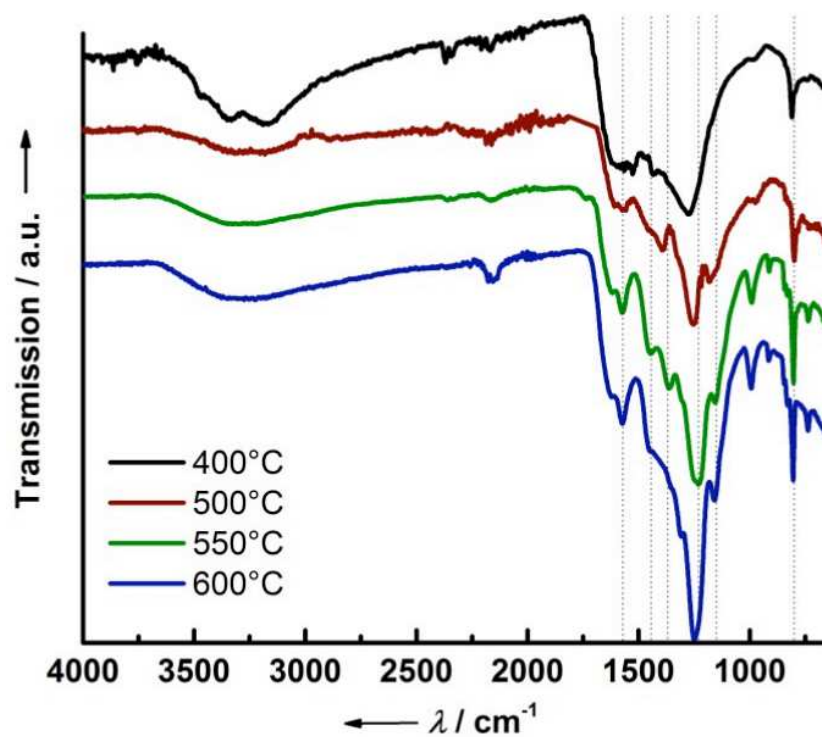


Figure S4. FTIR spectra of aPTI_{4AP16%} synthesized at 400 – 600°C.

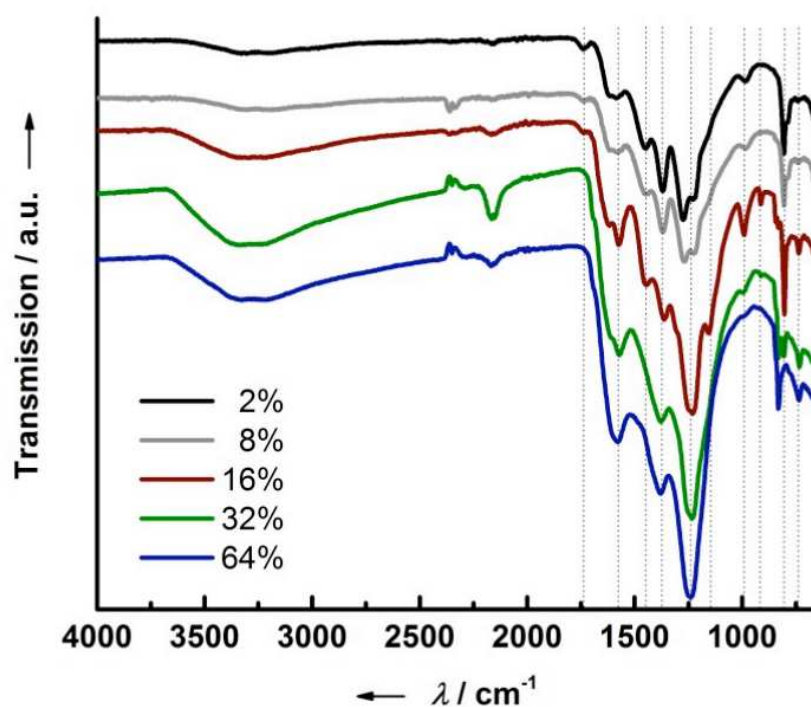


Figure S5. FTIR spectra of aPTI_{4AP}_{2-64%} synthesized at 550°C.

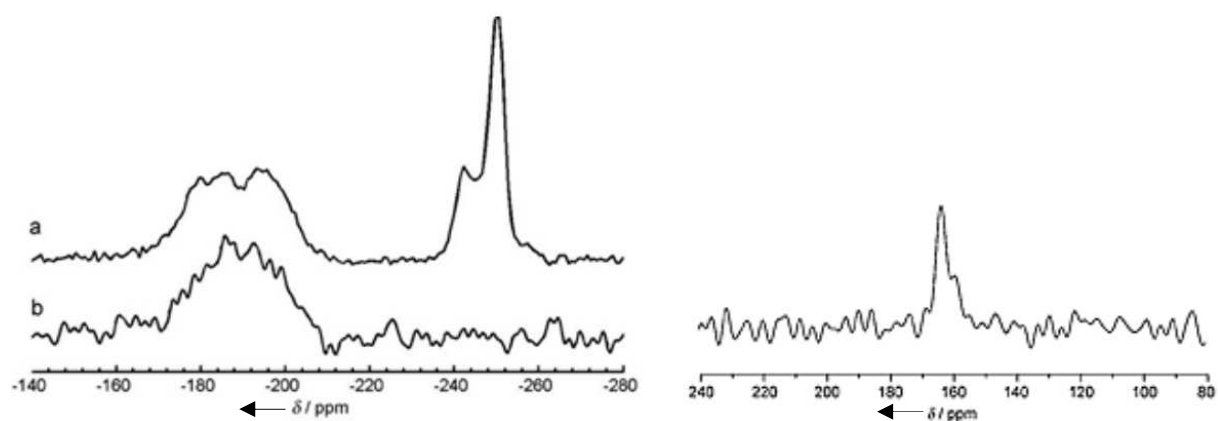


Figure S6. Left: ^{15}N CP-MAS NMR spectrum of PTI/ Li^+Cl^- (a) and a ^{15}N CPPI experiment with attenuation of NH_x signals (b). Right: ^{13}C CP-MAS NMR spectra recorded with 0.5 ms contact time.

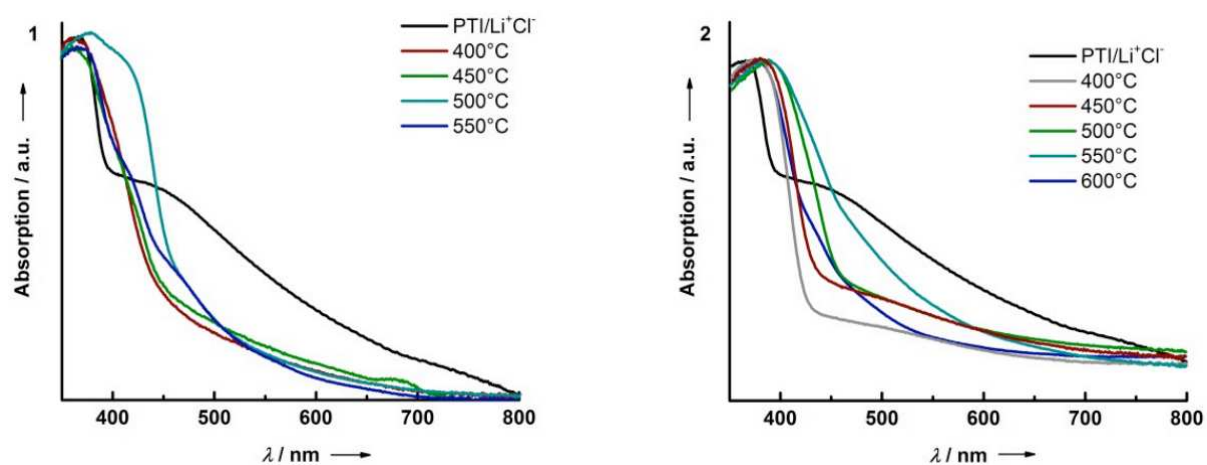


Figure S7. UV/Vis diffuse reflectance absorption spectra of aPTI synthesized at 400 – 600°C in 1) air and 2) inert atmosphere compared to crystalline PTI/Li⁺Cl⁻.

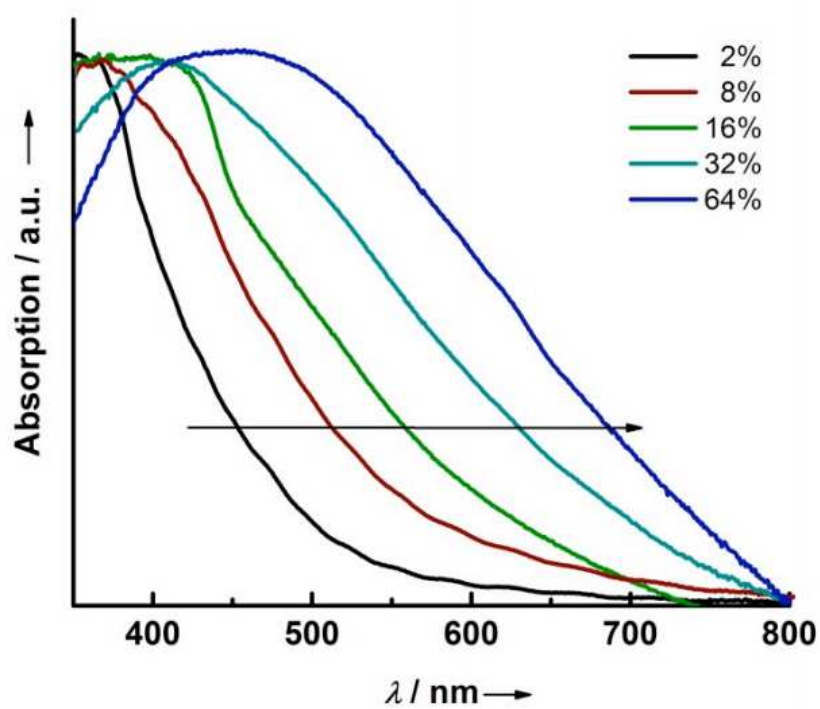


Figure S8. UV/Vis diffuse reflectance absorption spectra of aPTI_{4AP_{2-64%}} synthesized at 550°C.

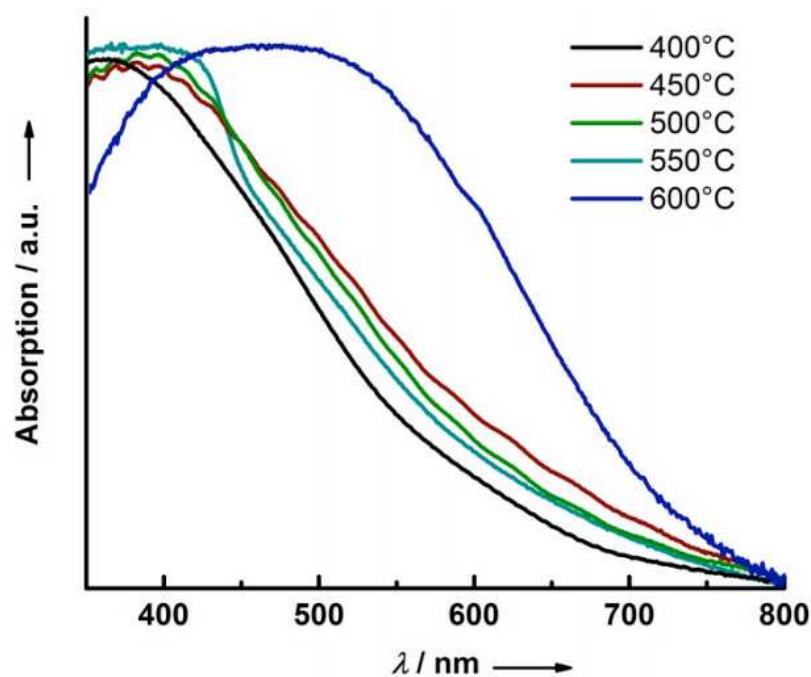


Figure S9. UV/Vis diffuse reflectance absorption spectra of aPTI_{4AP}_{16%} synthesized at 400 – 600°C.

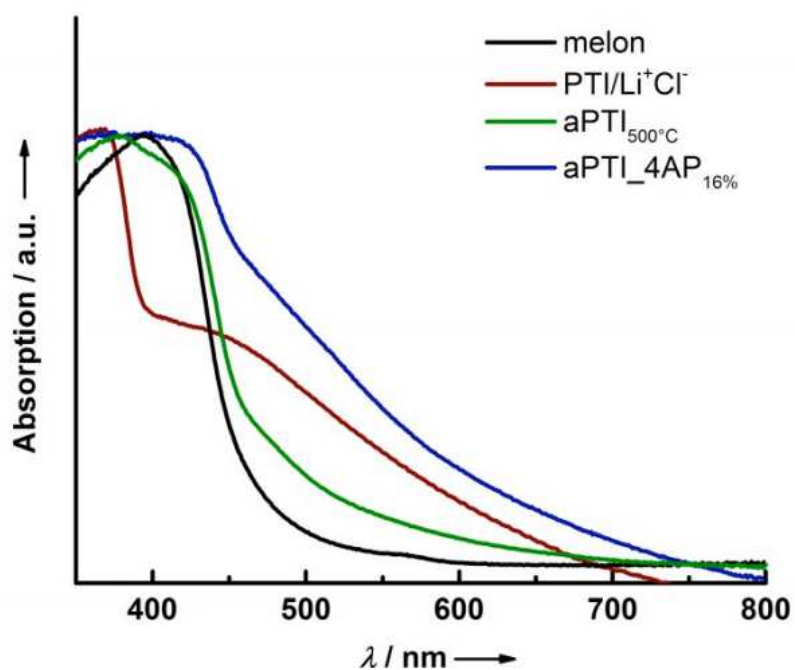


Figure S10. UV/Vis diffuse reflectance absorption spectra of aPTI_{4AP}_{16%} synthesized at 550°C, compared to crystalline PTI/Li⁺Cl⁻, aPTI synthesized at 550°C and melon.

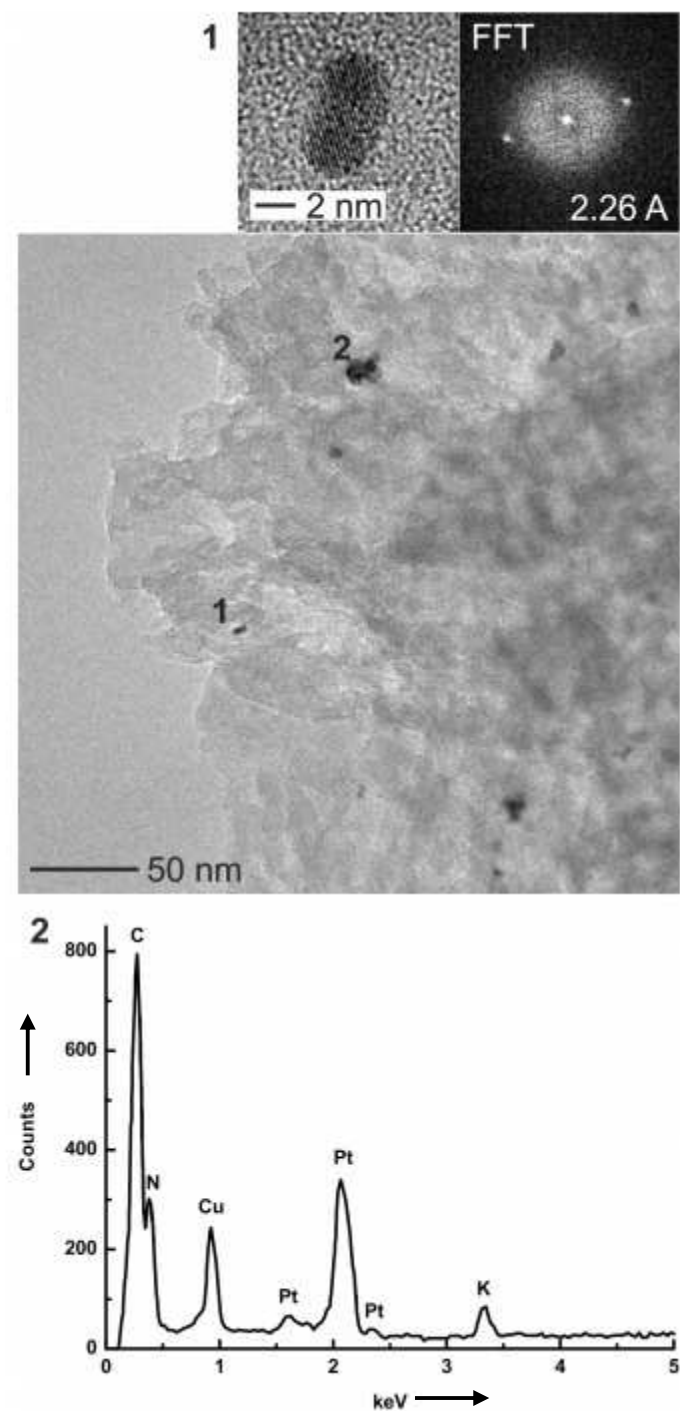


Figure S11. (1) A typical image of 2.3 wt% Pt-loaded aPTI_4AP after illumination for 3 h under visible light ($\lambda > 420$ nm), at higher magnification (top left) and its corresponding FFT (top right). The lattice planes correspond to elemental Pt. (2) The EDX spectrum of sample location 2 is shown below.

Synthesis of aPTI at elevated reaction temperatures (550 – 600°C) under inert atmosphere resulted in better photocatalytic activity of CNs than in air. On the other hand, synthesis at lower temperatures (400 – 500°C) in air resulted in marginally better photocatalytic activity compared to inert atmosphere conditions (Figure S12).

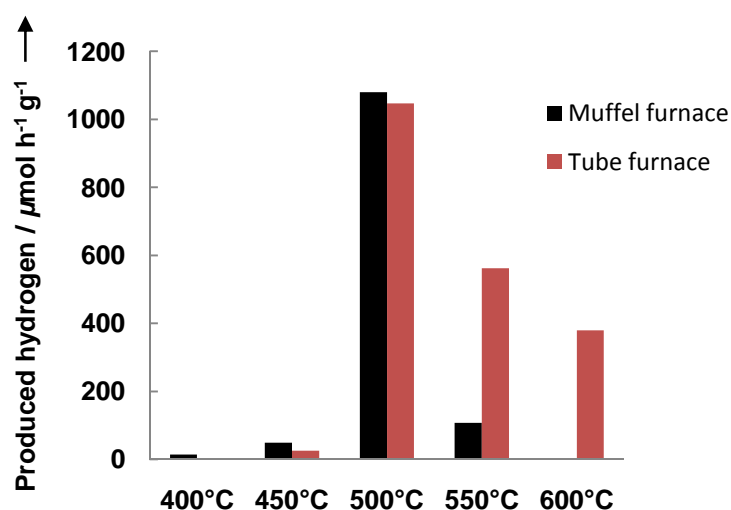


Figure S12. Photocatalytic activity of aPTI synthesized at 400 – 600°C in air (muffle furnace) or argon atmosphere (tube furnace).

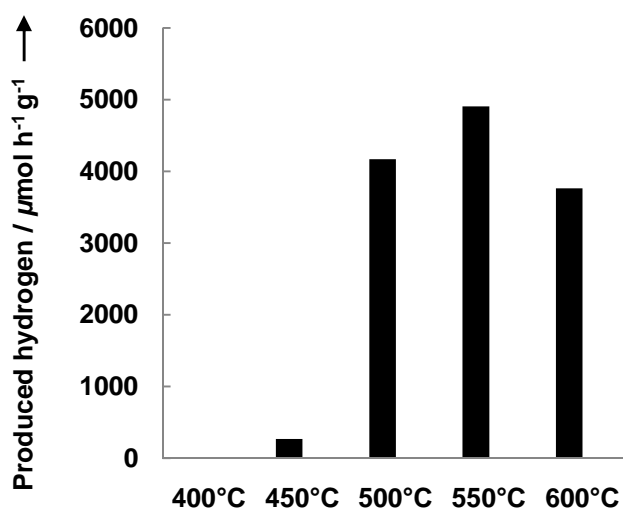


Figure S13. Photocatalytic activity towards hydrogen production of aPTI_{4AP_{16%}} synthesized at 400 – 600°C.

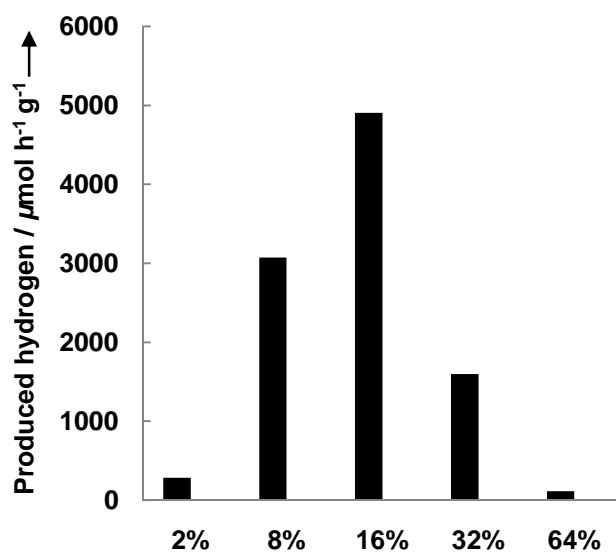


Figure S14. Photocatalytic activity towards hydrogen production of aPTI_4AP_{2-64%} synthesized at 550°C.

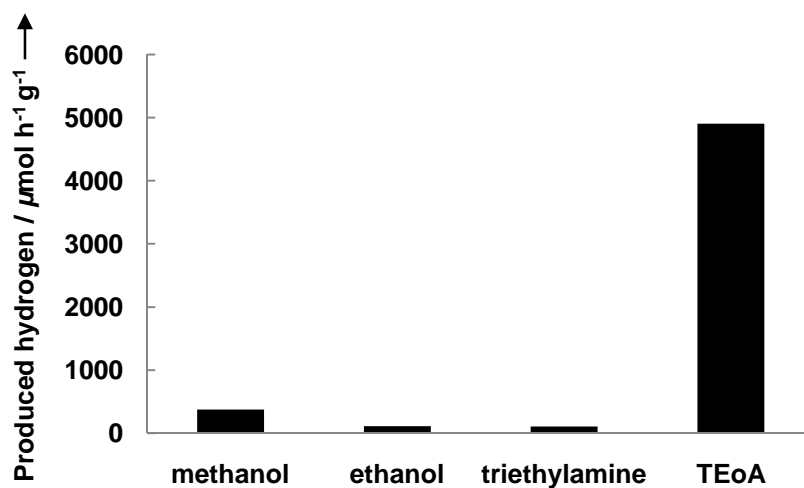


Figure S15. Steady rate of hydrogen production from water containing various electron donors (triethylamine, methanol, ethanol, triethanolamine TEoA; 10 vol%) under visible light ($\lambda > 420 \text{ nm}$) by 2.3 wt% Pt-loaded aPTI_4AP_{16%}.

Bibliography

- [S1] E. Wirnhier, M. Döblinger, D. Gunzelmann, J. Senker, B. V. Lotsch, W. Schnick, *Chem. Eur. J.* **2011**, *17*, 3213-3221.
- [S2] M. J. Bojdys, J.-O. Müller, M. Antonietti, A. Thomas, *Chem. Eur. J.* **2008**, *14*, 8177-8182.
- [S3] A. Sattler, Doctoral Thesis, University of Munich (LMU), **2010**.
- [S4] J. Zhang, X. Chen, K. Takanahe, K. Maeda, K. Domen, J. D. Epping, X. Fu, M. Antonietti, X. Wang, *Angew. Chem. Int. Ed.* **2010**, *49*, 441-444.
- [S5] (a) J. Tegenfeldt, U. Haeberlen, *J. Magn. Reson.* **1979**, *36*, 453-57; (b) K. Saito, C. Martineau, G. Fink, F. Taulelle, *Solid State Nucl. Mag.* **2011**, *40*, 66-71.

7.1.2 Supporting information for Chapter 5.1

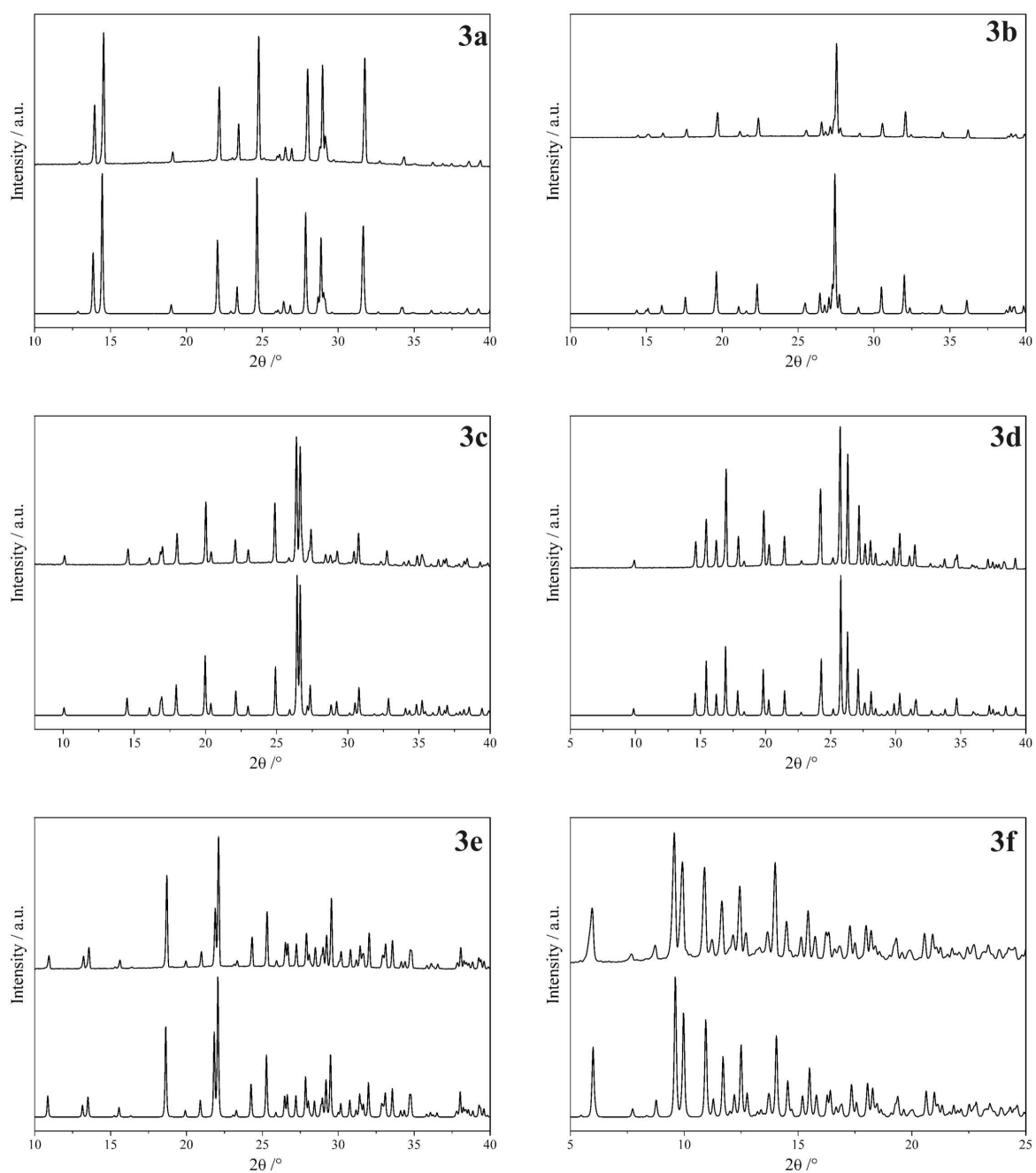


Figure S1. Powder X-ray diffraction patterns (**3a-e**: Cu- $K_{\alpha 1}$, **3f**: Mo- $K_{\alpha 1}$) of the alkali biuretooxophosphates **3a-f** (top: experimental, bottom: simulated).

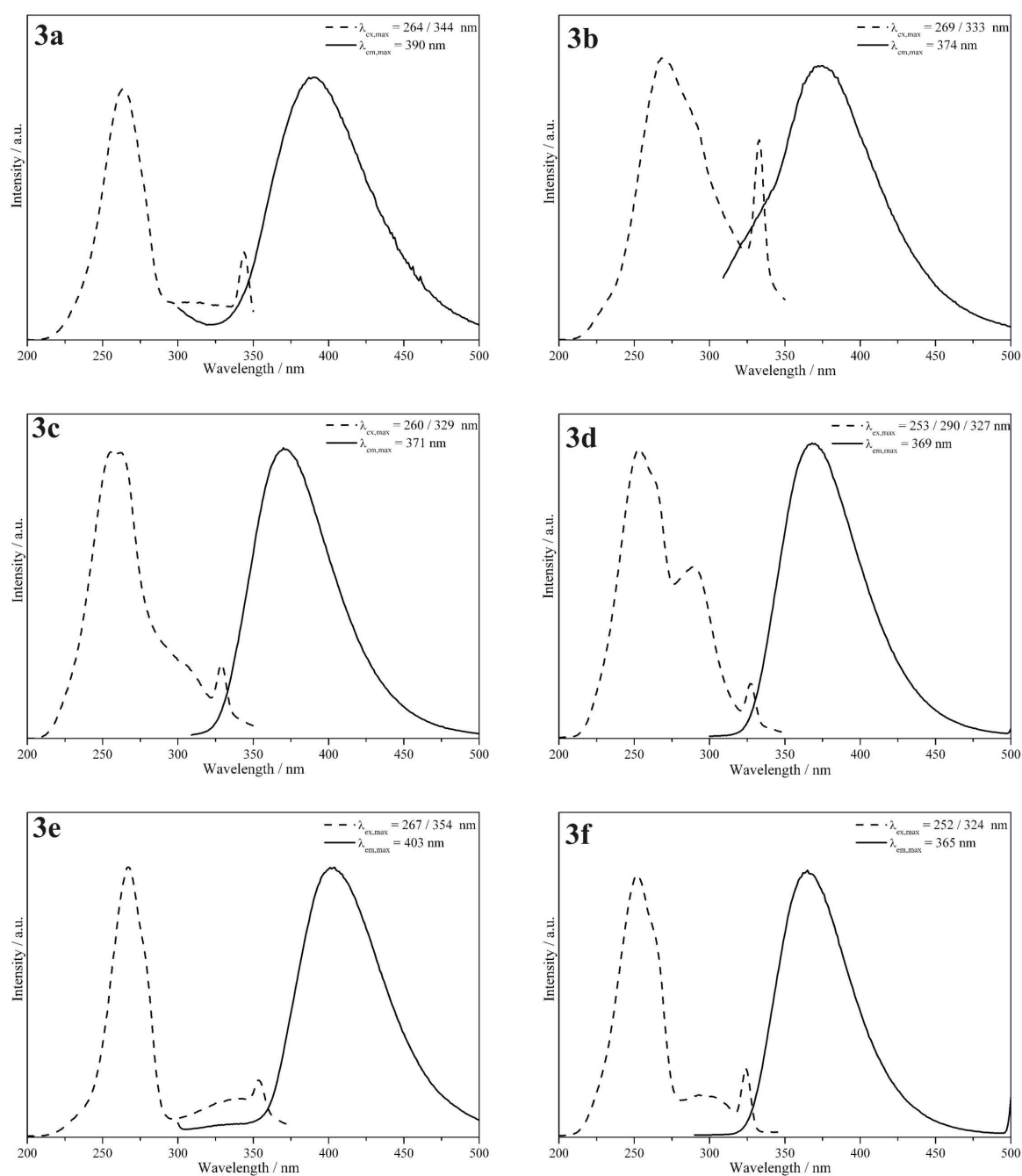


Figure S2. Photoluminescence spectra (dashed line: excitation, solid line: emission) of the alkali biuretooxophosphates **3a-f** in solution ($c = 2 \cdot 10^{-3} \text{ mol} \cdot \text{L}^{-1}$, solvent: water).

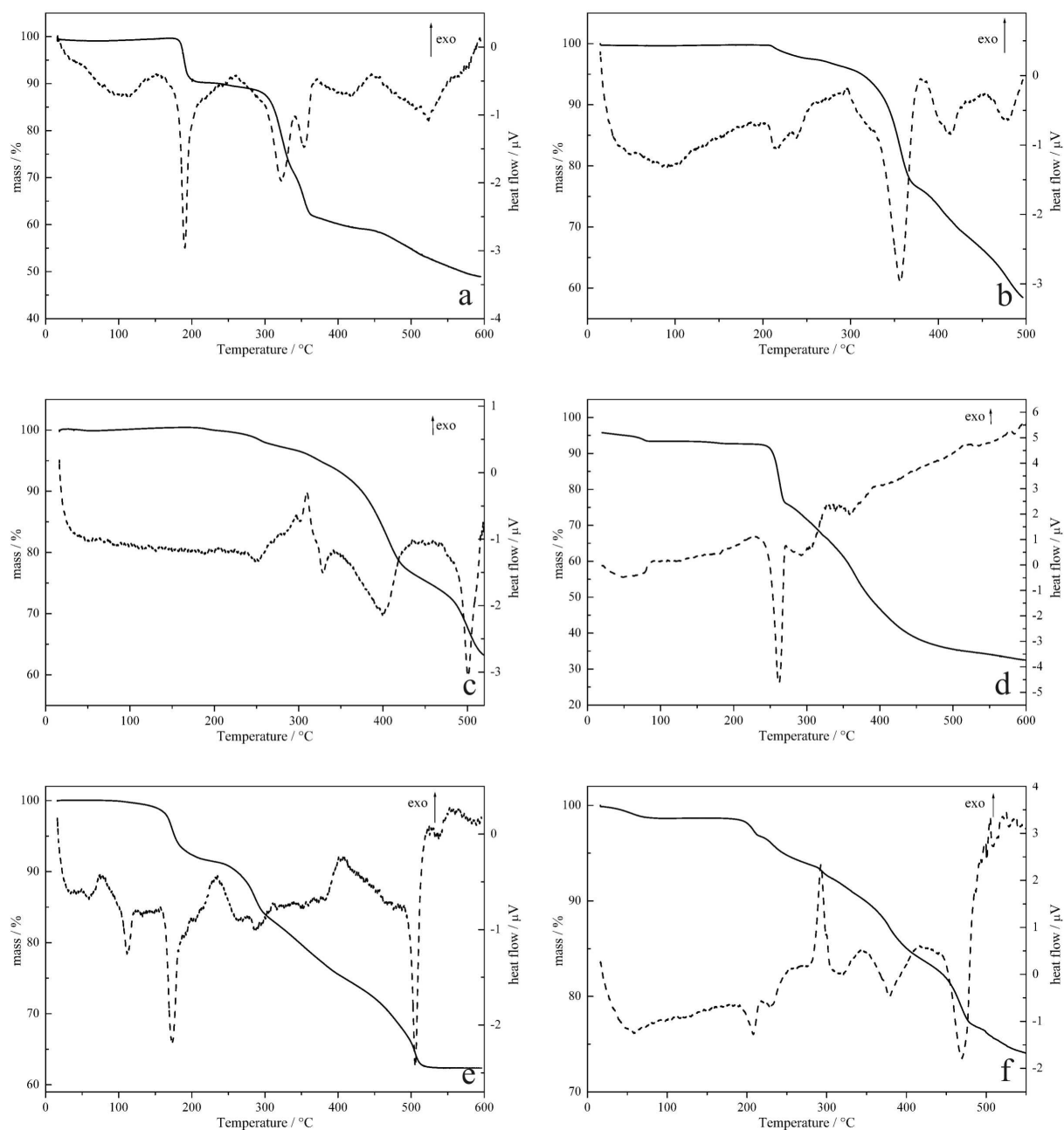


Figure S3: TG (solid line) and DTA (dashed line) curves of the alkali biuretooxophosphates **3a** (5.5 mg), **3b** (18.1 mg), **3c** (20.8 mg), **3d** (18.6 mg), **3e** (29.8 mg), and **3f** (34.1 mg), recorded with a heating rate of $5\text{ K}\cdot\text{min}^{-1}$.

7.1.3 Supporting Info for Chapter 5.2

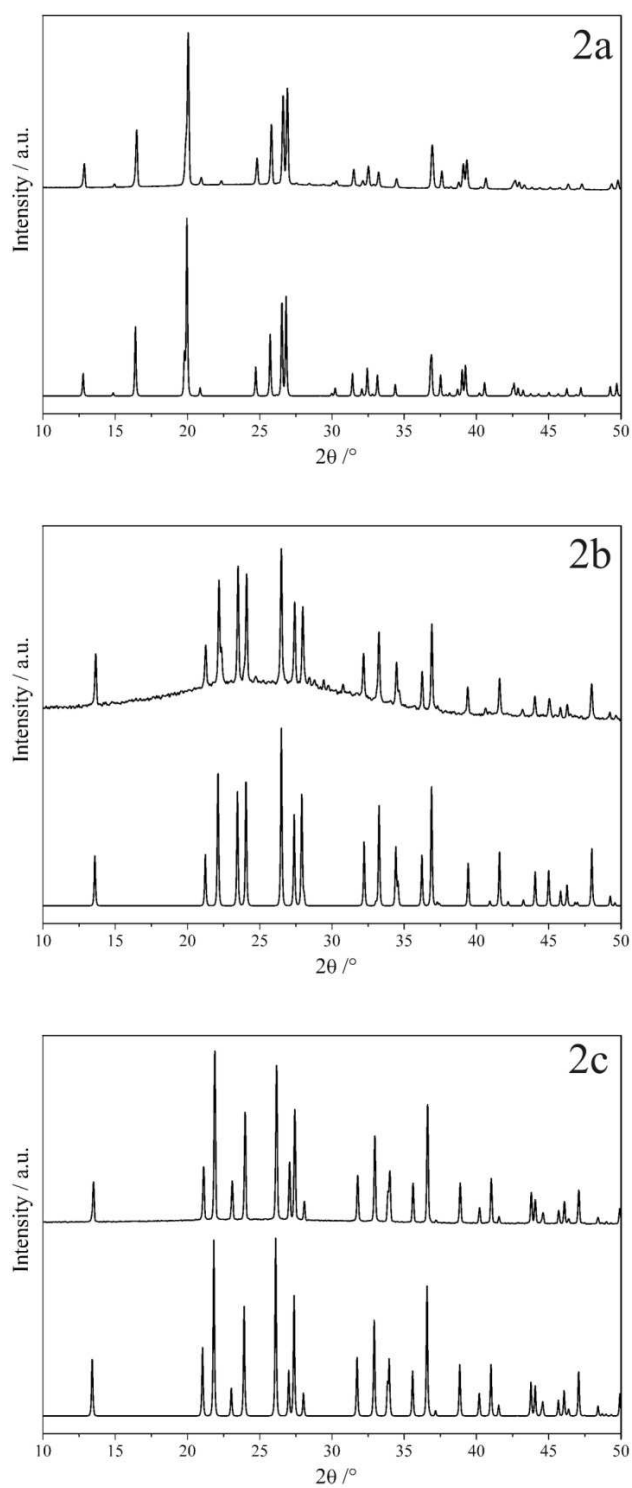


Figure S1. Powder X-ray diffraction patterns (Cu- $K_{\alpha 1}$) of **2a-c** (top: experimental, bottom: simulated).

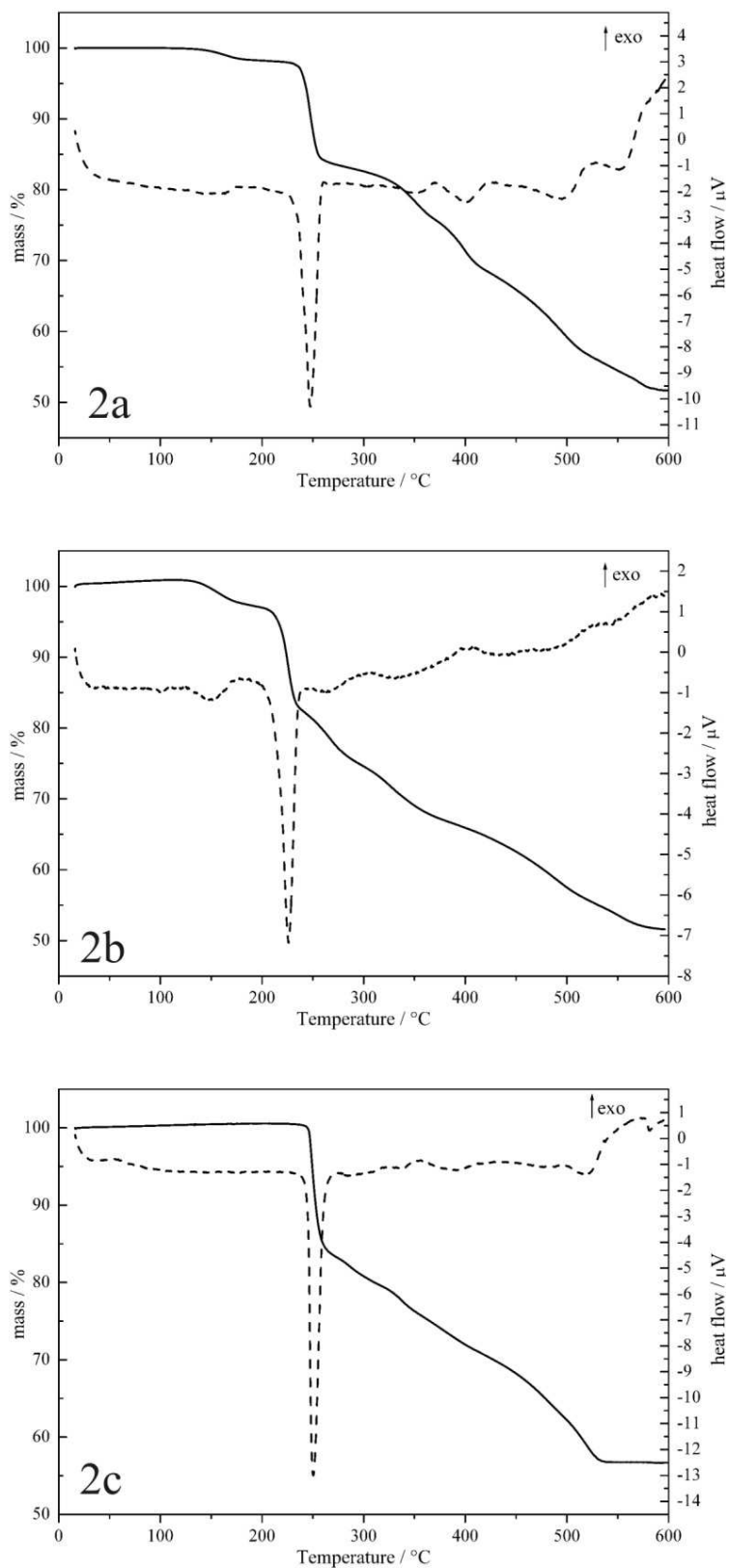


Figure S2. TG (solid line) and DTA (dashed line) curves of **2a** (24.0 mg), **2b** (28.7 mg), and **2c** (18.3 mg), recorded with a heating rate of $5 \text{ K}\cdot\text{min}^{-1}$.

7.2 List of Publications

A - Publications published as part of this thesis

Band gap reduction in poly(triazine imide) – an Organic Photocatalyst Candidate

E. McDermott, E. Wirnhier, W. Schnick, K. S. Viridi, C. Scheu, Y. Kauffmann, W. D. Kaplan, E. Z. Kurmaev, A. Moewes, *J. Phys. Chem. C* **2013**, *117*, 8806-8812.

Towards a New Generation of 2D Photocatalysts: Triazine-based Carbon Nitrides for Visible-Light Driven Hydrogen Evolution

K. Schwinghammer, B. Tuffy, M. B. Mesch, E. Wirnhier, C. Martineau, F. Taulelle, W. Schnick, J. Senker, B. V. Lotsch, *Angew. Chem.* **2013**, *125*, 2495-2499; *Angew. Chem. Int. Ed.* **2013**, *52*, 2435-2439.

Formation and Characterization of Melam, Melam Hydrate and a Melam-Melem Adduct

E. Wirnhier, M. B. Mesch, J. Senker, W. Schnick, *Chem. Eur. J.* **2013**, *19*, 2041-2049.

Ammonothermal Synthesis of Alkali *N,N'*-Bis(aminocarbonyl)phosphorodiamidates $M[PO_2(NHCONH_2)_2]$ (M = Na, K, Rb)

E. Wirnhier, R. D. Boller, W. Schnick, *Eur. J. Inorg. Chem.* **2012**, 3296-3301.

$Ca[PO_2(NH)_3(CO)_2]_2$ – The First Biuretooxophosphate with a Divalent Cation

E. Wirnhier, W. Schnick, *Z. Anorg. Allg. Chem.* **2012**, *638*, 920-924.

A Systematic Approach to Alkali Biuretooxophosphates

E. Wirnhier, W. Schnick, *Eur. J. Inorg. Chem.* **2012**, 1840-1847.

**Poly(triazine imide) with Intercalation of Lithium and Chloride Ions-
[(C₃N₃)₂(NH_xLi_{1-x})₃·LiCl]: A Crystalline 2D Carbon Nitride Network**

E. Wirnhier, M. Döblinger, D. Gunzelmann, J. Senker, B. V. Lotsch, W. Schnick, *Chem. Eur. J.* **2011**, *17*, 3213-3221.

B - Publications published prior to this thesis

**Activator-Controlled High Temperature In-Situ Ligand Synthesis for the Formation of
Rare Earth Thiolate Amide Coordination Polymers**

A. Zurawski, E. Wirnhier, K. Müller-Buschbaum, *Eur. J. Inorg. Chem.* **2009**, 2482-2486.

7.3 Contributions to Conferences

Phosphorhaltige Kohlenstoffnitride (oral presentation)

E. Wirnhier, W. Schnick,

Hirschegg-Seminar on Solid State Chemistry 2012, Hirschegg, Austria

**PTI – Poly(triazine imide): A new 2D Carbon Nitride Network with LiCl Intercalation
(oral presentation)**

E. Wirnhier, M. Döblinger, D. Gunzelmann, J. Senker, B. V. Lotsch, W. Schnick,

Hemdsärmelkolloquium – Symposium on Solid State Chemistry 2010, Stuttgart, Germany

**Poly(triazine imide) – A new 2D Carbon Nitride Network with Intercalation of Alkali
and Halide Ions (poster presentation)**

E. Wirnhier, M. Döblinger, D. Gunzelmann, J. Senker, W. Schnick,

Gordon Research Conference on Solid State Chemistry 2009, Oxford, United Kingdom

7.4 CSD and CCDC numbers

Crystallographic data were deposited with the Cambridge Crystallographic Data Centre (CCDC, http://www.ccdc.cam.ac.uk/data_request/cif; 12 Union Road, Cambridge CB2 1EZ, UK (fax: +44-1223-336-033, e-Mail: deposit@ccdc.cam.ac.uk) or the Fachinformationszentrum Karlsruhe (76344 Eggenstein-Leopoldshafen, Germany (fax: +49-7247-808-666, e-mail: crysdta@fiz-karlsruhe.de) and are available on quoting the respective CSD/CCDC depository numbers.

$C_6N_{11}H_9 \cdot 2H_2O$	CCDC-901046
$[(C_3N_3)_2(NH_xLi_{1-x})] \cdot LiCl$	CSD-422088
$Li[PO_2(NH)_3(CO)_2] \cdot H_2O$	CCDC-854273
$K[PO_2(NH)_3(CO)_2]$	CCDC-854274
$Rb[PO_2(NH)_3(CO)_2] \cdot 0.5H_2O$	CCDC-854276
$Cs[PO_2(NH)_3(CO)_2]$	CCDC-854275
$Ca[PO_2(NH)_3(CO)_2]_2$	CCDC-857517
$Na[PO_2(NHCONH_2)_2]$	CSD-424129
$K[PO_2(NHCONH_2)_2]$	CSD-424130
$Rb[PO_2(NHCONH_2)_2]$	CSD-424131

7.5 List of Abbreviations

2D	two-dimensional
4AP	4-amino-2,6-dihydropyrimidine
Å	Ångström
a.u.	arbitrary units
calcd.	calculated
CCD	charge coupled device
CCDC	Crystallographic Data Centre
cf.	confer
CN	carbon nitride
CP	cross polarization
CPPI	cross-polarization with polarization inversion
CSD	Cambridge Structural Database
CVD	chemical vapor deposition
DFT	density functional theory
DOS	density of states
DTA	differential thermal analysis
EA	elemental analysis
EELS	electron energy-loss spectroscopy
e.g.	<i>exempli gratia</i> , for example

et al.	<i>et alii</i> , and others
eV	electron volt
F_c	calculated structure factor
F_o	observed structure factor
FT	Fourier transformation
g-C ₃ N ₄	graphitic C ₃ N ₄
GOF / GooF	goodness of fit
h	hour
HOMO	highest occupied molecule orbital
ICP-AES	inductively coupled plasma – atomic emission spectroscopy
IPDS	imaging plate diffraction system
IR	infrared
M	molar
MAS	magic angle spinning
NMR	nuclear magnetic resonance
no.	number
PTI/LiCl	poly(triazine imide) with LiCl intercalation
PVD	physical vapor deposition
Ref.	reference
RXES	resonant X-ray emission spectroscopy
TEM	transmission electron microscope
TEoA	triethanolamine

TEY / TFY	total electron / fluorescence yield
TG	thermogravimetry
UV	ultra violet
VEELS	valence electron energy-loss spectroscopy
XANES	X-ray absorption near edge structure
XAS / XES	X-ray absorption / emission spectroscopy
XRD	X-ray diffraction
Z	formula units per unit cell
ZLP	zero-loss peak

7.6 Curriculum Vitae

Personal Details

Name	Eva Antonie Wirnhier
Date of birth	29.04.1985
Place of birth	Landau / Isar, Germany
Nationality	German

Education

Since 12/2012	BMW Group München, Technical Planning (Material and Process)
07/2009-12/2012	Research assistant in the group of Prof. Dr. W. Schnick (chair of solid-state chemistry, Department Chemie, LMU München) PhD thesis entitled: <i>“Solvothermal and Ionothermal Approaches to Carbon Nitride Chemistry”</i>
05/2009	Master of Science
12/2008-05/2009	Master thesis in the group of Prof. Dr. W. Schnick, entitled: <i>“Synthese and Charakterisierung von 2D-Kohlenstoffnitrid-Netzwerken mit Salz-Interkalation”</i> <i>„Synthesis and Characterization of 2D carbon nitride networks with salt intercalation“</i>
10/2007-05/2009	Master studies in Chemistry at LMU München
10/2007	Bachelor of Science

- 06/2007-10/2007 Bachelor thesis in the group of Prof. Dr. W. Schnick, entitled:
*“Synthese und Charakterisierung von Si/CN₂/NH-haltigen Precursoren
sowie deren Umsetzung zu Carbodiimido-Silicaten“*
*„Synthesis and Characterization of Si/CN₂/NH-Containing Precursors
and their Reaction to Carbodiimido-Silicates”*
- 10/2004-10/2007 Bachelor studies in Chemistry and Biochemistry at LMU München
- 06/2004 Allgemeine Hochschulreife (A-Levels)
- 09/1995-06/2004 High-school education at Gymnasium Landau
- 09/1991-07/1995 Primary school education at Grundschule Landau